UNIVERSITÀ DEGLI STUDI DI TORINO

SCUOLA DI DOTTORATO

DOTTORATO IN
SCIENZE AGRARIE, FORESTALI E ALIMENTARI

CICLO: XXXV

SAR DATA PROCESSING TECHNIQUES TO MONITOR VEGETATION STRUCTURAL PARAMETERS

Samuele De Petris

Docente guida:
Prof. Enrico Borgogno-Mondino

Coordinatori del Ciclo:
Prof. Eleonora Bonifacio
Prof. Domenico Bosco

ANNI
2019-2020; 2020-2021; 2021-2022

TABLE OF CONTENTS

1 Introduction 1

1.1 The Vegetation Structure Role 1

1.2 Monitoring Vegetation using SAR data 5

1.3 The Gap 10

2 Thesis Aims and Framework 14

3 Mapping SAR Geometric Distortions And Their Stability Along Time ... 22

4 Vegetation Structure Qualification 50

4.1 Amplitude-based Techniques 50

4.1.1 A Simplified Method for Water Depth Mapping Over Crops During Flood Based on Copernicus and DTM Open Data 50

4.2 Radar indices-based Techniques 81

4.2.1 Multitemporal Dual-Pol Sentinel-1 Data to Support Monitoring of Forest Post-Fire Dynamics 81

4.3 Polarimetry-based Techniques 115

4.3.1 Sentinel-1 Polarimetry to Map Apple Orchard Damage After a Storm 115

5 Vegetation Structure Quantification 143

5.1 Precision of the Reference Surveys 143

5.1.1 About Tree Height Measurement: Theoretical and Practical Issues for Uncertainty Quantification and Mapping 143

5.2 Phase-based Techniques 171

5.2.1 Uncertainties and Perspectives on Forest Height Estimates by Sentinel-1 Interferometry 171

5.2.2 Forest Height Estimation Using Sentinel-1 Interferometry. A Phase Unwrapping-Free Method Based on Least Squares Adjustment .. 195

6 Conclusions 211

1 INTRODUCTION

1.1 THE VEGETATION STRUCTURE ROLE

Vegetation Structure (VS) is a fundamental feature in environmental and agricultural sectors. It describes how the above-ground biomass (AGB) (Laurin et al., 2019; Segura and Kanninen, 2005) is distributed over the earth surface (Hao et al., 2007; Song et al., 1997; Spies, 1998) and reflects how plants search resources to growth. VS is also the most used feature to assess site's productivity, not only in ecology research, but also in forest/ agricultural management (Momo et al., 2021; Ochal et al., 2017; Skovsgaard et al., 1998). In fact, it is often used to define land cover type (Lund, 2002), to assess vegetation quality (Sillett et al., 2010) and vegetation ecosystem services (Hanewinkel et al., 2011) or to quantify biodiversity (Bohn and Huth, 2017; Martins et al., 2017). Moreover, it can be a good proxy of vegetation status and it is helpful in forecasting plants development and succession (Purves et al., 2008).

Nowadays, forests and crops have a crucial role in greenhouse gas sequestration (Pan et al., 2011) and in carbon market (Tavoni et al., 2007) highlighting the need of accurate VS measuring. For example, for forest inventories purposes VS is explored by measuring tree height and tree density and jointly adopted to estimate actual biomass volume (Neumann et al., 2016; Ter-Mikaelian and Korzukhin, 1997, p.; Zianis et al., 2005). Thus, a precise VS computation represents a necessary step for the estimation of carbon storage at local, national, and global scales. Moreover, VS monitoring allows to detect changes both in spatial and time domains permitting to analyse vegetation dynamics. Ordinarily, VS is classified in two main types (Fig.1):

(a) *Vertical Structure.* It describes how the plants colonize the epigean space determining different canopy layers. Vertical structure resulted from growing stage and disturbance effects. Canopy layers are bounded in

ideal planes, these strata regulate light access and therefore the competition between plants. Ordinarily, over crops only one canopy layer is present while in forest many layers are often present related to different cohorts. Vertical structure resulted by species diversity; monoplane canopy is often related to monospecific ecosystem while multiplane canopy is generated by different species association or different ages. Vertical structure also affects local environments factors (i.e., light availability, precipitation, wind) conditioning the new vegetation growing and succession.

(b) *Horizontal Structure*. It describes how the plants cover the ground creating more or less homogeneous patterns across the landscape. Horizontal structure and its spatial distribution is affected by many factors related to the ecological behaviour, microclimate, terrain features and species propagation strategy. In the first growing phase, horizontal structure depends on dissemination strategy and optimal nursery site. Subsequently, horizontal structure changes due to plants relationship (competition, species requirements). Homogeneous horizontal structure is common in crops due to human management, while is rare in forest where random or clustered structures are generally more common and are related to a greater size diversity and canopy gap presence. These features contribute to differentiate local environments within the same ecosystem improving the biodiversity (Piussi, 1994).

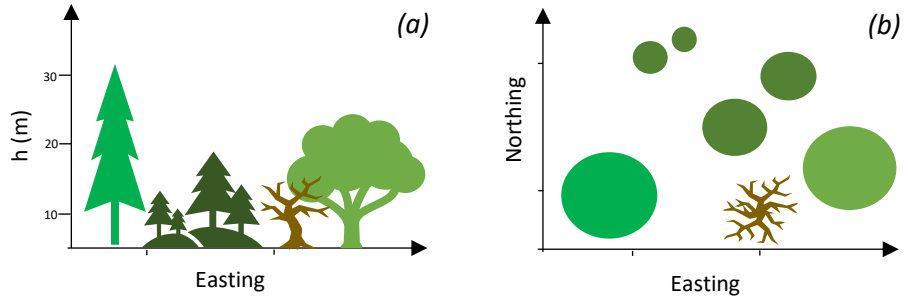

Figure 1. (a) Vertical structure of a forest; (b) Horizontal structure of a forest.

Both horizontal and vertical structure are characteristic features of a given vegetated ecosystem. For example, crops have a very homogeneous horizontal structure since they have been sown densely by farmer in order to optimize yield and harvesting. Also crop vertical structure is quite homogeneous until local anomalies or disturbances change the plants primary growth (e.g., nutrients/water deficit, disease or insect attack). Otherwise, natural vegetation (like forests or pastures) grows without human management, therefore no direct controls can be addressed to optimize benefits provided by these ecosystems. Other factors affecting VS are: the disturbance history and seeds dispersion strategy (Piussi, 1994). The former, changes VS by removing plants or their parts (e.g., crowns, branches, leaves) opening gaps in the canopy and differently affecting mortality in space (disturbance pattern) and in time according to severity (delayed effects). Otherwise, seeds dispersion strategy influences where plant starts to grow. For example, pioneer species like Larch colonize mineral soils exposed after soil erosion (Da Ronch et al., 2016) determining a patchy colonization (Albert et al., 2008); while Lodgepole pine tends homogeneously seeding after a fire (Pierce and Taylor, 2011). Finally, different environmental constrains like the topography (slope, aspect, altitude), competition, climate and soil proprieties affect VS spatial distribution (Lauenroth et al., 1993).

In this context, the measurement of VS is essential to objectively quantify vegetation biomass and dynamics permitting to analyse the actual status and forecast future behaviour to maximize benefits from plants.

In literature many methods were developed to measure VS at different scale of analysis, from large scale (high details) to small scale (low details). At large scale, the interest is focused on 3D features survey of single trees/crops or small vegetated areas (Hu and Li, 2020; Sperlich et al., 2014). Otherwise, small scale VS measure is often analysed at landscape level or over large areas (Graham and Blake, 2001). Adopted approaches range from traditional ground-based direct survey (La Marca, 2017; Piussi, 1994) to new instruments adoption based on digital analysis (Dandois and Ellis, 2010). The former approaches are the widely adopted ones in forestry and are based on protocols aiming at defining vertical and horizontal layers and elements (Assmann, 2013; La Marca, 2017; Laar and Akça, 2007; Piussi, 1994). The spatial structure can be quantified in terms of spatial distribution, species diversity, and variability of plants dimensions. The indices are either distance-independent or distance-dependent. The first group assess VS without any spatial reference, the second group assess the neighbourhood relations, accounting for small-scale differences in biodiversity. An exhaustive review of most adopted metrics and approaches based on ground survey were summarized by Pommerening (2002).

Currently, new technologies have been developed to measure VS mainly based on remote sensing. LiDAR (Light Detection And Ranging) (Dubayah and Drake, 2000), digital photogrammetry (Iglhaut et al., 2019; Tsouros et al., 2019, p.) and Spaceborne-sensors were extensively proposed to measure crops (Wójtowicz et al., 2016) or forest VS (Vali et al., 2020).

1.2 MONITORING VEGETATION USING SAR DATA

Especially spaceborne sensors allow a great data availability useful to monitor through the time and over large areas vegetation proprieties. Despite many works in literature involving points cloud by LiDAR and photogrammetry were developed to explore the 3D features of vegetated areas, these techniques proved to fail when large areas must be monitored or if a multitemporal analysis must be exploited (Richardson and Moskal, 2011). Conversely, if one has to work under such requirements, the only alternative is to adopt satellite remote sensing (Shoshany, 2000; Xue and Su, 2017). In this framework, space-borne Earth observation missions well-fit vegetation monitoring requirements making possible to map and detect wide areas, allowing a near-early change detection and a frequent updating of vegetation properties (Hüttich et al., 2014; Shanmugapriya et al., 2019). Synthetic aperture radar (SAR) is known to be to be useful for estimating vegetation geometric features recording data in all-weather condition included equatorial/tropical ones where clouds are almost constantly over (Liu et al., 2019; Sivasankar et al., 2018). Radar (radio detection and ranging) signal scattering is determined largely by geometric properties, such as shape and surface roughness, and by moisture content (Richards, 2009). As a result of all of these effects, radar imagery can capture a different set of properties of the region being imaged than optical data (Gerstl, 1990).

Despite optical data are widely used for mapping vegetation, radar still appears to be underused, in spite of its favourable peculiarities: independence from cloud coverage, haze layers and smoke plumes, sensibility to geometrical features of canopy and water content. Precisely in Italy (but also over the Alps), cloud cover is higher during spring and autumn making unavailable optical images exactly during the two most crucial phenological moments: the starting and ending of growing season. At the same time, in equatorial/ tropical areas clouds still persist for long time compromising optical data collection.

This condition affects the monitorability of vegetation both in Alpine and tropical contexts by optical remote sensing, making spaceborne radar proper to fill this gap. Moreover, while optical data strictly depend on surface and top of the canopy conditions, SAR signal can moderately penetrate tree crowns, making it possible to investigate moisture and structural properties of vegetated volumes (Szigarski et al., 2018). Changes in VS is one of the key features that allows detection and characterization of vegetation by SAR (Tanase et al., 2011). In particular, polarization state of SAR backscattered electro-magnetic signal appears to be a more sensible tool for analyzing vegetation geometrical properties than optical data and, therefore, it can be adopted to detect and monitor disturbance-induced effects on vegetation. SAR polarimetry is the technique that allows to analyse the polarization state of the electromagnetic signal backscattered by earth surface to the sensor. In particular, vegetation canopy determines the so-called volume scattering mechanism. The interaction with vegetation canopy generates a depolarization of electromagnetic wave. In fact, canopy elements (supposed as cylinder-like objects) induce a rotation of the polarization vector depending on dipoles orientation (Richards, 2009) (Fig. 2). Depolarization increases with canopy density due to random orientation of branches/twigs: the effect is a strong backscatter of the cross-polarized band. Differently, a cross-polarized signal show lower values while moving to sparse vegetation or bare soil conditions (Ulaby et al., 1981).

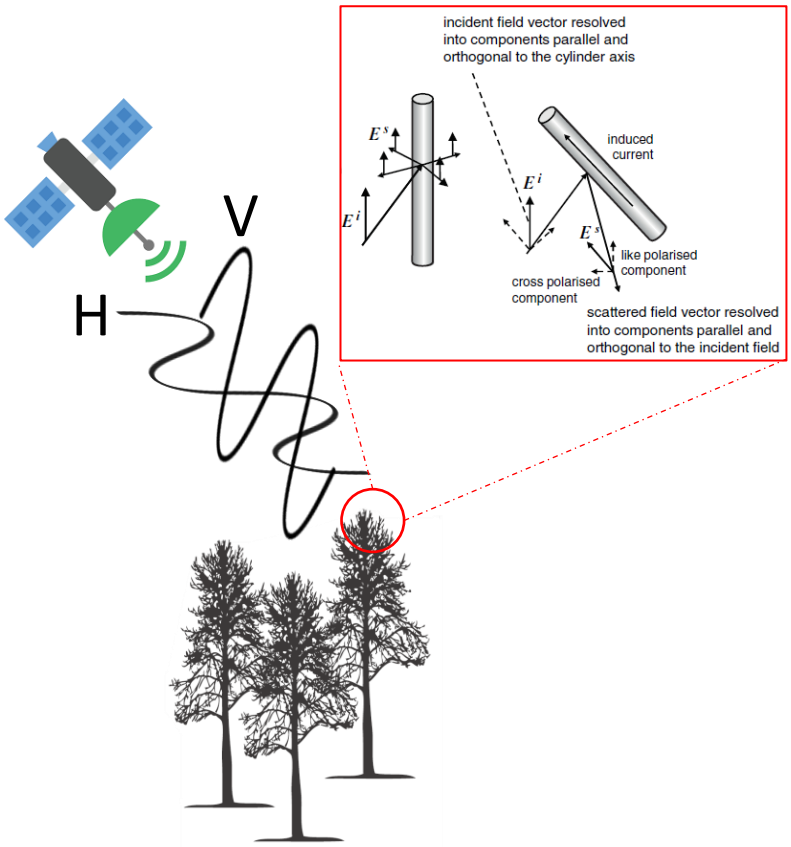

Figure 2. SAR signal depolarization induced by vegetation canopy elements (modified from Richards, 2009).

A disturbance (like forest fire, stems breakage, crop lodging by storm or crop flooding) could partially, or completely, remove tree canopy leaving stems and ground exposed. The disturbance effects on backscattering also depends on polarization; cross-polarized signal (HV or VH - horizontal/vertical transmitted/received signal) is known to be more sensitive to volume features of scatterers. A decrease of cross polarized backscattering might be observed as a consequence of canopy volume loss caused by fire (Minchella et al., 2009); instead, variations of the co-polarized backscattering generally depends on the rate of exposed soil within the pixel (Imperatore et al., 2017). Vertical polarization is known to be more sensitive to objects with a prevailing vertical

size, e.g. tree stems, that usually are not completely destroyed for example during a fire (Bernhard et al., 2012); double bounce and surface scattering effects tend, in fact, to become important where signal more easily penetrate tree crowns and reach the ground.

In literature, many approaches were adopted to monitor vegetation disturbances based on SAR polarimetry (Lee and Pottier, 2017). For example, the polarimetric decomposition (Cloude and Pottier, 1996) derives second-order statistics from the covariance matrix, i.e. Entropy - H, anisotropy - A, alpha - α permitting to assess changes in backscattered signal. Unfortunately, such an approach is based on raw (complex values) SAR data processing, making it difficult to approach multitemporal analysis over large areas. A possible more operational alternative is the one based on the computation of simple polarimetric indices like Radar Vegetation Index (RVI) (Kim et al., 2011) and Cross Ratio (CR) (Paloscia et al. 1999). The ratio of dual-pol bands, typically one co-polarized and the other cross-polarized, (e.g. VV and VH) proved to be effective in describing backscattering behaviour of vegetation providing a measure of the depolarization level. CR showed significant linear correlations with vegetation density, Normalized Difference Vegetation Index (NDVI), Leaf Area Index (LAI) and Vegetation Water Content (VWC) (De Petris et al., 2022; Kim et al., 2011; Vreugdenhil et al., 2018). In the multitemporal context, time series of optical-retrieved vegetation indices proved to effectively describe the effects of forest disturbances like fires (Telesca and Lasaponara, 2006). In particular, the present availability of big and free archives of remotely sensed images like Google Earth Engine (GEE) allows to improve this kind of analysis by densifying time series over wide areas. Nevertheless, the literature about multitemporal analysis of disturbance dynamics trough the SAR imagery adoption is still limited (Belenguer-Plomer et al., 2019; Bourgeau-Chavez et al., 2002; Carreiras et al., 2020; Engelbrecht et al., 2017; Gimeno et al., 2004; Kasischke et al., 1994; Lohberger et al., 2018; Verhegghen et al., 2016) and no works focusing on the post-disturbance

dynamics monitoring (i.e. severity and recovery processes) were extensively explored.

Among SAR application and methods, SAR interferometry (InSAR) technique has been extensively adopted to generate digital elevation models (DEM), that are intended to provide a continuous representation of Earth topography, included vegetated areas. Theoretically speaking, radar interferometry can generate highly precise height estimates related to the difference of path length between scattered signals received by two properly positioned antennas (Hanssen, 2001). Therefore, InSAR technique is a promising tool to measure vegetation vertical structure as deeply reported in literature. In fact, many methods based on SAR interferometry were proposed to estimate vegetation height and can be summarized into three main categories: (a) Pol-InSAR methodology (Cloude et al., 2013; Garestier et al., 2007; Managhebi et al., 2018); (b) Coherence-based methodology (Askne and Santoro, 2005; J. I. Askne et al., 1997; Soja et al., 2014) and (c) Interferometric phase-based methodology (Romero-Puig and Lopez-Sanchez, 2021; Santoro et al., 2005). Unfortunately, many SAR missions (e.g. Sentinel-1, ICEYE-X, PAZ) are not suitable for (a) due to their lack of quad-pol channels that would be required (Ainsworth et al., 2008; De Petris et al., 2021). Approach (b) is mainly applied using tandem acquisition mode that guarantees a higher coherence over vegetation. Since the majority of SAR missions do not support tandem acquisition, coherence values over vegetation are generally low limiting this approach. Consequently, approach (c) appears to be the most promising because it is somehow consistent with technical feature of the majority of SAR missions acquiring in single- or dual- pole mode.

1.3 THE GAP

SAR sensors allow to explore different vegetation features according to operation wavelength (band) designed. For example, long wavelengths like L- or S-band (15 cm and 30 cm of wavelength respectively) allow to penetrate the canopy acquiring data about vegetation ground level and canopy scattering proprieties, while shorter wavelengths like X-band (2.5 cm wavelength) allow to retrieve information about upper canopy features. Unfortunately, shorter the wavelengths more sensitive is the signal to small variations introducing some uncertainties in processed data especially for InSAR techniques (Ferretti et al., 2007). C-band sensors allows a moderate penetration constituting a trade-off between different approaches and techniques involved during vegetation analysis by SAR data.

Until 70's, more than 30 spaceborne SAR missions were lunched recording a lot of data (Fig. 3). Despite this great availability of SAR missions some operative problems still affect SAR users' community. The main issues are the following:

(a) *Imagery coverage.*

Few SAR missions, currently, are designed for the continuous earth observation. Therefore, available images have usually a small footprint compromising the spatial extent recorded by a single acquisition and finally negatively affect the temporal resolution and monitoring capability (Bovenga et al., 2018). As result, often entire earth zones are not surveyed.

(b) *Complex processing.*

According to Vollrath (2020) and Reiche (2016), the complexity of SAR data pre-processing is one of the main reasons for its slow uptake by a wider user community. In fact, SAR data are natively recorded as complex values (I/Q components) geocoded in SAR geometry (Range and Azimuth), making necessary signal focusing steps to generate a ready-to-use image. Moreover, due to SAR intrinsic acquisition

geometry many radiometric/geometric distortions are present, and a proper masking procedure is needed before any processing in order to remove unreliable observations and strengthen related deductions.

(c) *Data and Software availability.*

Although more than 30 SAR missions have provided data for different applications, their data access is not free to all users. Except commercial missions (e.g., ICEYE), the majority of SAR missions provide data after a formal request and for only research purposes, restricting the final potential users to only researchers. This fact limits the adoption of this kind data in operative contexts like the agro-forest ones, where institution or practitioners are often called to survey and properly process environmental data in order to plan/ manage natural resources. Furthermore, due to the complexity of data management, processing software were historically not free.

The importance of open access and data sharing in general, and in particular for earth observation data, has been acknowledged by many authors (Borowitz, 2017; Turner et al., 2015), however the same attention has not yet been put on the importance of code sharing or open source software to manage these data. Many commercial software were developed to support user in SAR data processing. Some examples are: GAMMA (Werner et al., 2000), ERDAS Imagine (Geosystems, 2004), SARscape (Sahraoui et al., 2006), PCI Geomatica (Geomatics, 2005); Matlab (Gorham and Moore, 2010). Unfortunately, despite the effectiveness of such software, their costs limited their adoption by a wider community of not-scientists. In this framework, free software could be a suitable choice for processing SAR data from a not-scientists due to their more availability, bur currently very few software or packages were developed (e.g. Orfeo toolbox by CNES, Python based routine, Sentinel Platform by ESA).

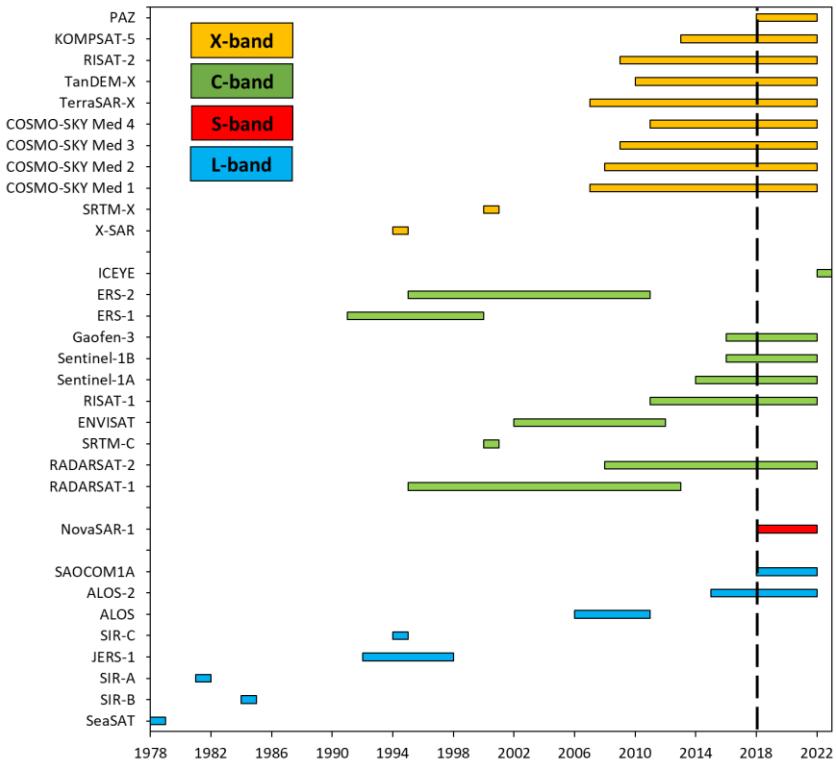

Figure 3. SAR missions timeline. Dotted line is the starting date of Ph.D. period.

All these issues negatively affect the theological transfer into operative agro-forestry sector of SAR data. In this framework it is clear how there is a gap concerning the use of SAR data and the development of standardize procedures to answer to operative agro-forest needs.

Currently (2022), among the existing spaceborne SAR missions, Sentinel-1 (S1) stood out since beginning; its data were made openly available to the public via the Copernicus Open Access Hub (https://scihub. copernicus.eu/). Although the data of historic missions, such as ERS or ENVISAT, become progressively released as well, Copernicus Programme provides unrestricted access to every citizen throughout the world and to foster science, economic growth, and decision-making the European Union (Aschbacher, 2017). Besides the actual open availability of S1 data the SNAP software (Veci et al., 2014) is continuously

being developed by ESA (European Space Agency) to assist all users in the exploitation of the products provided within the Copernicus Programme. More than 500’000 downloads at 2019 (Braun, 2021) proved how SNAP is the most actively used open-source software in the domain of remote sensing. It not only allows basic operations of SAR pre-processing and analysis but also provides all necessary tools to properly manage the most adopted SAR data processing techniques.

2 THESIS AIMS AND FRAMEWORK

Trying to fill the previous-mentioned gap, the thesis aims were aimed at exploring the potentialities and the limitations of S1 imagery for monitoring VS, longing for the technological transfer of proposed methodologies to local institutions/technicians involved in agro-forest resource management.

To achieve these tasks, the thesis was structured as reported in figure 4.

Two main parts according to the main approaches involved generally in remote sensing (Gomarasca, 2009) divide this manuscript: one aimed at qualifying the VS and its variation in time and space domains; and the other aimed at quantifying VS by mainly measuring vegetation height.

Four techniques were explored based on SAR signal proprieties:

(a) Amplitude-based

(b) Radar indices-based

(c) Polarimetry-based

(d) Phase-based

Concerning (a), VS was explored by monitoring through S1 amplitude imagery how flood changes horizontal structure of crops (Section 4.1.1). Subsequently, a morphological model based on DTM (Digital Terrain Model), and open data was proposed to estimate the flood water depth over the crops and used to assess flood-related crops damage.

Concerning (b), forest VS was explored using a multitemporal stack of radar index (i.e., cross-ratio) aiming at measuring VS change after a forest fire and measuring the VS recovery process (Section 4.2.1).

Concerning (c), polarimetry was applied to S1 data to detect and map apple orchards damaged after a storm (Section 4.3.1). Scattering matrix was

decomposed to derive metrics useful in order to describe the VS variation induced by the trees breakage/uprooting.

Concerning (d), the phase component of complex SAR signal was adopted to measure forest height by using the interferometric technique. Preliminary, a work (Section 5.2.1.) was proposed to define a method to proper select the interferometric pair and objectively set some operational parameters involving during the interferogram processing. Subsequently a new phase unwrapping-free approach was proposed in order to measure forest height by the jointly used of interferometric measures and levelling net adjustment approach (Section 5.2.2).

Concurrently, two propaedeutic works were also here proposed. The first one (Section 3) is aimed at mapping SAR geometric distortions and their stability along time to assess which land use is more monitorable by S1 multitemporal approach. The second one (Section 5.1.1) gives an idea about the accuracy of ordinary ground-based tree height measures in order to proper compare forest heights obtained by proposed approach based on InSAR respect to the ones usually surveyed in field.

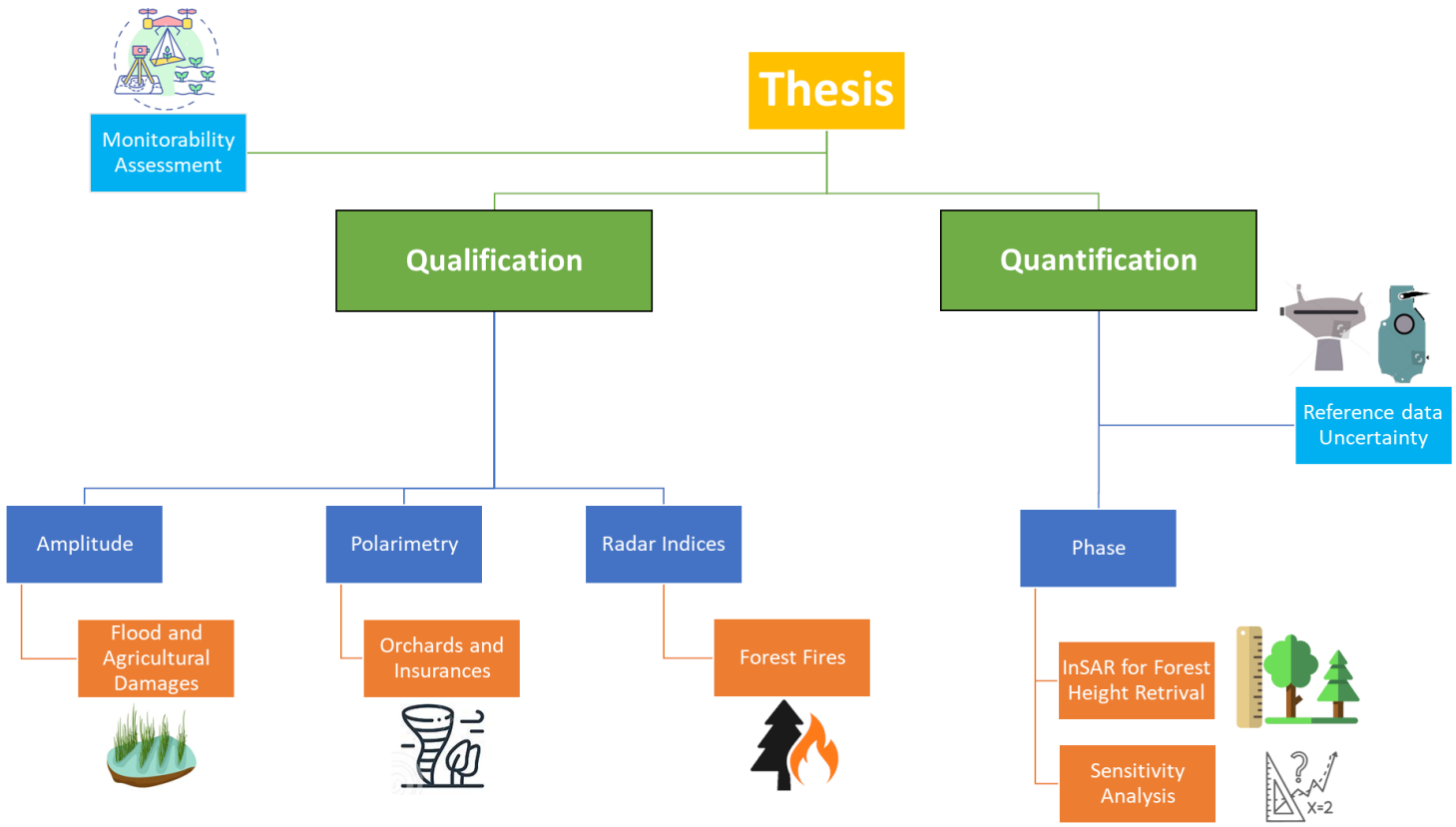

Figure 4. Thesis Framework. In green explored approaches. In blue adopted techniques. In orange developed works. In light-blue propaedeutic works.

References:

Ainsworth, T.L., Kelly, J., Lee, J.-S., 2008. Polarimetric analysis of dual polarimetric SAR imagery, in: 7th European Conference on Synthetic Aperture Radar. VDE, pp. 1–4.

Albert, C.H., Thuiller, W., Lavorel, S., Davies, I.D., Garbolino, E., 2008. Land-use change and subalpine tree dynamics: colonization of Larix decidua in French subalpine grasslands. Journal of Applied Ecology 45, 659–669.

Aschbacher, J., 2017. ESA's earth observation strategy and Copernicus, in: Satellite Earth Observations and Their Impact on Society and Policy. Springer, Singapore, pp. 81–86.

Askne, J., Dammert, P.B., Smith, G., 1997. Interferometric SAR observations of forested areas, in: Third ERS Symposium on Space at the Service of Our Environment. p. 337.

Askne, J., Santoro, M., 2005. Multitemporal repeat pass SAR interferometry of boreal forests. IEEE Transactions on Geoscience and Remote Sensing 43, 1219–1228.

Askne, J.I., Dammert, P.B., Ulander, L.M., Smith, G., 1997. C-band repeat-pass interferometric SAR observations of the forest. IEEE Transactions on Geoscience and Remote Sensing 35, 25–35.

Assmann, E., 2013. The principles of forest yield study: studies in the organic production, structure, increment and yield of forest stands. Elsevier.

Belenguer-Plomer, M.A., Tanase, M.A., Fernandez-Carrillo, A., Chuvieco, E., 2019. Burned area detection and mapping using Sentinel-1 backscatter coefficient and thermal anomalies. Remote Sensing of Environment 233, 111345.

Bernhard, E.-M., Stein, E., Twele, A., Gähler, M., 2012. SYNERGISTIC USE OF OPTICAL AND RADAR DATA FOR RAPID MAPPING OF FOREST FIRES IN THE EUROPEAN MEDITERRANEAN. The International Archives of the Photogrammetry, Remote Sensing and Spatial Information Sciences XXXVIII-4-W19, 27–32. https://doi.org/10.5194/isprsarchives-XXXVIII-4-W19-27-2011

Bohn, F.J., Huth, A., 2017. The importance of forest structure to biodiversity–productivity relationships. Royal Society open science 4, 160521.

Borowitz, M., 2017. Open space: The global effort for open access to environmental satellite data. MIT Press.

Bourgeau-Chavez, L.L., Kasischke, E.S., Brunzell, S., Mudd, J.P., Tukman, M., 2002. Mapping fire scars in global boreal forests using imaging radar data. International Journal of Remote Sensing 23, 4211–4234.

Bovenga, F., Belmonte, A., Refice, A., Pasquariello, G., Nutricato, R., Nitti, D.O., Chiaradia, M.T., 2018. Performance analysis of satellite missions for multi-temporal SAR interferometry. Sensors 18, 1359.

Bragg, D.C., 2014. Accurately Measuring the Height of (Real) Forest Trees. Journal of Forestry 112, 51–54. https://doi.org/10.5849/jof.13-065

Braun, A., 2021. Retrieval of digital elevation models from Sentinel-1 radar data–open applications, techniques, and limitations. Open Geosciences 13, 532–569.

Carreiras, J.M., Quegan, S., Tansey, K., Page, S., 2020. Sentinel-1 observation frequency significantly increases burnt area detectability in tropical SE Asia. Environmental Research Letters 15, 054008.

Cloude, S.R., Chen, H., Goodenough, D.G., 2013. Forest height estimation and validation using Tandem-X polinsar, in: 2013 IEEE International Geoscience and Remote Sensing Symposium-IGARSS. IEEE, pp. 1889–1892.

Cloude, S.R., Pottier, E., 1996. A review of target decomposition theorems in radar polarimetry. IEEE transactions on geoscience and remote sensing 34, 498–518.

Da Ronch, F., Caudullo, G., Tinner, W., de Rigo, D., 2016. Larix decidua and other larches in Europe: distribution, habitat, usage and threats.

Dandois, J.P., Ellis, E.C., 2010. Remote Sensing of Vegetation Structure Using Computer Vision. Remote Sensing 2, 1157–1176. https://doi.org/10.3390/rs2041157

De Petris, S., Berretti, R., Sarvia, F., Borgogno Mondino, E., 2020. When a definition makes the difference: operative issues about tree height measures from RPAS-derived CHMs. iForest-Biogeosciences and Forestry 13, 404.
De Petris, S., Sarvia, F., Borgogno-Mondino, E., 2022. SENTINEL-1 DATA TIME SERIES TO SUPPORT FOREST POLICE IN HARVESTINGS DETECTION. ISPRS Annals of the Photogrammetry, Remote Sensing and Spatial Information Sciences 3, 225–232.
De Petris, S., Sarvia, F., Gullino, M., Tarantino, E., Borgogno-Mondino, E., 2021. Sentinel-1 Polarimetry to Map Apple Orchard Damage after a Storm. Remote Sensing 13, 1030.
Dubayah, R.O., Drake, J.B., 2000. Lidar remote sensing for forestry. Journal of forestry 98, 44–46.
Engelbrecht, J., Theron, A., Vhengani, L., Kemp, J., 2017. A simple normalized difference approach to burnt area mapping using multi-polarisation C-Band SAR. Remote Sensing 9, 764.
Ferretti, A., Monti-Guarnieri, A.V., Prati, C.M., Rocca, F., Massonnet, D., 2007. INSAR Principles B. ESA publications.
Garestier, F., Dubois-Fernandez, P.C., Papathanassiou, K.P., 2007. Pine forest height inversion using single-pass X-band PolInSAR data. IEEE Transactions on Geoscience and Remote Sensing 46, 59–68.
Geomatics, P.C.I., 2005. PCI Geomatica User Guide.
Geosystems, L., 2004. ERDAS imagine. Atlanta, Georgia 7, 3209–3241.
Gerstl, S.A.W., 1990. Physics concepts of optical and radar reflectance signatures A summary review. International Journal of Remote Sensing 11, 1109–1117.
Gimeno, M., San-Miguel-Ayanz, J., Schmuck, G., 2004. Identification of burnt areas in Mediterranean forest environments from ERS-2 SAR time series. International Journal of Remote Sensing 25, 4873–4888.
Gomarasca, M.A., 2009. Basics of geomatics. Springer Science & Business Media.
Gorham, L.A., Moore, L.J., 2010. SAR image formation toolbox for MATLAB, in: Algorithms for Synthetic Aperture Radar Imagery XVII. SPIE, pp. 46–58.
Graham, C.H., Blake, J.G., 2001. Influence of patch-and landscape-level factors on bird assemblages in a fragmented tropical landscape. Ecological Applications 11, 1709–1721.
Hagberg, J.O., Ulander, L.M., Askne, J., 1995. Repeat-pass SAR interferometry over forested terrain. IEEE Transactions on Geoscience and Remote Sensing 33, 331–340.
Hanewinkel, M., Hummel, S., Albrecht, A., 2011. Assessing natural hazards in forestry for risk management: a review. European Journal of Forest Research 130, 329–351.
Hanssen, R.F., 2001. Radar interferometry: data interpretation and error analysis. Springer Science & Business Media.
Hao, Z., Zhang, J., Song, B., Ye, J., Li, B., 2007. Vertical structure and spatial associations of dominant tree species in an old-growth temperate forest. Forest Ecology and Management 252, 1–11.
Hu, X., Li, D., 2020. Research on a single-tree point cloud segmentation method based on uav tilt photography and deep learning algorithm. IEEE Journal of Selected Topics in Applied Earth Observations and Remote Sensing 13, 4111–4120.
Hüttich, C., Eberle, J., Shvidenko, A., Schepaschenko, D., 2014. Supporting a forest observation system for Siberia: Earth observation for monitoring, assessing and providing forest resource information.
Iglhaut, J., Cabo, C., Puliti, S., Piermattei, L., O'Connor, J., Rosette, J., 2019. Structure from motion photogrammetry in forestry: A review. Current Forestry Reports 5, 155–168.
Imperatore, P., Azar, R., Calò, F., Stroppiana, D., Brivio, P.A., Lanari, R., Pepe, A., 2017. Effect of the Vegetation Fire on Backscattering: An Investigation Based on Sentinel-1 Observations. IEEE Journal of Selected Topics in Applied Earth Observations and Remote Sensing 10, 4478–4492. https://doi.org/10.1109/JSTARS.2017.2717039
Kasischke, E.S., Bourgeau-Chavez, L.L., French, N.H., 1994. Observations of variations in ERS-1 SAR image intensity associated with forest fires in Alaska. IEEE Transactions on Geoscience and Remote Sensing 32, 206–210.
Kim, Y., Jackson, T., Bindlish, R., Lee, H., Hong, S., 2011. Radar vegetation index for estimating the vegetation water content of rice and soybean. IEEE Geoscience and Remote Sensing Letters 9, 564–568.

La Marca, O., 2017. Elementi di dendrometria. Pàtron.
Laar, A. van, Akça, A., 2007. Forest mensuration, 2. ed., completely rev. and supplemented. ed, Managing forest ecosystems. Springer, Dordrecht.
Lauenroth, W.K., Urban, D.L., Coffin, D.P., Parton, W.J., Shugart, H.H., Kirchner, T.B., Smith, T.M., 1993. Modeling vegetation structure-ecosystem process interactions across sites and ecosystems. Ecological Modelling 67, 49–80.
Laurin, G.V., Ding, J., Disney, M., Bartholomeus, H., Herold, M., Papale, D., Valentini, R., 2019. Tree height in tropical forest as measured by different ground, proximal, and remote sensing instruments, and impacts on above ground biomass estimates. International Journal of Applied Earth Observation and Geoinformation 82, 101899.
Lee, J.-S., Pottier, E., 2017. Polarimetric radar imaging: from basics to applications. CRC press.
Liu, C., Chen, Z.-X., Yun, S., Chen, J., Hasi, T., PAN, H., 2019. Research advances of SAR remote sensing for agriculture applications: A review. Journal of integrative agriculture 18, 506–525.
Lohberger, S., Stängel, M., Atwood, E.C., Siegert, F., 2018. Spatial evaluation of Indonesia's 2015 fire-affected area and estimated carbon emissions using Sentinel-1. Global change biology 24, 644–654.
Lund, H.G., 2002. When is a forest not a forest? Journal of Forestry 100, 21–28.
Managhebi, T., Maghsoudi, Y., Zoej, M.J.V., 2018. A volume optimization method to improve the three-stage inversion algorithm for forest height estimation using PolInSAR data. IEEE Geoscience and Remote Sensing Letters 15, 1214–1218.
Martins, A.C., Willig, M.R., Presley, S.J., Marinho-Filho, J., 2017. Effects of forest height and vertical complexity on abundance and biodiversity of bats in Amazonia. Forest Ecology and Management 391, 427–435.
Minchella, A., Del Frate, F., Capogna, F., Anselmi, S., Manes, F., 2009. Use of multitemporal SAR data for monitoring vegetation recovery of Mediterranean burned areas. Remote Sensing of Environment 113, 588–597.
Momo, E.J., De Petris, S., Sarvia, F., Borgogno-Mondino, E., 2021. Addressing Management Practices of Private Forests by Remote Sensing and Open Data: a Tentative Procedure. Remote Sensing Applications: Society and Environment 100563.
Neumann, M., Moreno, A., Mues, V., Härkönen, S., Mura, M., Bouriaud, O., Lang, M., Achten, W.M., Thivolle-Cazat, A., Bronisz, K., 2016. Comparison of carbon estimation methods for European forests. Forest Ecology and Management 361, 397–420.
Ochal, W., Socha, J., Pierzchalski, M., 2017. The effect of the calculation method, plot size, and stand density on the accuracy of top height estimation in Norway spruce stands. iForest-Biogeosciences and Forestry 10, 498.
Paloscia, S., Macelloni, G., Pampaloni, P., Sigismondi, S., 1999. The potential of C-and L-band SAR in estimating vegetation biomass: the ERS-1 and JERS-1 experiments. IEEE Transactions on Geoscience and Remote Sensing 37, 2107–2110.
Pan, Y., Birdsey, R.A., Fang, J., Houghton, R., Kauppi, P.E., Kurz, W.A., Phillips, O.L., Shvidenko, A., Lewis, S.L., Canadell, J.G., 2011. A large and persistent carbon sink in the world's forests. science 333, 988–993.
Pierce, A.D., Taylor, A.H., 2011. Fire severity and seed source influence lodgepole pine (Pinus contorta var. murrayana) regeneration in the southern cascades, Lassen volcanic National Park, California. Landscape Ecology 26, 225–237.
Piussi, P., 1994. Selvicoltura generale.
Pommerening, A., 2002. Approaches to quantifying forest structures. Forestry: An International Journal of Forest Research 75, 305–324.
Purves, D.W., Lichstein, J.W., Strigul, N., Pacala, S.W., 2008. Predicting and understanding forest dynamics using a simple tractable model. Proceedings of the National Academy of Sciences 105, 17018–17022.
Reiche, J., Lucas, R., Mitchell, A.L., Verbesselt, J., Hoekman, D.H., Haarpaintner, J., Kellndorfer, J.M., Rosenqvist, A., Lehmann, E.A., Woodcock, C.E., 2016. Combining satellite data for better tropical forest monitoring. Nature Climate Change 6, 120–122.
Richards, J.A., 2009. Remote sensing with imaging radar. Springer.

Richardson, J.J., Moskal, L.M., 2011. Strengths and limitations of assessing forest density and spatial configuration with aerial LiDAR. Remote Sensing of Environment 115, 2640–2651.
Romero-Puig, N., Lopez-Sanchez, J.M., 2021. A Review of Crop Height Retrieval Using InSAR Strategies: Techniques and Challenges. IEEE Journal of Selected Topics in Applied Earth Observations and Remote Sensing.
Sahraoui, O.H., Hassaine, B., Serief, C., Hasni, K., 2006. Radar interferometry with Sarscape software. Photogrammetry and Remote Sensing.
Santoro, M., Askne, J., Dammert, P.B., 2005. Tree height influence on ERS interferometric phase in boreal forest. IEEE Transactions on Geoscience and Remote Sensing 43, 207–217.
Segura, M., Kanninen, M., 2005. Allometric models for tree volume and total aboveground biomass in a tropical humid forest in Costa Rica 1. Biotropica: The Journal of Biology and Conservation 37, 2–8.
Shanmugapriya, P., Rathika, S., Ramesh, T., Janaki, P., 2019. Applications of remote sensing in agriculture-A Review. International Journal of Current Microbiology and Applied Sciences 8, 2270–2283.
Shoshany, M., 2000. Satellite remote sensing of natural Mediterranean vegetation: a review within an ecological context. Progress in Physical Geography 24, 153–178.
Sillett, S.C., Van Pelt, R., Koch, G.W., Ambrose, A.R., Carroll, A.L., Antoine, M.E., Mifsud, B.M., 2010. Increasing wood production through old age in tall trees. Forest Ecology and Management 259, 976–994.
Sivasankar, T., Kumar, D., Srivastava, H.S., Patel, P., 2018. Advances in radar remote sensing of agricultural crops: a review. Int. J. Adv. Sci. Eng. Inf. Technol 8, 1126.
Skovsgaard, J.P., Johannsen, V.K., Vanclay, J.K., 1998. Accuracy and precision of two laser dendrometers. Forestry: An International Journal of Forest Research 71, 131–139.
Soja, M.J., Persson, H., Ulander, L.M., 2014. Estimation of forest height and canopy density from a single InSAR correlation coefficient. IEEE Geoscience and remote sensing letters 12, 646–650.
Song, B., Chen, J., Desander, P.V., Reed, D.D., Bradshaw, G.A., Franklin, J.F., 1997. Modeling canopy structure and heterogeneity across scales: from crowns to canopy. Forest Ecology and Management 96, 217–229.
Sperlich, M., Kattenborn, T., Koch, B., Kattenborn, G., 2014. Potential of unmanned aerial vehicle based photogrammetric point clouds for automatic single tree detection. Gemeinsame Tagung 1–6.
Spies, T.A., 1998. Forest structure: a key to the ecosystem. Northwest science 72, 34–36.
Szigarski, C., Jagdhuber, T., Baur, M., Thiel, C., Parrens, M., Wigneron, J.-P., Piles, M., Entekhabi, D., 2018. Analysis of the Radar Vegetation Index and Potential Improvements. Remote Sensing 10, 1776. https://doi.org/10.3390/rs10111776
Tanase, M., de la Riva, J., Santoro, M., Pérez-Cabello, F., Kasischke, E., 2011. Sensitivity of SAR data to post-fire forest regrowth in Mediterranean and boreal forests. Remote Sensing of Environment 115, 2075–2085.
Tavoni, M., Sohngen, B., Bosetti, V., 2007. Forestry and the carbon market response to stabilize climate. Energy Policy 35, 5346–5353.
Telesca, L., Lasaponara, R., 2006. Pre-and post-fire behavioral trends revealed in satellite NDVI time series. Geophysical research letters 33.
Ter-Mikaelian, M.T., Korzukhin, M.D., 1997. Biomass equations for sixty-five North American tree species. Forest Ecology and Management 97, 1–24.
Tsouros, D.C., Bibi, S., Sarigiannidis, P.G., 2019. A review on UAV-based applications for precision agriculture. Information 10, 349.
Turner, W., Rondinini, C., Pettorelli, N., Mora, B., Leidner, A.K., Szantoi, Z., Buchanan, G., Dech, S., Dwyer, J., Herold, M., 2015. Free and open-access satellite data are key to biodiversity conservation. Biological Conservation 182, 173–176.
Ulaby, F.T., Moore, R.K., Fung, A.K., 1981. Microwave remote sensing: Active and passive. volume 1-microwave remote sensing fundamentals and radiometry.

Vali, A., Comai, S., Matteucci, M., 2020. Deep learning for land use and land cover classification based on hyperspectral and multispectral earth observation data: A review. Remote Sensing 12, 2495.

Veci, L., Prats-Iraola, P., Scheiber, R., Collard, F., Fomferra, N., Engdahl, M., 2014. The sentinel-1 toolbox, in: Proceedings of the IEEE International Geoscience and Remote Sensing Symposium (IGARSS). IEEE, pp. 1–3.

Verhegghen, A., Eva, H., Ceccherini, G., Achard, F., Gond, V., Gourlet-Fleury, S., Cerutti, P.O., 2016. The potential of Sentinel satellites for burnt area mapping and monitoring in the Congo Basin forests. Remote Sensing 8, 986.

Vollrath, A., Mullissa, A., Reiche, J., 2020. Angular-Based Radiometric Slope Correction for Sentinel-1 on Google Earth Engine. Remote Sensing 12, 1867.

Vreugdenhil, M., Wagner, W., Bauer-Marschallinger, B., Pfeil, I., Teubner, I., Rüdiger, C., Strauss, P., 2018. Sensitivity of Sentinel-1 backscatter to vegetation dynamics: An Austrian case study. Remote Sensing 10, 1396.

Werner, C., Wegmueller, U., Strozzi, T., Wiesmann, A., 2000. Gamma SAR and interferometric processing software, in: Proceedings of the Ers-Envisat Symposium, Gothenburg, Sweden. p. 1620.

Wójtowicz, M., Wójtowicz, A., Piekarczyk, J., 2016. Application of remote sensing methods in agriculture. Communications in Biometry and Crop Science 11, 31–50.

Xue, J., Su, B., 2017. Significant remote sensing vegetation indices: A review of developments and applications. Journal of sensors 2017.

Zianis, D., Muukkonen, P., Mäkipää, R., Mencuccini, M., 2005. Biomass and stem volume equations for tree species in Europe. FI.

3 MAPPING SAR GEOMETRIC DISTORTIONS AND THEIR STABILITY ALONG TIME

De Petris Samuele[a*], Sarvia Filippo[a], Tommaso Orusa[a] and Borgogno- Mondino Enrico[a]

[a]Department of Agricultural, Forest and Food Sciences (DISAFA), University of Turin, 10095 Grugliasco, Italy.

*Correspondence: samuele.depetris@unito.it

Published: 2021 in *International Journal of Remote Sensing,* IF (2021): 3.531

Abstract: Operational services based on SAR data from satellite missions are showing to have the potentialities of becoming a real scenario; nevertheless, the complexity of data pre-processing remains one of the main reasons for its slow uptake by a wider user community. Google Earth Engine (GEE) web-based platform allows an immediate access to SAR imagery (namely, Sentinel-1 – S1) making users able to directly focus on the expected application. SAR side-looking acquisition mode generates many geometric distortions within recorded images, especially in mountain areas, determining a different degree of reliability of deductions. Consequently, a mapping of these areas is desirable for a correct interpretation of derived information. In this work a trigonometry-based method for mapping was implemented in GEE. With reference to a time series made of 60 S1 images covering the whole Piemonte Region (NW Italy) in 2020, some maps of distortions were generated using the 30 m gridded SRTM DTM as topographic surface descriptor. S1 images, belonging to the analyzed time series, were acquired from both ascending and descending orbits. In particular, active/passive shadows, active/passive layover and foreshortening masks were computed and mapped. Distortion maps were finally intersected with land cover classes to test the correspondent degree of analysability by SAR data. The results show that such methodology can be proficiently used to mask unreliable observations, making possible to a priori be informed about the areas of a given territory that can be reasonably and reliably monitored by SAR data.

1. Introduction

Satellite SAR (Synthetic Aperture radar) systems can provide significant contribution to land management, especially concerning mapping and characterization of surface geometric features. Nowadays, space programs (e.g. EU Copernicus) provide a huge amount of data that represent a powerful tool to support environmental research and territory management. Unfortunately, technological transfer appears to be still limited, but the development of services based on these data is moving to be an actual scenario (De Petris, Boccardo, Borgogno-Mondino 2019; De Petris et al. 2020; Sarvia, De Petris, and Borgogno-Mondino 2020; De Petris, Sarvia, and Borgogno-Mondino 2020; Sarvia et al. 2021). As explained in chapter 1.3 (see page 10), the complexity of SAR data pre-processing is one of the main reasons for its slow uptake by a wider user community. From this point of view, Google Earth Engine (GEE) web-based platform allows an immediate access to SAR imagery (namely, Sentinel-1 – S1) making users able to directly focus on the expected information (Gorelick et al. 2017). However, the peculiar SAR side-looking acquisition determines many geometric distortions in the acquired image, especially in mountain areas. Therefore, geometric distortions mapping is a fundamental step while working with SAR data as required by the Committee on Earth Observation Satellites (CEOS) (Committee on Earth Observation Satellites 2020). Unfortunately, in spite of its powerful computational capability, GEE is not presently equipped with a tool providing these types of maps. Main SAR geometric distortions can be summarized in: layover, shadows, foreshortening. In the object space layover/shadow regions can be labelled as active and passive. Passive regions mapping requires a sequential search along the same across-track line (Kropatsch and Strobl 1990). Often, passive shadows are located at the end of the active shadow mostly caused by obstacles (e.g. a mountain) hiding the point along the sensor Line-Of-Sight (LOS). Another distortion type is the so-called foreshortening and occurs when the local terrain slope angle equals the local incidence angle causing a dramatically compression of a relief (mountain side) in

the image plane. Detection of these areas requires that target visibility from satellite is explored. Target visibility depends on the combination of local slope orientation with the acquisition geometry and mode of LOS. Non-ideal geometrical configurations may result in image geometric distortions that are strictly related with radiometric ones. In fact, slope modulates radar signal in a complicated way depending on slope steepness, aspect, land cover type, radar lighting geometry, wavelength and polarization (Ulaby, Moore, and Fung 1981; Richards 2009). In this context, radar-based monitoring applications have to take care about slope effects to mitigate, and compensate, for the geometric and radiometric distortions. These slope-induced effects majorly affect some land cover classes that ordinarily are located in steep slopes as forests or mountain bare soils/rocks. If dense time series are needed images from different look directions and incidence angles have to be properly combined. In (Hoekman and Reiche 2015), concerning biomass mapping from SAR imagery, for example, authors prove that an accurate estimate can be obtained only if a proper handling of slope effects is achieved. Radiometric distortions induced by SAR lighting geometry were explored by many authors. In particular, the majority of them analysed slope effects related to land cover classification (Atwood, Small, and Gens 2012) and bio-physical parameter estimation (Franklin et al. 1995; Castel et al. 2001; Luckman 1998; Beaudoin et al. 1995). Additionally, another important application sensible to SAR geometric distortions is radar interferometry, with special concerns about Persistent Scatterers Interferometry (PSI) or Small baseline subset interferometry (SBAS) techniques ordinarily adopted to monitor surface shifts. In layover and shadow areas, the application of both interferometric and non-interferometric techniques is difficult (Cigna et al. 2014). Moreover, phase unwrapping fails in such areas. Consequently, the a-priori detection of areas where these distortions are present is essential to plan SAR-based analyses, especially over hilly or mountainous regions. Moreover, assessment of the most suitable LOS geometry ensuring target visibility from sensor is strongly suggested when stacking long SAR images, especially when big data for small-scale analysis are required. These conditions are the ones that

deformations monitoring require, being based on a multitemporal approach. In this context, geometric distortions induce significant underestimation of surface deformation, or even hamper reflective targets identification over observed areas (Cigna et al. 2014; Cigna, Bianchini, and Casagli 2013).

1.1. Literature Gaps and Study Aims

Literature reports many methods concerning geometric distortions mapping. All of them are based on the adoption of a Digital Elevation Model (DEM) to describe local topography. Three main approaches can be recognized: (a) the distortion simulation method; (b) the range-ground plain compression factor method; (c) the angle-based method. (a) approach considers geometric distortions as an intrinsic error of SAR imaging, and distortion simulation is preferred to distortion correction; some examples of such an approach is proposed in (Richards 2009; Liu, Zhao, and Jezek 2004; Cascini, Fornaro, and Peduto 2010; Pourthie et al. 2010) and implemented in some common SAR processing data software as SNAP (Sentinel Application Platform) vs 8.0 (LUIS Veci 2015). (b) method refers to the R topographic index (also known as pixel compression factor) representing the ratio between the pixel size in slant and ground range geometry. R-index values close to 1 mean a good visibility of the pixel and, consequently, no geometric distortion is present. Values lower than 0.4 indicate a compression of the pixel in slant range with respect to its actual ground size making it distorted. Some applications of this method are proposed in (Cigna et al. 2014; Notti et al. 2011; Davide 2010). (c) method is a widely used and more formal one that relies on the assessment of the geometric conditions related to LOS and local terrain slope and aspect. Some applications of this method are reported by Kropatsch and Strobl (Kropatsch and Strobl 1990) that propose a layover and shadow mapping algorithm. Unfortunately, it suffers from some operational limits mainly related to some required parameters, as imaging time and nadir distance, whose approximated knowledge could lead to many uncertainties in mapping layover/shadow areas. Differently, Rees (Rees 2000) proposed a simpler

algorithm based on terrain slope computation from a suitable DEM. Planck (Plank et al. 2010) proposed a GIS-routine to accurately predict areas in which layover and shadowing will occur while using differential interferometry technique. Moreover, Colesanti (Colesanti and Wasowski 2006) proposed a method for simulating foreshortening and active layover/shadow, neglecting passive distortions. It is worth to remind that radar and map grids have nominally equal ground resolutions in flat terrain; this condition is not preserved in steep areas. It is known that slopes facing the sensor (fore slopes) can generate a single pixel in radar geometry, since all ground points show similar distance (time) from sensor. Conversely, in mountain back slopes (especially at their bottom) more pixels in radar geometry are placed in a single pixel in map geometry. One-to-one relationships are called homomorphic, while many-to-one and one-to-many relationships are said heteromorphic (Small 2011). All angle-based approaches cannot account for heteromorphic relationships between map and radar geometry; nevertheless, many authors (Small 2011; Frey et al. 2012; Vollrath, Mullissa, and Reiche 2020) proved that angle-based approaches are very accurate if the topological relationship between SAR and terrain geometry is considered. This approach requires a back-and-forward computation from ground and radar spaces determining high computation times; moreover, it requires that the state vector of satellite orbit is available. In this theoretical context, the present work was aimed at exploring the possibility of obtaining time-series of radar distortions map specifically using GEE and its current available routines and dataset. The use of GEE instead of traditional SAR data processing software and routines, allows to process/map big data over wide areas that are particularly time-expensive while working with SAR time-series taking the advantage of the high GEE computational capability. With these premises, the above-mentioned angle-based approaches could appear not proper, since GEE does not make available the state vector of satellite orbit and the accessible S1 dataset is already supplied in ground geometry (geocoded). If one intended to, however, operate by GEE some simplifying assumptions must be necessarily introduced. It is authors opinion that, the availability of a map showing those areas that potentially suffer from

distortion can increase the consciousness of where S1 imagery can be effectively used and where, deductions, could present a too high degree of uncertainty. The geometric assumption about the theoretical stability of mapped areas along time can be assumed as true only if no bias is present in the processed data that are at the basis of this mapping. The multi-temporal analysis that the authors propose is specifically aimed at testing this condition under the hypothesis that the underlying landscape did not change. Consequently, the quantification of the number of times that the single pixel is recognized as 'distorted' has exactly this meaning: lower the number of times, lower the robustness of deduction. In other words, if the same pixel is sometimes mapped as distorted and some others as not-distorted, one can be alerted about the robustness of the data pre-processing step and about the declared accuracy of involved parameters (specifically the georeferencing ones)." Currently, no works about geometric distortion mapping using GEE can be found in literature, especially concerning the multitemporal analysis of such distortions. Trying to fill this gap, in this work a multi-temporal approach aimed at mapping SAR geometric distortions using GEE is presented. The analysis was performed at year-level (2020) considering about 60 S1 images acquired in both ascending and descending nodes. In particular, shadows (active/passive), layover (active/passive) and foreshortening masks were detected and mapped. Obtained maps can, operationally, be used to mask out unreliable observations from SAR image time series making possible to have an estimate of the local temporal resolution of 'good' acquisitions to compare faced applications with to determine the degree of analysis feasibility. To exemplify the operational potential of this analysis, obtained masks were compared with some land cover classes covering the study area (see forward on). This was intended to demonstrate that the temporal resolution of 'good' S1 acquisitions can drastically reduce (or improve) depending on the explored land cover classes (that is often related to a specific application).

2. Materials and Methods

2.1. Study Area

The Piemonte Region (North-West Italy) was selected as area of interest (AOI). It sizes about 25000 km2 (Figure 1) and was selected since showing heterogeneous conditions from both landscape and geomorphological point of view. The latter, in particular, can dramatically affect monitorability of areas by SAR data. With reference to AOI, the 43%, the 30% and 27% of the territory correspond to mountain (Italian Western Alps), hill and flat areas, respectively.

2.2. Available Data

2.2.1. Sentinel-1 Imagery

Sentinel-1 is one of the current largest space-borne missions providing free and open accessible SAR data. S1 mission relies on a constellation of two satellites (Sentinel-1A and Sentinel-1B) operating in C-band (5.6 cm wavelength). The main acquisition mode over land is Interferometric Wide (IW) swath recording approximately 250 km in length at 5 × 20 m spatial resolution in single look. Ordinarily, S1 records data in a dual pole mode (VV and VH) where electromagnetic waves were polarized vertically (V) for transmission and Horizontally/Vertically for reception. Data are recorded as complex values (I/Q components) and in SAR geometry (Range and Azimuth). According to Vollrath (Vollrath, Mullissa, and Reiche 2020) and Reiche (Reiche et al. 2016), the complexity of SAR data pre-processing is one of the main reasons for its slow uptake by a wider user community. From this point of view, GEE web-based platform could represent a key tool for facilitate this process, making possible an immediate access to images and allowing users to directly focus on required information (Gorelick et al. 2017).

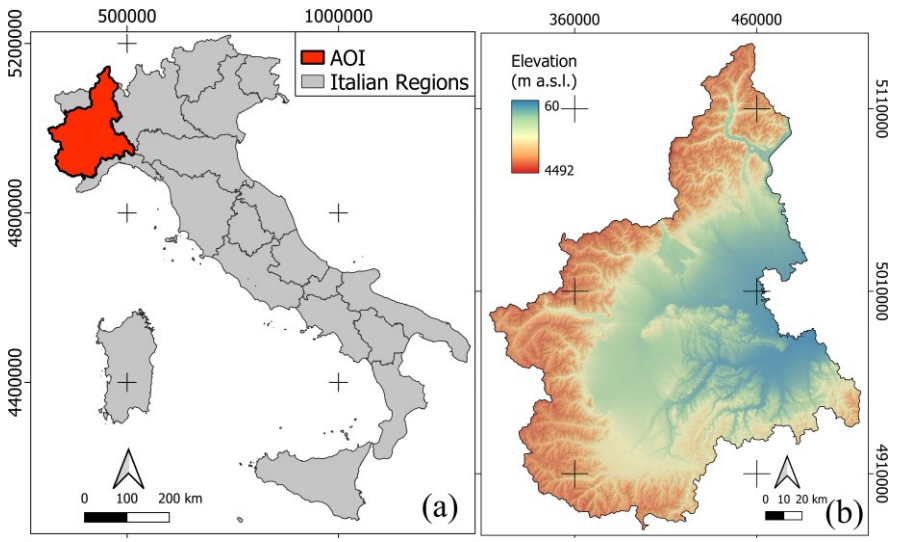

Figure 1. (a) Piemonte Region localization; (b) Digital Terrain Model showing altitude distribution in the area. Highly varying altitude conditions can be easily recognized (Reference frame: WGS84/UTM 32 N).

In this study, GEE was used with reference to the available S1 GRD (ground range detected) IW image collection. S1 GRD products consist of focused, detected and multi-looked SAR data projected to ground range according to the WGS84 Earth ellipsoid model. GRD product provides an approximately squared pixel with a spatial resolution of about 10 m (called GRDH collection). Speckle is reduced thanks to the multilook process. Within GEE, GRD product was already pre-processed by Sentinel-1 Toolbox (S1TBX) freely available from the European Space Agency's (ESA) (Luis Veci et al. 2014, 2). The result is the computation of the backscatter coefficient (σ° [dB]) at each pixel location. Pre-processing steps consist of: (1) application of orbit file metadata to provide an accurate satellite position and velocity information; (2) border low intensity noise and invalid edge data removal; (3) thermal noise removal, removing additive noise in sub-swaths; (4) radiometric calibration to compute backscatter intensity according to sensor calibration parameters supplied in the GRD metadata; (5) image orthoprojection to reproject image into an opportune map reference system; range-doppler terrain correction is applied using the 30 m gridded SRTM (Shuttle Radar Topography Mission) DEM (Digital Elevation Model). This step requires interpolation of missing data to fill occurring image gaps and, necessarily, introduces some radiometric distortions. GRD

data contains both VV and VH polarizations together with a layer mapping the nominal incidence angle (θ_i) and some basic metadata (Google Developers 2020a). All layers are supplied in terrain geometry; nominal reference system (adopted in GEE) is WGS 84/Pseudo-Mercator (EPSG: 3857) (Google Developers 2020b). Pixel positional accuracy of S1 GRDH data after orthoprojection is estimated in 2.3 m (1σ) (Small and Schubert 2019). GEE S1 GRDH collection has a nominal geometric resolution of 10 m. In this work, a total of 57 and 60 acquisitions acquired along ascending and descending nodes respectively, were used for this work covering the period 1 January 2020– 20 December 2020. AOI was completely contained in a single orbit swath for both ascending (relative orbit n. = 88) and descending (relative orbit n. = 66) nodes. Acquisition dates and image footprints are shown in Figure 2.

2.2.2. SRTM Digital Elevation Model

Ordinarily, DEM are used to model SAR distortions. In fact, terrain topography cannot be derived from the SAR image itself and, consequently, an auxiliary external information is required. Adopted DEM should ideally have the same resolution (or higher) of SAR images (Vollrath, Mullissa, and Reiche 2020). In this work, the gridded SRTM v3 product (Farr et al. 2007), available in GEE was used having a GSD (Ground Sampling Distance) of 1" (approximately 30 m). A nearest-neighbour method was used, in GEE, to oversample it at the S1 GRDH image resolution. It is worth to remind that SRTM was generated by In-SAR technique, adopting short wavelengths (C- and X- bands); sequently, it appears more similar to a DSM (Digital Surface Model) rather than to a DTM (Digital Terrain Model), mapping also height discontinuities related to buildings and tall objects (Gamba, Dell Acqua, and Houshmand 2002). These objects represent local abrupt changes in elevation and related geometric parameters (i.e. slope and aspect).

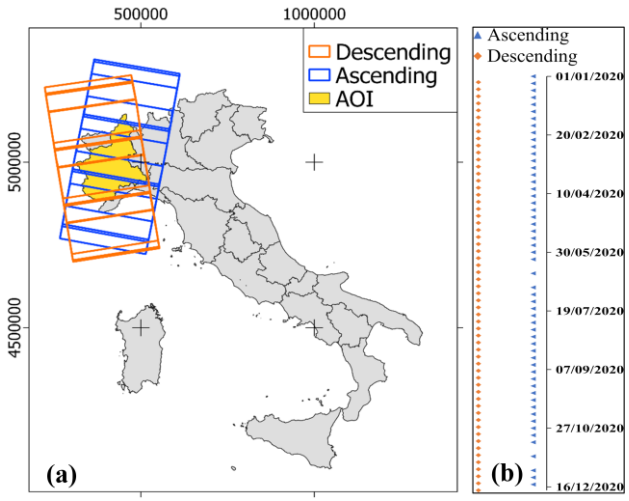

Figure 2. (a) Footprints of collected images; (b) timeline of collected images (Reference frame: WGS84/UTM 32 N).

2.2.3. Land Cover Piemonte

The Land Cover Piemonte dataset level 4 (LCP) map was used to describe land use and land cover in AOI. LCP was obtained, for free and in vector format, from the regional geoportal (www.geoportale.piemonte.it). It was supplied georeferenced in the WGS84/ UTM 32 reference system. Updating is dated 2010 and nominal scale is 1:25000. LCP results from the integration of different data: (a) the regional forest map and other auxiliary information from the so called Piemonte Territorial Forest Plans (PFT); (b) cadastral maps; (c) hydrological maps; (d) regional technical map; (e) regional transport map. Table 1 reports the list of classes and related codes considered in this work.

2.3. Data Processing

S1 imagery and DEM were processed directly in GEE and results downloaded and reprojected into the WGS84 UTM 32 N reference system. Following processing steps were conducted in SAGA GIS vs 7.0 (Conrad et al. 2015) and R software vs 3.6.1 (R Development Core Team 2013).

Table 1. LCP classes considered in this work. ID

ID	*LCP classes*	*ID*	*LCP classes*
C1	Urban	C11	Spruces forests
C2	Infrastructures	C12	Scots pine forests
C3	Agriculture	C13	Norway pruce forests
C4	Mixed forests	C14	Larch and stone pine forests
C5	Maple-tree-ash forests	C15	Pastures
C6	Chestnut forests	C16	Bare soil
C7	Black locust forests	C17	Wetlands
C8	Oak forests	C18	Rivers
C9	Beech forests	C19	Water channels
C10	Riparian forests	C20	Water basins

2.3.1. Mapping Image Distortions

Only those distortions related to the line of sight of the SAR image that could be mapped onto the DEM ground plane were considered. The proposed method is based on the angular dependencies between SAR image geometry parameters and local terrain conditions as schematically reported in Figure 3. It neglects topological relations among neighbour cells that, actually, should be considered to fully describe distortion effects. For this reason, and with respect to other methods (Kropatsch and Strobl 1990; Shimada 2010; Chen, Sun, and Jun 2018), the proposed approach is not able to rigorously map passive layover and shadow areas; conversely, it provides an easy approach to directly operate in the map geometry. A rough mapping of areas affected by passive distortions was however provided. We found a single work in literature (Vollrath, Mullissa, and Reiche 2020) where a trial was done to implement this approach within GEE.

2.3.1.1. Terrain Geometry

Terrain geometry was modelled by SRTM. It can be summarized by two angles: the slope angle and the terrain aspect angle (uphill direction) φs relative to the geographic North. SRTM was used to generate the correspondent slope and aspect maps. The ee.Terrain functions available in GEE were used for this task. Since SRTM also maps altitude variations related to objects overlaying the ground (e.g. buildings) some abrupt changes in local slope occur that cannot be considered as topographically induced distortions. These local oscillations are often related to objects covering an area less than a single DEM pixel resulting in bad estimate of buildings height as reported by (Gamba, Dell Acqua, and Houshmand 2002). To achieve this problem, a 'pseudo-normalized DSM' (p-nDSM) was generated in order to detect local 'high' objects and masking them out from subsequent steps. Using morphological filters, the local maxima and minima were computed by a circular kernel (50 m radius). p-nDSM was calculated as the difference between local maxima and local minima representing a rough model of local object height in respect of ground level. All SRTM pixels having p-nDSM lower than 30 m were masked out. Finally, aspect (φ_s) and slope (α_s) angles were derived from the masked SRTM.

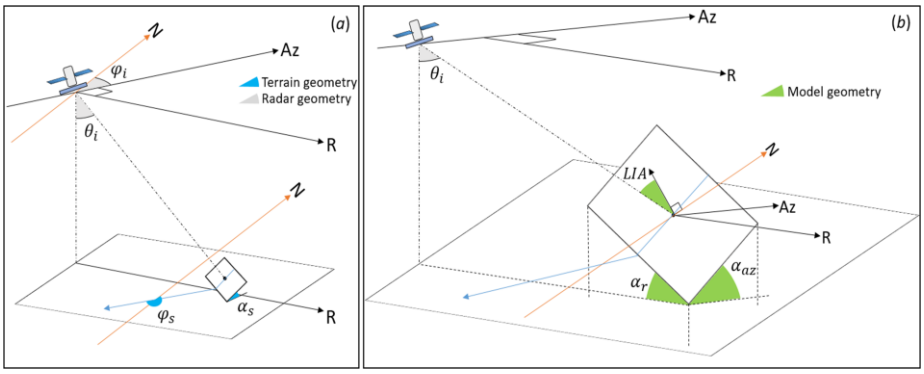

Figure 3. SAR acquisition geometry and related parameters. (a) Terrain and sensor geometries; (b) model geometry. The angles α_s and φ_s are the terrain slope and aspect respectively while θ_i is the look angle and φ_i is the angle, in the horizontal plane, between the orbit track and the geographic north; φr is an auxiliary angle that rotates the terrain geometry system into the sensorone; αr and α_{az} are the slope angle components in range and azimuth direction respectively.

2.3.1.2. SAR Geometry

Since SAR images are ordinary produced in a zero-doppler geometry, sensor attitude can be described by two angles the (nominal) incidence angle θi and orbit track angle φi. The look or incidence angle θi is defined as the angle between the line of sight and the nadir; it increases with the range distance (for S1 IW mode it ranges between 31° and 46°). The angle φi is the angle, in the horizontal plane, between the orbit track and the Geographic North. This information is not available in S1 metadata supplied by GEE, but can be approximately computed as the average aspect value of incidence angle layer (Vollrath, Mullissa, and Reiche 2020; Greifeneder 2018).

2.3.1.3. Model Geometry

Some simplified relationships were used to relate radar beam geometry to the terrain, linking image and terrain domains (Equations 1–4). In particular, the angle φ_r rotates the terrain geometry system into the sensor one (Equations 1). Consequently, the slope angle in range direction (α_r) and the slope angle in azimuth direction (α_{az}) were computed by Equations 2 and 3, respectively. These angles allow, knowing terrain geometry, to analysis the visibility conditions of a given pixel in sensor geometry.

$$\varphi_r = \varphi_i - \varphi_s \quad (1)$$

$$\alpha_r = tan^{-1}(tan\,\alpha_s \cdot cos\,\varphi_r) \quad (2)$$

$$\alpha_{az} = \tan^{-1}(\tan\alpha_s \cdot \sin\varphi_r) \quad (3)$$

The Local Incidence Angle (LIA), defined as the angle between radar ray direction and the normal surface direction considering the terrain was finally computed according to Equation 4.

$$LIA = \cos^{-1}[\cos\alpha_{az} \cdot \cos(\theta_i - \alpha_r)] \quad (4)$$

2.3.1.4. Geometric Distortion Masks

SAR systems record data in slant range plan (image geometry) where backscattered signal is recorded with reference to the time lag separating transmission and reception of pulses. In an ideal flat terrain, echoes are recorded coherently to the expected ground sequence (ground range). In sloped areas, topography dramatically changes this sequence resulting into an image composed by some geometric distorted pixels (GDPs). GDPs can be subdivided into: layover, shadow and foreshortening and occur especially in mountain or hilly areas. Active layover occurs when signal scattered by the top of a mountain is recorded before the one coming from its foot. It is generated when slope angle in range (φ_r) exceeds look angle (θ_i) from the slope facing the sensor (fore slope). Active layover can be detected testing condition of Equation 5 at pixel-level.

$$Active\ Layover = \alpha_r > \theta_i \quad (5)$$

Shadows occur when radar beam does not reach the terrain given a local incidence angle exceeding 90°. These areas present no signal and appear as dark regions (very low signal) within images. Active shadows can be detected at pixel level using LIA (Gelautz et al. 1998) assuming that no signal occurs when LIA is around 90°. Cautiously this threshold was set equal to 85° and shadowed areas detected by Equation 6.

$$Active\ Shadow = LIA > 85° \quad (6)$$

With reference to terrain geometry, layover and shadow regions can be divided into active and passive sub-regions (Kropatsch and Strobl 1990). Some areas that might not receive energy due to some obstacles (i.e. mountains) between sensor and ground surface are called passive shadows. Similarly, passive layover areas are those that are only affected by distortion induced by an adjacent active layover. Some methods have been reported in literature to map passive distortions (Rees 2000; Chen, Sun, and Jun 2018; Gelautz et al. 1998). The most of them are

based on slant range geometry or tend to model passive- active relationship. These methods, unfortunately and presently, cannot be implemented in GEE, given its present incapability of recovering slant range geometry and/or perform a proximity grid analysis (location-allocation tools). In spite of these limitations, passive distortions mapping was however considered in this work, adopting a buffering approach. The basic assumption was that passive distorted pixels are expected to be located close to active ones. A circular buffer with a 50 m radius was, consequently, generated around active shadow/layover areas and all pixels falling within the buffer zone were labelled as passive shadow, or layover, accordingly. The GEE *ee.fastDistanceTransform* algorithm was applied (Google Developers 2021) for this task. Mountain slopes facing sensor appear as shortened in SAR image when the local terrain slope angle is greater than look angle. This negatively affects range resolution and is usually addressed as foreshortening. It can be detected by Equation 7 (Chen, Sun, and Jun 2018).

$$Foreshortening = \alpha_s > \theta_i \quad (7)$$

According to the above-mentioned strategies and equations, the correspondent masks mapping active layover (ALM), active shadow (ASM), foreshortening (FM), passive shadow (PSM) and passive layover (PLM) were generated. Pixels belonging to mask layers were labelled as 0 if not distorted and 1 if distorted. All distortion types and occurrences were then summarized by combining the above-mentioned masks in a single layer: the geometric distorted pixels map (hereinafter called GDPs). Pixels showing at least one metric distortion were labelled as 1; pixel showing no distortion as 0.

2.3.2. Multi-Temporal Analysis of Distortions

Using the iterative function *ee.ImageCollection.map* of GEE, for each image in the considered period (1 year) ALM, ASM, FM, PSM, PLM and GDPs masks were computed and stacked as separate collections (DTS, distortion time series). Ascending and descending nodes images were stacked separately. These new

collections were analysed to describe the temporal behaviour of distortions. A synthetic representation of DTSs (NDO, number of distorted observations) was generated by computing, at pixel level, the number of times that the same pixel was seen as 'distorted.' NDO was separately computed for all distortion types (i.e. active/passive layover, active/passive shadow, foreshortening or GDPs). A total of 12 maps (6 in ascending and 6 in descending nodes) were generated: ALM-sum, ASM-sum, FM-sum, PSM-sum, PLM-sum and GDPs-sum, respectively for ascending e descending orbits.

2.3.3. Land Cover Classes *vs* Image Distortions

An intersection between the above-mentioned 12 maps and LCP was performed to assess the impact of unreliable SAR observations (distorted pixels) onto main land cover classes. Results were summarized by computing the frequency distribution of the occurrences of 'distorted' pixels in ALM-sum, ASM-sum, FM-sum, PSM-sum, PLM-sum. Differently, GDPs- sum images were used to synthetically map the extension of distortion (with no regard about the type) at LCP class level. For each class, after translating NDO as recorded in GDPs-sum into the correspondent 'distorted' area percentage (n. of 'distorted' hectares of a class in respect of the total hectares of the same class), the correspondent cumulative frequency distributions (CFD) were computed.

3. Results

3.1. Geometric Distortion Masks

According to the angle-based method, image geometric distortions were mapped for each of the analysed S1 acquisitions, keeping separated results for ascending and descending nodes (Figure 4). Maps of Figure 3 show that bright pixels in VV image (σ^0) are in general located in layover and foreshortened areas. Conversely, dark pixels are related to shadowed areas and were correctly detected. It is worth to remind that the simplified approach for passive distortions mapping based on buffering was not able to completely take into account the actual geometric

complexity; this limitation mainly resulted in an over mapping of 'distorted' pixels. In spite of this fact, presently, this approach appears to be the only one implementable in GEE to take care about passive distortions. In fact, currently, GEE does not implement proximity analysis tools that would permit to overcome this problem, making possible a rigorous assessment of such distortions (Kropatsch and Strobl 1990; Chen, Sun, and Jun 2018). GDPs maps are reported in Figure 5 for both the orbits.

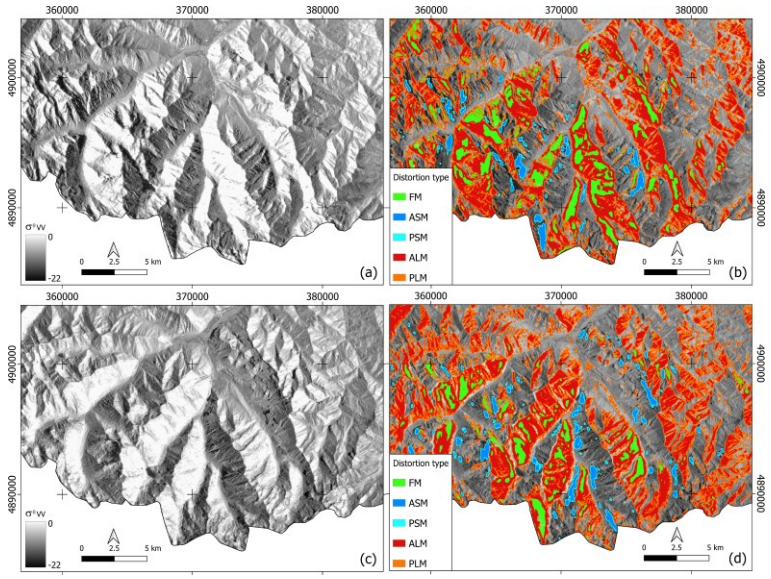

Figure 4. (a) Backscattering (σ^0) in ascending node VV image (17 June 2020); (c) Backscattering (σ^0) in descending node VV image (16 June 2020); (b-d) Map of distortion types as mapped by the angle-based method implemented in GEE for both (a) and (c) images (Reference frame: WGS84/UTM 32 N).

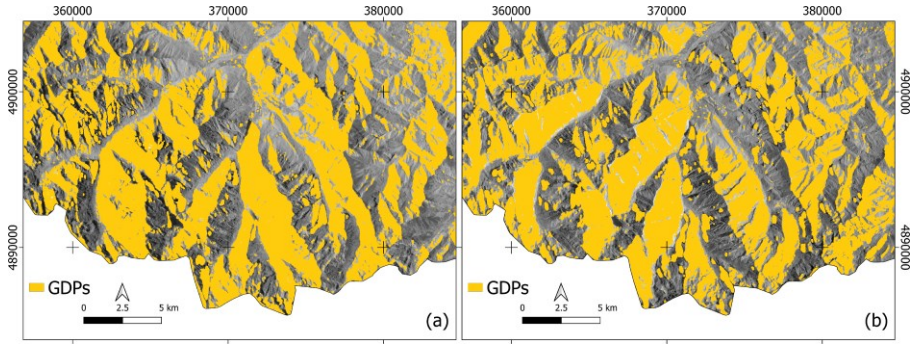

Figure 5. GDPs maps for (a) ascending node image (17 June 2020) and (b) for descending node image (16 June 2020) (Reference frame: WGS84/UTM 32 N).

3.2. Multi-Temporal Analysis of Distortions

All the previously mentioned maps were computed in GEE by a self-developed function, for all the images belonging to the analysed time series. Finally, ALM-sum, ASM-sum, FMsum, PSM-sum, PLM-sum maps (for ascending and descending nodes) were generated summarizing all distortion types and correspondent occurrences along the year. Figure 6 reports a focus area extracted from these maps and mapping NDO for the ascending node acquisitions. With reference to GDP maps, the correspondent GDP-sum maps were computed for the entire AOI for both the orbits (Figure 7). GDPs-sum maps could represent a useful tool for assessing the suitability of AOI to be monitored by S1 imagery.

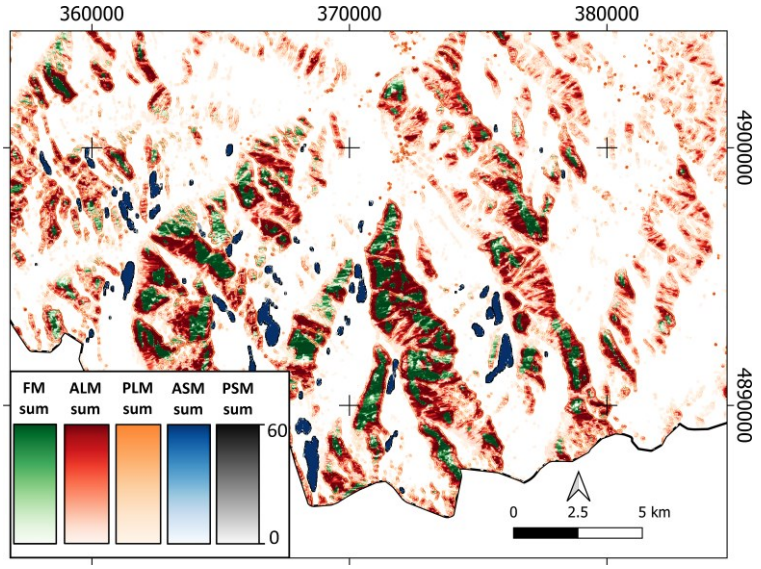

Figure 6. NDO map for ascending orbits showing occurrences and location of all analysed distortion types (Reference frame: WGS84/UTM 32 N).

3.3. Land Cover Classes *vs* Image Distortions

Each land cover class was assessed in term of NDO using the previously mentioned sum-maps. Figure 8 reports NDO frequency distribution as boxplots for each considered LCP class. Results showed that, in the reference period, the median value of distortion occurrences was lower than 20 for the urban class (C1) and lower than 10 for both infrastructures and agricultural classes (C2 and C3). Specifically, the favourable conditions related to C3 can be explained with the fact that in Piemonte, crops are majorly located in flat and low areas. With reference to forests, it can be observed that mixed forests (C4) showed a median NDO value higher than 25, being the majority of forested areas located over mountain slopes. Maple-lime-ash trees (C5) showed a NDO median value higher than 15, while Chestnut stands (C6) do not overcome 10. Many chestnut stands in fact, are located in smoothed hilly areas or at the bottom of mountain slopes. Black locust forests (C7) showed a particularly low NDO median value (<5). This probably depends on its invasive behaviour with respect to abandoned crops, that, as already said, in AOI are mostly located in lowlands or foothills. Oak and

Riparian forests (C8 and C10) showed median NDO value lower than 10 being located in flat areas, too. Conversely, beech stands (C9), fir (C11), pine forests (C12), larches and stone pines woods (C14), pastures (C15) and bare soils (C16) showed median NDO values even greater than 30, being mainly located in alpine valleys. Spruce forests (C13) showed the highest NDO median value, about 45. Even if it is not the most abundant forest species in Piedmont, this type of forest is mainly located where many forest disturbances as landslides, rockfalls, wildfires occurred in the past; spruce stands in fact, prefer steep mountain slopes that are known to be majorly affected by disturbances. These are exactly the conditions that determine SAR geometric distortions. Finally, water channels (C19), wetlands (C17), rivers (C18) and water basins (C20) showed GDP-sum NDO median values lower than 10, being majorly located in lowland.

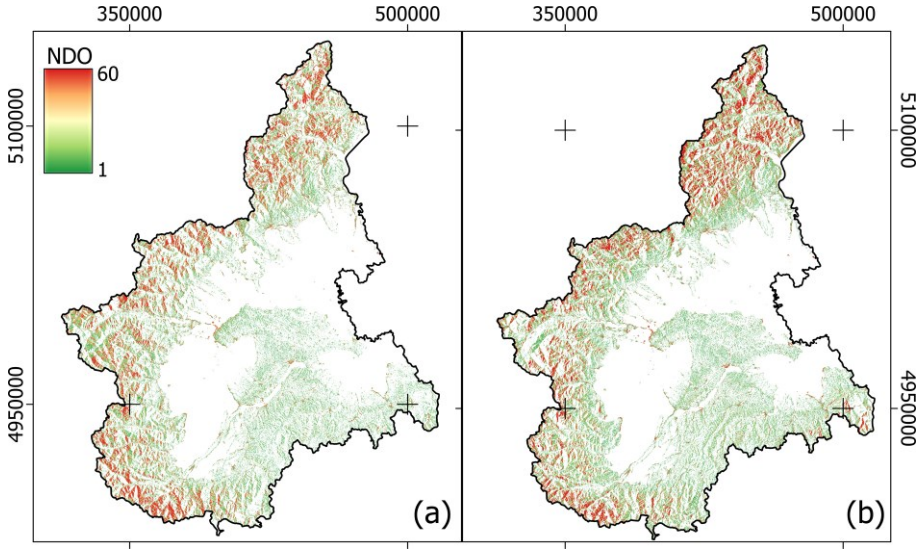

Figure 7. GDPs-sum for ascending (a) and descending (b) orbits considering 2020 observations for AOI (Reference frame: WGS84/UTM 32 N).

Comparing descending and ascending orbits (Figure 8(b,d,f,h,l,n)) a similar behaviour can be observed for all distortion types. Only for some forest types, namely C11 and C16, passive shadows appear to be more limited for descending acquisitions. As far as foreshortening is concerned, descending acquisitions

appear to favour class C8, while ascending acquisitions C12. In general results showed that ALM and PLM were characterized by low NDO values (Figure 8(a–d)) while ASM, PSM and FM are more frequent in AOI (Figure 8 (e–i,l)). In general, the percentage of distorted areas within classes varies between 10 and 60% (Figure 9). Ascending orbits seem to generate less distortions than the descending ones. In fact, the average class percentage of distorted areas (i.e. NDO > 1) in was about 26.5% and 30% for ascending and descending nodes, respectively. This difference could be related to the geometric relationship between S1 orbit and AOI topography. It is worth to remind that, Italian western Alps, where AOI is located, are characterized by a West-Est valleys orientation. This makes descending orbits intersecting them with an angle closer to 90° than ascending ones, determining more favourable conditions of observation from the distortion occurrences point of view. As far as ascending orbit is concerned, LCP class C13 (Norway pruce forests) showed the highest percentage of distorted areas (almost 50%). C11 – C15 forestry classes also appear to suffer from a too high percentage of not monitorable areas by S1 data (NDO > 50%).

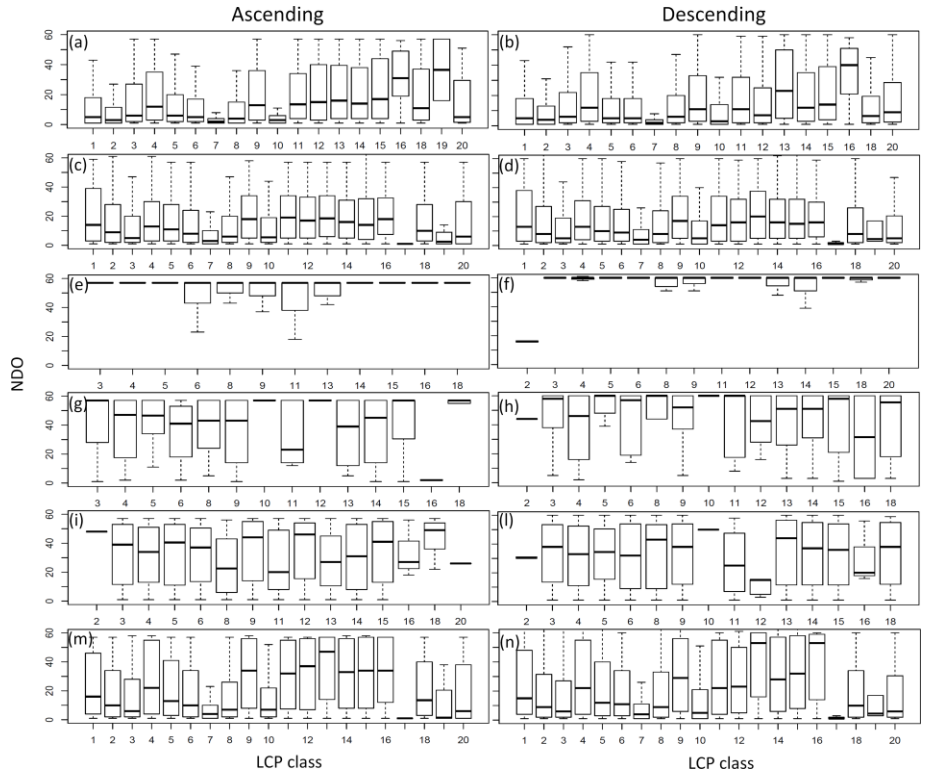

Figure 8. Boxplots summarizing NDO frequency distributions within considered LCP classes. (a-b) ALM-sum; (c-d) PLM-sum; (e-f) ASM-sum; (g-h) PSM-sum; (i-l) FM-sum; (m-n) GDPs-sum. In the plots, lines are (bottom-up): 5^{th} , 25^{th} , 50^{th} , 75^{th} and 95^{th} percentiles.

Some differences can be also recognized within the same LCP depending on the orbit type. In fact, the 60% of C16 (mountain bare soils) area was mapped as distorted in the descending orbit, while only 30% in the ascending one. Forests classes did not show this clear difference between the two acquisition orbits. These results suggests that S1 data acquired in ascending node is more proper to monitor not vegetated mountain areas that, where, possibly, landslides are more frequent. Water channels and water basins classes (C19 and C20, respectively) proved to be the less affected ones by distortions (less than 5% of the area); similarly, agriculture class (C3) showed a low percentage of distorted areas (<10%).

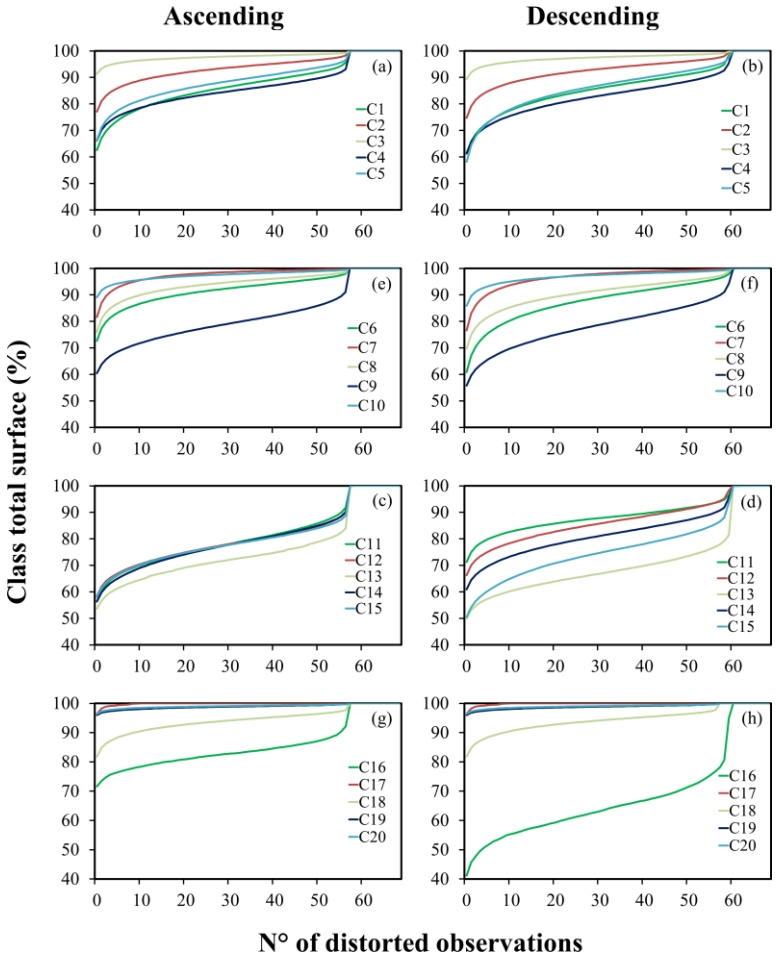

Figure 9. Cumulated frequency distributions (from GDP-sum) computed for the considered LCP classes (as class area percentages) and for ascending (a, c, e, g) and descending (b, d, f, h) node.

4. Discussions

A simple approach to map SAR acquisition-related image distortion was proposed in this work based on GEE available routines. Authors are aware that it still suffers from many limitations related to the LOS azimuth direction φi computation and, possibly, to DEM features like height accuracy and geometric resolution. As far as φi is concerned, orbits state vectors would be required for its precise determination. Unfortunately, GEE does not provide such information, requiring an approximated solution obtained by calculating the average direction

of the gradient from the incidence angle layer (Vollrath, Mullissa, and Reiche 2020; Greifeneder 2018). In spite of this, Cigna (Cigna et al. 2014) proved that geometric distortions are poorly sensitive to φi variation. Her study proved that for highly varying φi values (obtained from more than 10,500 ERS-1/2 SAR images acquired between 1991 and 2001 and covering the whole UK), related effects on image distortion were negligible if compared with the ones induced by other factors like αs and LIA. As far as DEM-related problems, SRTM height accuracy was extensively proved to be low (Gorokhovich and Voustianiouk 2006; Rodriguez, Morris, and Eric Belz 2006) often > 16 m over vegetation (Fissore et al. 2015). This condition together with its coarse resolution, certainly influenced the proposed method. The adoption of a higher resolution DEM is expected to improve modelling of distortions, thanks to a better description of topographic features that are smoothed by lower resolution data (Cigna et al. 2014). Gelautz (Gelautz et al. 1998) already proved DEM geometric resolution importance for SAR image simulation suggesting that detection of distortions, for ERS-1/2 and ENVISAT data, should require a DEM with a spatial resolution better than 25–30 m. Nevertheless, currently SRTM DEM is the only one available in GEE having a semi-world-wide coverage and therefore it can be used in many locations well- fitting at-regional-level analysis like the one required for distortions affecting wide areas. Additionally, the computation and utilization of p-nDSM to mask out abrupt height changes during αs mapping could furtherly reduce accuracy of detection. Nevertheless, this is expected to occur only in lowland and flat areas. Finally, all deductions presented in this work cannot be generalized being strictly related to AOI topography and land cover type and their spatial distribution.

5. Conclusions

In this work, a multitemporal mapping of SAR geometric distortions were performed using GEE and the available S1 imagery over Piemonte Region (NW Italy). An angle- based method was adopted and geometric conditions were tested

at-pixel-level mapping distortions types (layover, shadow and foreshortening). SRTM DEM and look angle maps available from GEE were used to relate radar to terrain geometry through formal relationships. To minimize the effects of SRTM abrupt height changes due to buildings a p-nDSM was calculated and used to mask out local DSM variations. The method is known to be not able to rigorously detect layover/shadow passive regions, given the present capabilities of GEE that, currently, not provide location- allocation tools needed to map areas affected by passive distortions. An operational application of the generated maps of distortions was given, concerning the possibility of monitoring different land cover classes in AOI. Thanks to this type of approach, it was possible to prove that, in AOI, ascending orbit S1 acquisitions perform better, minimizing image deformation. This is not a general conclusion since strictly depending on local topography. In spite of all the above-mentioned limitations, the proposed procedure represents a first trial to easily obtain information concerning SAR deformations based on the available GEE procedures. From an operational point of view, such an approach would permit to a-priori investigate if S1 data are suitable enough to monitor an area of interest.

References:

Atwood, Donald K., David Small, and Rüdiger Gens. 2012. "Improving PolSAR Land Cover Classification with Radiometric Correction of the Coherency Matrix." IEEE Journal of Selected Topics in Applied Earth Observations and Remote Sensing 5 (3). IEEE: 848–856.

Beaudoin, Amélie, N. Stussi, D. Troufleau, N. Desbois, Laurent Piet, and M. Deshayes. 1995. "On the Use of ERS-1 SAR Data over Hilly Terrain: Necessity of Radiometric Corrections for Thematic Applications." In 1995 International Geoscience and Remote Sensing Symposium, IGARSS'95. Quantitative Remote Sensing for Science and Applications, 3:2179–2182. IEEE.

Cascini, Leonardo, Gianfranco Fornaro, and Dario Peduto. 2010. "Advanced Low-and Full-Resolution DInSAR Map Generation for Slow-Moving Landslide Analysis at Different Scales." Engineering Geology 112 (1–4). Elsevier: 29–42.

Castel, Thierry, André Beaudoin, N. Stach, N. Stussi, Thuy Le Toan, and P. Durand. 2001. "Sensitivity of Space-Borne SAR Data to Forest Parameters over Sloping Terrain. Theory and Experiment." International Journal of Remote Sensing 22 (12). Taylor & Francis: 2351–2376.

Chen, Xiaohong, Qian Sun, and Jun Hu. 2018. "Generation of Complete SAR Geometric Distortion Maps Based on DEM and Neighbor Gradient Algorithm." Applied Sciences 8 (11). Multidisciplinary Digital Publishing Institute: 2206.

Cigna, Francesca, Luke B. Bateson, Colm J. Jordan, and Claire Dashwood. 2014. “Simulating SAR Geometric Distortions and Predicting Persistent Scatterer Densities for ERS-1/2 and ENVISAT C-Band SAR and InSAR Applications: Nationwide Feasibility Assessment to Monitor the Landmass of Great Britain with SAR Imagery.” Remote Sensing of Environment 152. Elsevier: 441–466.

Cigna, Francesca, Silvia Bianchini, and Nicola Casagli. 2013. “How to Assess Landslide Activity and Intensity with Persistent Scatterer Interferometry (PSI): The PSI-Based Matrix Approach.” Landslides 10 (3). Springer: 267–283.

Colesanti, Carlo, and Janusz Wasowski. 2006. “Investigating Landslides with Space-Borne Synthetic Aperture Radar (SAR) Interferometry.” Engineering Geology 88 (3–4). Elsevier: 173–199.

Committee on Earth Observation Satellites. 2020. “Analysis Ready Data For Land. Product Family Specification: Normalised Radar Backscatter, Version 5.0.” https://ceos.org/ard/files/PFS/NRB/v5.0/CARD4L-PFS_Normalised_Radar_Backscatter-v5.0.pdf.

Conrad, Olaf, Benjamin Bechtel, Michael Bock, Helge Dietrich, Elke Fischer, Lars Gerlitz, Jan Wehberg, Volker Wichmann, and Jürgen Böhner. 2015. “System for Automated Geoscientific Analyses (SAGA) v. 2.1. 4.” Geoscientific Model Development Discussions 8 (2).

De Petris, S., Roberta Berretti, Elisa Guiot, Fabio Giannetti, Renzo Motta, and Enrico Borgogno-Mondino. 2020. “Detection And Characterization of Forest Harvesting In Piedmont Through Sentinel-2 Imagery: A Methodological Proposal.” Annals of Silvicultural Research 45 (1): 92–98. doi:10.12899/asr-2018.

De Petris, Samuele, Piero Boccardo, and Enrico Borgogno-Mondino. 2019. “Detection and Characterization of Oil Palm Plantations through MODIS EVI Time Series.” International Journal of Remote Sensing, 1–15.

De Petris, Samuele, Filippo Sarvia, and Enrico Borgogno-Mondino. 2020. “RPAS-Based Photogrammetry to Support Tree Stability Assessment: Longing for Precision Arboriculture.” Urban Forestry & Urban Greening 55. Elsevier: 126862.

Farr, Tom G., Paul A. Rosen, Edward Caro, Robert Crippen, Riley Duren, Scott Hensley, Michael Kobrick, Mimi Paller, Ernesto Rodriguez, and Ladislav Roth. 2007. “The Shuttle Radar Topography Mission.” Reviews of Geophysics 45 (2). Wiley Online Library.

Fissore, Vanina, Renzo Motta, Brian Palik, and Enrico Borgogno Mondino. 2015. “The Role of Spatial Data and Geomatic Approaches in Treeline Mapping: A Review of Methods and Limitations.” European Journal of Remote Sensing 48 (1). Taylor & Francis: 777–792.

Franklin, S. E., M. B. Lavigne, E. R. Hunt Jr, B. A. Wilson, D. R. Peddle, G. J. McDermid, and P. T. Giles. 1995. “Topographic Dependence of Synthetic Aperture Radar Imagery.” Computers & Geosciences 21 (4). Elsevier: 521–532.

Frey, Othmar, Maurizio Santoro, Charles L. Werner, and Urs Wegmuller. 2012. “DEM-Based SAR Pixel-Area Estimation for Enhanced Geocoding Refinement and Radiometric Normalization.” IEEE Geoscience and Remote Sensing Letters 10 (1). IEEE: 48–52.

Gamba, P., F. Dell Acqua, and B. Houshmand. 2002. “SRTM Data Characterization in Urban Areas.” International Archives of Photogrammetry Remote Sensing and Spatial Information Sciences 34 (3/B). NATURAL RESOURCES CANADA: 55–58.

Gelautz, Margrit, H. Frick, J. Raggam, J. Burgstaller, and Franz Leberl. 1998. “SAR Image Simulation and Analysis of Alpine Terrain.” ISPRS Journal of Photogrammetry and Remote Sensing 53 (1). Elsevier: 17–38.

Google Developers. 2020a. “Sentinel-1 Algorithms.” https://developers.google.com/earthengine/sentinel1.

Google Developers. 2020b. “Projections.” https://developers.google.com/earth-engine/guides/projections.

Google Developers. 2021. “Scale in Google Earth Engine.” https://developers.google.com/earth-engine/guides/scale?hl=en.

Gorelick, Noel, Matt Hancher, Mike Dixon, Simon Ilyushchenko, David Thau, and Rebecca Moore. 2017. “Google Earth Engine: Planetary-Scale Geospatial Analysis for Everyone.” Remote Sensing of Environment 202. Elsevier: 18–27.

Gorokhovich, Y., and A. Voustianiouk. 2006. “Accuracy Assessment of the Processed SRTM-Based Elevation Data by CGIAR Using Field Data from USA and Thailand and Its Relation to the Terrain Characteristics.” Remote Sensing of Environment 104 (4). Elsevier: 409–415.

Greifeneder, F. 2018. “Discussion on Derivation of Local Incidence Angle from Sentinel-1.” Google Earth Engine Developer Group. https://groups.google.com/forum/#\protect\kern-.1667em\relaxmsg/google-earth-engine-developers/3-q0TEwa-Tk/h3J4havuBAAJ.

Hoekman, Dirk H., and Johannes Reiche. 2015. “Multi-Model Radiometric Slope Correction of SAR Images of Complex Terrain Using a Two-Stage Semi-Empirical Approach.” Remote Sensing of Environment 156. Elsevier: 1–10.

Kropatsch, Walter G., and Dieter Strobl. 1990. “The Generation of SAR Layover and Shadow Maps from Digital Elevation Models.” IEEE Transactions on Geoscience and Remote Sensing 28 (1). IEEE: 98–107.

Liu, Hongxing, Zhiyuan Zhao, and Kenneth C. Jezek. 2004. “Correction of Positional Errors and Geometric Distortions in Topographic Maps and DEMs Using a Rigorous SAR Simulation Technique.” Photogrammetric Engineering & Remote Sensing 70 (9). American Society for Photogrammetry and Remote Sensing: 1031–1042.

Luckman, Adrian J. 1998. “The Effects of Topography on Mechanisms of Radar Backscatter from Coniferous Forest and Upland Pasture.” IEEE Transactions on Geoscience and Remote Sensing 36 (5). IEEE: 1830–1834.

Notti, D., C. Meisina, F. Zucca, and A. Colombo. 2011. “Models to Predict Persistent Scatterers Data Distribution and Their Capacity to Register Movement along the Slope.” In Fringe 2011 Workshop, 19–23.

Notti, Davide, J. C. Davalillo, G. Herrera, and Oscar Mora. 2010. “Assessment of the Performance of X-Band Satellite Radar Data for Landslide Mapping and Monitoring: Upper Tena Valley Case Study.” Natural Hazards and Earth System Sciences 10 (9). Copernicus GmbH: 1865.

Plank, S., J. Singer, K. Thuro, and Ch Minet. 2010. “The Suitability of the Differential Radar Interferometry Method for Deformation Monitoring of Landslides—a New GIS Based Evaluation Tool.” In Proceedings of the 11th IAEG Congress Geologically Active, Auckland, New Zealand, 5–10.

Pourthie, Nadine, Aurélie Sand, R. Fjortoft, Fifamè Koudogbo, Javier Duro, and Anne Urdiroz. 2010. “SARVisor: An Integrated Tool to Facilitate SAR Data Selection.” In 30th EARSeL Symposium Remote Sensing for Science, Education, and Natural and Cultural Heritage, 45–52. UNESCO Paris, France.

R Development Core Team, RFFSC. 2013. R: A Language and Environment for Statistical Computing. R foundation for statistical computing Vienna, Austria. http://www.R-project.org/.

Rees, W. G. 2000. “Simple Masks for Shadowing and Highlighting in SAR Images.” Taylor & Francis.

Reiche, Johannes, Richard Lucas, Anthea L. Mitchell, Jan Verbesselt, Dirk H. Hoekman, Jörg Haarpaintner, Josef M. Kellndorfer, Ake Rosenqvist, Eric A. Lehmann, and Curtis E. Woodcock. 2016. “Combining Satellite Data for Better Tropical Forest Monitoring.” Nature Climate Change 6. Nature Publishing Group: 120–122.

Richards, John Alan. 2009. Remote Sensing with Imaging Radar. Vol. 1. Springer.

Rodriguez, Ernesto, Charles S. Morris, and J. Eric Belz. 2006. “A Global Assessment of the SRTM Performance.” Photogrammetric Engineering & Remote Sensing 72 (3). American Society for Photogrammetry and Remote Sensing: 249–260.

Sarvia, F., S. De Petris, and Borgogno-Mondino E. 2020. “Multi-Scale Remote Sensing to Support Insurance Policies in Agriculture: From Mid-Term to Instantaneous Deductions.” GIScience & Remote Sensing 57 (6): 770–784. doi:10.1080/15481603.2020.1798600.

Sarvia, Filippo, Elena Xausa, Samuele De Petris, Gianluca Cantamessa, and Enrico Borgogno-Mondino. 2021. “A Possible Role of Copernicus Sentinel-2 Data to Support Common Agricultural Policy Controls in Agriculture.” Agronomy 11 (1): 110.

Shimada, Masanobu. 2010. “Ortho-Rectification and Slope Correction of SAR Data Using DEM and Its Accuracy Evaluation.” IEEE Journal of Selected Topics in Applied Earth Observations and Remote Sensing 3 (4). IEEE: 657–671.

Small, David. 2011. “Flattening Gamma: Radiometric Terrain Correction for SAR Imagery.” IEEE Transactions on Geoscience and Remote Sensing 49 (8). IEEE: 3081–3093.

Small, David, and Adrian Schubert. 2019. “Guide to Sentinel-1 Geocoding.” University of Zurich / RSL. UZH-S1-GC-AD.

Ulaby, Fawwaz T., Richard K. Moore, and Adrian K. Fung. 1981. “Microwave Remote Sensing: Active and Passive. Volume 1-Microwave Remote Sensing Fundamentals and Radiometry.”

Veci, LUIS. 2015. “SENTINEL-1 Toolbox SAR Basics Tutorial.” ARRAY Systems Computing, Inc. and European Space Agency: Paris, France.

Veci, Luis, Pau Prats-Iraola, Rolf Scheiber, Fabrice Collard, Norman Fomferra, and Marcus Engdahl. 2014. “The Sentinel-1 Toolbox.” In Proceedings of the IEEE International Geoscience and Remote Sensing Symposium (IGARSS), 1–3. IEEE.

Vollrath, Andreas, Adugna Mullissa, and Johannes Reiche. 2020. “Angular-Based Radiometric Slope Correction for Sentinel-1 on Google Earth Engine.” Remote Sensing 12 (11). Multidisciplinary Digital Publishing Institute: 1867.

4 VEGETATION STRUCTURE QUALIFICATION

4.1 AMPLITUDE-BASED TECHNIQUES

4.1.1 A Simplified Method for Water Depth Mapping Over Crops During Flood Based on Copernicus and DTM Open Data

De Petris Samuele[a*], Ghilardi Federica[a], Sarvia Filippo[a] and Borgogno- Mondino Enrico[a]

[a]Department of Agricultural, Forest and Food Sciences (DISAFA), University of Turin, 10095 Grugliasco, Italy.

*Correspondence: samuele.depetris@unito.it

Published: 2022 in *Agricultural Water Management,* IF (2021): 6.611

Abstract: After an extreme rainy event agricultural fields can be submerged by water. Stagnant water can be generated by river' flooding or by soil saturation causing different damage level to crops. In this work, the flood event occurred on 3rd October 2020 in NW Italy along the Sesia river was assessed with special concern about damages affecting rice crop fields. A method was proposed aimed at detecting flooded areas and giving an estimate of water depth (WD) based on free available Copernicus data (Sentinel-1 and Sentinel-2) and digital terrain model (DTM). In particular, Sentinel-1 pre- and post-event images were compared by differencing (ΔVV). ΔVV was processed at pixel level to detect submerged areas through the thresholding Otsu's method. A simplified morphological analysis was then performed by DTM tessellation to map WD. A further step aimed at classifying submerged areas was achieved based on DTM and a proximity analysis, making possible to separate areas where water was related to soil saturation from areas where water was coming from the river. Corine Land Cover 2018 level-3 and NDVI from a Sentinel-2 pre-event image were used to map crops that were still to be harvested at the time of flood. These were the ones that were considered while estimating the potential economic loss. A total of 255 ha of rice that still to be harvested were submerged but only 211 ha were affected by river overflow. Using local rice yield and price the resulting economic loss was about 2200000 €.

Keywords: SAR; Sentinel-1; Sentinel-2; Watershed Segmentation; Flood Mapping, Crops Damage Mapping

1. Introduction

Floods and in general extreme meteorological events occur more frequently due to climate change. Their effects are particularly evident on crops and forests (Brown et al., 2012; Orusa et al., 2020; Sarvia et al., 2021a). Agricultural damage assessment after extreme rainy events is, ordinarily, based on the joint evaluation of the local agricultural situation, by mapping land use and soil characteristics, and the hydraulic conditions of the event (i.e. duration, velocity, intensity and amount transported material quantity). Floods can generate damages at different scales of analysis (Boccardo et al., 2007). At the farm scale, the impacts can affect buildings, rural infrastructures (e.g. irrigation channels) and machineries, resulting into extra costs for recovery efforts that can certainly condition revenues for several years apart (Morris and Brewin, 2014). Within fields, damages mainly concern soils, that can be eroded and moved away by water, depauperating top soil or accumulating new materials (Wilson, J. A., S. L. Olson, and J. Callan, 2011); moreover, depending on the time of flood with respect to the growing season of local crops, the yearly yield can be totally or partially compromised, even depending on water flow strength and debris content (Morris and Brewin, 2014). Monitoring conditions affecting flooded areas in the very next days after the events can certainly support damage assessment (Romali et al., 2018) permitting a refinement of estimates and developing a support for the insurance companies in quantifying and mapping risks (Borgogno-Mondino et al., 2019; F. Sarvia et al., 2020; Sarvia et al., 2019). In particular, one important hydraulic parameter to be considered is the above ground level (AGL) water depth (WD). Many experiences proved a strict relationship between crops damage degree and WD (Molinari et al., 2019; Shrestha et al., 2013; Vozinaki et al., 2015). Negative consequences on crops can be: root asphyxiation, soil contamination and disease spreading. With these premises, the growing availability of free satellite data from Earth Observation missions are enormously increasing the opportunities of monitoring floods (Lin et al., 2019, 2016; Rahman et al., 2019) and their effects (De Petris et al., 2021a). Different remote sensing techniques and hydrological

models have been proposed for these purposes. Tarpanelli et al. (Tarpanelli et al., 2018) used radar altimetry, while Westra and De Wulf (Westra and De Wulf, 2009) based their deductions on Moderate-Resolution Image Spectroradiometer (MODIS) data. Wang and Xie and Dano et al. (Dano et al., 2011; Wang and Xie, 2018) reported an exhaustive review of remote sensing-based applications for floods assessment. Synthetic aperture radar (SAR) and multispectral data, with special concern about those related to the Copernicus program, have been widely used to support emergency situations as natural disasters, floods and vegetation-related problems (Bian et al., 2018; Mason et al., 2021). They are known to represent an efficient tool for civil protection purposes especially in rapid response, where an immediate (even rough) damage estimate is required (Ajmar et al., 2015; De Petris et al., 2020, 2019; Smith, 1997). Ordinarily, flood monitoring and risk assessment are achieved by hydrological modelling based on flow energy balance equations involving several physical inputs (i.e. precipitations, air temperature, physical parameters of soil, topography, vegetation) (Puno et al., 2021, 2020). These models allow to simulate superficial and groundwater dynamics accounting for different hydrological processes (including WD) and can be summarized as it follows: one-dimensional 1D models as ESTRY, HEC-RAS, ISIS, MIKE 11, RUBICON, SOBEK, SWMM (Knebl et al., 2005; Kourgialas and Karatzas, 2014; Stoleriu et al., 2020; Vozinaki et al., 2012) or 2D models for flood mapping, as TUFLOW, MIKE 21, DELFT-FLS, RMA, FESWMS, TELEMAC (Banks et al., 2014; Ghimire, 2013; Ligier, 2016; Robins and Davies, 2011; Syme, 2001). These models are known to require many inputs that are often not easily available, especially far away from rivers (Devia et al., 2015), making difficult their application in a rapid mapping context. Typically, these physical-based models require a detailed geometric description of the river bed like flow rate, Manning's values, river sections, bottom slope and roughness of the analyzed river trait. Moreover, the entire river system must be schematically represented taking care about all the connected elements interacting with the river: stream junctions, bridges and culverts or lateral structures (Pistocchi and Mazzoli, 2002). Despite the huge literature concerning

SAR data application to monitor flood risk and its effects on urban and human activities, SAR imagery were poorly adopted to map flood damages in agricultural sector (Manavalan, 2017; Sanyal and Lu, 2004; Shen et al., 2019; Tsyganskaya et al., 2018). In this context, this work presents a new method based on free available data (satellite and elevation data) to detect flooded crops and estimate WD allowing a near-real time and continuous mapping of these variables. The procedure is presented with reference to the flooding event occurred on 3rd October 2020 by the Sesia river (NW Italy). Finally, a rough economic loss assessment was proposed concerning the rice fields.

The main issues explored in this work are: (a) a statistical based threshold selection criteria for flood delineation using SAR data, based on an adaptive method that makes it possible to automatically detect a threshold value accordingly to the specific area one is considering; (b) water depth mapping over flooded crops avoiding hydrological models; (c) stagnant water classification according to its source i.e. by river overflow or by soil saturation for better characterizing the effects of the event on crops. All these issues were presented and discussed in the following sections. The jointly used of free and near-real-time updated data allows to define a new procedure that could potentially give a rapid assessment of the effects of a flood on the agricultural sector supporting local restoration policies.

2. Material and Methods

2.1. Study Area

On 2nd October 2020, according to local meteorological data (http://www.arpa.piemonte.it), North-West Italy was affected by an intense rainfall (450 mm·d-1). Rainfall caused the flooding of the Sesia river, that develops at the border between Piemonte and Lombardia regions. Unfortunately, the event occurred on a critical period, close to the harvesting of rice, the main crop in the area, resulting in a significant damage to the local agriculture. An area of interest (AOI), sizing about 1105 km2 (Fig. 1) was selected including 58 Italian

municipalities (the most of them located within the Piemonte region) that the river was running through. In particular the flattest trait of the river was considered.

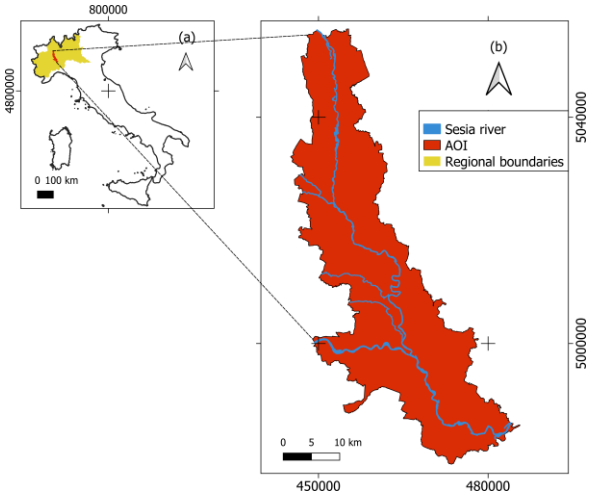

Figure 1. AOI is located close to the Sesia river. It develops between Piemonte and Lombardia regions, NW Italy. Reference frame is WGS 84 UTM zone 32N.

2.2. Available Data

2.2.1. Sentinel-1 Imagery

Sentinel-1 (S1) is one of the current largest space-borne missions providing free and open accessible SAR data having high temporal resolution from 6 to 2 days (combining ascending-descending orbits) well-fitting crop multi-temporal monitoring requirements. SAR da-ta processing is very complex and often data are not available free of charge as well stressed by Grimaldi et al. (Grimaldi et al., 2016). The complexity of SAR data pre-processing appears a key factor for SAR data slow uptake by a wider user community (Reiche et al., 2016; Vollrath et al., 2020). Conversely, Google Earth Engine (GEE) web-based platform allows an immediate access to pre-processed images making users to directly focus on their specific ap-plications (Gorelick et al., 2017). In this work, S1 ground range detected (GRD) interferometric-wide (IW) swath image collection available in GEE, was used. In particular, S1 GRD high resolution (GRDH) collection is released with a squared pixel having a geometrical resolution of 10 m,

georeferenced into a user defined cartographic reference frame (in this work set equal to WGS84 UTM 32N). This collection was already pre-processed by the Sentinel-1 Toolbox (S1TBX, (Veci et al., 2014) and the correspondent backscattering coefficient (σ° [dB]) for VV and VH polarizations mapped as separate raster layers. Ordinarily, water surfaces show very low backscattered signal in all polarizations (Manavalan, 2017; Manavalan et al., 2017, p.) but the co-polarized VV signal proved to be poorly affected by vegetation presence allow-ing a better detection of partially submerged areas (Manjusree et al., 2012). Therefore, two VV-polarized images, one pre-event and one post-event, were selected and directly processed by GEE. The reference image (pre-event) was acquired on 28th September 2020, while the post-event one was acquired on 3rd October 2020. The latter was used to explore flooded water distribution in the area (Fig. 2).

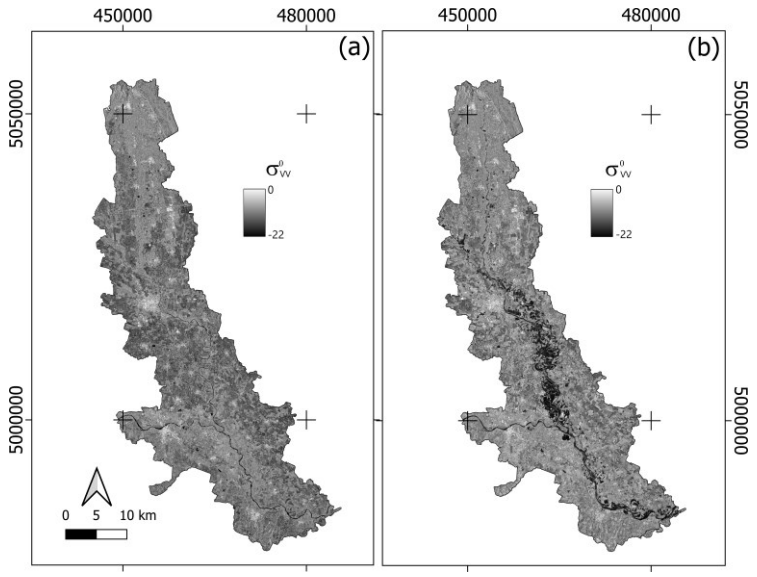

Figure 2. S1 backscattering (σ_{VV}^{0}) maps (a) before the event; (b) after the event. Reference frame is WGS84 UTM 32N.

2.2.2.Sentinel-2 Imagery

Sentinel-2 (S2) multispectral imagery was extensively adopted in vegetation mapping. In order to map vegetated areas a single S2 image, acquired on 28th September 2020, was selected and processed by GEE (collection titled: "COPERNICUS/S2_SR"). The image obtained was already calibrated in at-the-ground reflectance (processing level 2A) and orthoprojected into the WGS84 UTM 32N reference frame. Red (band 4, λ=665 nm) and NIR (band 8, λ=842 nm) bands were used for Normalized Difference Vegetation Index (NDVI) computation having a geometric resolution of 10 m. Some additional layers were also obtained mapping pixel quality (Scene Classification Map - SCL) useful to masking out unreliable pixels.

2.2.3. Digital Terrain Model

Two gridded DTMs available from Piemonte and Lombardia regional geoportals (https://www.geoportale.piemonte.it/cms/; http://www.geoportale.regione.lombardia.it/) were used. Piemonte DTM is updated at 2011 and has a height precision of ± 30 cm (1σ_DTM) (Borgogno Mondino et al., 2016). Lombardia DTM is update at 2015 and has a precision of ± 30 cm (1σ_DTM) (Biagi et al., 2013). Both were supplied in grid format with 5 m ground sample distance (GSD). In spite of the different updates, these DTMs represent the best resolute and accurate terrain models available for the AOI. They were preventively mosaicked (average was applied in overlapping areas) and unitarily used for next processing.

2.2.4. Sesia River Area

A polygon vector layer mapping the Sesia river area (SRA) was extracted from the Piemonte regional hydrologic network vector layer that was downloaded by the regional geoportal (https://www.geoportale.piemonte.it/cms/bdtre/modalita-

di-pubblicazione-e-fruizione). This layer was updated in 2020 having a nominal scale of 1:10000.

2.2.5.Corine Land Cover Map

The 2018 Corine Land Cover (CLC2018) dataset level 3 was used to locate and map agricultural areas in AOI. CLC2018 was released, for free, from the Land Monitoring Service Copernicus (https://land.copernicus.eu/pan-european/corine-land-cover) as vector layer having a nominal scale equal to 1:100000. Level 3 of CLC2018 is the most detailed level according to the hierarchical classification system adopted by the CORINE Land Cover project since it is design with a minimum mapping unit of 25 ha and minimum mapping unit of 100 m (Büttner, 2014). Table 1 shows agricultural classes and correspondent codes of CLC2018 level 3 classification levels considered in this work.

Table 1. Classes as encoded by CLC2018 level 3 in the study area.

Code class CLC2018 level 3	***Code meaning***
211	Not-irrigated arable land
213	Rice fields
231	Pastures
242	Complex cultivation patterns
243	Land principally occupied by agriculture, with significant areas of natural vegetation

2.2.6. Reference Ground Data

To validate the proposed methodology, the "Azienda agricola Martinengo Luigi Sebastiano", an important local farm located in the municipality of Langosco (province of Pavia), was involved in order to collect reference data (RD) on WD after the Sesia river overflow. A field survey campaign was carried out by the farm employees. In particular, WD was measured in the accessible fields using a graduated pole (Fig. 3).

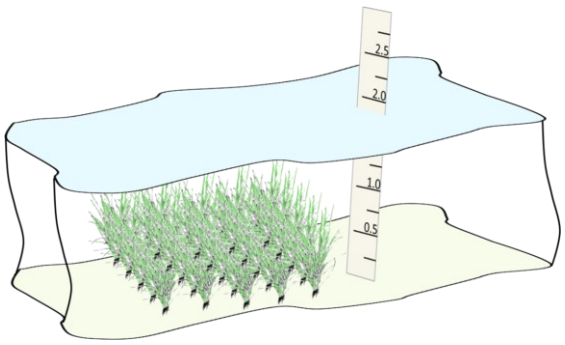

Figure 3. Reference scheme used during the field survey campaign for WD measurement.

The agricultural field recorded were delineated as polygons vector layer by photointer-pretation on true-color orthomosaic, available on the Piemonte regional geoportal (www.geoportale.piemonte.it), updated to 2010 and having a geometric resolution of 20 cm. Subsequently, the WD data obtained from the field survey were associated with the respec-tive polygon. A total of 61 rice plots were recorded and labelled as damaged (46) and (15) as undamaged fields. RD are located in the municipality of Caresana, Rosasco, Motta de' Conti and Langosco within the AOI (Fig. 4).

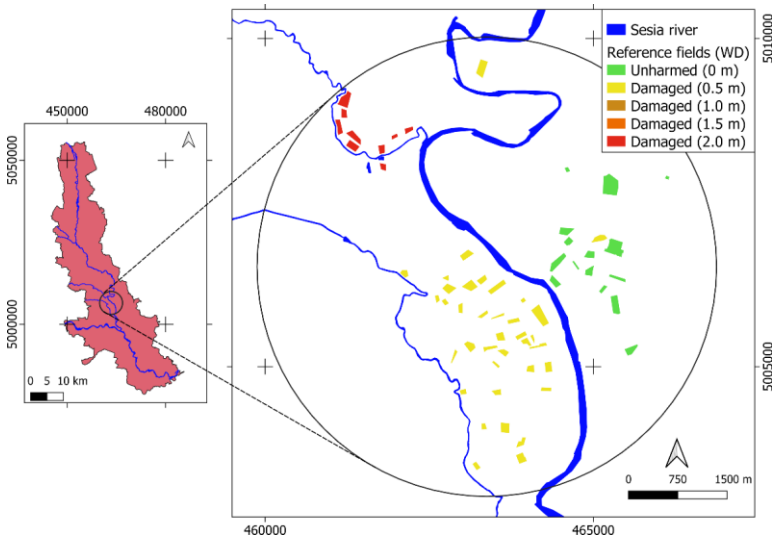

Figure 4. Reference fields used for validation. Reference frame is WGS84 UTM 32N.

Unfortunately, the size of fields is limited and authors are aware that this dataset does not perfectly fit statistical requirements, nevertheless, it represents ordinary availability of ground data from farmers when data are not directly managed by scientists. In fact, the most data from farmers, generally, rely on their autonomous collections and decision of making them public. It should be noted that data regarding WD outside river/brook are not ordinary available, especially in the absence of an experimental design or moreover after an extreme and unexpected event such as a flood. Furthermore, it is a fact that, when dealing with floods, a sample design cannot be programmed, being impossible to a-priori know where water will be present. Moreover, water persistence above ground is limited in time making further difficult to get data about the situation before it is absorbed by soil. Nevertheless, the average size of the collected fields was about 1.36 ha. The authors found that the sample provided by local farmers including 61 rice fields (having a total area about to 83 ha) corresponding to about 3.4% of the expected flooded rice fields within the AOI (about 2400 ha).

2.2.7.Agricultural Economic Loss Assessment

Rice yield and market price were also considered in this work to complete the proce-dure with an estimation step as usually required when quantifying the impact of a flood after the event. The average rice yield in this area was set to 7 $t \cdot ha^{-1}$ (Tesio et al., 2014), and the local price to 340 $€ \cdot t^{-1}$ (ISMEA, 2021).

2.3. Data Processing

In figure 5 is presented the workflow adopted in this work. Datelined information and acronyms are reported in the next sections.

2.3.1. Flooded Area Mapping

S1 data have already proved to be an effective tool to detect flooded areas (Bioresita et al., 2018; Ezzine et al., 2020; Twele et al., 2016). Flood detection is

possible thanks to the strong specular reflection that affects SAR signal lighting water surfaces; this peculiar scattering mechanism makes a water pixel poorly scattering (low signal) all the polarizations. Based on this fact, many methods were developed to map flooded pixels by thresholding (Manavalan, 2017). Many of them are based on an automatic selection of a proper threshold value; in this context, Sezgin and Sankur (Sezgin and Sankur, 2004) provided an exhaustive comparison about the performance of several grey level image thresholding techniques. Among these techniques, the Otsu's method (Otsu, 1979) was cited as an effective technique (Kurita et al., 1992; Trier and Jain, 1995) to define automatic threshold based on image histo-gram. Such method is a nonparametric and unsupervised one based on the separability maximization of the tested classes in the image digital number domain. In particular, threshold that dichotomize the pixels into two classes (i.e., flooded and not-flooded areas) is defined itera-tively covering the entire histogram values range. For each iteration within and between classes variances are calculated. Consequently, the problem is reduced to an optimization problem searching for a threshold that minimize within-class variances and maximize between-class one.

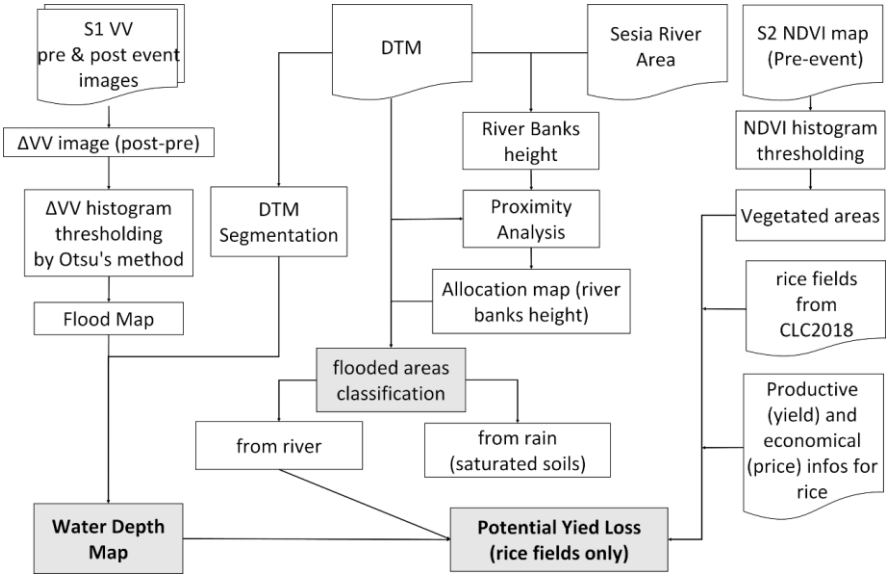

Figure 5. Flowchart of the proposed method. In grey the main outputs: Water Depth Map (i.e. WD(x,y)), Flood areas classification (PFAM) and potential rice yield loss. All steps will be discussed in the following sections.

Given the difficulty of finding a robust threshold value by using only one post-event acquisition, the authors tried to achieve this problem proposing a thresholding method applied to the image difference resulting from the pre- and a post-event acquisition. In particular, the Otsu's method was applied directly within GEE to generate a binary classification mapping flooded and not-flooded areas from the VV images difference (pre- and post-event S1 images). Pre- and post-event images were preventively filtered by a circular median filter (50 m kernel size) in order to minimize speckle-related noise. The VV image of 28th September (RI) and the one of the 3rd October 2020 were used to map the pre- and post-event situation, respectively. Comparison was achieved by grid differencing to generate a new image (hereinafter called ΔVV) mapping local differences. Expectation for flooded pixels was that differences (post- minus pre-) were negative; consequently, all ΔVV pixels showing a value > 0 were masked out. With reference to remaining pixels, ΔVV histogram was analyzed by Otsu's method and an optimal threshold defined. Finally, a classification (hereinafter called Flooded Map - FM) mapping flooded (value = 1) and not-flooded (value = 0) pixels was produced. A further refinement was applied to remove small/isolated flooded patches, by counting FM inter-pixel connections using the *ee.connectedPixelCount()* operator available in GEE. Patches having less than 100 connections (corresponding to a minimum mapping unit of 1 hectare approximately) were masked out.

2.3.2. Vegetation Masking

Flooded areas strictly depend on ground morphology, while damage can vary according to local land cover and crops phenology. Flood can improve crop condition by depositing nutrients or water in the very early phenological stages; differently, in late stages it could compromise final yield. Moreover, it also can be possible that a given crop was already harvested and therefore no damage occurred. Trying to map these different situations, a vegetation mask was

generated with reference to the NDVI image mapping the pre-event conditions. Not-vegetated pixels were masked out by thresholding the NDVI map (NDVI < 0.4). The threshold was selected according to several previous studies (Burgan and Hartford, 1993; Gao, 1996; Ormsby et al., 1987; Zhang et al., 2003) that proved that, ordinarily, vegetated areas show NDVI greater than 0.4. The initial assumption was that, in the area the most diffused and valuable crop still to be harvested at the time of the flood, was the rice. NDVI was not used to get an estimate of the phenological stage of rice, that was a-priori known being the time of flood close to the harvest. NDVI was just used to detect vegetated from not-vegetated areas at the moment of the flood, making possible to separate rice fields that had been already harvested (NDVI < 0.4) from the one still hosting rice (NDVI > 0.4). The resulting raster mask (Vegetation Mask - VM) was used to address successive operations towards the only vegetated pixels (included crops). Crops were finally mapped intersecting VM with the available CLC2018. Finally, rice mapping was obtained with reference to the CLC2018, but only rice fields showing NDVI > 0.4 were assumed as still waiting for harvest and, consequently, determining an economical loss.

2.3.3. Water Depth Mapping

As already mentioned, crop damage is proportional to the AGL WD (Molinari et al., 2019; Shrestha et al., 2013). Rapid mapping and timely damage estimation are important requirements while working with catastrophically event (Sarvia, De Petris, and Borgogno-Mondino 2020; De Petris et al. 2021) in order to recover and restore farmers. In this context, geographical Information Systems (GIS) and free geographical data can support such analysis. In particular, this work relies on the adoption of a simple morphological analysis of DTM to give an estimate of WD within flooded areas (Fig. 6). DTM was properly segmented through the watershed algorithm available in System for Automated Geoscientific Analyses GIS (SAGA GIS) vs 7.9.0 with the aim of identifying local terrain depressions naturally hosting water. Segmentation was performed using the following parameters: method = maxima; join segments on saddle difference using a

threshold equal to 0.8. Resulting patches (hereinafter called Depression Patches - DPs) were mapped as polygons vectors layer. DPs was then intersected with FM to refine size patches to fit only flooded areas as detected by SAR. For each refined DP the minimum (h^i_{min}) and maximum (h^i_{max}) values of height from DTM were calculated by zonal statistics. Their difference (Δh^i) defines the maximum potential thickness of the water layer that DP can contain. Δh^i was computed by the field calculator tool within SAGA GIS and saved as new field in the correspondent attribute table according to eq.1.

$$\Delta h^i = h^i_{max} - h^i_{min} \quad (1)$$

Subsequently, WD can be estimated according to eq. 2.

$$WD_{(x,y)} = \Delta h^i - [DTM(x,y) - h^i_{min}] \quad (2)$$

By taking eq.1 into eq.2, it can be noted that WD is only related to h^i_{max} and local elevation value (DTM (x,y)). Therefore, a new raster layers, $h^i_{max}(x,y)$, was then generated, aligned to the available DTM, by gridding DP with reference to h^i_{max} fields. Finally, eq. 3 was used to map WD(x,y) in the area.

$$WD(x,y) = h^i_{max}(x,y) - DTM(x,y) \quad (3)$$

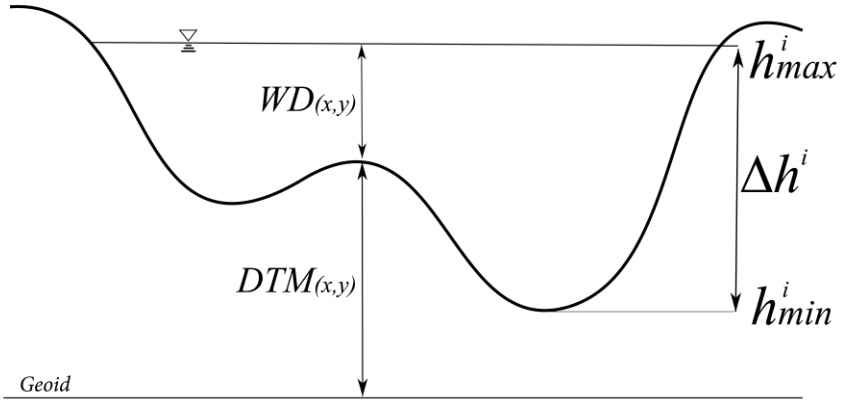

Figure 6. Reference scheme used during the morphological analysis to map WD. Computation was done for all DPs as defined during DTM tessellation.

2.4. Validation

Flooded areas detection accuracy was assessed by using RD. In fact, 61 reference fields were used for this purpose and they were labelled as flooded or not flooded during ground survey campaign. RD polygons were rasterized into a gridded layer having the same resolution of FM. Finally, the confusion matrix and related accuracies were computed comparing at the pixel-level RD raster and FM. Subsequently, for each RD field zonal statistics were performed in order to determine the mode value of WD. Consequently the mean absolute error (MAE) between the value of WD derived from the field survey campaign and the estimated one was calculated using eq. 4 at field level in order to test the WD map accuracy (Will-mott and Matsuura, 2005).

$$MAE = \frac{\sum_{i=1}^{n} |x_i^r - x_i^o|}{n} \quad (4)$$

where n is total number of fields in RD, x_i^r is reference WD value in the i-th fields of RD, x_i^o is the observed WD resulted by applying the proposed method. Authors are conscious that this sample size does not fully fit the ordinary statistical requirements. Nevertheless, this situation can frequently appear during a common technology transfer operation, especially in the agricultural sector.

2.5. Potential Loss of Rice Yield

During extreme rainy events, submerged areas as detectable from satellite, can be related to flood or to soil saturation. In soil saturated areas, stagnant water is clearer (less sediments) since mainly caused by rain. Conversely, flooded areas are characterized by water caused by river dynamics where many sediments and debris are present. Additionally, given the high laminar force of water flowing across fields, lodged plants can also be present. These phenomena, therefore, affect crops in a very different way. In soil saturated areas, stagnant water can submerge plants, but after few hours it can be absorbed by soil or flowed away, resulting in a minor damage. With these premises, a method to separate potential flooded areas from the soil saturated ones, was proposed based again on the

available DTM. A mask of potential flooded areas was generated testing, at pixel-level, if the local DTM(x,y) value was lower than the altitude of the nearest river bank. In this case, the pixel was labelled as 1 (flooded); differently, it was labeled as 0 (not flooded). The above mentioned condition was based on the assumption that ordinary water flow unlikely spreads along positive slopes gradient but, conversely, it naturally moves along a negative slope gradient (Lighthill and Whitham, 1955; Zimmermann and Church, 2001). This assumption could be violated during extreme flows where flood mass can even move along positive gradients. Nevertheless, some flow approximations are always needed to model hydrological processes (Bout and Jetten, 2018). A proximity grid analysis was performed considering DTM(x,y) and river banks altitude. The latter was obtained by clipping DTM by SRA. The allocation tool available in SAGA GIS was used to associate the altitude of the closest river bank to the generic pixel. A raster layer hereafter called river banks altitude (RBA) having the same GSD of DTM was generated mapping allocation values. A grid difference between RBA and DTM(x,y) was then performed and thresholded. All pixels where difference value was greater than -0.5 m, i.e. lower bound of uncertainty of DTM differences ($\sqrt{2}\ \sigma_{DTM} = \pm 0.5\ m$, were labelled as potentially flooded (code = 1); all the other pixels were labelled as not-flooded (code = 0). Resulting classification (Potential flooded areas map, PFAM), assumed to map the potentially flooded areas, was intersected with VM and FM in order to map vegetated (potentially hosting crops) flooded areas, from the submerged ones, where water was detected but possibly related to rain and not to river flood. Therefore, from the intersection of PFAM, FM and VM, only active crops flooded by river overflow were isolated and remaining areas were masked out from subsequently computation. A further investigation was then achieved to get an estimate of the potential yield loss and, consequently, of the associated economic lost income.

3. Results

3.1. Flooded Area Mapping

Otsu's method was applied to ΔVV histogram (Fig. 7a) and the correspondent thresh-old values were found. All ΔVV pixel values less than the threshold were labelled as flooded (code = 1 in FM) and the others as not-flooded (code = 0 in FM) (Fig. 7b). The assumption was that flooded areas should present highly negative ΔVV values due to the dominant specular scattering mechanism that occurs when a water film covers the surface. The found thresh-old value was equal to -6.94 ΔVV. Flooded area, as mapped on 3rd October 2020 by S1, proved to be about 4300 ha.

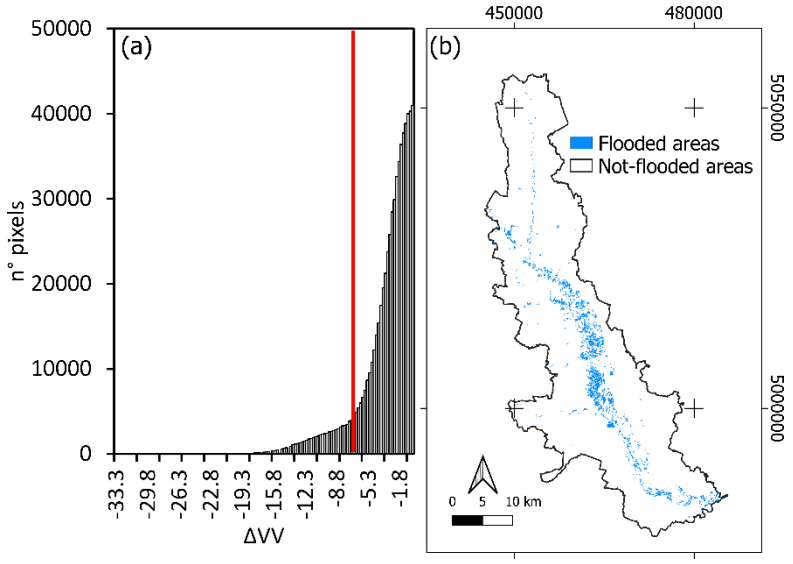

Figure 7. (a) ΔVV histogram. Red line corresponds to the threshold value defined through the Otsu's method; (b) FM. Reference frame: WGS84 UTM 32N.

In terms of land cover classes (CLC2018 level 3), table 2 shows the impact of floods in the agricultural context. This analysis proved that rice was the most affected crop with more than 2390 flooded hectares (over 72 % of the flooded area. Classes 221 and 231 appeared to be not affected by the event.

Table 2. Amounts of flooded areas divided per CLC 2018 level 3 classes.

CLC code class	***211***	***213***	***231***	***242***	***243***
Flooded area (ha)	492.68	2396.03	0.00	8.92	390.79
Flooded area (%)	14.98	72.86	0.00	0.27	11.88

3.2. Vegetation Masking

An NDVI map characterizing vegetation before the event was generated (Fig. 8a). All values greater than 0.4 were labelled as vegetated (VM code = 1) and the other ones were masked out. VM (Fig. 8b) layer covers about 665.8 km^2.

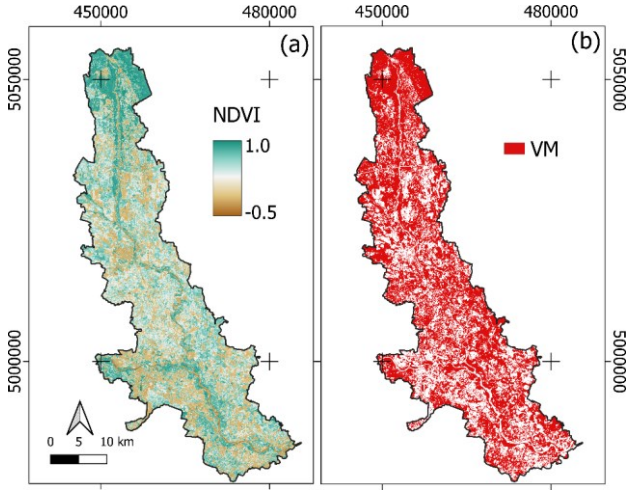

Figure 8. (a) NDVI map obtained from the available pre-event S2 multispectral image; (b) VM mapping active vegetation before the event. Reference frame: WGS84 UTM 32N.

An intersection between VM and agricultural CLC classes was performed in order to map active vegetated crops (Fig. 8b) that probably were affected by flood. Whereby, a total of 1151 ha of affected rice crops were found in AOI, while the remaining 1244 hectares of rice, from the VM map, appeared to be already harvested. Other CLC classes (such as 211) were also affected by the event (Tab. 3). Unfortunately, at the CLC level it is not possible to specify these crops and consequently estimate the level of damage on this class.

Table 3. Amount of vegetated and not-vegetated areas (ha) in AOI during the 3rd October 2020 flood event. They are supplied separately according to the CLC 2018 level 3 classes.

CLC code class	***211***	***213***	***242***	***243***
Vegetated (ha)	255.36	1151.80	6.82	259.32
Not Vegetated (ha)	237.32	1244.23	0.00	0.00

3.3. Water Depth Mapping and Validation

FM accuracy was assessed by confusion matrix computation involving rasterized RD and FM. According to table 4, proposed method results to be an effective tool to separate flooded areas from not-flooded ones (overall accuracy was 96%). Producer's and User's Accuracy were found to be equal to 94% and 100% for flooded areas respectively. Moreover, similar accuracies for not-flooded areas were found to be high (100% and 89% respectively).

Table 4. Confusion matrix resulted from FM and RD comparison at the pixel-level.

Classes	***Flooded***	***Not flooded***	***Total***	***User's Accuracy***
Flooded	20685	0	20685	100%
Not flooded	1332	11223	12555	89%
Total	22017	11223	Kappa	91%
Producer's Accuracy	94%	100%	Overall Accuracy	96%

WD map and relative cumulative frequency distribution are reported in figure 9. MAE of WD map, calculated accordingly to equation 4, was about 0.42 m. This result well fits the theoretical accuracy of DTM differences (0.5 m). Due to the high geometric regularity of soil surface in rice plots, MAE value suggests that the WD variation within a plot is insignificant and mainly driven by the random nature of the DTM accidental error common to all measurements.

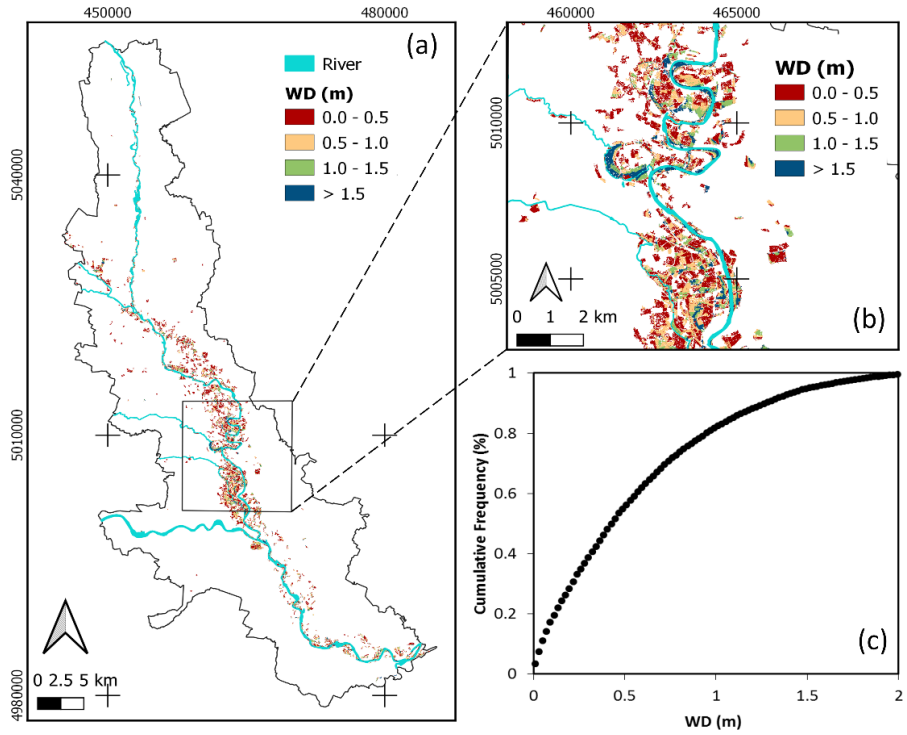

Figure 9. (a) WD map; (b) WD map focus area; (c) Cumulative frequency distribution of WD over the whole AOI. Reference frame is WGS84 UTM 32N.

3.4. Potential Loss of Rice Yield

According to PFAM (Fig. 10a), potentially floodable areas resulted to be 46245 ha. With reference to VM and FM possibly flooded active crops (mainly rice) were detected. These sized about 930 ha (Fig. 10b). Additionally, 221 ha were recognized as "submerged", i.e showing water related to soil saturation from rain (Tab. 5). Since only in flooded areas (riv-er related) crop damage was retained as significant, an assessment was performed to give an estimate of rice yield loss. According to the above mentioned ("Agricultural Economic Loss Assessment" section) data, potential yield loss resulted in 6510 tons, corresponding to an economical income loss of 2214354 €.

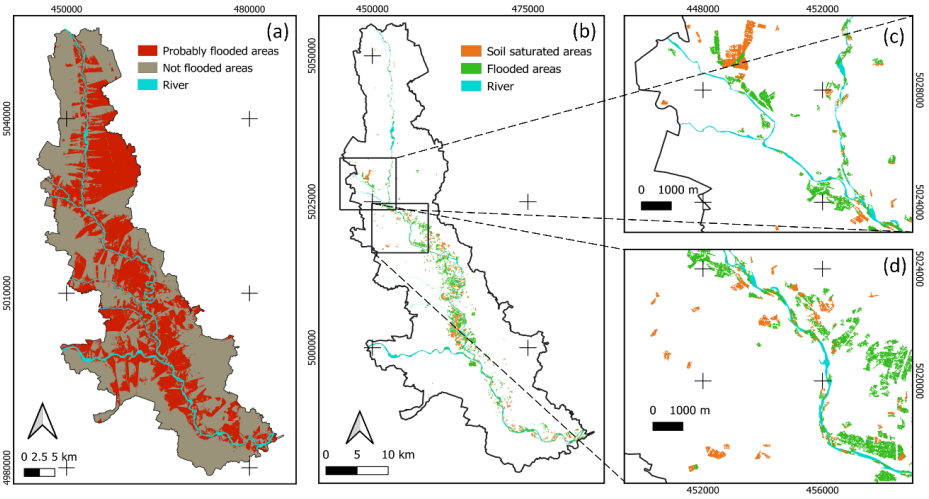

Figure 10. (a) PFAM representing potential flooded areas as mapped according to DTM proximity analysis; (b) Classification of submerged areas that were separated in flood-related and rainfall-related (soil saturation) classes; (c-d) two focus areas of submerged areas classification. Reference frame is WGS84 UTM 32N.

Table 5. Amount of submerged vegetated areas (ha) on 3rd October 2020. They are reported with reference to the CLC 2018 level 3 classes and to the type of submersion.

Areas	***211***	***213***	***242***	***243***
Flooded (ha)	211.60	930.40	6.79	208.74
Submerged - Soil saturation (ha)	43.75	221.40	0.02	50.58

4. Discussions

Ordinarily, flooded areas mapping by hydrological models relies on physically-based simulations involving meteorological data, DTMs, river and soil features. These models generate outputs resulting from local assumptions and simplifications as deeply discussed by (Devia et al., 2015; Sood and Smakhtin, 2015). Differently, SAR satellite-based approaches allows to detect actual submerged areas based on physical scattering mechanism (i.e. surface scattering). This reduces uncertainty related to the definition of the correct empirical parameters that hydrological models require. SAR image-based methods are strictly dependent on a thresholding processing step whose performance strictly relies on the time, after the event, that a proper im-age can be available. In fact it is expected that the number of flooded pixels decreases with the passing of days,

making weaker statistical deductions concerning ΔVV distribution analysis especially related to class separability (De Petris et al., 2021a). It is worth to remind that the majority of image thresholding techniques depends on patch size, making Otsu's method an exception since operating regardless of object size and, consequently, well-fitting crop detection (i.e. small patches) (Lee et al., 1990). As far as obtained results are concerned, FM proved to correctly detect flooded fields with the respect to RD. Authors again remark that, given the very small size of RD fields, a rigorous validation was actually not possible. This is a common condition while dealing with natural hazards related problems, where data for validation are often missing due to unfavorable environmental conditions, sometimes unsafe, characterizing hit areas after the event. Nevertheless, literature confirmed that the joint use of Otsu's method and SAR imagery is effective in flooded areas detection as reported by (Pulvirenti et al., 2013; Schumann et al., 2010) with respect to study cases exactly concerning areas that are very closed to our study area (i.e. Northwestern part of Po Valley). With special concerns about new issues that this work dealt with, the problem related to the distinction between are-as hosting water coming from rainfall (soil saturation) and those actually flooded by the river is certainly the most interesting one. These two situations contemporarily occurring after a flooding event, are expected to determine different damage levels to crops. To take care about this, PFAM was generated based on proximity analysis (allocation tool). PFAM proved to be affected by several simplifications: (a) proximity analysis depends on DTM and SRA geometric resolution and both altimetric and planimetric precision (Awange and Kiema, 2013; Boc-cardo et al., 2003); (b) water flow was assumed to only run along a negative slope gradient; (c) since proximity analysis only maps the closest RBA to the generic position, an underestimation of flooded areas is expected. In fact, other points can also contribute to supply water to the same location; (d) during the flood some obstacles can interrupt water flow from river to the generic point and, consequently, not taking care about this can generate an overestimation of areas potentially flooded by river. For a complete transfer of this method to the operational compart, further investigations are

expected to be done. The first one concerns the analysis of the effects of spatial connectivity and patchiness affecting both river and crops. From this point of view, only few works exist in literature, suggesting that an important knowledge gap still persists thus requiring a proper investigation (Alaoui et al., 2018; Western et al., 1998). Moreover, the lack of an updated crop type map represents a limit for a proper damage assessment over difference crops. Therefore, future developments will be expected to involve in the proposed approach a crop type detection derived by remotely sensed data (Sarvia et al., 2021b). The second one concerns the effect of DTM accuracy in both the segmentation process and robustness of WD estimates, specifically looking for the separated contribution of DTM absolute and relative accuracies. DTM accuracy and spatial resolution is basic while dealing with geometric issues like water level mapping. One constraint of the method is in fact that the DTM vertical uncertainty is lower than the expected value of the measure one is going to do. It is well known that global DTMs, like ASTER (Advanced Spaceborne Thermal Emission and Reflection Radiometer) DTM v2 and SRTM (Shuttle Radar Topography Mission) show a reduced absolute vertical accuracy (about 10 m) coupled with a pixel size of 30 and 90 m respectively. These features make them not compliant with this type of analysis. Nevertheless, the most of countries make available through their institutional geoportals, more detailed and site specific DTMs, the most of them from LiDAR acquisitions, having accuracies and resolutions consistent with the one we adopted for this work. An absolute vertical accuracy of 0.5 m could be enough while working at the landscape level and when ground has to be compared with a water level that, during a flood, could significantly be over the meter. Moreover, when a vertical absolute accuracy of 0.5 m is declared by suppliers, it is expected that relative accuracy (concerning height differences between points from the same DTM) is higher, making the data more and more proper. As far as geometric resolution is concerned, a DTM having a 5 x 5 m pixel size is perfectly consistent with a 1:25000 scale map and, consequently proper for at-landscape-level analysis like the one required for floods affecting wide areas. Some refinements would be desirable concerning WD and water persistence effects on

crop damage, introducing a preliminary step for crop classification from satellite data and its characterization in terms of phenology (Sarvia et al., 2021b). This information will certainly drive to develop a more robust crop damage assessment making possible to overcome those approximations related to the adoption of a low-resolution crop map like the Corine Land Cover one is. We remind that the CLC minimum mapping unit is 25 ha and not all the crops are taken into considerations separately, suggesting a more specific classification. As far as flooded crops mapping is concerned, the joint use of VM and CLC2018 proved to effectively support rice damage assessment. A critical point still persists concerning NDVI thresholding since, depending on the adopted threshold value, crop detection and related economic loss estimates can greatly vary. Concerning WD mapping, accuracy of estimates was found to be 0.42 m (MAE). This result is consistent with those other methods can generate. Specifically, results obtained by the RAPIDE tool proposed by Scorzini et al. (Scorzini et al., 2018) showed a MAE ranging be-tween 0.28 and 0.79 m for the flood event occurred in Lombardia region in November 2002. Gatti (Gatti, 2016) found a WD MAE varying between 0.42 and 0.73 m for the flood event occurred in Sardegna region (Italy) in November 2013. Finally, WD uncertainty from the pre-sent work was also consistent with the one from 2D hydrological models like FwDET that was applied in Brazos River area (Texas, USA) during the flooding event occurred in Septem-ber 2013 where an accuracy of 0.37 m was found (Cohen et al., 2018). Concerning agronomic issues, it is worth to remind that water persistence (De Petris et al., 2021a) and vegetation stage can significantly affect the damage impact of crops (Rahman and Di, 2020). In this regard, several indices were proposed in the literature for the evaluation of crop damage following natural disasters, such as the Vegetation Condition Index or the Disaster Vegetation Damage Index (L. Di et al., 2018; S. Di et al., 2018), however no works aim at estimating the WD with Copernicus and DTM open data are currently present. The pos-sibility of mapping WD can be therefore useful to locally test, in this particular case, if rice was significantly or totally submerged. Since rice average height close to the harvest is about 0.80 m (Fogliatto et al., 2012) WD information

makes it possible to better quantify potential crop damage. This is strictly related to the economic loss that the event possibly determined. From this point of view, according to the local price of rice (340 €·t-1) and to the nominal yield (7 t·ha-1), the potential income loss was found to be equal to 2214354 €. This result can probably vary according to local damage level, farmer's recovery effort, rice varieties; nevertheless, it represents a first rapid estimate of local economic loss that well fits the requirements needed while working with disastrous events (De Petris et al. 2021; Sarvia, De Petris, and Borgogno-Mondino 2020).

5. Conclusions

In this work, the flood event occurred on 3rd October 2020 in NW Italy along the Sesia river was assessed with special concern about damages affecting rice crop fields. A method was proposed aimed at detecting flooded areas and giving an estimate of WD based on free available Copernicus data (Sentinel-1 and Sentinel-2) and DTMs. In particular, S1 GRD IW pre- and post-event images were compared by differencing (ΔVV). ΔVV was processed at pixel level to detect submerged areas through the thresholding Otsu's method. A ΔVV value of -6.94 was found able to separate areas with and without stagnant water (about the 4% of the AOI). Otsu's method was adopted to make objective the selection of the proper threshold value to map areas with and without water from S1 data. The method is adaptive, making possible to automatically detect the threshold value accordingly to the specific area one is considering. A simplified morphological analysis was then performed by DTM tessellation to map DPs. These were interpreted as elementary units to refer WD estimates to. The WD accuracy was tested in respect of local ground data resulting in a MAE of 0.42 m. A further step aimed at classifying submerged areas was achieved based on DTM and SRA proximity analysis, making possible to separate areas where water was related to soil saturation from areas where water was coming from the river. CLC2018 level-3 and NDVI from a S2 pre-event image were used to map crops that were still to be harvested at the time of flood. These were the ones that were considered

while estimating the potential economic loss. About 211 ha of rice were submerged by river flooding determine an economic loss of about 2200000 €.

Concluding, in this work a simplified approach based on GIS and free available data was proposed to support flood related damage estimation. Simplicity and cheapness of the approach, coupled with the obtained WD uncertainty, are certainly interesting if compared with more complex methods based on hydrological models. These ordinarily require many inputs that are rarely available outside rivers and difficultly available for agricultural areas, especially during an unexpected and extreme event such as flood.

References:

Ajmar, A., Boccardo, P., Disabato, F., Tonolo, F.G., 2015. Rapid Mapping: geomatics role and research opportunities. Rendiconti Lincei 26, 63–73.

Alaoui, A., Rogger, M., Peth, S., Blöschl, G., 2018. Does soil compaction increase floods? A review. J. Hydrol. 557, 631–642.

Awange, J., Kiema, J.B., 2013. Environmental geoinformatics. Berl. Heidelb. Springer Berl. Heidelb. Doi 10, 978–3.

Banks, J.C., Camp, J.V., Abkowitz, M.D., 2014. Adaptation planning for floods: a review of available tools. Nat. Hazards 70, 1327–1337.

Biagi, L., Carcano, L., Lucchese, A., Negretti, M., 2013. Creation of a multiresolution and multiaccuracy DTM: problems and solutions for HELI-DEM case study. Int Arch Photogramm Remote Sens XL-5 W 3.

Bian, X., Shao, Y., Wang, S., Tian, W., Wang, X., Zhang, C., 2018. Shallow water depth retrieval from multitemporal sentinel-1 SAR data. IEEE J. Sel. Top. Appl. Earth Obs. Remote Sens. 11, 2991–3000.

Bioresita, F., Puissant, A., Stumpf, A., Malet, J.-P., 2018. A method for automatic and rapid mapping of water surfaces from sentinel-1 imagery. Remote Sens. 10, 217.

Boccardo, P., Giulio Tonolo, F., Perez, F., Disabato, F., Borgogno Mondino, E.C., 2007. ITHACA: a new project in the field of emergency management, in: 32nd International Symposium on Remote Sensing of Environment, ISRSE (CRI). ISRSE/ISPRS, pp. 1–4.

Boccardo, P., Mondino, E.B., Tonolo, F.G., 2003. High resolution satellite images position accuracy tests, in: IGARSS 2003. 2003 IEEE International Geoscience and Remote Sensing Symposium. Proceedings (IEEE Cat. No. 03CH37477). IEEE, pp. 2320–2322.

Borgogno Mondino, E., Fissore, V., Lessio, A., Motta, R., 2016. Are the new gridded DSM/DTMs of the Piemonte Region (Italy) proper for forestry? A fast and simple approach for a posteriori metric assessment. IForest-Biogeosciences For. 9, 901.

Borgogno-Mondino, E., Sarvia, F., Gomarasca, M.A., 2019. Supporting insurance strategies in agriculture by remote sensing: a possible approach at regional level, in: International Conference on Computational Science and Its Applications. Springer, pp. 186–199.

Bout, B., Jetten, V.G., 2018. The validity of flow approximations when simulating catchment-integrated flash floods. J. Hydrol. 556, 674–688.

Brown, M.E., De Beurs, K.M., Marshall, M., 2012. Global phenological response to climate change in crop areas using satellite remote sensing of vegetation, humidity and temperature over 26 years. Remote Sens. Environ. 126, 174–183.

Burgan, R.E., Hartford, R.A., 1993. Monitoring vegetation greenness with satellite data. Gen Tech Rep INT-GTR-297 Ogden UT US Dep. Agric. For. Serv. Intermt. Res. Stn. 13 P 297. https://doi.org/10.2737/INT-GTR-297

Büttner, G., 2014. CORINE land cover and land cover change products, in: Land Use and Land Cover Mapping in Europe. Springer, pp. 55–74.

Cohen, S., Brakenridge, G.R., Kettner, A., Bates, B., Nelson, J., McDonald, R., Huang, Y.-F., Munasinghe, D., Zhang, J., 2018. Estimating floodwater depths from flood inundation maps and topography. JAWRA J. Am. Water Resour. Assoc. 54, 847–858.

Dano, U.L., Abdul-Nasir, M., Ahmad, M.H., Imtiaz, A.C., Soheil, S., Abdul-Lateef, B., Haruna, A.A., 2011. Geographic information system and remote sensing applications in flood hazards management: a review. Res. J. Appl. Sci. Eng. Technol. 3, 933–947.

De Petris, S., Berretti, R., Sarvia, F., Borgogno-Mondino, E., 2019. Precision arboriculture: a new approach to tree risk management based on geomatics tools, in: Remote Sensing for Agriculture, Ecosystems, and Hydrology XXI. International Society for Optics and Photonics, p. 111491G.

De Petris, S., Sarvia, F., Borgogno Mondino, E., 2021a. Multi-temporal mapping of flood damage to crops using sentinel-1 imagery: a case study of the Sesia River (October 2020). Remote Sens. Lett. 12, 459–469. https://doi.org/10.1080/2150704X.2021.1890262

De Petris, S., Sarvia, F., Borgogno-Mondino, E., 2020. A New Index for Assessing Tree Vigour Decline Based on Sentinel-2 Multitemporal Data. Application to Tree Failure Risk Management. Remote Sens. Lett. 12, 58–67. https://doi.org/10.1080/2150704X.2020.1837985

De Petris, S., Sarvia, F., Gullino, M., Tarantino, E., Borgogno-Mondino, E., 2021b. Sentinel-1 Polarimetry to Map Apple Orchard Damage after a Storm. Remote Sens. 13, 1030.

Devia, G.K., Ganasri, B.P., Dwarakish, G.S., 2015. A review on hydrological models. Aquat. Procedia 4, 1001–1007.

Di, L., Yu, E., Shrestha, R., Lin, L., 2018. DVDI: A new remotely sensed index for measuring vegetation damage caused by natural disasters, in: IGARSS 2018-2018 IEEE International Geoscience and Remote Sensing Symposium. IEEE, pp. 9067–9069.

Di, S., Guo, L., Lin, L., 2018. Rapid estimation of flood crop loss by using DVDI, in: 2018 7th International Conference on Agro-Geoinformatics (Agro-Geoinformatics). IEEE, pp. 1–4.

Ezzine, A., Saidi, S., Hermassi, T., Kammessi, I., Darragi, F., Rajhi, H., 2020. Flood mapping using hydraulic modeling and Sentinel-1 image: Case study of Medjerda Basin, northern Tunisia. Egypt. J. Remote Sens. Space Sci.

Fogliatto, S., Vidotto, F., Ferrero, A., 2012. Morphological characterisation of Italian weedy rice (Oryza sativa) populations. Weed Res. 52, 60–69.

Gao, B.-C., 1996. NDWI—A normalized difference water index for remote sensing of vegetation liquid water from space. Remote Sens. Environ. 58, 257–266.

Gatti, F., 2016. Stima del Rischio Alluvionale per le Attività Economiche: Il Caso Studio di Olbia (OT). Università degli Studi di Milano, Milan, Italy.

Ghimire, S., 2013. Application of a 2D hydrodynamic model for assessing flood risk from extreme storm events. Climate 1, 148–162.

Gorelick, N., Hancher, M., Dixon, M., Ilyushchenko, S., Thau, D., Moore, R., 2017. Google Earth Engine: Planetary-scale geospatial analysis for everyone. Remote Sens. Environ. 202, 18–27.

Grimaldi, S., Li, Y., Pauwels, V.R., Walker, J.P., 2016. Remote sensing-derived water extent and level to constrain hydraulic flood forecasting models: Opportunities and challenges. Surv. Geophys. 37, 977–1034.

ISMEA, 2021. Riso - News mercati. Il settimanale Ismea di informazione sui prodotti agricoli e agroalimentari. [WWW Document]. http://www.ismeamercati.it. URL https://www.ismeamercati.it/flex/cm/pages/ServeBLOB.php/L/IT/IDPagina/11283 (accessed 7.29.21).

Knebl, M.R., Yang, Z.-L., Hutchison, K., Maidment, D.R., 2005. Regional scale flood modeling using NEXRAD rainfall, GIS, and HEC-HMS/RAS: a case study for the San Antonio River Basin Summer 2002 storm event. J. Environ. Manage. 75, 325–336.

Kourgialas, N.N., Karatzas, G.P., 2014. A hydro-sedimentary modeling system for flash flood propagation and hazard estimation under different agricultural practices. Nat. Hazards Earth Syst. Sci. 14, 625–634.

Kurita, T., Otsu, N., Abdelmalek, N., 1992. Maximum likelihood thresholding based on population mixture models. Pattern Recognit. 25, 1231–1240.

Lee, S.U., Chung, S.Y., Park, R.H., 1990. A comparative performance study of several global thresholding techniques for segmentation. Comput. Vis. Graph. Image Process. 52, 171–190.

Lighthill, M.J., Whitham, G.B., 1955. On kinematic waves I. Flood movement in long rivers. Proc. R. Soc. Lond. Ser. Math. Phys. Sci. 229, 281–316.

Ligier, P.-L., 2016. Implementation of a rainfall-runoff model in TELEMAC-2D, in: Proceedings of the XXIIIrd TELEMAC-MASCARET User Conference 2016, 11 to 13 October 2016, Paris, France. pp. 13–19.

Lin, L., Di, L., Tang, J., Yu, E., Zhang, C., Rahman, M., Shrestha, R., Kang, L., 2019. Improvement and validation of NASA/MODIS NRT global flood mapping. Remote Sens. 11, 205.

Lin, L., Di, L., Yu, E.G., Kang, L., Shrestha, R., Rahman, M.S., Tang, J., Deng, M., Sun, Z., Zhang, C., 2016. A review of remote sensing in flood assessment, in: 2016 Fifth International Conference on Agro-Geoinformatics (Agro-Geoinformatics). IEEE, pp. 1–4.

Manavalan, R., 2017. SAR image analysis techniques for flood area mapping-literature survey. Earth Sci. Inform. 10, 1–14.

Manavalan, R., Rao, Y.S., Krishna Mohan, B., 2017. Comparative flood area analysis of C-band VH, VV, and L-band HH polarizations SAR data. Int. J. Remote Sens. 38, 4645–4654.

Manjusree, P., Kumar, L.P., Bhatt, C.M., Rao, G.S., Bhanumurthy, V., 2012. Optimization of threshold ranges for rapid flood inundation mapping by evaluating backscatter profiles of high incidence angle SAR images. Int. J. Disaster Risk Sci. 3, 113–122.

Mason, D.C., Dance, S.L., Cloke, H.L., 2021. Floodwater detection in urban areas using Sentinel-1 and WorldDEM data. J. Appl. Remote Sens. 15, 032003.

Molinari, D., Scorzini, A.R., Gallazzi, A., Ballio, F., 2019. AGRIDE-c, a conceptual model for the estimation of flood damage to crops: development and implementation. Nat. Hazards Earth Syst. Sci. 19, 2565–2582.

Morris, J., Brewin, P., 2014. The impact of seasonal flooding on agriculture: the spring 2012 floods in Somerset, England: Impact of seasonal flooding on agriculture. J. Flood Risk Manag. 7, 128–140. https://doi.org/10.1111/jfr3.12041

Ormsby, J.P., Choudhury, B.J., Owe, M., 1987. Vegetation spatial variability and its effect on vegetation indices. Int. J. Remote Sens. 8, 1301–1306.

Orusa, T., Orusa, R., Viani, A., Carella, E., Borgogno Mondino, E., 2020. Geomatics and EO Data to Support Wildlife Diseases Assessment at Landscape Level: A Pilot Experience to Map Infectious Keratoconjunctivitis in Chamois and Phenological Trends in Aosta Valley (NW Italy). Remote Sens. 12, 3542.

Otsu, N., 1979. A threshold selection method from gray-level histograms. IEEE Trans. Syst. Man Cybern. 9, 62–66.

Pistocchi, A., Mazzoli, P., 2002. Use of HEC-RAS and HEC-HMS models with ArcView for hydrologic risk management.

Pulvirenti, L., Marzano, F.S., Pierdicca, N., Mori, S., Chini, M., 2013. Discrimination of water surfaces, heavy rainfall, and wet snow using COSMO-SkyMed observations of severe weather events. IEEE Trans. Geosci. Remote Sens. 52, 858–869.

Puno, G.R., Amper, R.A.L., Opiso, E.M., Cipriano, J.A.B., 2020. Mapping and analysis of flood scenarios using numerical models and GIS techniques. Spat. Inf. Res. 28, 215–226.

Puno, G.R., Puno, R.C., Maghuyop, I.V., 2021. Two-dimensional flood model for risk exposure analysis of land use/land cover in a watershed. Glob. J. Environ. Sci. Manag. 7, 225–238.

Rahman, M., Di, L., Yu, E., Lin, L., Zhang, C., Tang, J., 2019. Rapid flood progress monitoring in cropland with NASA SMAP. Remote Sens. 11, 191.

Rahman, M.S., Di, L., 2020. A systematic review on case studies of remote-sensing-based flood crop loss assessment. Agriculture 10, 131.

Reiche, J., Lucas, R., Mitchell, A.L., Verbesselt, J., Hoekman, D.H., Haarpaintner, J., Kellndorfer, J.M., Rosenqvist, A., Lehmann, E.A., Woodcock, C.E., 2016. Combining satellite data for better tropical forest monitoring. Nat. Clim. Change 6, 120–122.

Robins, P., Davies, A., 2011. Application of TELEMAC-2D and SISYPHE to complex estuarine regions to inform future management decisions. Proc. XVIIIth Telemac Mascaret User Club 2011 19-21 Oct. 2011 EDF RD Chatou 86–91.

Romali, N.S., Yusop, Z., Ismail, A.Z., 2018. Application of HEC-RAS and Arc GIS for floodplain mapping in Segamat town, Malaysia. Int. J. 14, 125–131.

Sanyal, J., Lu, X.X., 2004. Application of remote sensing in flood management with special reference to monsoon Asia: a review. Nat. Hazards 33, 283–301.

Sarvia, F., De Petris, S., Borgogno Mondino, E., 2020. Multi-scale remote sensing to support insurance policies in agriculture: From mid-term to instantaneous deductions.

Sarvia, F., De Petris, S., Borgogno-Mondino, E., 2021a. Exploring Climate Change Effects on Vegetation Phenology by MOD13Q1 Data: The Piemonte Region Case Study in the Period 2001–2019. Agronomy 11, 555.

Sarvia, Filippo, De Petris, S., Borgogno-Mondino, E., 2020. A Methodological Proposal to Support Estimation of Damages from Hailstorms Based on Copernicus Sentinel 2 Data Times Series, in: International Conference on Computational Science and Its Applications. Springer, pp. 737–751.

Sarvia, F., De Petris, S., Borgogno-Mondino, E., 2019. Remotely sensed data to support insurance strategies in agriculture, in: Remote Sensing for Agriculture, Ecosystems, and Hydrology XXI. International Society for Optics and Photonics, p. 111491H.

Sarvia, F., Xausa, E., Petris, S.D., Cantamessa, G., Borgogno-Mondino, E., 2021b. A Possible Role of Copernicus Sentinel-2 Data to Support Common Agricultural Policy Controls in Agriculture. Agronomy 11, 110.

Schumann, G., Di Baldassarre, G., Alsdorf, D., Bates, P.D., 2010. Near real-time flood wave approximation on large rivers from space: Application to the River Po, Italy. Water Resour. Res. 46.

Scorzini, A.R., Radice, A., Molinari, D., 2018. A new tool to estimate inundation depths by spatial interpolation (RAPIDE): design, application and impact on quantitative assessment of flood damages. Water 10, 1805.

Sezgin, M., Sankur, B., 2004. Survey over image thresholding techniques and quantitative performance evaluation. J. Electron. Imaging 13, 146–165.

Shen, X., Wang, D., Mao, K., Anagnostou, E., Hong, Y., 2019. Inundation extent mapping by synthetic aperture radar: A review. Remote Sens. 11, 879.

Shrestha, B.B., Okazumi, T., Tanaka, S., Sugiura, A., Kwak, Y., Hibino, S., 2013. Development of flood vulnerability indices for lower Mekong basin in cambodain floodplain. J. Jpn. Soc. Civ. Eng. Ser B1 Hydraul. Eng. 69, I_1-I_6.

Smith, L.C., 1997. Satellite remote sensing of river inundation area, stage, and discharge: A review. Hydrol. Process. 11, 1427–1439.

Sood, A., Smakhtin, V., 2015. Global hydrological models: a review. Hydrol. Sci. J. 60, 549–565.

Stoleriu, C.C., Urzica, A., Mihu-Pintilie, A., 2020. Improving flood risk map accuracy using high-density LiDAR data and the HEC-RAS river analysis system: A case study from north-eastern Romania. J. Flood Risk Manag. 13, e12572.

Syme, W.J., 2001. Modelling of bends and hydraulic structures in a two-dimensional scheme, in: 6th Conference on Hydraulics in Civil Engineering: The State of Hydraulics; Proceedings. Institution of Engineers, Australia, p. 127.

Tarpanelli, A., Santi, E., Tourian, M.J., Filippucci, P., Amarnath, G., Brocca, L., 2018. Daily river discharge estimates by merging satellite optical sensors and radar altimetry through artificial neural network. IEEE Trans. Geosci. Remote Sens. 57, 329–341.

Tesio, F., Tabacchi, M., Cerioli, S., Follis, F., 2014. Sustainable hybrid rice cultivation in Italy. A review. Agron. Sustain. Dev. 34, 93–102.

Trier, O.D., Jain, A.K., 1995. Goal-directed evaluation of binarization methods. IEEE Trans. Pattern Anal. Mach. Intell. 17, 1191–1201.

Tsyganskaya, V., Martinis, S., Marzahn, P., Ludwig, R., 2018. SAR-based detection of flooded vegetation–a review of characteristics and approaches. Int. J. Remote Sens. 39, 2255–2293.

Twele, A., Cao, W., Plank, S., Martinis, S., 2016. Sentinel-1-based flood mapping: a fully automated processing chain. Int. J. Remote Sens. 37, 2990–3004.

Veci, L., Prats-Iraola, P., Scheiber, R., Collard, F., Fomferra, N., Engdahl, M., 2014. The Sentinel-1 Toolbox, in: Proceedings of the IEEE International Geoscience and Remote Sensing Symposium (IGARSS). Presented at the IEEE International Geoscience and Remote Sensing Symposium (IGARSS), IEEE, Québec, Canada, pp. 1–3.

Vollrath, A., Mullissa, A., Reiche, J., 2020. Angular-based radiometric slope correction for Sentinel-1 on google earth engine. Remote Sens. 12, 1867.

Vozinaki, A.-E.K., Karatzas, G.P., Sibetheros, I.A., Varouchakis, E.A., 2015. An agricultural flash flood loss estimation methodology: the case study of the Koiliaris basin (Greece), February 2003 flood. Nat. Hazards 79, 899–920.

Vozinaki, A.E.K., Kourgialas, N.N., Karatzas, G.P., 2012. Estimation of agricultural flood loss in the Koiliaris river basin in Crete, Greece. Eur Water 39, 53–63.

Wang, X., Xie, H., 2018. A review on applications of remote sensing and geographic information systems (GIS) in water resources and flood risk management. Water 10, 608.

Western, A.W., Blöschl, G., Grayson, R.B., 1998. How well do indicator variograms capture the spatial connectivity of soil moisture? Hydrol. Process. 12, 1851–1868.

Westra, T., De Wulf, R.R., 2009. Modelling yearly flooding extent of the Waza-Logone floodplain in northern Cameroon based on MODIS and rainfall data. Int. J. Remote Sens. 30, 5527–5548.

Willmott, C.J., Matsuura, K., 2005. Advantages of the mean absolute error (MAE) over the root mean square error (RMSE) in assessing average model performance. Clim. Res. 30, 79–82.

Wilson, J. A., S. L. Olson, and J. Callan, 2011. Farming after the Flood. An Inside Look at Post-Flooding Management of Agricultural Soils [WWW Document]. URL Soil Science Society of America, American Society of Agronomy. (accessed 2.15.21).

Zhang, X., Friedl, M.A., Schaaf, C.B., Strahler, A.H., Hodges, J.C., Gao, F., Reed, B.C., Huete, A., 2003. Monitoring vegetation phenology using MODIS. Remote Sens. Environ. 84, 471–475.

Zimmermann, A., Church, M., 2001. Channel morphology, gradient profiles and bed stresses during flood in a step–pool channel. Geomorphology 40, 311–327.

4.2 RADAR INDICES-BASED TECHNIQUES

4.2.1 Multitemporal Dual-Pol Sentinel-1 Data to Support Monitoring of Forest Post-Fire Dynamics

De Petris Samuele[a*], Evelyn Joan Momo[a], Sarvia Filippo[a] and Borgogno- Mondino Enrico[a]

[a]Department of Agricultural, Forest and Food Sciences (DISAFA), University of Turin, 10095 Grugliasco, Italy.

*Correspondence: samuele.depetris@unito.it

Published: 2022 in *Geocarto International,* IF (2021): 3.450

Abstract: Approaches based on multitemporal analysis of optical-retrieved vegetation index time series were successfully applied to describe forest disturbances like forest fires; conversely, only few works make use of multitemporal Synthetic Aperture Radar (SAR) data. In this work, a multi-temporal approach based on Sentinel-1 data (S1) is proposed based on CR polarimetric index to monitor forest canopy along the considered period (2016-2019) preceding and following an important fire event occurred in the Piemonte Region (NW Italy) in November 2017. The Pettitt test, applied to the polarimetric index time series, was used for testing fire occurrence date and map burned areas (795 ha) resulting in user's accuracy of burned area equal to 88%. A trend analysis was also conducted, on "burned" pixels only, to describe tree canopy damage and strength of the consequent recovery process at pixel level using linear trend slope values of cross ratio polarimetric index time series. Finally, a k-means cluster analysis was applied to define classes having the same ecological behavior with respect to two different criteria: one aimed at mapping type and intensity of damage and a second one aimed at describing the ecological behaviour in terms of resistance and resilience of burned patches. In the study area, the cluster layer called forest damage map classifies about the 22% of burned area as characterized by an early high severity whiled the residual by moderate-low severity levels. The second cluster layer called ecological response map defined the 61% of the burned area as resistant forests, the 20% as resilient forests and the 19% as increasing forest zones. All maps were generated with the aim of supporting post-fire assessment and management with free satellite SAR data.

Keywords: SAR; Sentinel-1; Google Earth Engine; Forest Fire; Recovery process mapping; Fire severity mapping; polarimetric index time series.

1. Introduction

Mapping fire extent and severity is essential to assess ecological effects (Reilly et al., 2017) and to plan mitigation measures and restoration activities after the fire season (Suresh Babu et al., 2018). Remote sensing is widely used to map burned areas and to measure fire severity (Keeley, 2009). It proved to be effective especially in those regions that are characterized by low accessibility and extensive burned areas (Kato et al., 2020). In particular, Italian forests are sensitive to wildfires that represent one of the main natural disturbance in the European forests (Carlucci et al., 2019). Wildfires are prevalent in the Mediterranean area, but they are also relevant in the Alps where about 4000 ha□yr-1 per fire can occur (Valese et al., 2014). Despite optical data are widely used for mapping fire effects, radar (radio detection and ranging) still appears to be underused, in spite of its favourable peculiarities: independence from cloud coverage, haze layers and smoke plumes frequently present during forest fire, sensibility to geometrical features of canopy and water content. Precisely in the Alps, winter is the forest fire season (Ascoli et al., 2013), when cloud cover is higher. The latter condition affects the monitorability of fires in the Alps by optical remote sensing, making spaceborne radar proper to fill the gap. Moreover, while optical data strictly depend on surface and top of the canopy conditions, radar can moderately penetrate tree crowns, making it possible to investigate moisture and structural properties of vegetated volumes (Szigarski et al., 2018). Changes in vegetation structure is one of the key features that allows detection and characterization of burned forest by SAR (Synthetic Aperture Radar) (Tanase et al., 2011). In particular, polarization state of SAR backscattered electro-magnetic signal appears to be a more sensible tool for analyzing forest geometrical properties than optical data and, therefore, it can be adopted to detect and monitor fire-induced effects on forest. SAR polarimetry is the technique that allows to analyse the polarization state of the electromagnetic signal backscattered by earth surface to the sensor. In particular, vegetation canopy determines the so-called volume scattering mechanism. The interaction with

vegetation canopy generates a depolarization of electromagnetic wave. In fact, canopy elements (supposed as cylinder-like objects) induce a rotation of the polarization vector depending on dipoles orientation (Richards, 2009). Depolarization increases with canopy density due to random orientation of branches/twigs: the effect is a strong backscatter of the cross-polarized band. Differently, a cross-polarized signal show lower values while moving to sparse vegetation or bare soil conditions (Ulaby et al., 1981). A wildfire could partially, or completely, remove tree canopy leaving stems and ground exposed. The effects of fire on backscattering also depends on polarization; cross-polarized signal (HV or VH - horizontal/vertical transmitted/received signal) is known to be more sensitive to volume features of scatterers. A decrease of cross polarized backscattering might be observed as a consequence of canopy volume loss caused by fire (Minchella et al., 2009); instead, variations of the co-polarized backscattering generally depends on the rate of exposed soil within the pixel (Imperatore et al., 2017). Vertical polarization is known to be more sensitive to objects with a prevailing vertical size, e.g. tree stems, that usually are not completely destroyed by fire (Bernhard et al., 2012); double bounce and surface scattering effects tend, in fact, to become important where signal more easily penetrate tree crowns and reach the ground.

In literature, many approaches were adopted to monitor vegetation disturbances based on SAR polarimetry (Lee and Pottier, 2017). For example, the polarimetric decomposition (Cloude and Pottier, 1996) derives second-order statistics from the covariance matrix, i.e. Entropy - H, anisotropy - A, alpha - α permitting to assess changes in backscattered signal (De Petris et al., 2021). Unfortunately, such an approach is based on raw (complex values) SAR data processing, making difficult to approach multitemporal analysis over large areas. A possible more operational alternative is the one based on the computation of simple polarimetric indices like Radar Vegetation Index (RVI) (Kim et al., 2011) and Cross Ratio (CR) (Paloscia et al. 1999). The ratio of dual-pol bands, typically one co-polarized and the other cross-polarized, (e.g. Sentinel 1 VV and VH) proved to

be effective in describing backscattering behaviour of vegetation providing a measure of the depolarization level. CR showed significant linear correlations with vegetation density, Normalized Difference Vegetation Index (NDVI), Leaf Area Index (LAI) and Vegetation Water Content (VWC) (De Petris et al., 2022; Kim et al., 2011; Vreugdenhil et al., 2018). In the multitemporal context, time series of optical-retrieved vegetation indices proved to effectively describe the effects of forest disturbances like fires (Telesca and Lasaponara, 2006). In particular, the present availability of big and free archives of remotely sensed images like Google Earth Engine (GEE) allows to improve this kind of analysis by densifying time series over wide areas. Nevertheless, the literature about multitemporal analysis of post-fire dynamics trough the SAR imagery adoption is still limited (Belenguer-Plomer et al., 2019; Bourgeau-Chavez et al., 2002; Carreiras et al., 2020; Engelbrecht et al., 2017; Gimeno et al., 2004; Kasischke et al., 1994; Lohberger et al., 2018; Verhegghen et al., 2016) and no works focusing on the post-fire dynamics monitoring (i.e. severity and recovery processes) were available. The crucial point in ordinary forest fire effects mapping is the one related to the a-priori identification of the date when all the induced (direct and indirect) effects of the event are assumed to be detectable and concluded. According to this arbitrary post-fire date the most of the approaches proceed by comparing a “before” and an “after” image to map fire severity, e.g the differenced Normalized Burn Ratio - dNBR (Key and Benson, 2006), the Relative dNBR - RdNBR, (Miller and Thode, 2007) and the Relativized Burn Ratio - RBR (Parks et al., 2014), excluding possible delayed effects affecting the whole vegetated ecosystem in the area. In this work, this issue was carefully considered and an alternative approach, based on dense time series of SAR-based indices exploring a large period preceding and following the date of the fire, was investigated. Proposed approach made possible to avoid any a-priori setting of the post-fire date to use for deriving differences relatable to severity and obtaining true estimate of the actual date when the local ecosystem reached its maximum of damage and, consequently, the rate of system decay. Such information was

used to derive severity maps that are expected to more properly represent the actual after-event situation.

Moreover, the same approach, made it possible to investigate the reaction of the system (recovery) at local (pixel) level providing a spatial representation of forest behaviour in terms of both resistance and resilience. Such mapping procedure is rare to be found in literature (even considering optical-based approaches). Anyway, even if proposed, the adoption of SAR data in place of optical ones is expected to provide, during recovery, a more focused representation of those forest components related to significant volume changes (i.e. trees and shrubs) making other vegetated players, like grass, negligible.

Trying to fill these lacks, a multi-temporal approach based on Sentinel-1 data (S1) is proposed. In particular, the CR polarimetric index was adopted to monitor forest canopy along the considered period (2016-2019) preceding and following an important fire event occurred in the Piemonte Region (NW Italy) in November 2017. A map of burned areas was therefore generated looking for a unique significant breakpoint occurring along CR image time series that was additionally processed to derive some ecological indices useful for mapping disturbance severity and describing the recovery process. A final interpretation of the event was then given with reference to a clustering approach aiming at recognizing zones showing a different post-disturbance behaviour.

2. Materials and Methods

2.1. Study Area

The area of interest (AOI) sizes about 53 km2 corresponds to that part of the Susa Valley (Italian Western Alps) that was affected by a large wildfire at the end of October 2017. It covers the municipalities of Bussoleno, Mompantero, Susa, Chianocco, Novalesa and Venaus (Fig. 1). AOI is characterized by a dominant south slope aspect; altitude ranges from 450 m to 2000 m a.s.l. Climatic conditions are particular for the Alps: low annual rainfall, frequent wind, and temperature rarely below 0°C, represent good predisposing conditions for wild

fire. In addition, October 2017 was characterized by anomalous weather conditions with higher temperature and prolonged lack of rainfall. Within AOI, about 3378 ha are covered by forests dominated by different species: scots pine (20% of forest surface), larch (10%), beech (27%), downy oak (14%) and other broadleaves (21%) like chestnut, maple, ash and linden. According to the post-fire assessment operated by the Piemonte Region (Regione Piemonte, 2019) about 50% of the area interested by fire was characterised by medium or high fire severity (about 1698 ha), especially in the beech and scots pine stands and, secondly, by larch and downy oak (De Petris et al., 2020). Some of these stands were already interested by a fire event in the 2003 (Ascoli et al., 2013).

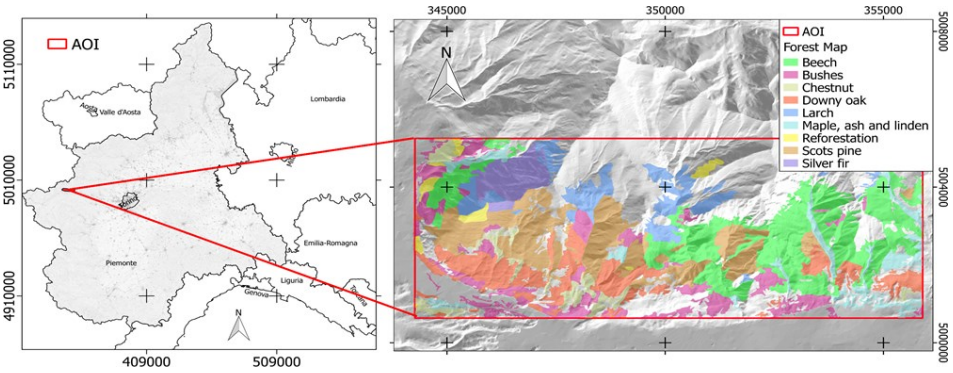

Figure 1. (Left) Area Of Interest (AOI) localization within Piemonte Region; (Right) AOI with forest types map. (Reference frame: WGS84 UTM 32N).

2.2. Available Data

2.2.1. Sentinel-1 Data

Copernicus S1 is one of the current biggest space missions acquiring SAR data that are released to users for free. Their medium-high spatial resolution and high revisit time (6 days) make them useful for a wide range of applications. S1 mission is a constellation of two satellites (Sentinel-1A and Sentinel-1B) operating in the microwave C-band (5.6 cm wavelength). Main acquisition mode over land is the interferometric wide swath (IW) recording backscattered signal in dual pole mode (VV and VH). Data are natively recorded as complex values (I/Q components) geocoded in SAR geometry (Range and Azimuth). According

to Vollrath (2020) and Reiche (2016), the complexity of SAR data pre-processing is one of the main reasons for its slow uptake by a wider user community. From this point of view, GEE web-based platform allows an immediate access to images and allows users to directly focus on the expected information (Gorelick et al., 2017). For this work S1 ground range detected (GRD) IW image collection, available in GEE, was used. S1 GRD products consist of focused, detected, multi-looked SAR data projected to ground range. The product has an approximately squared pixel with a spatial resolution of about 10 m, and a reduced speckle obtained through the multi-look process. In GEE, GRD product pre-processing is achieved by the Sentinel-1 Toolbox (S1TBX) supplied by the European Space Agency's (ESA) and the correspondent backscatter coefficient (σ° [dB]) images obtained. Pre-processing steps consist of: (1) application of orbit file metadata, providing an accurate satellite position and velocity information; (2) border noise removal, removing low intensity noise and invalid data on scene edges; (3) thermal noise removal, removing additive noise in sub-swaths; (4) radiometric calibration, computing backscatter intensity using sensor calibration parameters supplied in the GRD metadata; (5) image orthoprojection, correcting the intrinsic image geometric distortions caused by topography whose description is derived from the 30 m gridded SRTM (Shuttle Radar Topography Mission) DEM (Digital Elevation Model). GRD dataset is known to have some limitations related to radiometric distortions over rugged terrain originated by the side-looking SAR imaging geometry within the backscatter products (Vollrath et al., 2020). Nevertheless, while working with pixel-based multitemporal approaches, relative differences of backscattering are more important that absolute ones. With these premises, in this work GEE S1 GRD collection was used covering a sensing period between 1st January 2016 to 31st December 2019. Both ascending and descending orbits were considered for a total of 215 descending (relative orbit number = 139) and 218 ascending (relative orbit number = 161) images. Ordinary, pixel positional accuracy of S1 GRD data after the orthoprojection was 2.3 m (1σ) (Small and Schubert, 2019).

2.2.2. Auxiliary Forest Map

The forest map (FM) of the Piemonte Region (Camerano et al., 2017), containing information about forest types, was used as auxiliary information in this study. The map, updated 2016, has a nominal scale of 1:10000 and was freely obtained as vector layer (at: https://www.geoportale.piemonte.it/cms).

2.2.3. Reference Data

Piemonte Region post-fire map (PRPFM) was used to test and interpret results from this study. It was obtained, in vector format, from the "Extraordinary regional plan of interventions to restore the territory covered by forest fires of autumn 2017" (Regione Piemonte, 2019). It has a 1:100000 nominal scale and reports three different fire-severity classes as mapped at the end of the fire event by optical remotely sensed data (Copernicus Sentinel-2) supported by field measurements. This map was generated adopting the FIREMON (Fire Effects Monitoring and Inventory System) protocol and has a nominal cover classes uncertainty of about 10% (Lutes et al., 2006). PRPFM thematic accuracies were equal to 53% for low severity, 61% for medium severity and 95% for high severity. The overall accuracy was 66 % (Regione Piemonte, 2019).

2.3. Data Processing

The workflow adopted in this work is reported in figure 2. SAR imagery was processed directly in GEE and then downloaded and analysed by self-developed routines. Finally, several maps were generated and the spatial distribution of fire effects assessed and properly mapped. A detailed explanation of each step is provided in the following sections.

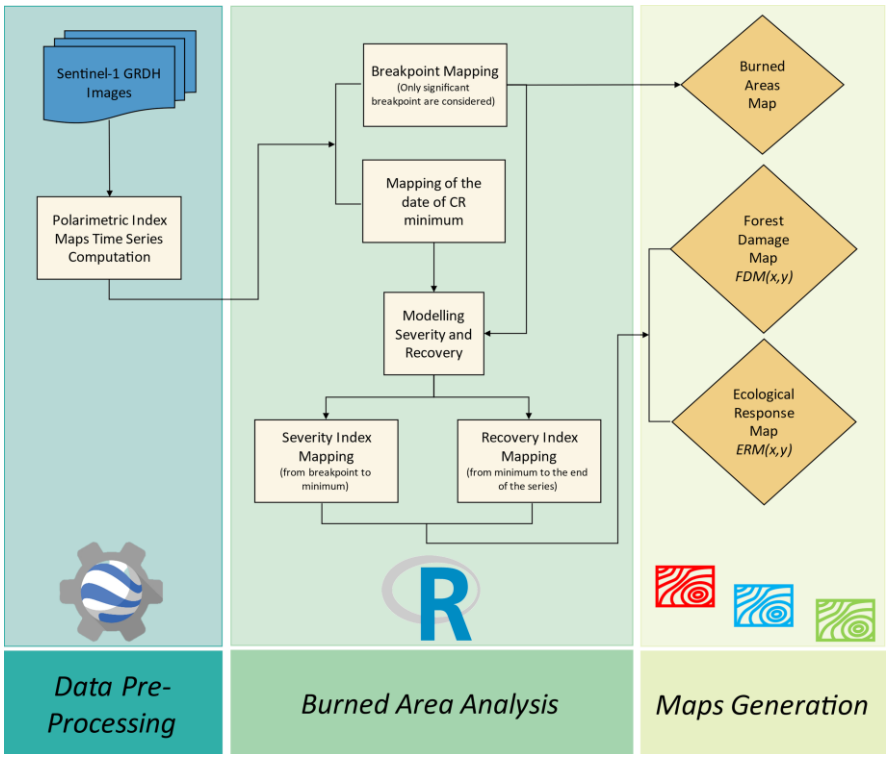

Figure 2. Workflow adopted in this work. Data were collected and directly processed in Google Earth Engine (GEE). Polarimetric Index Maps were stacked along a time series and downloaded. Self-routines were developed to analyse fire effects on forests. Finally, maps (rhomb) were generated and properly assessed to give a spatial interpretation of performed analyses.

2.3.1. Polarimetric Index Time Series

Both ascending and descending nodes of S1 data from GEE GRD collection were used and the correspondent polarimetric index time series generated in GEE. Maps were obtained in the WGS84/ UTM 32N reference frame. In particular, to reduce speckle, VV and VH images were monthly averaged (about 5 images per month) generating a time series of 48 images. This type of de-speckle technique was adopted to preserve image geometric resolution (10 m), thus avoiding local smoothing that would have possibly compromised detection of small sized disturbance patches (Mermoz and Le Toan, 2016). In order to minimize radar shadows, ascending and descending orbits datasets were combined at pixel level; accordingly, the above-mentioned images, from ascending and descending

acquisitions, were compared and a new one generated (monthly) by locally selecting the correspondent maximum σ^0 value (at-pixel-level) for the only VH images. The correspondent VV image was therefore retained to compute the cross-ratio coefficient as described below. This made possible to select, at the single month, the most proper acquisition between the available descending and ascending ones. In spite of this approach some limitations were known to still affect data like radiometric distortion due to layover and/or incidence angle effects. Nevertheless, this method was expected to minimize the problem related to masked hidden areas that, differently, would remain void. This is, in fact, a very common problem while working in mountain areas.A further issue concerns the area effects that the combination of ascending and descending acquisitions can introduce. The backscatter coefficient is known to depend on the real scattering area that is expected to be different if the viewing geometry is different. This is one of the reasons that drove us to select the cross-ratio (CR) polarimetric index (eq. 1) as privileged parameter able to describe scattering properties of surfaces along time.

$$CR = \frac{\sigma^0_{VH}}{\sigma^0_{VV}} = [\sigma^0_{VH}]_{dB} - [\sigma^0_{VV}]_{dB} \quad (1)$$

Where $\sigma^0_{VH}, \sigma^0_{VV}$ are the normalized radar cross section in linear scale and $[\sigma^0_{VH}]_{dB}, [\sigma^0_{VV}]_{dB}$ are the correspondent values in dB. For its definition, CR guarantees that area and target-to-sensor distance related issues could be neglected making observations consistent. This can be easily demonstrated with reference to the fundamental equation of the normalized radar cross section (eq. 2).

$$\sigma^0_{VV,VH} = \frac{P_R}{P_T} \cdot \frac{(4\pi)^3}{G^2 \cdot \lambda^2} \cdot R^4 \cdot \frac{4 \sin(\theta)}{L \cdot c \cdot \tau} \quad (2)$$

Where P_R and P_T are the received and transmitted power respectively; G is antenna gain; λ is the operational wavelength; R is the slant range; L is the real antenna length, c is the speed of light, τ is the pulse duration, θ is the look/

incidence angle. When computing CR with reference to its linear definition (eq. 1) constant parameters of eq. 2 can be mathematically eliminated, included the scattering area term, i.e. $\frac{4 \sin(\theta)}{L \cdot c \cdot \tau}$, making values from different viewing geometry comparable. CR computation was achieved in GEE as difference between σ^0_{VH} and σ^0_{VV} for each image generating 48 CR maps. This index represents the ratio between backscattered power in H polarization respect to V one. CR values tend to 0 for highly depolarizing vegetation (high density of canopy) and decrease with canopy reduction. CR is known to coarsely separate volume and surface scattering mechanisms. According to Minchella (2009) volume backscattering significantly decreases and is replaced by surface backscattering when working over burnt areas. A time series of 48 CR maps (hereinafter called CRTS, Cross-Ratio Time Series) was obtained covering about 4 years (2016-2019) with monthly frequency. CRTS was finally downloaded and all subsequent operations managed by R vs. 3.6.3 (R. Core Team, 2013) and SAGA GIS vs. 7.7 (Conrad et al., 2015).

2.3.2. Burned Areas Mapping

CRTS was, initially, clipped by FM in order to focus on forested areas. Mapping of forest burned areas was achieved by change detection. In particular, a pixel based temporal profile analysis was performed looking for a single breakpoint occurrence in the period October-November 2017. A unique breakpoint analysis was performed to detect the moment when disturbance occurrence changed CRTS ordinary trend. A significant change is admitted to determine a drastic variation of the state of the area from the period preceding the vent and the one following it. No changing situations where the initial state is recovered after a while can be considered a "significant" change. Consequently, leaves falling from deciduous trees, being a yearly recurrent event that separates two similar vegetative states, has to be excluded from recognition. The Pettitt's test is exactly aimed at finding this type of situations; it is a non-parametric test based on Mann-Whitney two sample test (rank based) (Pettitt, 1979) that look for a single

breakpoint at an unknown time t. The null hypothesis is that no change occurs along the time series; the alternative hypothesis is that the probability distribution function F1(x) built in the range $[X_1,X_t]$ is significantly different from the one, F2(x), built in the range $[X_{t+1},X_T]$. If the correspondent p-value is lower than the selected significance level ($\alpha = 0.05$ in this work), one can reject the null hypothesis; consequently, the time series can be divided into two sub-series located before and after the breakpoint. Xie (Xie et al., 2014) highlighted that Pettitt method is influenced by some properties of the analysed series: sample size, magnitude of shift and breakpoint position. Mallakpour (Mallakpour and Villarini, 2016) examined the sensitivity of the Pettitt test and highlighted that abrupt changes are more easily detected when they occur between one third - half of the time series. Nevertheless, this breakpoint detection method was preferred in this work because breakpoint was a-priori expected to be located between October-November 2017, therefore around the 20th-21th observations out of the available 48. The Pettitt's test was run at pixel level on CRTS; the date of breakpoint and the correspondent p-value were mapped in two separate raster layers. All pixels having a p-value > 0.05 were masked out. A further refinement was performed masking out all those pixels that showed a breakpoint date far away from the expected one (October-November 2017). It is worth to remind that the role of the Pettitt's test in this work was not to position a date for an unknown fire event. Conversely, it was used to automatically recognize as "significantly burnt" a pixel around the date of a known fire event with the aim of locate more precisely the borders of the burnt area. This is a required operation that is institutionally due according to the Italian regulation. Moreover, and more specifically for this work, the automatic recognition is desirable of burnt pixels, internally consistent with the data used to operate the following evaluation concerning fire severity mapping and recovering description. The need of masking out breakpoints falling in a date far away from the one of the event was considered to take care about those similar situations that can come from other forest disturbance sources, like harvesting and forest diseases. A raster map (hereafter called Burned Map – BM) was finally created showing all those pixels

that proved to have significantly changed between October and November 2017. Burned and not-burned pixels of BM were codified as 1 and 0, respectively. Accuracy of burned pixels mapping was tested with respect to PRPFM, that was preventively rasterized at the same resolution of BM. The correspondent confusion matrix was computed.

2.3.3. Severity Index

Since CRTS was known to be still affected by noise (i.e. speckle remainders or CR statistical fluctuations), a time series decomposition was computed to separate significant signal (trend component) from noise (Forkel et al., 2013; Jonsson and Eklundh, 2002). Trend component was extracted using LOESS (Locally Estimated Scatterplot Smoothing) algorithm (Coltuc et al., 2000). LOESS hyper-parameters selection was automatically defined by fANCOVA R package (Wang, 2010) searching for those that minimized the bias-corrected Akaike Informative Criterion (AICc) as proposed by (Basak et al., 2017; Hurvich et al., 1998). Cai (2017) and Hird (2009) proved that LOESS is an effective technique to denoise vegetation index time series data. Some experiences used this approach for multitemporal SAR data analysis (Coltuc et al., 2000). After LOESS application a new smoothed CRTS (hereinafter called sCRTS) was obtained where the noise (high frequencies in temporal profile) component was removed; sCRTS represents trend and seasonal components of CRTS and therefore permits a better analysis of actual forest polarimetric behaviour. Assessment of forest fire effects is a key concept for addressing post-fire management decisions (e.g. reforestation, salvage logging or natural development). Fire changes landscape and causes an economical value loss of damaged trees. Specifically, fire can damage trunks of trees, the so called “cat face” (McBride, 1983), or their crowns. Knowledge about fire-induced damages, in particular canopy-related ones, is needed in mountain areas where forests often provide protection against natural hazards (i.e. rainfall erosion, landslides, snow avalanches, rockfalls, etc.). Both trunk and crown damages by fire can influence timber quality (Marschall et al., 2014) and tree mortality (Catry et al., 2010). It’s

worth to remind that tree mortality may occur immediately after very severe fires or be delayed by several years after low-to-moderate severe fires (Maringer et al., 2016). Many studies highlighted that forest mortality can occur with a time lag after fire occurrence (Keyser et al., 2006; Linder et al., 1998). In particular, Ascoli and Maringer (Ascoli et al., 2013; Maringer et al., 2016) observed this phenomenon on burned forest stands in Piemonte. Tree mortality or crown damages change polarimetric behaviour of forest canopy causing a CR decline that stops when, reaching its minimum, forest recovery processes start, inverting the trend. Trend analysis was performed with respect to burned pixels of sCRTS (Fig. 2). A linear regression was calibrated (at pixel level) with reference to those observations ranging from the date of breakpoint to the one when the minimum of sCRTS (t_{min}) occurred. The latter was retained as the moment of maximum damage for trees. The gain value (G_s) of the locally calibrated linear regression was assumed as a decline rate for CR after fire. Only pixels showing negative G_s values were consequently considered. Two new raster maps, t_{min}(x,y) and G_s (x,y) were generated locally mapping t_{min} and the correspondent G_s value, respectively.

Being a gain value, G_s is not sensitive to the absolute CR difference occurring between the breakpoint date and t_{min}; consequently, a new raster layer (hereinafter called ΔCR(x,y)) was generated computing the local difference between the CR value at breakpoint and the correspondent t_{min}. ΔCR(x,y) was finally normalized into the range [0;1] according to eq 3.

$$n\Delta CR_i = \frac{(\Delta CR_i - \Delta CR_{min})}{(\Delta CR_{max} - \Delta CR_{min})} \quad (3)$$

where ΔCRi is the ΔCR value of the generic i-th pixel; ΔCRmin and ΔCRmax are the minimum and maximum ΔCR values, respectively. nΔCR was adopted as weighting factor to compute the proposed forest fire Severity Index (SI, eq.4).

$$SI(x,y) = n\Delta CR(x,y) \cdot G_s(\mathrm{x,y}) \quad (4)$$

Highly negative values of SI(x,y) denote high fire severity; differently, values close to 0 denote low severity. It has to be remarked that this approach was based on the joint adoption of two parameters concerning the analysed temporal profile: $n\Delta CR(x,y)$ and $G_s(\mathrm{x},\mathrm{y})$. This was specifically aimed at minimizing possible effects on signal related to local conditions (stand fertility). In particular $n\Delta CR(x,y)$ was specifically in charge of summarizing local conditions making pixels showing the same slope, possibly different.

2.3.4. Recovery Index

Burn severity and forest regrowth are different issues of the post-fire process. Burn severity is considered a first-order fire effect (e.g. greenhouse gasses emission and plant death); forest regrowth is a second-order effect that might be evident many decades after the fire (Tanase et al., 2011). Consequently, after a forest fire, assessment of damage severity and its spatial patterns are important issues to address recovery planning (Ryu et al., 2018), especially for those forests that provide a direct protection against natural hazards. Post-fire management can accelerate forest restoration and enhancing stand structures linked to provision of ecosystem services (Moreira et al., 2009). Nevertheless, post-fire rehabilitation measures and silvicultural prescriptions are the result of a complex decision-making process (Barbati et al., 2010) that should consider ecological-related problems (Beghin et al., 2010). From the hazard protection point of view, recovery planning have to take into account, firstly, canopy cover changes and stand structural variations (Shakesby, 2011) in order to focus restoration interventions only onto the most critical areas, leaving the other ones under natural or partial silviculture-guide recovery. Post-fire vegetation recovery assessment is often derived from short-term plot level measurements that attempt to infer long-term vegetation recovery trajectories (Jones et al., 2013). Satellite remote sensing offers a relatively low-cost, rapid, and repeatable method to measure post-fire vegetation recovery over large regions. Remotely-sensed vegetation indices have largely been used to analyses post-fire recovery (Di Mauro et al., 2014; João et al., 2018). Also SAR data were involved in post-fire

recovery monitoring (Zhou et al., 2019). In fact, forests may need decades to reach the mature stage and the short period within which optical based vegetation indices reach pre-disturbance levels implies limited value for longer-term monitoring. SAR data have the potential to significantly extend the monitoring period since the backscattered signal is directly influenced by forest structure (Tanase et al., 2011). Backscattered signal from forests is the result of complex interactions between microwave radiation and ground + vegetation components. According to Dobson (1992) radar backscattering increases approximately linearly with increasing biomass. Therefore, radar backscattering is expected to change after a fire since the most of vegetation is removed leaving soil and tree trunks exposed. In order to evaluate sensitivity of radar backscattering to post-fire vegetation regrowth, it is important to identify the scattering mechanisms that act before and after the fire. Before a fire, radar C-band interacting with the canopy, generates a backscattering mostly related to a volume scattering mechanism operated by the canopy layer (Smith et al., 1996), that prevails on soil moisture and roughness. After a fire, radar waves primarily interact with soil according to a surface scattering mechanism; in these conditions, backscattering is majorly conditioned by roughness and soil moisture. Some years after the fire, radar signal turns to interact with the newly regenerated vegetation and, consequently, the effects of soil moisture and roughness on backscattering gradually diminish. Once vegetation density and structure reach the pre-fire level, volume scattering goes again to be the dominant mechanism (Zhou et al., 2019). With these premises, polarimetric index time series could provide useful information on post-fire recovery process. A trend analysis of sCRTS was, therefore, performed on BM pixels to quantify the recovery strength and velocity of the local vegetated component in the considered period. t_{min}, when fire severity effects are maxima, was assumed as the starting one for the recovery process that was analysed on mid-terms temporal basis. A linear regression relating CR values with time was calibrated at pixel level (Fig 3) with reference to the [t_{min},t_{end}] time range, where tend is the final date of the series (December 2019). The estimated gain of regression was assumed as forest recovery rate (hereinafter called

Recovery Index, RI). Two years is not a proper time range to appreciate a complete forest recovery process, nevertheless, one can exclude any contribution from grass component, since it does not participate to a continuous process, behaving yearly; conversely, shrubs could somehow contribute to the signal, leading to some misunderstandings about forest recovery. In spite of this, the main fact that remains is that an area showing a new increasing trend of its vegetated component suggests that a canopy recovery, whatever it is, is occurring.

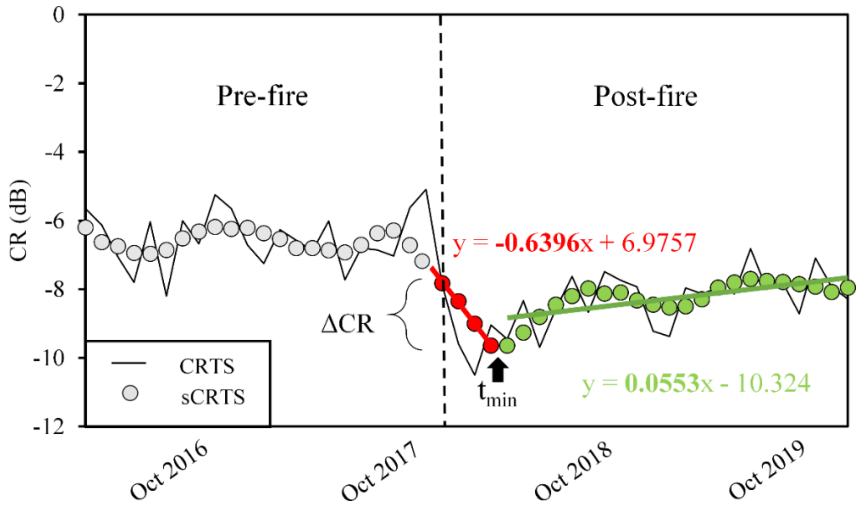

Figure 3. Cross-Ratio Time Series (CRTS) analysis. Dashed line is the breakpoint moment related to forest fire occurrence. Red line is the local linear regression used to analyse forest decline dynamics, in bold red the Gain (G) used to compute Severity Index (SI). Green line is the local linear regression used to analyse forest recovery, in bold green the gain value used to compute Recovery Index (RI).

2.3.5. Burned Area Zoning

BM, SI, RI, t_{min} are here proposed as new ecological-related indices able to measure some post-fire processes based on forest polarimetric behaviour. With the aim of exploring and summarizing spatial variability of indices at patch level, a vector graticule with 50 m x 50 m cell size was created covering the whole study area. The following statistics were computed by zonal statistics for each cell of graticule from indices maps: a) the 5th percentile of SI, b) the RI 95th percentile,

c) t_{min} median, d) number of BM pixels falling in each cell. Graticule cells with less than 4 BM pixels were deleted assuming 4000 m2 as minimum mapping unit in the area. In ecology, resistance is the ability of a forest to remain unchanged when a disturbance occurs (DeRose and Long, 2014; Grimm and Wissel, 1997); resilience is the capacity of a system to absorb disturbance and reorganize itself to still retain essentially the same function, structure, identity, and feedbacks (Holling, 1973; Walker et al., 2004). Taking in to account these issues, Chambers (2019) highlight the need to implement a resilience-based approach for prioritizing areas of intervention after a forest disturbance. Accordingly, two different cluster analysis were operated by a k-means approach with reference to the above-mentioned graticule by SAGA GIS, looking for peculiar ecological behaviours. A first cluster analysis was computed considering $t_{min}(x,y)$ and SI(x,y) layers and resulted in a map made of 4 clusters (hereinafter called $C1_{FDM}$, $C2_{FDM}$, $C3_{FDM}$, $C4_{FDM}$) that was assumed as Forest Damage Map, FDM(x,y). FDM(x,y) is expected to locate different damage levels of forest burned areas. Clusters showing high SI and low t_{min} values indicate a high level of disturbance impact that spread in a short time and that is probably related to stand replacing fire; low SI and medium t_{min} denote zones where fire has delayed effects determining diversified tree mortality. A second cluster analysis was run with reference to SI and RI and resulted in a map made of 4 clusters (hereinafter called $C1_{ERM}$, $C2_{ERM}$, $C3_{ERM}$, $C4_{ERM}$) that was assumed as Ecological Response Map (ERM(x,y)). ERM(x,y) is intended to locate zones with different fire severity and recovery rate permitting to recognize resistant and resilient patches. Patches having high SI and RI values represent highly damaged forest patches that showed strong regrowth; i.e. the most resilient ones. Conversely, patches with low SI and RI values can be interpreted as more resistant. It is worth to remind that resilience and resistance are not only related to forest parameters but they result from the contribution of several interacting factors like local topography, meteorological conditions, land use, firefighters' interventions. Nevertheless, FDM(x,y) and ERM(x,y) could effectively support post-fire management

according to ecological criteria. All the obtained classified vector maps were rasterized with a pixel size of 50 m.

3. Results

3.1. Burned Area Mapping

As far as burned area mapping is concerned, with reference to the above-mentioned method, a map reporting the local breakpoint date as recognized by Pettitt test was generated together with the correspondent map of p-value (figure 3). A joint interpretation of the two maps, based on the selection of significant breakpoints occurred within the target period (i.e. October - November 2017) lead to derive BM (figure 4).

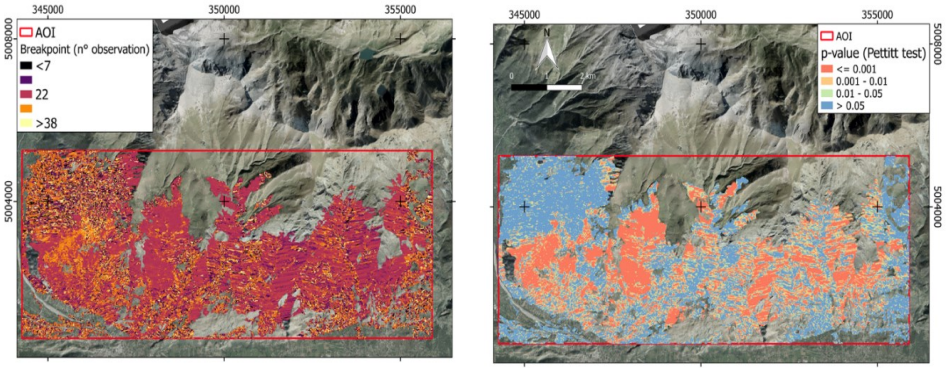

Fig.3 – Area Of Interest (AOI) Pettitt test results. (Left) Map of breakpoint occurrence date (expressesd in number of images along time series) as detected by the Pettitt's test; (Right) Map of the correspondent significance level obtained by comparng statistic distributions before and after breakpoint. (Reference frame: WGS84 UTM 32N).

According to BM, in the study area, about 795 ha of forested areas were burned. These appear to be majorly concentrated in stands dominated by beech and scots pine and, secondly, by larch and downy oak (table 1).

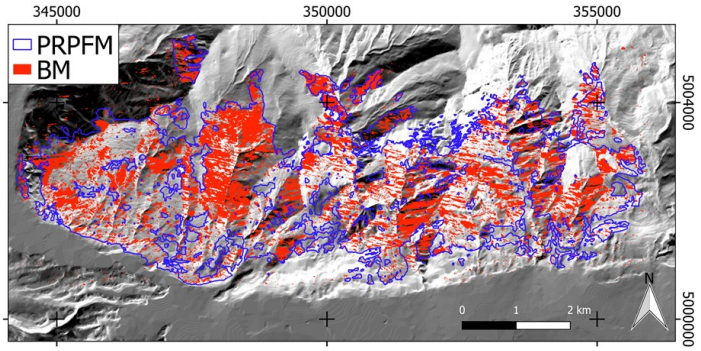

Figure 4. Burned Map (BM) derived by Pettitt's test (in red). In blue Piemonte Region post-fire map (PRPFM) vector map (reference frame: WGS84 UTM 32N).

Table 1 – Percentage distribution of forest types within burned areas as resulting from Burned Map (BM) and Piemonte Region post-fire map (PRPFM) (reference).

Forest type	***BM (%)***	***PRPFM (%)***	***Difference (%)***
Beech	28	28	0
Scots pine	27	26	1
Larch	15	11	4
Downy oak	14	16	-2
Secondary woodlands	6	7	-1
Maple, ash and linden	3	4	-1
Bushes	2	4	-2
Reforestation	2	1	1
Chestnut	2	3	-1
Silver fir	1	1	0

The accuracy of BM was tested with respect to the available PRPFM, whose fire severity classes were preventively dissolved to simply locate burned and not-burned areas as defined on ground survey basis by Piemonte Region. Confusion matrix (table 2) reports classification accuracies. Concerning the Not-Burned area PA and UA values were found to be equal to 96% and 66% respectively, while

concerning the Burned area accuracies values were found to be equal to 34% and 88 % PA and UA respectively, resulting in an OA equal to 69%.

Table 2 - Confusion matrix and accuracies between Burned Map (BM) and Piemonte Region post-fire map (PRPFM). Total number of reference pixel used to test the classification was 537306.

Classification \ Reference	*Not-Burned*	*Burned*	*User's accuracy*
Not-Burned	2929.01 ha	1541.02 ha	0.66
Burned	107.64 ha	795.39 ha	0.88
Producer's accuracy	0.96	0.34	Overall Accuracy = 0.69

3.1. Severity Index and Recovery Index Maps

SI(x,y) and RI(x,y) maps are reported in figure 5. SI(x,y) map is intended to synthesize the information about fire severity on forest canopy structure (Fig 5-left); RI(x,y) map (Fig 5-right) is intended to synthesize the information about the recovery process that started after fire occurrence and somehow describing the increasing rate of canopy structure. The joint use of these maps can improve interpretation of the post-fire ecological behavior of burned areas as shown in the following paragraph concerning zoning of burnt areas.

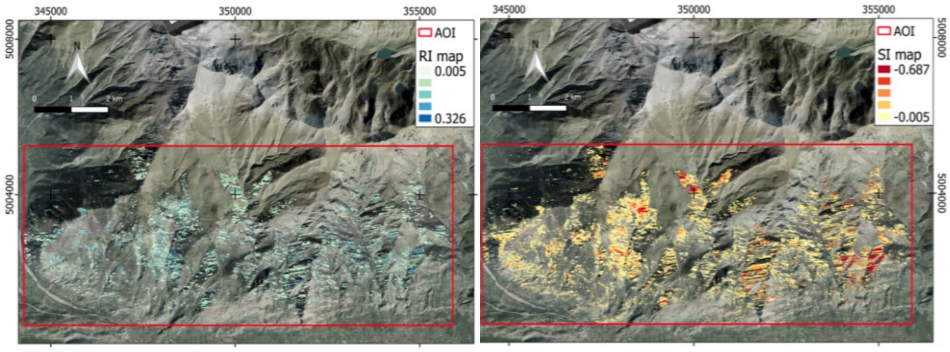

Figure 5. (Left) Recovery Index (RI) map; (Right) Severity Index (SI) map of the Area Of Interest (AOI) (Reference frame: WGS84 UTM 32N).

3.2. Zoning Burned Areas

Two cluster analysis were performed considering SI(x,y), RI(x,y) and $t_{min}(x,y)$, aggregating burned pixels in 4 groups with respect to two different criteria: one was aimed at mapping type and intensity of damage and drove to FDM(x,y) generation ($C1_{FDM}$, $C2_{FDM}$, $C3_{FDM}$, $C4_{FDM}$); a second one was aimed at describing the ecological behaviour in terms of resistance and resilience of burned patches. It drove to generate ERM(x,y) map that considered $C1_{ERM}$, $C2_{ERM}$, $C3_{ERM}$, $C4_{ERM}$ classes representing different ecological behaviours. Since these classifications are unsupervised, clusters meaning is a-priori unknown. Consequently, to recover class meaning a zonal statistics-based approach was applied on SI(x,y), RI(x,y) and $t_{min}(x,y)$ (figure 6).

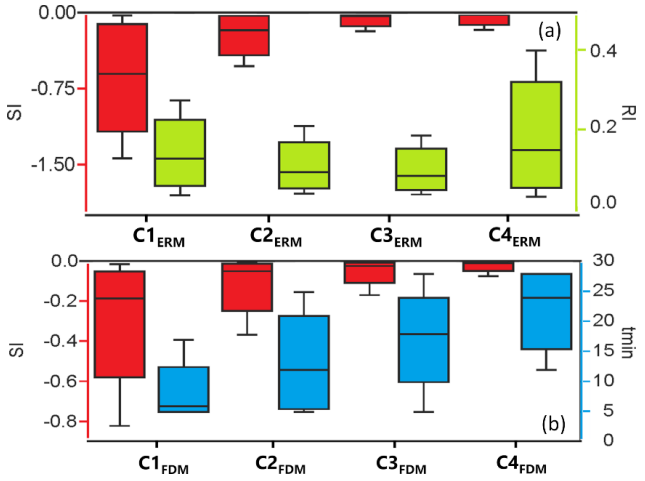

Fig. 6 – Box plots of Ecological Response Map (ERM-x,y) and (a) Forest Damage Map (FDM-x,y) (b) clusters used to recover single class meaning. From bottom to up 5th, 25th,50th, 75th ,95th percentiles.

As far as FDM(x,y) is concerned (figure 7), clusters showed different values of both SI(x,y) and $t_{min}(x,y)$. C1FDM showed the highest and the lowest mean values of SI and t_{min} respectively, suggesting it represents pixels that showed heavy damages in a short time after fire occurrence. $C2_{FDM}$, $C3_{FDM}$ and $C4_{FDM}$ present progressively decreasing SI values and progressively increasing t_{min} values,

suggesting that they somehow represent stands poorly affected by fire with low tree mortality through time. According to this interpretation, clusters were labelled as it follows: $C1_{FDM}$ = early high severity stands; $C2_{FDM}$ = early moderate severity stands; $C3_{FDM}$ = late moderate severity stands; $C4_{FDM}$ = late low severity stands. About 543 ha (22%) were characterized by an early high severity; 732 ha (29%) by early moderate severity; 336 ha (14%) by late moderate severity and 877 ha (35%) by late low severity.

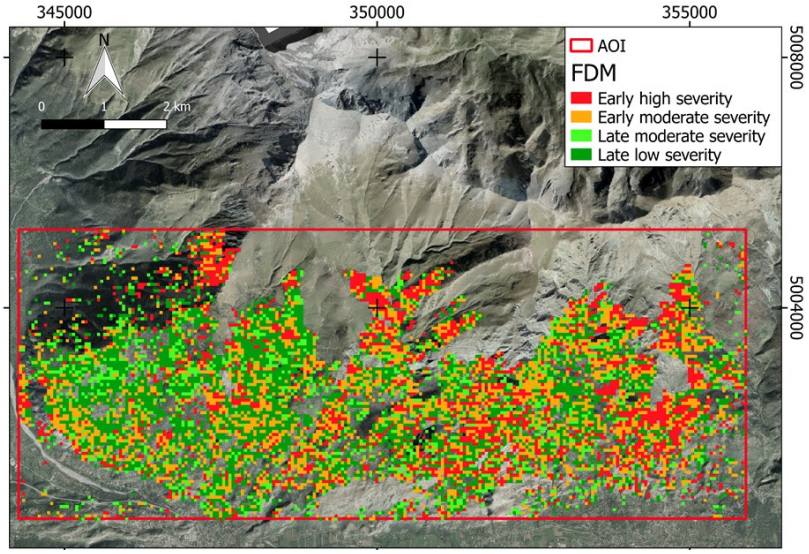

Figure 7. Forest Damage Map (FDM) representing damage levels classes related to lagged tree mortality within the Area Of Interest (AOI) (Reference frame: WGS84 UTM32N).

As far as ERM(x,y) is concerned (Fig. 8), clusters presented different values of both SI and RI. $C1_{ERM}$ showed the highest and the lowest SI and RI mean value, respectively denoting a strong damage level combined with moderate recovery rate, suggesting that it could be representative of resilient stands. $C2_{ERM}$ showed lower values of both SI and RI mean values, suggesting conditions of intermediate resilience. $C3_{ERM}$ showed SI mean values around 0 and very low RI mean values suggesting the presence of resistant stands that were poorly affected

by fire and post-fire dynamics were consequently poorly influenced. $C4_{ERM}$ showed very high RI mean values and SI mean value around 0. ERM(x,y) clusters were labelled as it follows: $C1_{ERM}$ = high resilient stands; $C2_{ERM}$ = moderate resilient stands; $C3_{ERM}$ = resistant stands; $C4_{ERM}$ = increasing stands. About 1346 ha (61%) were classified as resistant stands; 427 ha (19%) by increasing stands; 385 ha (17%) as moderate resilient stands and 53 ha (3%) as high resilient stands.

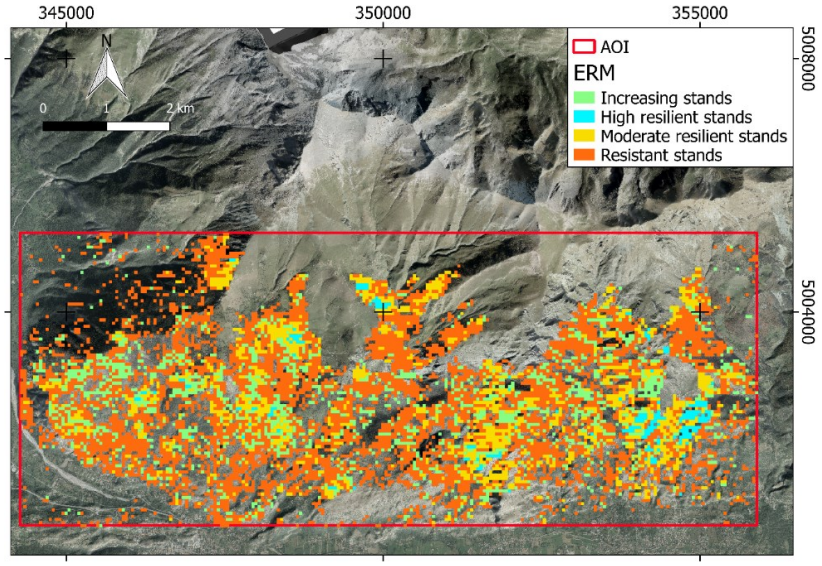

Figure 8. Ecological Response Map (ERM-x,y) map representing ecological post-fire recovering dynamics within the Area Of Interest (AOI) (reference frame: WGS84 UTM32N).

3.3. Accuracy Assessment

Testing the accuracy of BM in respect to PRPFM, a moderate balanced accuracy (BA) and high user's accuracy (UA) were found. Conversely, producer's accuracy (PA) was very low. Regarding low PA value, it has to be considered that PRPFM is known to overestimate burned areas. Specifically, PRPFM overall accuracy was 66 % while user's accuracy was equal to 53% for low severity, 61% for medium severity and 95% for high severity (Regione Piemonte, 2019). Similar accuracies were found by Engelbrecht that used multi-polarisation C-

Band SAR to detect burned area in the South Africa achieving a PA and UA equal to 71% and 62% respectively (Engelbrecht et al., 2017). Similar accuracies were found by De Luca (De Luca et al., 2021; De Luca et al., 2022) using an object-based geographic analysis (GEOBIA) process combined to random forest (RF) classifier, involving optical and SAR composite images as input layers. Nevertheless, they proved that the accuracy of results indicate that the integrated use of optical and SAR datasets reduces commission errors, correcting the erroneous identification of burned areas that could occur using individual types of sensors. While, Belenguer-Plomer using the S1 backscatter coefficient and thermal anomalies in the Amazon basin and Iberian Penisula achieving a PA and UA in the burned area detection equal to 63% and 61% respectively (Belenguer-Plomer et al., 2019). In this situation, an approach based on an immediate (after minus before) change detection relying on optical data, cannot distinguish between a natural change related to leaves falling and the one induced by fire, especially in a transitional seasonal period like the autumn when leaves fall from deciduous trees. Consequently, an overestimation of burnt area is expected. To prove such information, some checks operated through photointerpretation with reference to an available true color orthoimage (GSD = 0.2 m) acquired on 10th November 2017 just after the fire stopped and supplied by Digisky s.r.l., an aerial survey company, confirmed this situation (De Petris et al., 2020). Unfortunately, the dataset did not cover the whole area and, consequently, it could not be used as reference for validation. Nevertheless, it made possible, with reference to two focus areas (hereafter called Photo-interpreted Burned Areas – PBA), to get an estimate of such overestimation of burnt areas potentially affecting PRPFM and refine accuracy measures about the proposed method (Fig. 9). This analysis showed that PRPFM tends to overestimate of about 225% the actual burnt areas (PBA) and that our method accuracy, with respect to the aerial orthoimage, was 40%. A further unexpected result was therefore found during this work concerning reliability of official maps produced in standard mode.

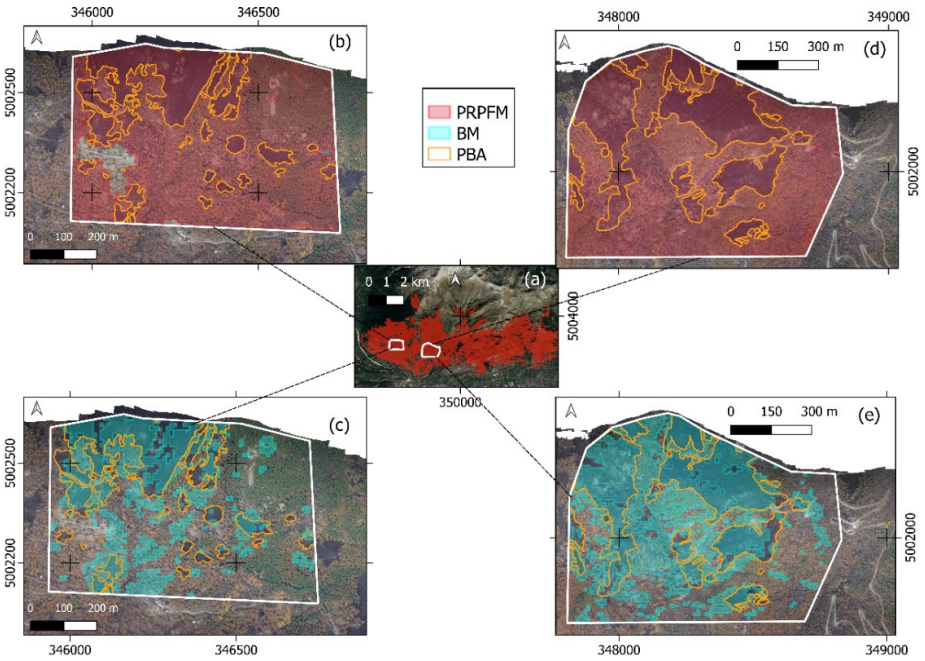

Figure 9. Burnt areas mapping obtained by photointerpretation of the available true color orthoimage (PBA). (a) Two representative check areas were selected within the study area; (b-d) comparison between Piemonte Region post-fire map (PRPFM) and Photo-interpreted Burned Areas (PBA); (c-e) comparison between Burned Map (BM) and PBA (reference frame: WGS84 UTM 32N). It can be noted that PRPFM highly over-estimate actual conditions. The same, but highly reduced, for BM.

A further element supporting this limitation of PRPFM is the map itself, where the low severity class is the prevailing one in AOI. Since a high commission is expected between unburned and low severity classes (Arnett et al., 2015) one can assume this as a very probable feature of PRPFM. All these considerations make clear that the intention was not having an absolute error estimate of their BM map, but comparing it with available “official” data, especially focusing on relative correspondences. To give an estimate of burnt areas a relative errors assessment was conducted considering total affected areas according to FM and PRPFM. In table 1 was reported the distributions (%) of forest types within mapped burned areas and compared with those obtained from the reference, and official, map (PRPFM). In spite of low PA, it can be easily noted that BM and PRPFM, show similar percentages of forest types affected by fire resulting in

percentage differences always lower than 5%. A final comparison between fire severity from PRPFM and BM (Fig. 10) showed that 23%, 28% and 37% of BM pixels were assigned to the high, low and medium severity PRPFM classes, respectively.

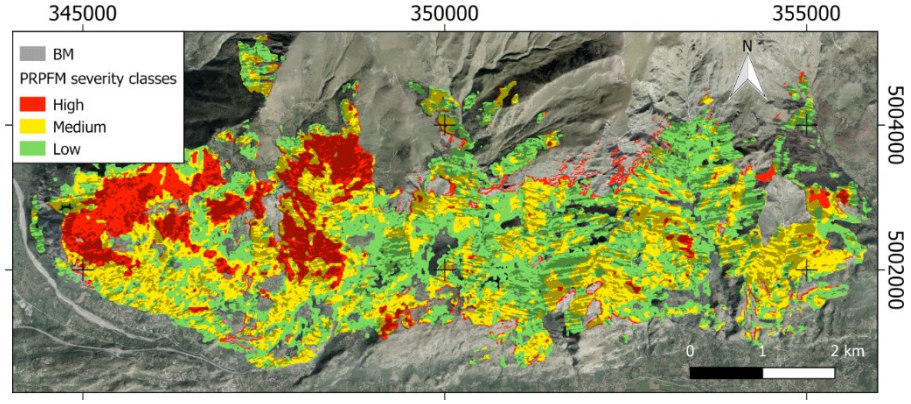

Figure 10. Burned Map (BM) and Piemonte Region post-fire map (PRPFM) comparison. BM can equally map fire effects under different instantaneous severity conditions (Reference frame: WGS84 UTM32N).

This proves that the proposed method can equally map burnt areas under different severity conditions (as detected immediately after the event) with no regard about its level. This capability also suggests that SAR multi-temporal data moves around different mapping criteria if compared with the present official one. These criteria are related to geometrical and dielectrical proprieties of vegetation canopy. Especially the polarization of backscattered signal seems to be a good proxy of vegetation status before and after a disturbance able to describe a relative change in temporal domain. Similar results were found by Lasaponara (Lasaponara and Tucci, 2019) who carried out a survey in Metaponto (Southern Italy), highlighting the effectiveness of S1 data for fire area detection and fire severity characterization.

4. Discussions

Concerning FDM(x,y), authors are aware of the scientific weaknesses of deductions concerning clusters meaning. Nevertheless, they retain that remote

sensing-derived information always require an interpretation based on specific skills and knowledge from the field of application that those data have been generated for. Cluster analysis in particular requires an a-posteriori interpretation to recover a "possible" ecological meaning of evidences that clusters represent. Authors strongly believe that interpretation of data still remain a crucial point while dealing with the technology transfer, confirming that human being still preserves some sparks of knowledge that automatisms of data processing, in spite of ongoing AI-based approaches, cannot still fill properly. It is worth to remind that a knowledge-based interpretation can be also aimed at overcoming field validation, making possible to indirectly recover the "possible" meaning of clusters by synthesizing statistical proxies, photointerpretation of both spatial and temporal patterns, forest/ecological knowledge of researchers. This appears to be more fundamental when a ground validation is not operationally possible, like in this work. In fact, if one wanted to validate late mortality of trees, he should be able to locate some ground plots exactly in those areas where a future event (late mortality) will occur after the fire. Since this type of forecasting is not possible, a validation is not, reasonably, possible too and cluster interpretation is mandatory. FDM(x,y) (figure 9) can be certainly useful to better address restoration policies and, in particular, to focus on early high severity zones where fire compromised forest values from an economic, recreative and natural point of view (Poratelli et al., 2020). Concerning ERM(x,y), the majority of the burned area (61%) is characterized by the presence of resistant stands while only 20% by resilient stands. About 427 ha were classified as increasing stands. Especially in the latter cluster, could represent patches where forest canopy increases due to the presence of pioneer species as ailanthus or European aspen that were favoured by fire occurrence and characterized by agamic regeneration. This peculiar dynamic was proved by Ascoli in the same study area (Ascoli and Bovio, 2010). This map could be a useful support to focus and assess post-fire restoration polices in burned areas according to more ecological-based criteria. For example, from a management point of view, post-fire treatments could be not necessarily in resistant stands, while in moderate resilient stands local restoration policy are

expected where forest structure was compromised by fire and could strongly reduce natural hazard protection.

5. Conclusions

In this work S1-retrived polarimetric index time series was adopted in order to map and characterized forest burned areas considering a monitoring period of 4 years (2016-2019). In particular, Pettitt test performed on CRTS has proved to be an effective test to detect and map burned moment (UA for burned areas was 0.88). The time series decomposition in noise and trend components using LOESS permits to better minimize SAR data noise. Based on local linear regression in sCRTS two new indices SI and RI were computed in order to describe forest severity and recovery processes respectively. The k-means cluster analysis considering these indices couple with t_{min} layer resulting in FDM(x,y) and ERM(x,y) allowed AOI zoning according to ecological criteria. FDM(x,y) layer can tell information about the damage time dynamics aim at describing tree mortality lag through the years. According to this layer about the 22% of burned area is characterized by an early high severity whiled the residual by moderate-low severity levels. Otherwise, ERM(x,y) layer can define resistant (61% of the burned area), resilient (20%) and increasing forest zones (19%). SAR polarimetry data, in particular CR index time series, has proved to be an effective technique able to map forest structure changes after a disturbance supporting early- and mid-term post-fire forest assessment.

References

Arnett, J.T., Coops, N.C., Daniels, L.D., Falls, R.W., 2015. Detecting forest damage after a low-severity fire using remote sensing at multiple scales. International Journal of Applied Earth Observation and Geoinformation 35, 239–246.

Ascoli, D., Bovio, G., 2010. Tree encroachment dynamics in heathlands of North-West Italy: the fire regime hypothesis. iForest 3: 137–143.

Ascoli, D., Castagneri, D., Valsecchi, C., Conedera, M., Bovio, G., 2013. Post-fire restoration of beech stands in the Southern Alps by natural regeneration. Ecological Engineering 54, 210–217. https://doi.org/10.1016/j.ecoleng.2013.01.032

Ascoli, Davide, Castagneri, D., Valsecchi, C., Conedera, M., Bovio, G., 2013. Post-fire restoration of beech stands in the Southern Alps by natural regeneration. Ecological Engineering 54, 210–217.

Barbati, A., Arianoutsou, M., Corona, P., De Las Heras, J., Fernandes, P., Moreira, F., Papageorgiou, K., Vallejo, R., Xanthopoulos, G., 2010. Post-fire forest management in southern Europe: a COST action for gathering and disseminating scientific knowledge. iForest-Biogeosciences and Forestry 3, 5.

Basak, A., Mengshoel, O.J., Kulkarni, C., Schmidt, K., Shastry, P., Rapeta, R., 2017. Optimizing the decomposition of time series using evolutionary algorithms: soil moisture analytics, in: Proceedings of the Genetic and Evolutionary Computation Conference. pp. 1073–1080.

Beghin, R., Lingua, E., Garbarino, M., Lonati, M., Bovio, G., Motta, R., Marzano, R., 2010. Pinus sylvestris forest regeneration under different post-fire restoration practices in the northwestern Italian Alps. Ecological Engineering 36, 1365–1372.

Belenguer-Plomer, M.A., Tanase, M.A., Fernandez-Carrillo, A., Chuvieco, E., 2019. Burned area detection and mapping using Sentinel-1 backscatter coefficient and thermal anomalies. Remote Sensing of Environment 233, 111345.

Bernhard, E.-M., Stein, E., Twele, A., Gähler, M., 2012. SYNERGISTIC USE OF OPTICAL AND RADAR DATA FOR RAPID MAPPING OF FOREST FIRES IN THE EUROPEAN MEDITERRANEAN. The International Archives of the Photogrammetry, Remote Sensing and Spatial Information Sciences XXXVIII-4-W19, 27–32. https://doi.org/10.5194/isprsarchives-XXXVIII-4-W19-27-2011

Bourgeau-Chavez, L.L., Kasischke, E.S., Brunzell, S., Mudd, J.P., Tukman, M., 2002. Mapping fire scars in global boreal forests using imaging radar data. International Journal of Remote Sensing 23, 4211–4234.

Cai, Z., Jönsson, P., Jin, H., Eklundh, L., 2017. Performance of smoothing methods for reconstructing NDVI time-series and estimating vegetation phenology from MODIS data. Remote Sensing 9, 1271.

Camerano, P., Terzuolo, P.G., Guiot, E., Giannetti, F., 2017. La Carta Forestale del Piemonte – Aggiornamento 2016. IPLA S.p.A. – Regione Piemonte.

Carlucci, M., Zambon, I., Colantoni, A., Salvati, L., 2019. Socioeconomic Development, Demographic Dynamics and Forest Fires in Italy, 1961–2017: A Time-Series Analysis. Sustainability (2071-1050) 11, 1305. https://doi.org/10.3390/su11051305

Carreiras, J.M., Quegan, S., Tansey, K., Page, S., 2020. Sentinel-1 observation frequency significantly increases burnt area detectability in tropical SE Asia. Environmental Research Letters 15, 054008.

Catry, F.X., Rego, F., Moreira, F., Fernandes, P.M., Pausas, J.G., 2010. Post-fire tree mortality in mixed forests of central Portugal. Forest Ecology and Management 260, 1184–1192.

Chambers, J.C., Allen, C.R., Cushman, S.A., 2019. Operationalizing ecological resilience concepts for managing species and ecosystems at risk.

Cloude, S.R., Pottier, E., 1996. A review of target decomposition theorems in radar polarimetry. IEEE transactions on geoscience and remote sensing 34, 498–518.

Coltuc, D., Trouvé, E., Bujor, F., Classeau, N., Rudant, J.-P., 2000. Time-space filtering of multitemporal SAR images, in: IGARSS 2000. IEEE 2000 International Geoscience and Remote Sensing Symposium. Taking the Pulse of the Planet: The Role of Remote Sensing in Managing the Environment. Proceedings (Cat. No. 00CH37120). IEEE, pp. 2909–2911.

Conrad, O., Bechtel, B., Bock, M., Dietrich, H., Fischer, E., Gerlitz, L., Wehberg, J., Wichmann, V., Böhner, J., 2015. System for automated geoscientific analyses (SAGA) v. 2.1. 4. Geoscientific Model Development Discussions 8.

De Luca, G., Silva, J. M., & Modica, G. 2021. A workflow based on Sentinel-1 SAR data and open-source algorithms for unsupervised burned area detection in Mediterranean ecosystems. GIScience & Remote Sensing, 58(4), 516-541.

De Luca, G., Silva, J. M., & Modica, G. 2022. Regional-scale burned area mapping in Mediterranean regions based on the multitemporal composite integration of Sentinel-1 and Sentinel-2 data. GIScience & Remote Sensing, 59(1), 1678-1705.

De Petris, S., Momo, E.J., Borgogno-Mondino, E., 2020. Supporting Assessment of Forest Burned Areas by Aerial Photogrammetry: The Susa Valley (NW Italy) Fires of Autumn 2017, in: International Conference on Computational Science and Its Applications. Springer, pp. 829–844.

De Petris, S., Sarvia, F., Borgogno-Mondino, E., 2022. SENTINEL-1 DATA TIME SERIES TO SUPPORT FOREST POLICE IN HARVESTINGS DETECTION. ISPRS Annals of the Photogrammetry, Remote Sensing and Spatial Information Sciences 3, 225–232.

De Petris, S., Sarvia, F., Gullino, M., Tarantino, E., Borgogno-Mondino, E., 2021. Sentinel-1 Polarimetry to Map Apple Orchard Damage after a Storm. Remote Sensing 13, 1030.

DeRose, R.J., Long, J.N., 2014. Resistance and resilience: a conceptual framework for silviculture. Forest Science 60, 1205–1212.

Di Mauro, B., Fava, F., Busetto, L., Crosta, G.F., Colombo, R., 2014. Post-fire resilience in the Alpine region estimated from MODIS satellite multispectral data. International Journal of Applied Earth Observation and Geoinformation 32, 163–172.

Dobson, M.C., Ulaby, F.T., LeToan, T., Beaudoin, A., Kasischke, E.S., Christensen, N., 1992. Dependence of radar backscatter on coniferous forest biomass. IEEE Transactions on Geoscience and remote Sensing 30, 412–415.

Engelbrecht, J., Theron, A., Vhengani, L., Kemp, J., 2017. A simple normalized difference approach to burnt area mapping using multi-polarisation C-Band SAR. Remote Sensing 9, 764.

Forkel, M., Carvalhais, N., Verbesselt, J., Mahecha, M.D., Neigh, C.S., Reichstein, M., 2013. Trend change detection in NDVI time series: Effects of inter-annual variability and methodology. Remote Sensing 5, 2113–2144.

Gimeno, M., San-Miguel-Ayanz, J., Schmuck, G., 2004. Identification of burnt areas in Mediterranean forest environments from ERS-2 SAR time series. International Journal of Remote Sensing 25, 4873–4888.

Gorelick, N., Hancher, M., Dixon, M., Ilyushchenko, S., Thau, D., Moore, R., 2017. Google Earth Engine: Planetary-scale geospatial analysis for everyone. Remote sensing of Environment 202, 18–27.

Grimm, V., Wissel, C., 1997. Babel, or the ecological stability discussions: an inventory and analysis of terminology and a guide for avoiding confusion. Oecologia 109, 323–334.

Hird, J.N., McDermid, G.J., 2009. Noise reduction of NDVI time series: An empirical comparison of selected techniques. Remote Sensing of Environment 113, 248–258.

Holling, C.S., 1973. Resilience and stability of ecological systems. Annual review of ecology and systematics 4, 1–23.

Hurvich, C.M., Simonoff, J.S., Tsai, C.-L., 1998. Smoothing parameter selection in nonparametric regression using an improved Akaike information criterion. Journal of the Royal Statistical Society: Series B (Statistical Methodology) 60, 271–293.

Imperatore, P., Azar, R., Calò, F., Stroppiana, D., Brivio, P.A., Lanari, R., Pepe, A., 2017. Effect of the Vegetation Fire on Backscattering: An Investigation Based on Sentinel-1 Observations. IEEE

Journal of Selected Topics in Applied Earth Observations and Remote Sensing 10, 4478–4492. https://doi.org/10.1109/JSTARS.2017.2717039

João, T., João, G., Bruno, M., João, H., 2018. Indicator-based assessment of post-fire recovery dynamics using satellite NDVI time-series. Ecological Indicators 89, 199–212.

Jones, M.O., Kimball, J.S., Jones, L.A., 2013. Satellite microwave detection of boreal forest recovery from the extreme 2004 wildfires in A laska and C anada. Global change biology 19, 3111–3122.

Jonsson, P., Eklundh, L., 2002. Seasonality extraction by function fitting to time-series of satellite sensor data. IEEE Transactions on Geoscience and Remote Sensing 40, 1824–1832. https://doi.org/10.1109/TGRS.2002.802519

Kasischke, E.S., Bourgeau-Chavez, L.L., French, N.H., 1994. Observations of variations in ERS-1 SAR image intensity associated with forest fires in Alaska. IEEE Transactions on Geoscience and Remote Sensing 32, 206–210.

Kato, A., Thau, D., Hudak, A.T., Meigs, G.W., Moskal, L.M., 2020. Quantifying fire trends in boreal forests with Landsat time series and self-organized criticality. Remote Sensing of Environment 237, 111525. https://doi.org/10.1016/j.rse.2019.111525

Keeley, J.E., 2009. Fire intensity, fire severity and burn severity: a brief review and suggested usage. Int. J. Wildland Fire 18, 116–126. https://doi.org/10.1071/WF07049

Key, C.H., Benson, N.C., 2006. LA-1 Landscape Assessment (LA) Sampling and Analysis Methods. FIREMON: Fire Effects Monitoring and Inventory System; Lutes, DC, Keane, RE, Caratti, JF, Key, CH, Benson, NC, Sutherland, S., Gangi, LJ, Eds.

Keyser, T.L., Smith, F.W., Lentile, L.B., Shepperd, W.D., 2006. Modeling postfire mortality of ponderosa pine following a mixed-severity wildfire in the Black Hills: the role of tree morphology and direct fire effects. Forest Science 52, 530–539.

Kim, Y., Jackson, T., Bindlish, R., Lee, H., Hong, S., 2011. Radar vegetation index for estimating the vegetation water content of rice and soybean. IEEE Geoscience and Remote Sensing Letters 9, 564–568.

Lasaponara, R., Tucci, B., 2019. Identification of burned areas and severity using SAR Sentinel-1. IEEE Geoscience and Remote Sensing Letters 16, 917–921.

Lee, J.-S., Pottier, E., 2017. Polarimetric radar imaging: from basics to applications. CRC press.

Linder, P., Jonsson, P., Niklasson, M., 1998. Tree mortality after prescribed burning in an old-growth Scots pine forest in northern Sweden. Silva Fennica 32, 339–349.

Lohberger, S., Stängel, M., Atwood, E.C., Siegert, F., 2018. Spatial evaluation of Indonesia's 2015 fire-affected area and estimated carbon emissions using Sentinel-1. Global change biology 24, 644–654.

Lutes, D.C., Keane, R.E., Caratti, J.F., Key, C.H., Benson, N.C., Sutherland, S., Gangi, L.J., 2006. FIREMON: Fire effects monitoring and inventory system. Gen. Tech. Rep. RMRS-GTR-164. Fort Collins, CO: US Department of Agriculture, Forest Service, Rocky Mountain Research Station. 1 CD. 164.

Mallakpour, I., Villarini, G., 2016. A simulation study to examine the sensitivity of the Pettitt test to detect abrupt changes in mean. Hydrological Sciences Journal 61, 245–254.

Maringer, J., Ascoli, D., Küffer, N., Schmidtlein, S., Conedera, M., 2016. What drives European beech (Fagus sylvatica L.) mortality after forest fires of varying severity? Forest Ecology and Management 368, 81–93.

Marschall, J.M., Guyette, R.P., Stambaugh, M.C., Stevenson, A.P., 2014. Fire damage effects on red oak timber product value. Forest ecology and management 320, 182–189.

McBride, J.R., 1983. Analysis of tree rings and fire scars to establish fire history.

Mermoz, S., Le Toan, T., 2016. Forest disturbances and regrowth assessment using ALOS PALSAR data from 2007 to 2010 in Vietnam, Cambodia and Lao PDR. Remote Sensing 8, 217.

Miller, J.D., Thode, A.E., 2007. Quantifying burn severity in a heterogeneous landscape with a relative version of the delta Normalized Burn Ratio (dNBR). Remote Sensing of Environment 109, 66–80.

Minchella, A., Del Frate, F., Capogna, F., Anselmi, S., Manes, F., 2009. Use of multitemporal SAR data for monitoring vegetation recovery of Mediterranean burned areas. Remote Sensing of Environment 113, 588–597.

Moreira, F., Catry, F., Lopes, T., Bugalho, M.N., Rego, F., 2009. Comparing survival and size of resprouts and planted trees for post-fire forest restoration in central Portugal. Ecological Engineering 35, 870–873.

Paloscia, S., Macelloni, G., Pampaloni, P., Sigismondi, S., 1999. The potential of C-and L-band SAR in estimating vegetation biomass: the ERS-1 and JERS-1 experiments. IEEE Transactions on Geoscience and Remote Sensing 37, 2107–2110.

Parks, S.A., Dillon, G.K., Miller, C., 2014. A new metric for quantifying burn severity: the relativized burn ratio. Remote Sensing 6, 1827–1844.

Pettitt, A.N., 1979. A non-parametric approach to the change-point problem. Journal of the Royal Statistical Society: Series C (Applied Statistics) 28, 126–135.

Piano straordinario di interventi di ripristino del territorio percorso dagli incendi boschivi dell'autunno 2017, n.d. 244.

Poratelli, F., Cocuccioni, S., Accastello, C., Steger, S., Schneiderbauer, S., Brun, F., 2020. State-of-the-art on ecosystem-based solutions for disaster risk reduction: The case of gravity-driven natural hazards in the Alpine region. International Journal of Disaster Risk Reduction 51, 101929.

R. Core Team, 2013. R: A language and environment for statistical computing. Vienna, Austria.

Regione Piemonte, 2019. Piano straordinario di interventi di ripristino del territorio percorso dagli incendi boschivi dell'autunno 2017.

Reiche, J., Lucas, R., Mitchell, A.L., Verbesselt, J., Hoekman, D.H., Haarpaintner, J., Kellndorfer, J.M., Rosenqvist, A., Lehmann, E.A., Woodcock, C.E., 2016. Combining satellite data for better tropical forest monitoring. Nature Climate Change 6, 120–122.

Reilly, M.J., Dunn, C.J., Meigs, G.W., Spies, T.A., Kennedy, R.E., Bailey, J.D., Briggs, K., 2017. Contemporary patterns of fire extent and severity in forests of the Pacific Northwest, USA (1985–2010). Ecosphere 8, e01695. https://doi.org/10.1002/ecs2.1695

Richards, J.A., 2009. Remote sensing with imaging radar. Springer.

Ryu, J.-H., Han, K.-S., Hong, S., Park, N.-W., Lee, Y.-W., Cho, J., 2018. Satellite-based evaluation of the post-fire recovery process from the worst forest fire case in South Korea. Remote Sensing 10, 918.

Shakesby, R.A., 2011. Post-wildfire soil erosion in the Mediterranean: review and future research directions. Earth-Science Reviews 105, 71–100.

Small, D., Schubert, A., 2019. Guide to Sentinel-1 Geocoding.

Smith, G., Dammert, P.B., Askne, J., 1996. Decorrelation mechanisms in C-band SAR interferometry over boreal forest, in: Microwave Sensing and Synthetic Aperture Radar. International Society for Optics and Photonics, pp. 300–310.

Suresh Babu, K.V., Roy, A., Aggarwal, R., 2018. MAPPING OF FOREST FIRE BURNED SEVERITY USING THE SENTINEL DATASETS. Int. Arch. Photogramm. Remote Sens. Spatial Inf. Sci. XLII–5, 469–474. https://doi.org/10.5194/isprs-archives-XLII-5-469-2018

Szigarski, C., Jagdhuber, T., Baur, M., Thiel, C., Parrens, M., Wigneron, J.-P., Piles, M., Entekhabi, D., 2018. Analysis of the Radar Vegetation Index and Potential Improvements. Remote Sensing 10, 1776. https://doi.org/10.3390/rs10111776

Tanase, M., de la Riva, J., Santoro, M., Pérez-Cabello, F., Kasischke, E., 2011. Sensitivity of SAR data to post-fire forest regrowth in Mediterranean and boreal forests. Remote Sensing of Environment 115, 2075–2085.

Telesca, L., Lasaponara, R., 2006. Pre-and post-fire behavioral trends revealed in satellite NDVI time series. Geophysical research letters 33.

Ulaby, F.T., Moore, R.K., Fung, A.K., 1981. Microwave remote sensing: Active and passive. volume 1-microwave remote sensing fundamentals and radiometry.

Valese, E., Conedera, M., Held, A.C., Ascoli, D., 2014. Fire, humans and landscape in the European Alpine region during the Holocene. Anthropocene 6, 63–74.

Verhegghen, A., Eva, H., Ceccherini, G., Achard, F., Gond, V., Gourlet-Fleury, S., Cerutti, P.O., 2016. The potential of Sentinel satellites for burnt area mapping and monitoring in the Congo Basin forests. Remote Sensing 8, 986.

Vollrath, A., Mullissa, A., Reiche, J., 2020. Angular-Based Radiometric Slope Correction for Sentinel-1 on Google Earth Engine. Remote Sensing 12, 1867.

Vreugdenhil, M., Wagner, W., Bauer-Marschallinger, B., Pfeil, I., Teubner, I., Rüdiger, C., Strauss, P., 2018. Sensitivity of Sentinel-1 backscatter to vegetation dynamics: An Austrian case study. Remote Sensing 10, 1396.

Walker, B., Holling, C.S., Carpenter, S.R., Kinzig, A., 2004. Resilience, adaptability and transformability in social–ecological systems. Ecology and society 9.

Wang, X.-F., 2010. fANCOVA: nonparametric analysis of covariance. R package, Version 0.5-1.

Xie, H., Li, D., Xiong, L., 2014. Exploring the ability of the Pettitt method for detecting change point by Monte Carlo simulation. Stochastic environmental research and risk assessment 28, 1643–1655.

Zhou, Z., Liu, L., Jiang, L., Feng, W., Samsonov, S.V., 2019. Using Long-Term SAR Backscatter Data to Monitor Post-Fire Vegetation Recovery in Tundra Environment. Remote Sensing 11, 2230.

4.3 POLARIMETRY-BASED TECHNIQUES

4.3.1 Sentinel-1 Polarimetry to Map Apple Orchard Damage After a Storm

De Petris Samuele[a*], Sarvia Filippo[a], Gullino Michele[b], Tarantino Eufemia[c] and Borgogno-Mondino Enrico[a]

[a]Department of Agricultural, Forest and Food Sciences (DISAFA), University of Turin, 10095 Grugliasco, Italy.

[b]Az. Agr. Fessia Franca, v. Lagnasco 6, 12030, Manta, Italy;

[c]DICATECh, Politecnico di Bari, Via Orabona 4, 70125 Bari, Italy;

*Correspondence: samuele.depetris@unito.it

Published: 2021 in *Remote Sensing,* IF (2021): 5.349

Abstract: Climate change increases extreme whether events such as floods, hailstorms, or storms, which can affect agriculture, causing damages and economic loss within the agro-food sector. Optical remote sensing data have been successfully used in damage detections. Cloud conditions limit their potential, especially while monitoring floods or storms that are usually related to cloudy situations. Conversely, data from the Polarimetric Synthetic Aperture Radar (PolSAR) are operational in all-weather conditions and are sensitive to the geometrical properties of crops. Apple orchards play a key role in the Italian agriculture sector, presenting a cultivation system that is very sensitive to high-wind events. In this work, the H-α-A polarimetric decomposition tech-nique was adopted to map damaged apple orchards with reference to a stormy event that had occurred in the study area (NW Italy) on 12 August 2020. The results showed that damaged orchards have higher H (entropy) and α (alpha angle) values compared with undamaged ones taken as reference (Mann–Whitney one-tailed test $U = 14{,}514$, $p < 0.001$; $U = 16604$, $p < 0.001$ for H and α, respectively). By contrast, A (anisotropy) values were significantly lower for damaged orchards (Mann–Whitney one-tailed test $U = 8616$, $p < 0.001$). Based on this evidence, the authors generated a map of potentially storm-damaged orchards, assigning a probability value to each of them. This map is intended to support local funding restoration policies by insurance companies and local administrations.

Keywords: Sentinel-1; apple orchard damage; polarimetric decomposition; entropy; anisotropy; alpha angle; storm damage mapping; economic loss; insurance support.

1. Introduction

Climate change and related natural disasters affect several sectors [1]. Agriculture is one of the most vulnerable [2,3]. Between 2005 and 2015, the impact of natural disasters on the agricultural sector was estimated to be 96 billion dollars in damaged, or completely lost, crops [4]. Climate change-related effects (e.g., temperature and precipitation increasing in terms of level, time, and variability) are expected to reduce the yield and quality of many crops, especially cereals and fodder cereals [5]. Storms and hail also can cause serious damage to crops [6]. Hurricanes can cause much damage, with grass lodging, uprooting of orchards, and falling trees [7,8]. These critical events, potentially highly impacting farmers' income, must be carefully accounted for in the context of risk management in agriculture. Fruits and vegetables represent (year 2018) about 14% of the total value of European (EU) agricultural production [9,10]. These crops are very important for many EU member states, in particular for Mediterranean countries such as Spain, Italy, and France. Italy is one of the main European leaders in the apple sector [11]. Consequently, the yield loss risks concerning the fruit and vegetable sector must be minimized. Major threats concern diseases, insects, and natural disasters such as hail, drought, frost, and storms. Apple cultivation is very intensive today, with a plant density around 2000 plants per hectare [12]. Such density allows a very high yearly production (about 45 tons per hectare) [13], which is obtained by a row-based cultivation strategy where young plants begin to be productive after the third year. The adoption of low-vigor rootstocks enables an increase in planting density and rapid fruiting. Unfortunately, this kind of cultivation determines a very underdeveloped root system, not enough to guarantee plant stability un-der unfavorable conditions. The situation is more critical during extreme weather events, especially when there are many weighty fruits, i.e., before harvesting [14,15]. Steel cables anchored to concrete or wooden poles are used to improve row stability. Within this context, when a stormy event

occurs, it is important to assess the spatial level and extent of damage to start remedial actions and minimize crop loss. Farmers are interested in damage estimation especially when a refund is due by insurance companies [16,17]. In this case, damage is assessed through on-the-spot checks by an expert surveyor from the insurance company, who determines the extent, type, and quality of damage. Such an approach depends on a high level of subjectivity related to the expert's skill and experience. Moreover, these operations require a lot of time and are expensive, especially where large areas have been affected by the event. In this operative context concerning crop damage analysis, a more objective monitoring could play a key role, providing more robust forecasts about potential yield or yield losses. Many agricultural stakeholders, such as farmers, consortia, agronomists, insurance companies, and local administrations, require a continuous monitoring of crops over large spatial extents. A method based on free Earth Observation (EO) data can certainly represent an effective support [18] and the consequent technological transfer desirable [19–24].In particular, optical remote sensing data have been successfully used in several operational frameworks, as proved by many works [25–32]; unfortunately, cloud conditions limit the nominal temporal resolution of this type of data, especially while monitoring natural disasters (e.g., floods or storms) that ordinarily occur when clouds are present. Data from synthetic aperture radar (SAR) systems can operate during all-weather conditions, and, while exploring agronomical issues, they can be used to analyze the moisture and geometrical conditions of crops [33–35]. In particular, dual-polarimetric SAR acquisitions from Copernicus Sentinel-1 mission (S1) provide unique opportunities to disseminate operational monitoring for several application communities [36,37]. Dual-pol acquisition mode has a larger swath and a lower data volume compared with full-pol acquisitions, thus improving data collection and processing for operational activities [38,39]. Polarimetric data can provide information about polarization amplitude and phase, allowing scattering mechanism definition (i.e., single-bounce, double-bounce, or volume scattering) induced by target properties. SAR polarimetry (PolSAR) is a technique that analyzes SAR polarization with respect to the vector

of polarized electromagnetic waves. When a signal passes through a medium, the refraction index changes, or when it strikes an object, it is reflected; the so-called backscattering matrix [40] contains information about the reflectivity, shape, and orientation of the reflecting target. An important improvement in the extraction of physical information from the ordinary coherent backscattering matrix was achieved by Cloude and Pottier [41,42], who proposed the composition of system vectors. Most studies have assessed the sensitivity of polarimetric indicators derived from the C-band space-borne SAR to derive crop parameters [43]. The PolSAR technique was successfully applied to monitor crop growth and give estimates of yield. For example, Betberder [44] analyzed temporal trends of polarimetric indicators, proving their high potential to detect crop growth changes. Valcarce [45] used polarimetric data time series for land-cover classification, adopting a decision tree classification algorithm per-forming high crop class detection accuracies. Mercier and Qi [46,47] used PolSAR to support/integrate vegetation phenology monitoring based on optical data. Only few works referring to PolSAR application in crop damage analysis are present in the literature [48,49], denoting a lack of scientific production about this issue. Nevertheless, hailstorms and storms are known to change vegetation structure, resulting in lodging or tree uprooting/breaking. Therefore, this peculiar effect changes polarimetric response and could be used to detect and characterize tree structure [50]. In general, it can be said that decomposition techniques offer a new insight into PolSAR data for describing vegetation structural proprieties [51]. The polarimetric decomposition technique decomposes the signal into its individual scattering components, permitting identification of the dominant scattering type [42,52]; this information is related to the target structural properties [18,53,54]. Various decomposition techniques have been proposed, and Lee and Cloude provided a comprehensive re-view about this topic [42,55]. Model-based [56] and eigenvector-based [41] algorithms have been preferred by many researchers [51]. According to Ji and his collaborators [57], the Cloude–Pottier H-α-A decomposition seems to be the most promising approach. It is based on second-order statistics extracted by a set of neighbor pixels that are used

to calculate the local entropy H and the α angle (related to average scattering mechanisms). These are used to define a Cartesian space, H-α, that is linearly divided into nine zones describing the main scattering mechanisms. Recently, eigenvector decomposition has been widely applied in several applications [55,58–61]. The method was originally developed for quad-polarization data. Nevertheless, it was also adapted to work with du-al-pol data [57,62,63], and consequently, it can be successfully used to retrieve polarimetric information also from S1 data that are unable to collect quad-pol data.

In this work, the applicability of the H-α-A polarimetric decomposition technique to the detection and mapping of damages from storms affecting fruit orchards was tested. In particular, the proposed case study refers to the stormy event that occurred in Northwest Italy on 12 August 2020. Consequently, a map of potentially damaged orchards was generated with the aim of supporting insurance companies and local administrations to address their funding restoration policies.

2. Materials and Methods

2.1. Study Area

On 12 August 2020, an exceptional storm affected the Northwest of Italy. In particular, the storm uprooted many apple orchards in the province of Cuneo (Piemonte region, NW Italy). Moreover, it occurred in a critical period of the year, when the main fruits (apples, pears, and peaches) were still to be harvested (Figure 1). Because in this period the farmers are focused on harvesting, no early recovery efforts were performed in the dam-aged fields. Therefore, the majority of the uprooted trees were not removed until October.

Figure 1. An apple orchard (cultivar “Gala”) with hail nets uprooted by the storm on 12 August 2020. At the bottom, many mature apples can be noted, suggesting the economic loss caused by the storm.

The study area includes four municipalities: Saluzzo, Verzuolo, Manta, and Lagnasco (Figure 2). The area of interest (AOI) is sized about 132.23 km^2. It plays a crucial economic role in Piemonte fruit production. In fact, this zone is suitable for this cultivation: the loose soil without water stagnation, sunny and dry atmosphere, and strong temperature difference between day and night allow the correct ripening and coloring of fruits. Apples rep-resent the primary crop in Manta. Since August is a droughty period in the AOI, no significative previous precipitations had occurred before the event; 1.2 mm had cumulated in the previous week, as reported by the regional environmental agency (www.arpa.piemonte.it). Therefore, the authors supposed that moisture-related conditions cannot significantly affect the SAR signal.

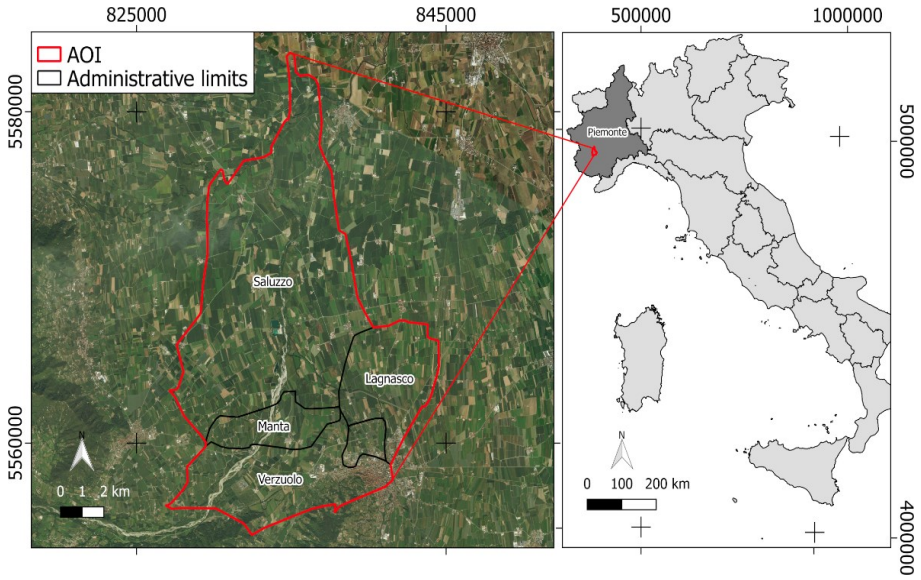

Figure 2. Italian regions (light gray) and the Piemonte region (dark gray). (Red) The AOI includes the Saluzzo, Manta, Lagnasco, and Verzuolo municipalities (reference frame: WGS84 UTM32N).

2.2. Data and Data Collection

2.2.1. Sentinel-1 Data

Sentinel-1 is currently one of the largest space-borne missions providing free and openly accessible SAR data. The S1 mission relies on a constellation of two satellites (Sen-tinel-1A and Sentinel-1B) operating in the C-band (5.54 cm wavelength). The main acquisition mode over land is the Interferometric Wide (IW) swath, recording approximately 250 km in length at 5 × 20 m spatial resolution in a single look. Ordinarily, S1 records data in a dual pole mode (VV and VH), where electromagnetic waves are polarized vertically (V) for transmission and horizontally/vertically for reception. The data are recorded as complex values (I/Q components) and in SAR geometry (range and azimuth). A descend-ing single-look complex (SLC) IW image (relative orbit no. 139), acquired after the storm (14 August 2020), was obtained from the Copernicus Open Access Hub (https://scihub.copernicus.eu/dhus/#/home, accessed: 20 December 2020).

2.2.2. Cadastral Data

A cadastral map coupled with farmers' applications for EU Common Agricultural Policy (CAP) incentives was used in this work to classify the orchards in the AOI. The correspondent map (hereafter called orchard map (OM)) was consequently generated. The damaged orchards were analyzed at cadastral parcel level. The cadastral map was obtained for free from the regional geoportal in vector format georeferenced in the WGS84 UTM zone 32N reference frame and updated in 2018 (nominal scale was 1:2000). Databases containing farmers' applications for EU CAP incentives of 2019 were used to map orchard types in the AOI (2020 data are not yet available). Every year, farmers support their activities with CAP incentives. These data were obtained for free from the regional public information system for agriculture. CAP applications contain the cadastral parcel code and the declaration of the most relevant crops as communicated by farmers. In this way, it is possible to couple the cadastral map with crop type information at parcel level by an ordinary join operation available in the Geographical Information System (GIS) software. In this work, 2040 (about 1136 ha) apple orchards were selected from the joined data to test the procedure.

2.2.3. Ground Dataset

A ground survey was conducted to gather the field data needed to calibrate and vali-date the PolSAR-based mapping procedure. In total, 72 apple orchards were surveyed (about 3.5% of the apple orchards in the AOI) during a ground campaign aimed at labelling damaged (22) and undamaged (50) fields. Specifically, the surveyed fields have an average size of about 0.92 ha, fitting well with the S1 geometrical resolution. In fact, about 40 S1 pixels can characterize each field. In particular, a visual assessment aimed at recognizing the following conditions was performed: if the majority of the trees were uprooted, the field was labelled as damaged; otherwise, it was labelled undamaged, and the related cadastral parcel was selected from the OM layer.

The dataset was split in a training (60%) and a test set (40%) by random selection from the surveyed parcels. In total, 13 damaged fields (hereafter called DTFs) and 28 un-damaged ones (hereafter called UTFs) were assigned to the training set. Conversely, 10 damaged fields (hereafter called DVFs) and 21 undamaged ones (hereafter called UVFs) were assigned to the test set. The training and test set parcels are shown in Figure 3. This dataset was provided by local farmers. The authors found that the supplied sample includes 72 fields corresponding to about 3.5% of the apple orchards in the AOI. The authors had just the opportunity of comparing the sample size with the expected total number of apple orchards in the AOI (about 2050). The authors are aware that this sample size does not perfectly fit statical requirements. Nevertheless, it well represents ordinary availability of ground data from farmers when working with actual data not directly managed by scientists. This situation well represents a common operational condition when working with technology transfer issues, especially in the agronomic sector. In fact, the most of data from farmers, generally, rely on their autonomous collections and decision of making them public. Moreover, the private property of parcels is an objective limiting factor for all the analyses, since free access is not guaranteed. With these premises, we proceed to process the data.

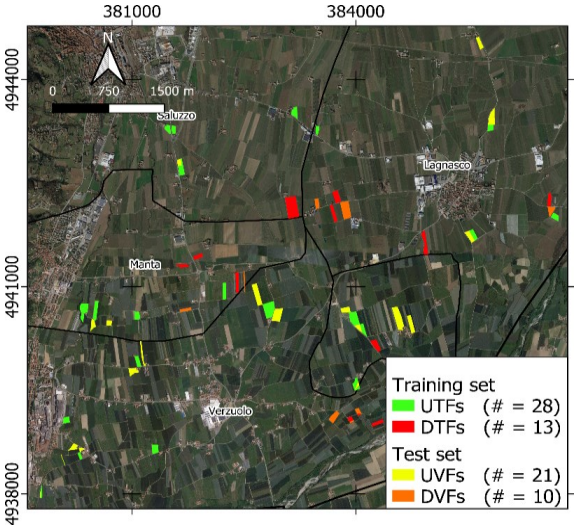

Figure 3. Parcels belonging to the training and test sets. Colours (see legend) define the state of the surveyed parcel (damaged/undamaged). Reference frame is WGS84 UTM 32N.

A preliminary economic assessment was also performed since the storm occurred close to the apple harvesting period, determining a significant problem for local apple yield in 2020. This was obtained considering, for damaged parcels, a potential yield equal to the average one in the Piemonte region (31 $t \cdot ha^{-1}$) and a reference unitary price of 380 $€ \cdot t^{-1}$. These values were obtained from the Italian Statistics Institute (ISTAT) [64].

2.3. Data Processing

2.3.1. Polarimetric Decomposition

The available S1 IW SLC image was processed to compute the polarimetric decom-position parameters. The adopted workflow is shown in Figure 4 and proposed by [65]. The target polarimetric analysis is ordinarily performed starting from the coherency matrix [66,67] or from the 2×2 covariance matrix (C2). Preprocessing steps were managed using the ESA SNAP v. 7.0.0 software [68].

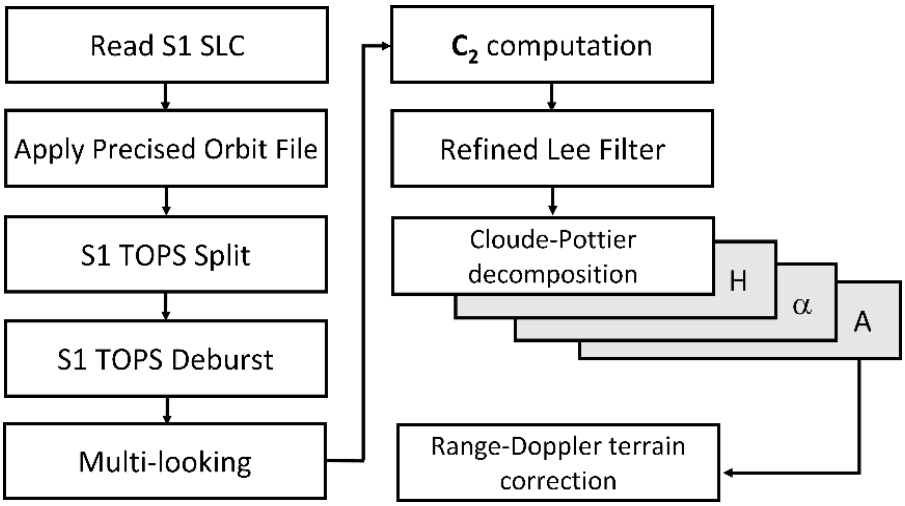

Figure 4. The adopted workflow. All steps were managed in SNAP ESA v. 7.0.

First, the precise orbit state vector data were downloaded from the ESA archive (https://qc.sentinel1.eo.esa.int/, accessed: 20 December 2020) and applied to refine the satellite position. Precise orbit files are delivered within 20 days after data acquisition and provide accurate satellite position and velocity information. Using the TOPS split module, 1 sub-swath and 2 bursts were selected based on AOI coverage. A radiometric calibration was applied and the result saved in a complex-valued format needed to compute C2. TOPS deburst was applied by merging different bursts into a single SLC image. A spatial subset was then generated covering the AOI. The subset was multi-looked by 4 × 1 (range and azimuth direction, respectively) to generate squared pixels. The resulting multi-looked image, with a geometrical resolution equal to 15 m, was used to generate the local C2 at pixel level. With respect to quad polarization, dual-polarimetric SAR sensors generate a matrix showing the half of the totally occurring scattering components involved in fully polarimetric imagery [69]. In particular, the covariance matrix for dual polarization (e.g., Sentinel-1) is often calculated with reference to a second-order scattering information [18] generated from the spatial averaging of the scattering vector $k = [\sigma_{VV}, \sigma_{VH}]^T$ as expressed in Equation (1):

$$\boldsymbol{C_2} = \begin{bmatrix} C_{11} & C_{12} \\ C_{21} & C_{22} \end{bmatrix} = \begin{bmatrix} \langle |S_{VV}| \rangle & \langle S_{VH} {S_{VV}}^* \rangle \\ \langle S_{VH} {S_{VV}}^* \rangle & \langle |S_{VH}| \rangle \end{bmatrix} \quad (1)$$

where $*$ denotes the complex conjugate and $\langle\ \rangle$ the local mean value in a 5×5 moving window. Each C2 element (C11, C22, $\Re$(C12), and $\Im$(C12)) is stored individually and successively refined by Lee filtering (5 × 5 kernel size) to minimize speckle-related noise. H-α-A polarimetric decomposition was obtained by eigenvector computation as proposed by different authors [57,62,63]. The modified formula for dual-pol data, as proposed by [66], is reported in Equations (2a) and (2b).

$$\langle \boldsymbol{C_2} \rangle = [\boldsymbol{U}] \begin{bmatrix} \lambda_1 & 0 \\ 0 & \lambda_2 \end{bmatrix} [\boldsymbol{U}]^{*T} = \lambda_1 \boldsymbol{u_1} {\boldsymbol{u_1}}^{*\boldsymbol{T}} + \lambda_2 \boldsymbol{u_2} {\boldsymbol{u_2}}^{*\boldsymbol{T}} \quad (2a)$$

$$[\boldsymbol{U}] = \begin{bmatrix} U_{11} & U_{12} \\ U_{21} & U_{22} \end{bmatrix} = [\boldsymbol{u_1}\, \boldsymbol{u_2}] = \begin{bmatrix} \cos\alpha & -\sin\alpha e^{-j\delta} \\ \sin\alpha e^{j\delta} & \cos\alpha \end{bmatrix} \quad (2b)$$

where $\lambda_1 \geq \lambda_2 \geq 0$ are the local eigenvalues, [U] is the orthogonal unitary matrix, * and T represents the complex conjugate and transpose matrices, respectively. The angles α and δ define the orientation and size of the polarization ellipse of the recorded signal [62]. The eigenvector dual-pol decomposition results in three roll-invariant parameters: polarimetric scattering entropy (H), mean scattering angle (α), and scattering anisotropy (A). H was calculated from Equation (3)

$$H = -\sum_{i=1}^{2} (-P_i \log_2 P_i) \quad (3)$$

Where:

$$P_i = \frac{\lambda_i}{\lambda_1 + \lambda_2}$$

H defines scatter randomness; it can vary between 0 and 1 and is related to the number of dominant scattering mechanisms, being proportional to the degree of depolarization [70]. H = 0 means that the coherency matrix shows only one eigenvalue and, therefore, the relative orientation of the correspondent pixel elements is quite simplified (e.g., single-bounce reflection). Anisotropy A

(Equation (4)) provides additional information about H in terms of the difference between scattering mechanisms.

$$A = \frac{\lambda_1 - \lambda_2}{\lambda_1 + \lambda_2} \quad (4)$$

The anisotropy quantifies the relative strength between first and second dominant scattering mechanisms. It is strictly related to the degree of signal polarization [18,71,72]. According to Mandal [18], the state of polarization of an electromagnetic (EM) wave is characterized in terms of the degree of polarization ($0 \leq A \leq 1$). The latter is defined as the ratio between the average intensity of the polarized portion of the signal and its total in-tensity [73]. A = 1 and A = 0 for a completely polarized and completely unpolarized wave, respectively. The unpolarized part of the received wave, (1 − A), is assumed to represent the volume scattering component from the distributed targets [74]. Average scattering mechanisms (i.e., surface, double-bounce, and volume scattering) can be identified with respect to the α parameter, which is computed according to Equation (5):

$$\alpha = \sum_{i=1}^{2} P_i \cos^{-1}\left(\frac{|\lambda_1 + \lambda_2|}{\sqrt{2}\sqrt{|\lambda_1|^2 + |\lambda_2|^2}}\right) \quad (5)$$

The α angles close to 0° denote a diffuse surface scattering, α close to 45° means di-pole scattering (caused by volumes), and α close to 90° means double-bounce scattering mechanisms. With these premises, the raster layer mapping local H, α, and A values was computed from the pre-processed SLC image. It was projected onto the WGS84 UTM 32N reference frame, applying the range–Doppler terrain correction. The adopted digital terrain model (DTM) needed for this step was the one freely obtainable from the Piemonte region geoportal [75]. It is supplied with a 5 m grid size and a height accuracy of ±0.30 m and was generated in 2011. The nearest-neighbor resampling method was adopted during the range–Doppler terrain correction.

2.3.2. Testing H-α-A Values After the Storm

To assess how the storm changed the orchards' polarimetric behavior, a preliminary analysis was performed with reference to the training set. In particular, DTF and UTF pixels distributions were compared using the Mann–Whitney (MW) nonparametric test (one-tailed) [76]. The MW null hypothesis is that DTFs and UTFs have an identical distribution. The one-sided alternative "greater" was set, assuming that the DTF cumulated frequency distribution was expected to have shifted to the right of the UTF one (i.e., DTFs were greater than UTFs) [77]. The authors preliminary explored the polarimetric indices' behavior using reference ground data. In particular, the frequency distributions were perceptively assessed using boxplots (see section 3.1.). The median value of distribution highlights a shift between damaged and undamaged fields. Therefore, to test these perceptive differences, the authors performed one tail test since the direction of changes is a priori known. Three MW tests were performed to test if the DTF distributions of the H-α-A pixels within the parcels were statistically different from the UTF ones. All statistical analyses were performed using R software v. 3.6.3 [78]; conversely, spatial analysis was done using SAGA GIS 7.0 [79].

2.3.3. Detection of Damaged Orchards

The main goal of this work was to test the capability of the PolSAR technique to recognize damaged orchards. For this task, UTFs were assumed as representatives of the state of undamaged orchards. Samples were sized about 23 ha and represented about 2% of OM. In spite of this small sample size, the UTFs preliminarily resulted in a good dataset, whose reliability was confirmed by ground surveys. With these premises, the H-α-A distributions within UTFs were used to represent the reference distributions of the un-damaged orchards. All H-α-A distributions from the AOI mapped parcels were tested against undamaged ones by the MW test, checking the following conditions: (i) parcel H distribution was greater than that of the UTFs; (ii) parcel α distribution was greater than that

of the UTFs; (iii) parcel A distribution was lower than that of the UTFs. The resulting MW U-statistic and related p-value were then mapped for each orchard parcel. Moreover, the compound probability (CP) [80] was also calculated according to Equation (6) using R software v. 3.6.3. CP represents the probability that the previously mentioned three conditions were simultaneously satisfied.

$$CP = (1 - p_H)(1 - p_\alpha)(1 - p_A) \quad (6)$$

where p_H is the p-value resulting from the MW test under condition (i), p_α is the *p-value* resulting from the MW test under condition (ii), and p_A is the p-value resulting from the MW test under condition (iii). The resulting CP was then mapped for all OM parcels, rep-resenting its compound probability to have been damaged by the storm. A threshold value of CP able to separate damaged fields from undamaged ones has to be necessarily selected by final users, e.g., the insurance company or local public administration, according to their specific policies and strategies. Nevertheless, a possible solution is proposed here, relying on the standard error of the mean (SEM) of the CP distributions of the DTFs and UTFs. The estimated threshold value was used to generate the map of damaged orchards (DM): parcels showing a CP value lower than the threshold was classified as "undam-aged," otherwise as "damaged." The DMs were then tested against the previously mentioned test set and the correspondent confusion matrix calculated to assess the accuracy of detection.

3. Results

3.1. H-α-A Analysis

The statistical distributions of H-α-A were computed with reference to DTFs and UTFs (Figure 5).

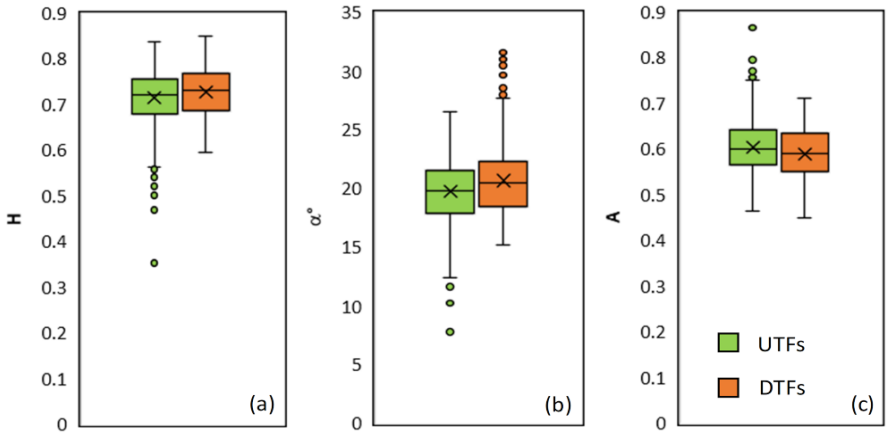

Figure 5. Boxplots of H-α-A distributions for UTFs and DTFs The boxplot values are from bottom to top, respectively, 5th, 25th, 50th—cross is mean value—75th, and 95th percentiles. (a) Entropy pixel distribution; (b) alpha angle pixel distribution; (c) anisotropy pixel distribution.

The MW test results (Table 1) show that the H and α distributions of DTFs presented values significantly greater than UTFs; conversely, the A distribution of the DTFs was lower than that of the UTFs.

Table 1. MW test results obtained by comparing the H-α-A pixel distributions of DTFs and UTFs.

	U	***p-value***
H	14514	0.000159
α	16604	3.83×10^{-10}
A	8616	0.000161

3.2. Damaged Orchards' Mapping

Based on the assumption that a storm can change the polarimetric behavior of orchards according to previously mentioned dynamics, a map of CP representing the parcel probability of being recognized as damaged was generated using the UTF dataset as reference (Figure 6).

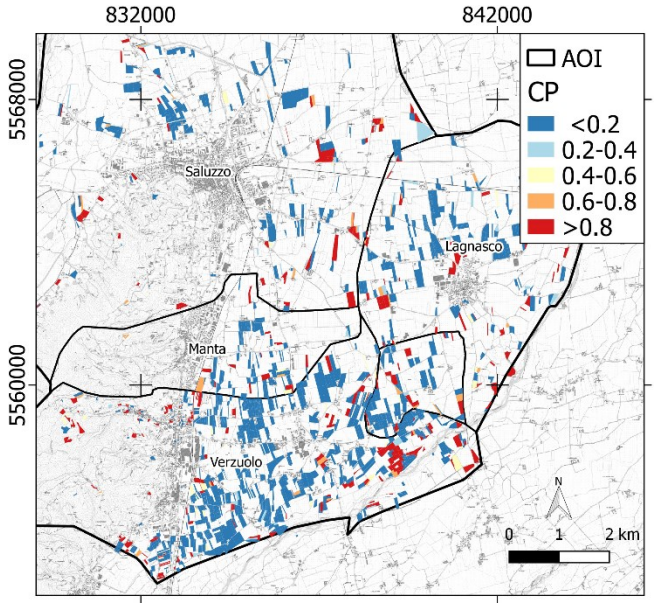

Figure 6. A CP map of apple orchards in the AOI (Reference frame: WGS84 UTM32N).

With reference to CP, a threshold value was estimated to separate damaged fields from undamaged ones based on the SEM of CP statistic distributions of the DTFs and UTFs (Figure 7b). The DTFs showed a CP mean and SEM value of 0.715 and 0.125, respectively; consequently, one can assume that the CP mean value of all damaged orchards reasonably falls in the range 0.715 ± 0.125, about 0.6 being the lower boundary. A thresh-old equal to 0.6 was therefore selected to generate the DM binary classification (Figure 7a).

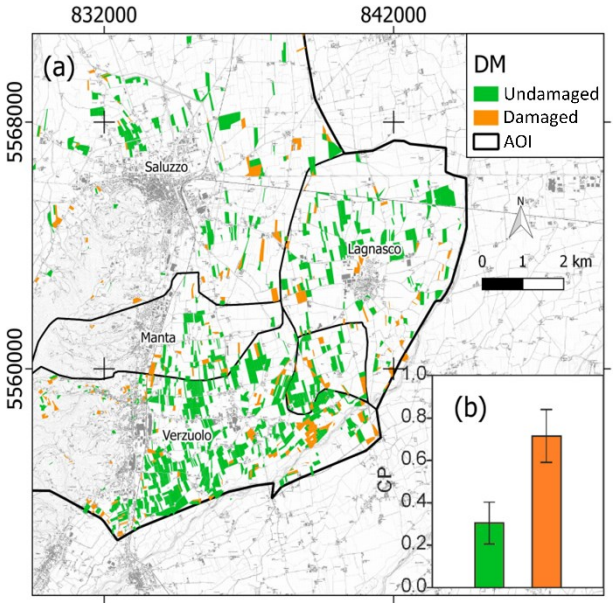

Figure 7. (a) DM binary classification of the OM in the AOI (reference frame is WGS84 UTM 32N); (b) bar chart representing mean and 1 SEM of the CP for DTFs and UTFs.

A total of 217 ha (430 orchards) of potentially damaged apple orchards were detected in the AOI. According to the OM layer, 19% of the apple orchards were damaged after the event. The DM was validated with respect to the test set, and the correspondent confusion matrix computed (Table 2). Classification accuracy is defined here as the one for binary classification of imbalanced data [81–83] since, in the test set, the number of undamaged fields was significantly greater than that of damaged fields. The resulting precision and specificity were pretty high (0.80 and 0.71, respectively), while balanced accuracy was found to be 0.75. Overall accuracy was 0.74, while F1 score (harmonic mean of the precision and recall) and G-mean (geometric mean of sensitivity and precision) were both about 0.67.

Table 2. Metrics derived from the confusion matrix of the DM with respect to the test set. True positives (TPs): number of damaged elements predicted as damaged; false positives (FPs): number of undamaged elements predicted as damaged; false negatives (FNs): number of damaged elements predicted as undamaged; true negatives (TNs): number of undamaged elements predicted as undamaged.

		Classification	
		Damaged	**Undamaged**
Reference	**Damaged**	8	2
	Undamaged	6	15
Accuracies			
Measure		**Value**	**Formula**
Sensitivity		0.80	TPR = TP/ (TP + FN)
Specificity		0.71	SPC = TN/ (FP + TN)
Precision		0.57	PPV = TP/ (TP + FP)
Negative Predictive Value		0.88	NPV = TN/ (TN + FN)
False Positive Rate		0.28	FPR = FP/ (FP + TN)
False Discovery Rate		0.42	FDR = FP/ (FP + TP)
False Negative Rate		0.20	FNR = FN/ (FN + TP)
Overall Accuracy		0.74	OA = (TP + TN) / (TP + TN + FP + FN)
F1 Score		0.66	F1 = 2TP/ (2TP + FP + FN)
Balanced Accuracy		0.75	BA = TPR + TNR/2
G-Mean		0.67	G-mean= sqrt (TPR *PPV)

Furthermore, it is worth stressing that the storm occurred close to the harvesting period, determining a significant problem for local apple yield in 2020. With reference to the AOI, a preliminary estimate of economic loss was computed to be about €2,500,000. Re-ported estimates could certainly vary according to the apple orchards' age, apple variety, plant density, agronomic management, and local soil properties. Nevertheless, these estimates constituted a preliminary assessment of storm damage that occurred on 12 Au-gust 2020. Future validation is expected to test these economic deductions.

4. Discussions

Concerning the damaged orchards' H-α-A distributions (Figure 5 and Table 1), high-er values of H and α in the damaged parcels could be attributed to the changes in vegetation structure (Figure 8). In fact, the inter-row spaces of the damaged orchards, after the storm, were completely covered with the crowns of the broken or uprooted plants, which determined a different scattering geometry. Pre-event plant row geometry was characterized by a regular pattern, which drastically changed to a more disordered one, where the fallen crown elements increased the H values. Since the pre-event scattering mechanism was determined by regularly aligned and spaced plants (rows) alternating with bare soil/grass (inter-rows), it determined intermediate α values. After the storm, it can be assumed that the scattering mechanism was strongly influenced by crown volume, inducing an increase in the α values. Conversely, A appeared to reduce after the event. This could be possibly related to a reduction in the eigenvalue difference $\lambda_1 - \lambda_2$ related to the slightly different scattering mechanism after the storm. The volumetric mechanism appeared to be the prevailing one in the damaged parcels, as proved by the H increase. Since the canopy causes a strong depolarization of the SAR signal, the degree of depolarization (i.e., 1-A) tends to increase with crown closure [18]. Given these interpretation keys, the results obtained seem to support the idea that, after a relevant event able to significantly change vegetation structure, the orchards' polarimetric behavior significantly changes. Based on the collected reference data, damaged orchards tend to show (i) higher values of H and α due to the increased contribution of the volume scattering mechanism, and (ii) lower A values, possibly due to the inter-row closure generated by broken/fallen trees, which increase signal depolarization.

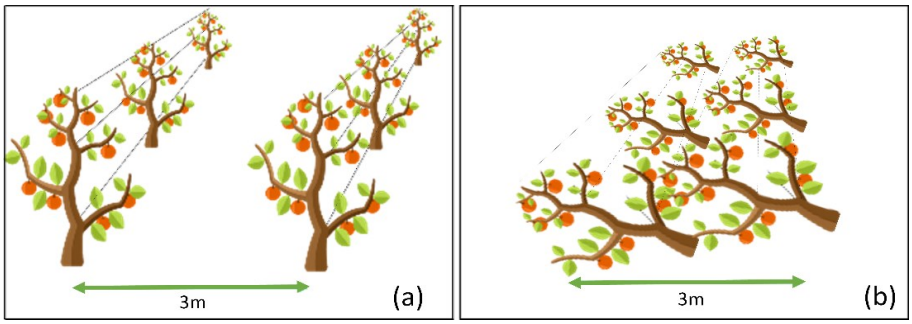

Figure 8. A sketch representing orchard condition before (a) and after (b) the storm. In (a) the pattern row/inter-row is well defined; (b) after the storm, apple tree uprooting occurred, altering the row/inter-row pattern, and crowns covering the ground increased volumetric scattering.

Concerning the mapping of damaged orchards, the results reported in Table 2 suggest that polarimetric decomposition of S1 data is an effective approach to map orchards affected by a storm, especially during cloudy weather situations. Nevertheless, it is worth stressing that some limitations still persist while working with dual-pol decomposition. In comparison to quad polarization, dual-pol SAR sensors collect half of the scattering matrix components involved in fully polarimetric imagery. Therefore, dual-pol derived products may vary from the classical Wishart distribution. In fact, [57] highlighted that entropy/alpha decomposition using one co-polarization and one cross-polarization does not adequately extract scattering mechanisms in the H-α plane. Nevertheless, Cloude [62] proved how these differences result similarly to the conventional quad-pol one while working with vegetation. In spite of these differences, many operative frameworks were proposed proving how information lost during the dual-pol acquisition can be compensated for enhancing image swath and satellite revisit frequency. Moreover, often quad-pol SAR data are not available free of charge and not readily available for operative purposes. S1 is currently one of the largest space-borne missions providing free and open-access SAR data having high temporal resolution, fitting well with vegetation dynamics monitoring requirement. Future developments are expected to test if pre- and post-H-α-A differences can be used to semi-automatically detect significance changes. It is worth highlighting that the majority of apple orchards in the study area are

covered by plastic nets to protect the trees against hail. Probably, plastic nets can influence the complex permittivity of the analyzed volume and therefore affect the polarimetric response of the observed uprooted trees. Since in the study area, a few fields do not have hail nets, the authors did not survey such or-chards, and therefore no assessment looking for the effects of nets on polarimetric response was performed. A specific research should be addressed to assess how plastic hail nets can affect backscattered signal.

5. Conclusions

In this work, a preliminary assessment about the polarimetric behavior of orchards after a storm was performed. The analysis was aimed at proposing a first methodological approach to detect orchard damage by a storm based on the PolSAR decomposition technique using S1 data. The joint adoption of free accessible S1 data, institutional free auxiliary data (a cadastral map and farmers' CAP application database), and open software (SNAP) constituted a peculiar trait of the proposed approach. It moves in the direction of technological transfer, aiming at making SAR data/techniques an operational tool for agronomic applications, with special concern about weather-related damages to crops, which could be of interest to insurance companies or public administrations. The results proved that storm damages significantly increase the H and α parameters. By contrast, the A parameter tends to be lower in the damaged orchards. This phenomenon is possibly related to the changes affecting vegetation structure in the damaged fields, where the crowns and branches of fallen/broken plants fill the inter-row space, changing the regular pattern ordinarily characterizing apple orchards. Based on this evidence, the authors proposed a methodology to map possibly damaged orchards that relies on the knowledge about the behavior of witness (and neighboring) undamaged orchards. The method permitted the mapping of the probability that an orchard is damaged or not, constituting a new free tool able to improve orchard monitoring after a calamitous event by regional agencies and insurance companies. It is worth reminding that only apple orchards were considered for this case study. Future developments are expected to test the

effectiveness of this method in other orchard types, as pear or peach, which are very diffuse in the AOI.

References:

1. Hsiang, S.; Kopp, R.; Jina, A.; Rising, J.; Delgado, M.; Mohan, S.; Rasmussen, D.J.; Muir-Wood, R.; Wilson, P.; Oppenheimer, M. Estimating Economic Damage from Climate Change in the United States. Science 2017, 356, 1362–1369.

2. Nelson, G.C.; Valin, H.; Sands, R.D.; Havlík, P.; Ahammad, H.; Deryng, D.; Elliott, J.; Fujimori, S.; Hasegawa, T.; Heyhoe, E. Climate Change Effects on Agriculture: Economic Responses to Biophysical Shocks. Proc. Natl. Acad. Sci. USA 2014, 111, 3274–3279.

3. Moore, F.C.; Baldos, U.; Hertel, T.; Diaz, D. New Science of Climate Change Impacts on Agriculture Implies Higher Social Cost of Carbon. Nat. Commun. 2017, 8, 1–9.

4. FAO The Impact of Natural Hazards and Disasters on Agriculture and Food Security and Nutrition–A Call for Action to Build Resilient Livelihoods, Available online: http://www.fao.org/emergencies/resources/documents/resources-detail/zh/c/280784/. 2015, accessed: 20 December 2020.

5. Welbergen, J.A.; Klose, S.M.; Markus, N.; Eby, P. Climate Change and the Effects of Temperature Extremes on Australian Flying-Foxes. Proc. R. Soc. B. Biol. Sci. 2008, 275, 419–425.

6. Wang, E.; Bertis, B.L.; Jimmy, R.W.; Yu, Y. Simulation of Hail Effects on Crop Yield Losses for Corn-Belt States in USA. Trans. Chin. Soc. Agric. Eng. 2012, 28, 177–185.

7. Reighard, G.L.; Parker, M.L.; Krewer, G.W.; Beckman, T.G.; Wood, B.W.; Smith, J.E.; Whiddon, J. Impact of Hurricanes on Peach and Pecan Orchards in the Southeastern United States. HortScience 2001, 36, 250–252.

8. Crane, J.; Balerdi, C.; Campbell, R.; Campbell, C.; Goldweber, S. Managing Fruit Orchards to Minimize Hurricane Damage. HortTechnology 1994, 4, 21–27.

9. Notarnicola, B.; Tassielli, G.; Renzulli, P.A.; Castellani, V.; Sala, S. Environmental Impacts of Food Consumption in Europe. J. Clean. Prod. 2017, 140, 753–765.

10. Bos-Brouwers, H.E.J.; Graf, V.; Aramyan, L.; Oberc, B. Food Redistribution in the EU–Mapping and Analysis of Existing Regulatory and Policy Measures Impacting Food Redistribution from EU Member States. Available online: https://research.wur.nl/en/publications/food-redistribution-in-the-eu-mapping-and-analysis-of-existing-re, accessed: 20 De-cember 2020 .

11. FAO FAOSTAT. Available online: http://www.fao.org/faostat/en/#home (accessed on 13 November 2020).

12. Eccher, T.; Granelli, G. FRUIT QUALITY AND YIELD OF DIFFERENT APPLE CULTIVARS AS AFFECTED BY TREE DENSITY. Acta Hortic. 2006, 535–540, doi:10.17660/actahortic.2006.712.66

13. Childers, N.F.; Morris, J.R.; Sibbett, G.S. Modern Fruit Science. Orchard and Small Fruit Culture . Horticultural Publications. Gainesville, USA, 1995.

14. Lordan, J.; Gomez, M.; Francescatto, P.; Robinson, T.L. Long-Term Effects of Tree Density and Tree Shape on Apple Orchard Performance, a 20 Year Study–Part 2, Economic Analysis. Sci. Hortic. 2019, 244, 435–444.

15. Lauri, P. Apple Tree Architecture and Cultivation-a Tree in a System. In Proceedings of the I International Apple Symposium 1261;

ISHS Acta Horticulturae, Yangling, China, 2016; pp . 173–184.

16. Prabhakar, M.; Gopinath, K.A.; Reddy, A.G.K.; Thirupathi, M.; Rao, C.S. Mapping Hailstorm Damaged Crop Area Using Multispectral Satellite Data. Egypt. J. Remote Sens. Space Sci. 2019, 22, 73–79.

17. Botzen, W.J.W.; Bouwer, L.M.; Van den Bergh, J. Climate Change and Hailstorm Damage: Empirical Evidence and Implications for Agriculture and Insurance. Resour. Energy Econ. 2010, 32, 341–362.

18. Mandal, D.; Kumar, V.; Ratha, D.; Dey, S.; Bhattacharya, A.; Lopez-Sanchez, J.M.; McNairn, H.; Rao, Y.S. Dual Polarimetric Radar Vegetation Index for Crop Growth Monitoring Using Sentinel-1 SAR Data. Remote Sens. Environ. 2020, 247, 111954.

19. De Petris, S.; Berretti, R.; Guiot, E.; Giannetti, F.; Motta, R.; Borgogno-Mondino, E. Detection And Characterization of Forest Harvesting In Piedmont Through Sentinel-2 Imagery: A Methodological Proposal. Ann. Silvic. Res. 2020, 45, 92–98, doi:10.12899/asr-2018.

20. Sarvia, F.; De Petris, S.; Borgogno-Mondino, E. Remotely sensed data to support insurance strategies in agriculture. In Pro-ceedings of the Remote Sensing for Agriculture, Ecosystems, and Hydrology XXI. SPIE-Intl. Soc. Opt. Eng. 2019, 11149, 111491H.

21. Sarvia, F.; De Petris, S.; Borgogno-Mondino E. Multi-Scale Remote Sensing to Support Insurance Policies in Agriculture: From Mid-Term to Instantaneous Deductions. GIScience Remote Sens. 2020, 57, 770–784, doi:10.1080/15481603.2020.1798600.

22. Borgogno-Mondino, E.; Sarvia, F.; Gomarasca, M.A. Supporting Insurance Strategies in Agriculture by Remote Sensing: A Possible Approach at Regional Level. In Proceedings of the Lecture Notes in Computer Science; Springer Science and Business Media LLC: Berlin/Heidelberg, Germany, 2019; pp. 186–199

23. Sarvia, F.; De Petris, S.; Borgogno-Mondino, E. A Methodological Proposal to Support Estimation of Damages from Hailstorms Based on Copernicus Sentinel 2 Data Times Series. In Proceedings of the International Conference on Computational Science and Its Applications; Springer, Berlin/Heidelberg, Germany, 2020; pp. 737–751.

24. Sarvia, F.; Xausa, E.; Petris, S.D.; Cantamessa, G.; Borgogno-Mondino, E. A Possible Role of Copernicus Sentinel-2 Data to Support Common Agricultural Policy Controls in Agriculture. Agronomy 2021, 11, 110.

25. Boryan, C.; Yang, Z.; Mueller, R.; Craig, M. Monitoring US Agriculture: The US Department of Agriculture, National Agri-cultural Statistics Service, Cropland Data Layer Program. Geocarto Int. 2011, 26, 341–358.

26. López-Lozano, R.; Duveiller, G.; Seguini, L.; Meroni, M.; García-Condado, S.; Hooker, J.; Leo, O.; Baruth, B. Towards Regional Grain Yield Forecasting with 1 Km-Resolution EO Biophysical Products: Strengths and Limitations at Pan-European Level. Agric. For. Meteorol. 2015, 206, 12–32.

27. Chipanshi, A.; Zhang, Y.; Kouadio, L.; Newlands, N.; Davidson, A.; Hill, H.; Warren, R.; Qian, B.; Daneshfar, B.; Bedard, F. Evaluation of the Integrated Canadian Crop Yield Forecaster (ICCYF) Model for in-Season Prediction of Crop Yield across the Canadian Agricultural Landscape. Agric. For. Meteorol. 2015, 206, 137–150.

28. de Wit, A.; Duveiller, G.; Defourny, P. Estimating Regional Winter Wheat Yield with WOFOST through the Assimilation of Green Area Index Retrieved from MODIS Observations. Agric. For. Meteorol. 2012, 164, 39–52.

29. Doraiswamy, P.C.; Sinclair, T.R.; Hollinger, S.; Akhmedov, B.; Stern, A.; Prueger, J. Application of MODIS Derived Parameters for Regional Crop Yield Assessment. Remote Sens. Environ. 2005, 97, 192–202.

30. Chen, Y.; Zhang, Z.; Tao, F. Improving Regional Winter Wheat Yield Estimation through Assimilation of Phenology and Leaf Area Index from Remote Sensing Data. Eur. J. Agron. 2018, 101, 163–173.

31. Patel, N.R.; Bhattacharjee, B.; Mohammed, A.J.; Tanupriya, B.; Saha, S.K. Remote Sensing of Regional Yield Assessment of Wheat in Haryana, India. Int. J. Remote Sens. 2006, 27, 4071–4090.

32. Orusa, T.; Orusa, R.; Viani, A.; Carella, E.; Borgogno Mondino, E. Geomatics and EO Data to Support Wildlife Diseases As-sessment at Landscape Level: A Pilot Experience to Map Infectious Keratoconjunctivitis in Chamois and Phenological Trends in Aosta Valley (NW Italy). Remote Sens. 2020, 12, 3542.

33. Ulaby, F.T.; Moore, R.K.; Fung, A.K. Microwave Remote Sensing: Active and Passive. Volume 1-Microwave Remote Sensing Fundamentals and Radiometry. 1981.

34. Ulaby, F. Radar Response to Vegetation. IEEE Trans. Antennas Propag. 1975, 23, 36–45.

35. McNairn, H.; Shang, J. A review of multitemporal synthetic aperture radar (SAR) for crop monitoring. In Multitemporal Remote Sensing; Springer, Berlin, Germany, 2016; pp. 317–340.

36. Karagiannopoulou, A.; Tsiakos, C.; Tsimiklis, G.; Tsertou, A.; Amditis, A.; Milcinski, G.; Vesel, N.; Protic, D.; Kilibarda, M.; Tsakiridis, N. An Integrated Service-Based Solution Addressing the Modernised Common Agriculture Policy Regulations and Environmental Perspectives. In Proceedings of the Remote Sensing for Agriculture, Ecosystems, and Hydrology XXII; International Society for Optics and Photonics, Bellingham, USA, 2020; Volume 11528, p. 115280C.

37. Kanjir, U.; DJurić, N.; Veljanovski, T. Sentinel-2 Based Temporal Detection of Agricultural Land Use Anomalies in Support of Common Agricultural Policy Monitoring. ISPRS Int. J. Geo-Inf. 2018, 7, 405.

38. Lee, J.-S.; Grunes, M.R.; Pottier, E. Quantitative Comparison of Classification Capability: Fully Polarimetric versus Dual and Single-Polarization SAR. IEEE Trans. Geosci. Remote Sens. 2001, 39, 2343–2351.

39. Ainsworth, T.L.; Kelly, J.P.; Lee, J.-S. Classification Comparisons between Dual-Pol, Compact Polarimetric and Quad-Pol SAR Imagery. ISPRS J. Photogramm. Remote Sens. 2009, 64, 464–471.

40. Boerner, W.-M.; Mott, H.; Luneburg, E. Polarimetry in Remote Sensing: Basic and Applied Concepts. In Proceedings of the IGARSS'97. 1997 IEEE International Geoscience and Remote Sensing Symposium Proceedings. Remote Sensing-A Scientific Vision for Sustainable Development Singapore, 3–8 August 1997; Volume 3, pp. 1401–1403.

41. Cloude, S.R.; Pottier, E. An Entropy Based Classification Scheme for Land Applications of Polarimetric SAR. IEEE Trans. Geosci. Remote Sens. 1997, 35, 68–78.

42. Cloude, S.R.; Pottier, E. A Review of Target Decomposition Theorems in Radar Polarimetry. IEEE Trans. Geosci. Remote Sens. 1996, 34, 498–518.

43. Nasirzadehdizaji, R.; Balik Sanli, F.; Abdikan, S.; Cakir, Z.; Sekertekin, A.; Ustuner, M. Sensitivity Analysis of Multi-Temporal Sentinel-1 SAR Parameters to Crop Height and Canopy Coverage. Appl. Sci. 2019, 9, 655.

44. Betbeder, J.; Fieuzal, R.; Philippets, Y.; Ferro-Famil, L.; Baup, F. Contribution of Multitemporal Polarimetric Synthetic Ap-erture Radar Data for Monitoring Winter Wheat and Rapeseed Crops. J. Appl. Remote Sens. 2016, 10, 026020.

45. Valcarce-Diñeiro, R.; Arias-Pérez, B.; Lopez-Sanchez, J.M.; Sánchez, N. Multi-Temporal Dual-and Quad-Polarimetric Synthetic Aperture Radar Data for Crop-Type Mapping. Remote Sens. 2019, 11, 1518.

46. Mercier, A.; Betbeder, J.; Baudry, J.; Le Roux, V.; Spicher, F.; Lacoux, J.; Roger, D.; Hubert-Moy, L. Evaluation of Sentinel-1 & 2 Time Series for Predicting Wheat and Rapeseed Phenological Stages. ISPRS J. Photogramm. Remote Sens. 2020, 163, 231–256.

47. Qi, Z.; Yeh, A.G.-O.; Li, X. A Crop Phenology Knowledge-Based Approach for Monthly Monitoring of Construction Land Expansion Using Polarimetric Synthetic Aperture Radar Imagery. ISPRS J. Photogramm. Remote Sens. 2017, 133, 1–17.

48. Zhao, L.; Yang, J.; Li, P.; Shi, L.; Zhang, L. Characterizing Lodging Damage in Wheat and Canola Using Radarsat-2 Polarimetric SAR Data. Remote Sens. Lett. 2017, 8, 667–675.

49. Yang, H.; Chen, E.; Li, Z.; Zhao, C.; Yang, G.; Pignatti, S.; Casa, R.; Zhao, L. Wheat Lodging Monitoring Using Polarimetric Index from RADARSAT-2 Data. Int. J. Appl. Earth Obs. Geoinf. 2015, 34, 157–166.

50. Dickinson, C.; Siqueira, P.; Clewley, D.; Lucas, R. Classification of Forest Composition Using Polarimetric Decomposition in Multiple Landscapes. Remote Sens. Environ. 2013, 131, 206–214, doi:10.1016/j.rse.2012.12.013.

51. Trisasongko, B.H. The Use of Polarimetric SAR Data for Forest Disturbance Monitoring. Sens. Imaging 2010, 11, 1–13, doi:10.1007/s11220-010-0048-8.

52. Le Toan, T.; Beaudoin, A.; Riom, J.; Guyon, D. Relating Forest Biomass to SAR Data. IEEE Trans. Geosci. Remote Sens. 1992, 30, 403–411.

53. Ruiz, J.S.; Ordonez, Y.F.; McNairn, H. Corn Monitoring and Crop Yield Using Optical and Microwave Remote Sensing. Geosci. Remote Sens. 2008, 10, 405–420.

54. Mandal, D.; Kumar, V.; Lopez-Sanchez, J.M.; Bhattacharya, A.; McNairn, H.; Rao, Y.S. Crop Biophysical Parameter Retrieval from Sentinel-1 SAR Data with a Multi-Target Inversion of Water Cloud Model. Int. J. Remote Sens. 2020, 41, 5503–5524.

55. Lee, J.-S.; Grunes, M.R.; Ainsworth, T.L.; Du, L.-J.; Schuler, D.L.; Cloude, S.R. Unsupervised Classification Using Polarimetric Decomposition and the Complex Wishart Classifier. IEEE Trans. Geosci. Remote Sens. 1999, 37, 2249–2258.

56. Freeman, A.; Durden, S.L. A Three-Component Scattering Model for Polarimetric SAR Data. IEEE Trans. Geosci. Remote Sens. 1998, 36, 963–973.

57. Ji, K.; Wu, Y. Scattering Mechanism Extraction by a Modified Cloude-Pottier Decomposition for Dual Polarization SAR. Remote Sens. 2015, 7, 7447–7470.

58. McNairn, H.; Shang, J.; Jiao, X.; Champagne, C. The Contribution of ALOS PALSAR Multipolarization and Polarimetric Data to Crop Classification. IEEE Trans. Geosci. Remote Sens. 2009, 47, 3981–3992.

59. Lopez-Sanchez, J.M.; Cloude, S.R.; Ballester-Berman, J.D. Rice Phenology Monitoring by Means of SAR Polarimetry at X-Band. IEEE Trans. Geosci. Remote Sens. 2011, 50, 2695–2709.

60. Ramsey III, E.; Rangoonwala, A.; Suzuoki, Y.; Jones, C.E. Oil Detection in a Coastal Marsh with Polarimetric Synthetic Aperture Radar (SAR). Remote Sens. 2011, 3, 2630–2662.

61. Yonezawa, C.; Watanabe, M.; Saito, G. Polarimetric Decomposition Analysis of ALOS PALSAR Observation Data before and after a Landslide Event. Remote Sens. 2012, 4, 2314–2328.

62. Cloude, S.R. The Dual Polarisation Entropy/Alpha Decomposition. In Proceedings of the Proceedings of the 3rd International Workshop on Science and Applications of SAR Polarimetry and Polarimetric Interferometry, Noordwijk, The Netherlands; 2007; pp. 22–26.

63. Ghods, S.; Shojaedini, S.V.; Maghsoudi, Y. A Modified H- α Classification Method for Dcp Compact Polarimetric Mode by Reconstructing Quad h and α Parameters from Dual Ones. IEEE J. Sel. Top. Appl. Earth Obs. Remote Sens. 2016, 9, 2233–2241.

64. ISTAT ISTAT Data Available online: http://dati.istat.it/ (accessed on 13 November 2020).

65. Mandal, D.; Vaka, D.S.; Bhogapurapu, N.R.; Vanama, V.S.K.; Kumar, V.; Rao, Y.S.; Bhattacharya, A. Sentinel-1 SLC Prepro-cessing Workflow for Polarimetric Applications: A Generic Practice for Generating Dual-Pol Covariance Matrix Elements in SNAP S-1 Toolbox. 2019.

66. Lee, J.-S.; Pottier, E. Polarimetric Radar Imaging: From Basics to Applications; CRC Press, Boca Raton, FL, USA, 2017.

67. Shan, Z.; Wang, C.; Zhang, H.; Chen, J. H-Alpha Decomposition and Alternative Parameters for Dual Polarization SAR Data. In proceedings of the PIERS proceedings, SuZhou, China, 12–16 September 2011.

68. Veci, L.; Prats-Iraola, P.; Scheiber, R.; Collard, F.; Fomferra, N.; Engdahl, M. The Sentinel-1 Toolbox. In Proceedings of the Proceedings of the IEEE International Geoscience and Remote Sensing Symposium (IGARSS); Quebec City, QC, Canada, 13–18 July2014; pp. 1–3.

69. Ainsworth, T.L.; Kelly, J.; Lee, J.-S. Polarimetric Analysis of Dual Polarimetric SAR Imagery. In Proceedings of the 7th Eu-ropean Conference on Synthetic Aperture Radar; VDE, Friedrichshafen, Germany, 2008 ; pp. 1–4.

70. Crabbe, R.A.; Lamb, D.W.; Edwards, C.; Andersson, K.; Schneider, D. A Preliminary Investigation of the Potential of Sentinel-1 Radar to Estimate Pasture Biomass in a Grazed Pasture Landscape. Remote Sens. 2019, 11, 872.

71. Chang, J.; Shoshany, M. Radar Polarization and Ecological Pattern Properties across Mediterranean-to-Arid Transition Zone. Remote Sens. Environ. 2017, 200, 368–377.

72. Chang, J.G.; Shoshany, M.; Oh, Y. Polarimetric Radar Vegetation Index for Biomass Estimation in Desert Fringe Ecosystems. IEEE Trans. Geosci. Remote Sens. 2018, 56, 7102–7108.

73. Cloude, S. Polarisation: Applications in Remote Sensing; OUP Oxford, 2009;

74. Raney, R.K.; Cahill, J.T.; Patterson, G.W.; Bussey, D.B.J. The M-Chi Decomposition of Hybrid Dual-Polarimetric Radar Data with Application to Lunar Craters. J. Geophys. Res. Planets 2012, 117, doi:10.1029/2011JE003986

75. Borgogno Mondino, E.; Fissore, V.; Lessio, A.; Motta, R. Are the New Gridded DSM/DTMs of the Piemonte Region (Italy) Proper for Forestry? A Fast and Simple Approach for a Posteriori Metric Assessment. iFor. Biogeosci. For. 2016, 9, 901–909, doi:10.3832/ifor1992-009.

76. Nachar, N. The Mann-Whitney U: A Test for Assessing Whether Two Independent Samples Come from the Same Distribution. Tutor. Quant. Methods Psychol. 2008, 4, 13–20.

77. Hollander, M.; Wolfe, D.A.; Chicken, E. Nonparametric Statistical Methods; John Wiley & Sons, Hoboken, NJ, USA, 2013; Volume 751.

78. R Development Core Team, R. R: A Language and Environment for Statistical Computing; R Foundation for Statistical Computing Vienna, Austria, 2013.

79. Conrad, O.; Bechtel, B.; Bock, M.; Dietrich, H.; Fischer, E.; Gerlitz, L.; Wehberg, J.; Wichmann, V.; Böhner, J. System for Au-tomated Geoscientific Analyses (SAGA) v. 2.1. 4. Geosci. Model Dev. Discuss. 2015, 8, 1991–2007.

80. Wallis, W.A. Compounding Probabilities from Independent Significance Tests. Econom. J. Econom. Soc. 1942, 10, 229–248.

81. Zliobaite, I. On the Relation between Accuracy and Fairness in Binary Classification. a rXiv 2015, arXiv:1505.05723.

82. Akosa, J. Predictive Accuracy: A Misleading Performance Measure for Highly Imbalanced Data. In Proceedings of the Pro-ceedings of the SAS Global Forum; Orlando, USA, 2017; pp. 2–5.

83. Guo, X.; Yin, Y.; Dong, C.; Yang, G.; Zhou, G. On the Class Imbalance Problem. In Proceedings of the 2008 Fourth International Conference on Natural Computation; IEEE, Jinan, China, 20 08; Volume 4, pp. 192–201.

5 VEGETATION STRUCTURE QUANTIFICATION

5.1 PRECISION OF THE REFERENCE SURVEYS

5.1.1 About Tree Height Measurement: Theoretical and Practical Issues for Uncertainty Quantification and Mapping

De Petris Samuele[a*], Sarvia Filippo[a], and Borgogno- Mondino Enrico[a]

[a]Department of Agricultural, Forest and Food Sciences (DISAFA), University of Turin, 10095 Grugliasco, Italy.

*Correspondence: samuele.depetris@unito.it

Published: 2022 in *Forests*. IF (2021): 3.282

Abstract: Forest height is a fundamental parameter in forestry. Tree height is widely used to assess site's productivity both in forest ecology research and forest management. Thus, a precise height measure represents a necessary step for the estimation of carbon storage at local, national, and global scales. In this context, error in height measurement necessarily affects the accuracy of related estimates. Ordinarily, forest height is surveyed by ground sampling adopting hypsometers. The latter suffers from many errors mainly related to the correct tree apex identification (not always well visible in dense stands) and to the measurement process itself. In this work, a statistically based operative method for estimating height measurement uncertainty (σ_H) was proposed using the variance propagation law. Some simulations were performed involving several combinations of terrain slope, tree height and survey distances by modelling the σ_H behaviour and its sensitivity to such parameters. Results proved that σ_H could vary between 0.5 m up to 20 m (worst case). Sensitivity analysis shows that terrain slopes and distance poorly affect σ_H, while angles are the main drivers of height uncertainty. Finally, to give a practical example of such deductions, tree height uncertainty was mapped at the global scale using Google Earth Engine and summarized per forest biomes. Results proved that tropical biomes have higher uncertainty (from 1 m to 4 m) while shrublands and tundra the lowest (under 1 m).

Keywords: Tree Height Uncertainty; Hypsometer; Forest Biomes; Variance Propagation Law; Google Earth Engine.

1. Introduction

Tree height (H) is a fundamental measure in forestry. It is strictly related to above-ground biomass [1,2] and canopy vertical structure [3–5]. H is also the most used parameters to assess site's productivity, not only in forest ecology research, but also in forest management [6–8]. In fact, it is often used to define forest cover [9], to assess timber quality [10] and forest ecosystem services like forest protection against natural hazard [11] or biodiversity [12,13]. Moreover, it can be a good proxy of forest status and it is helpful in forecasting stand development and succession [14]. Nowadays, forests have a crucial role in greenhouse gas sequestration [15] and in carbon market [16] highlighting the need of accurate tree measuring. For example, for forest inventories purposes height measurement is the most important factor, along with diameter at breast height, in estimating stand volume [17–19]. Thus, a precise forest volume computation represents a necessary step for the estimation of carbon storage at local, national, and global scales. In this context, error in height measurement necessarily affects the accuracy of related estimates. Moreover, tree height surveyed at the ground are usually assumed as reference data to evaluate the accuracy of the remote deductions like the ones derived by geomatics techniques like: satellite remote sensing, light detection and ranging (LiDAR) and photogrammetry [20–22]. Ordinarily, forest height is surveyed by ground sampling adopting hypsometers [23]. The latter are lightweight instruments that can perform angular and distance measurements from which, by applying trigonometric principles, tree height is computed [24,25]. This method suffers from many errors mainly related to the correct tree apex identification (not always well visible in dense stands) and to the measurement process itself [26]. For operative reasons, in fact, hypsometric measurement is carried out without fixed supports. The hand motion during treetop/bottom collimation affects the accuracy of the angular measurement and consequently the height one [26]. In addition, operational conditions such as: measuring distances, terrain slope, stem curvature, crown shape, can further affect the hypsometric measurements introducing errors hardly to detect and fix.

Nevertheless, hypsometers constitute the standard instrument for dendrometric surveys especially for forest and urban inventory purposes [27,28].

In this framework, tree height uncertainty is not ordinarily considered by users raising some doubts about the accuracy of related forest estimates [29]. A quantification of the potential uncertainty of tree height is, therefore, essential to assess the reliability of deductions alerting the user about the significance of difference that one could test between forest stands (or single tree) or between the same stand at different time. The uncertainty knowledge is desirable especially if tree height is adopted as reference data to estimate timber volume, above-ground biomass or carbon sink in the plant. Unfortunately, literature about the accuracy of tree height estimates by hypsometer is very limited. Although many works compared tree height derived by different instruments [6,30–33], no work can be currently found in literature about how hypsometer-based procedure affects the final estimates. In fact, for a great number of applications there is no possibility to obtain low-cost validations concerning tree heights. This could be probably due to the fact that, while measuring tree height no reference data exists for a-posteriori validation, that can be only achieved by comparing more instruments suppose showing higher accuracy. Unfortunately, this procedure requires that height survey is made contemporarily using different instruments or by cutting the tree or climbing by expensive experimental campaigns. Literature is not so exhaustive concerning this issue [26,34,35]. However, no specific work can be found concerning a comprehensive study of theoretical uncertainty affecting tree height by indirect measurements (like the ones obtained by hypsometers). A validation based on reference datasets would be required, for example for very accurate and reliable measurements the use of height poles/sticks with climbing is mostly used method by re-searchers and arborists [32,36]. Although this was possible (albeit expensive) for research purposes, it would be no longer applicable for operative purposes. The only alternative is therefore to model the expected theoretical uncertainty.

In the proposed study, a statistically based operative method for estimating height measurement uncertainty was proposed using the variance propagation law (VPL) [37]. VPL uses the accuracies of direct measurements (in this work angles and distances), assumed to be known, to estimate the theoretical variance of the indirect measurement (in this work the tree height). Some simulations were performed involving several combinations of terrain slope, tree height and distances by modelling the behaviour of height un-certainty and its sensitivity to such parameters. The results have been summarized in graphs that constitute an operational tool giving an estimate of the uncertainty of tree height and assess its goodness compared to the expected application avoiding tree cut or climbing on. Finally, to give a practical example of such deductions tree height uncertain-ty was mapped at the global scale using Google Earth Engine (GEE) and summarized per forest biomes.

2. Materials and Methods

The workflow adopted in this work is reported in figure 1. Using field surveys, the angular error of hypsometer was modelled. Subsequently, tree height uncertainty was modelled by VPL and a sensitivity analysis of this model performed. Some theoretical scenarios were given to explore tree uncertainty behaviour under different environmental and operative conditions. Finally, to give a practical interpretation of theoretical deductions, using Google Earth Engine (GEE) platform the height uncertainty at the global scale was mapped and summarized according to forest biomes.

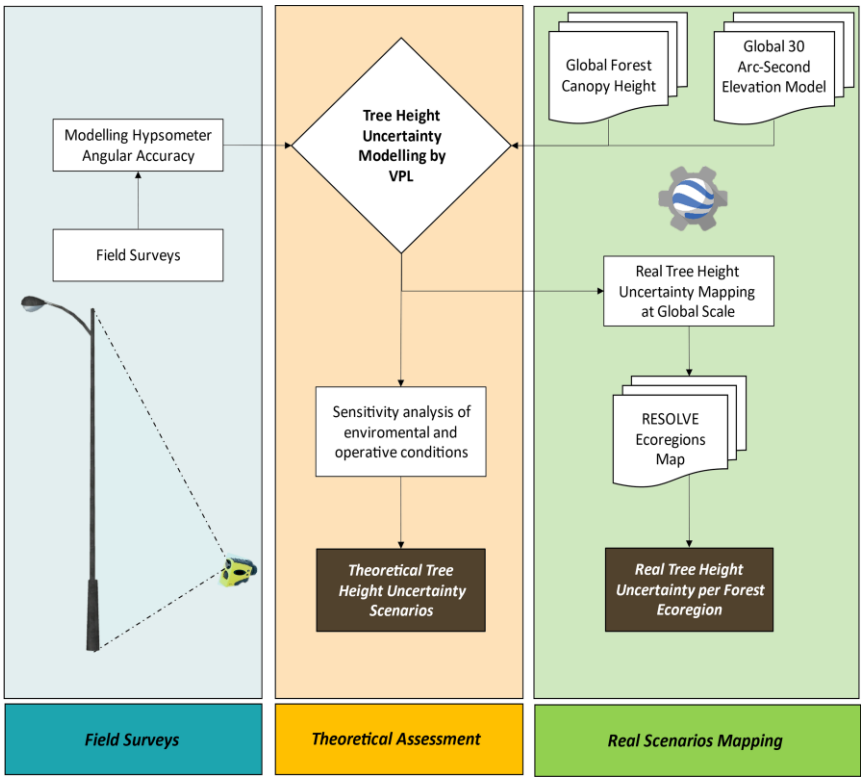

Figure 1. Workflow adopted. Starting from field surveys, the hypsometer accuracy was modelled. Theoretical evaluations were performed concerning the formalization of tree height uncertainty model. Subsequently a sensitivity analysis and theoretical scenarios were provided. Finally, globally available data in GEE was used to explore real tree height uncertainty for each forest ecoregion.

2.1. Available Data

2.1.1. Experimental Design of Field Surveys

Hypsometric measures are ordinarily performed with no fixed support thus introducing a variability due to operator's hand motion in collimation that affects angle measures. The controlled laboratory environment provided an important test for bias, but could not provide a realistic evaluation of instrument performance under field conditions [6]. The latter is affected by three kinds of uncertainty: instrumental, environmental and operative uncertainty. The first one, is related to instrumental feature/quality and can be estimated in laboratory. The second one, is related to environmental conditions like: terrain slope, air moisture, temperature, tree apex visibility, tree stem shape and inclination. Unfortunately,

these conditions cannot be directly controlled by user during the survey. Otherwise, operative conditions like slant range (SR) between tree and instrument can be managed by operator and properly set to optimize final accuracy. Nevertheless, due to terrain asperity or cost/time-related limitations, operative conditions are often not properly considered and addressed. All these issues deeply affect the angular measures of hypsometer reflecting into not neglectable errors in tree height computation. Currently, very few works about angular accuracy of forest hypsometers are present in literature. Trying to fill this lack, in this work, a reference light pole was used to test the precision of the hypsometer angle measures under operative conditions. The choice of adopting a static and invariant object like a light pole, moves deductions from a particular context to general one. This is mainly related to the well-known and objective operational difficulty of selecting the proper apex of a tree (especially from different users). For this reason, we repeated our experiment with reference to a pole located in a flat and open area. It is worth to remind that repetition from different users was differently aimed at providing a more robust estimate of actual instrument uncertainty completing the one supplied by producer with the one related to the user (that has to be intended as part of the instrument). It is obvious that provided estimates will be "optimistic" since, operationally speaking, one has, for example, to consider that the apex of the tree is not so unique to be defined as the apex of a pole. A light pole, having a height of 15 m, placed in the Campus of Department of Agriculture, Forest and Food Sciences of Torino University (NW Italy, 45° 3'55.38"N - 7°35'30.61"E) was selected. It is isolated and therefore its apex well visible from the ground. The pole is not inclined and terrain slope around is lower than 5°. The TruPulse 200/B laser rangefinder was used. It operates through a laser (near infrared pulse) coupled to a tilt sensor. TruPulse has nominal slant range accuracy (σ_{SR}) equal to 1 m and angular accuracy (σ_{ang}) equal to 0.25° [38]. Before the survey, tilt sensor was calibrated according to manual requirements. Four expert operators performed pole height surveys according to the follows experimental design (Fig. 2). Angle measures (respectively pointing at pole top and pole bottom) were surveyed three times per operator moving

around the pole along 3 geographical directions (N, SW, SE) placed at 120° to each other. For each direction, SR changes from 10 m to 40 m with 10 m steps. It is worth to highlight that, additional measurements were operated by positioning the instrument in open field and pointing the laser of the TruPulse towards a reflecting signal placed closed to the pole (at 1.6 m from ground) in order to measure and compensate for the terrain slope contribution. Then, angles collimating top (θ) and bottom (α) were surveyed. A total of 144 height surveys and 288 angle measures were performed over the same pole.

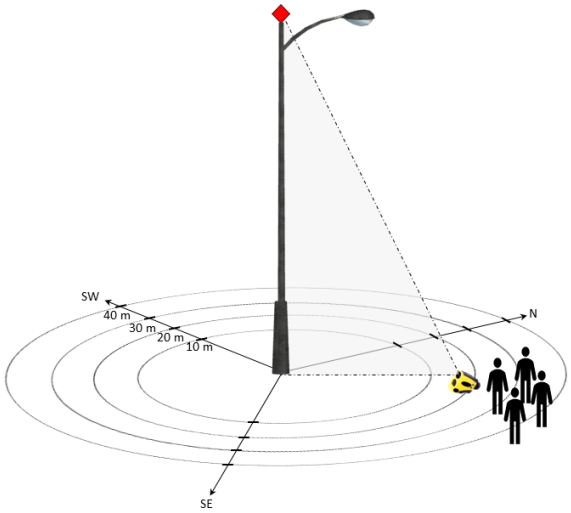

Figure 2. Experimental design adopted in this work involving 4 operators. Three geographic al direction placed at 120° apart were used pointing to the: North, South-Est and South-West. For each position 3 replica were measured. Red rhombus is the pole top collimated during the height survey placed at 10 m, 20 m ,30 m, 40 m distance respectively.

2.1.2. Geographical Data

The Global Forest Canopy Height (GFCH) represents global tree heights based on a fusion of spaceborne-lidar data from the Geoscience Laser Altimeter System (GLAS) and ancillary geospatial data [39]. GFCH is provided in GEE as raster layer having a geometric resolution of 1 km and updated in 2005. The accuracy in forest height estimation ranges between 3.8 m to 6 m according to forest types [39,40]. The Global 30 Arc-Second Elevation (GTOPO30) is a global digital elevation model (DEM) with geometric resolution of about 1 km. The DEM was derived from several raster and vector sources of topographic information and

was updated in 1996 [41]. Currently, it represents the only available DEM in GEE covering the entire globe including high latitude zones (i.e. Boreal, Artic and Antarctic zones). In order to explore and summarize tree height uncertainty over the world, the RE-SOLVE Ecoregions map (REM) was adopted in GEE. REM is a vector layer representing about 476 forested ecoregions grouped in 14 forests biomes. It is updated in 2017 and is the most update dataset on remaining habitat in each terrestrial ecoregion [42]. Table 1 reports the REM biomes and the code adopted in this work.

Table 1. Forest biomes present in the RESOLVE Ecoregions map.

Biomes	***Code (ID)***
Tropical and Subtropical Moist broadleaf Forests	B1
Montane Grassland and Shrublands	B10
Tundra	B11
Mediterranean Forests, Woodlands, and Scrub	B12
Deserts and Xeric Shrublands	B13
Mangroves	B14
Tropical and Subtropical Dry broadleaf Forests	B2
Tropical and Subtropical Coniferous Forests	B3
Temperate Broadleaf and Mixed Forests	B4
Temperate Conifer Forests	B5
Boreal Forests or Taiga	B6
Tropical and Subtropical Grassland, Savannas, and Shrublands	B7
Temperate Grassland, Savannas, and Shrublands	B8
Flooded Grassland and Savannas	B9

2.2. Data Processing

2.2.1. Uncertainty Modelling

Tree height measurement by hypsometer is effective and widely used in forestry being the standard and reference procedure to validate measures from remote sensing. Tree height uncertainty is not ordinarily considered by users [43]; conversely, it could proficiently support deductions, especially to assess significant differences in both spatial and time domain. A quantification of the potential uncertainty of tree height is, therefore, essential to support the reliability of deductions especially if tree height is adopted as reference data to estimate wood volume, above-ground biomass or carbon stocked. Although a precise reference value can be obtained for research purposes, it would be no longer applicable for operative purposes. The only alternative is therefore to model the

expected theoretical uncertainty. The variance propagation law (VPL - eq.1) is the statistical tool that ordinarily can be used for this task [37]. It models the effect of variance (ordinarily assumed as indicator of squared precision) of direct measures (i.e. angular and distance measures) onto the variance of the derived measures (i.e. tree height)

$$\sigma_y^2 = \left(\frac{\partial y}{\partial x_1}\right)^2 \cdot \sigma_{x_1}^2 + \left(\frac{\partial y}{\partial x_2}\right)^2 \cdot \sigma_{x_2}^2 + \cdots + \left(\frac{\partial y}{\partial x_n}\right)^2 \cdot \sigma_{x_n}^2 + 2\sum_{i=1}^{n-1}\sum_{j=i+1}^{n}\left(\frac{\partial y}{\partial x_i}\right)\left(\frac{\partial y}{\partial x_j}\right) COV(i,j) \quad (1)$$

where $y = f(x_1, x_2, \ldots, x_n)$ is the dependent variable, xi the independent ones and $\sigma_{x_i}^2$ their variance (supposed known); $COV(i,j)$ is the covariance between the i-th and j-th independent variables. The starting point to successfully operate with VPL is to define the model formula it has to be applied to. Ordinarily, tree height is computed by hypsometer according to eq. 2 following the procedure summarized in figure 3.

$$H = (SR \cdot \cos\varphi) \cdot (\tan\theta + \tan\alpha) \quad (2)$$

Where SR is the slant range between tree stem and operator; φ is the terrain slope measured by pointing the reflecting pole near trunk at operator eye level (here set 1.6 m); θ and α are the angles derived by the collimation of tree top and tree bottom respectively.

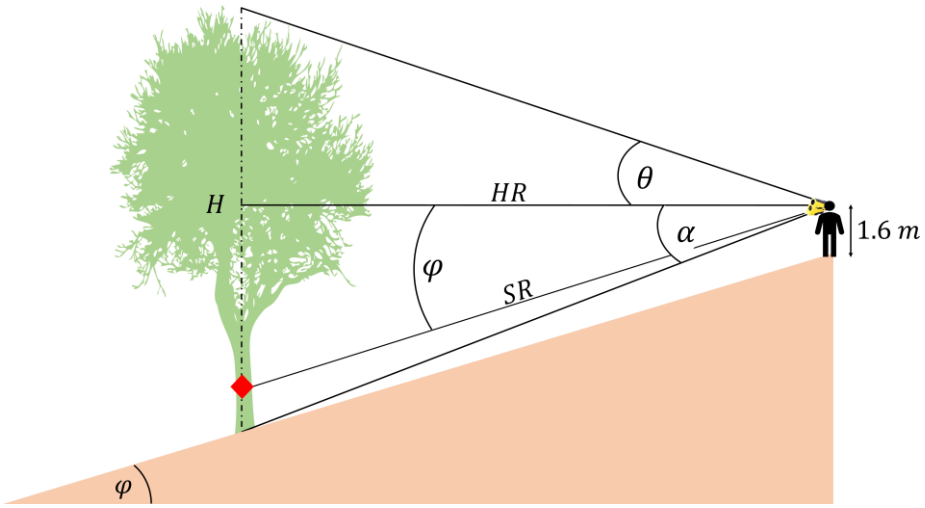

Figure 3. Reference framework involved during hypsometer survey. H is the tree height above-ground; φ is the terrain slope measured by pointing the rangefinder to the reflecting pole near the trunk (red rhomb); SR is the slant range (tree-operator distance) and HR is the horizontal distance; θ and α are the angles measured by tilt sensor (digital clinometer) collimating tree top and tree bottom respectively. For this work, operator height is fixed at 1.6 m.

Direct measures involved in H computation are the angles and distance measures (i.e. φ, θ , α and SR); consequently H uncertainty (σ_H - eq. 3) can be computed applying eq. 1 to eq.2 considering that trigonometric relationships exist between variables.

$$\sigma_H = \sqrt{\begin{array}{c}\left(\frac{\partial H}{\partial SR}\right)^2 \sigma_{SR}^2 + \left(\frac{\partial H}{\partial \varphi}\right)^2 \sigma_{\varphi}^2 + \left(\frac{\partial H}{\partial \alpha}\right)^2 \sigma_{\alpha}^2 + \left(\frac{\partial H}{\partial \theta}\right)^2 \sigma_{\theta}^2 \\ +2\left(\frac{\partial H}{\partial SR}\right)\left(\frac{\partial H}{\partial \alpha}\right) COV(SR,\alpha) + 2\left(\frac{\partial H}{\partial SR}\right)\left(\frac{\partial H}{\partial \theta}\right) COV(SR,\theta)\end{array}} \quad (3)$$

Where partial derivatives involved in eq. 3 are reported in table 2. Precision values are: σ_{SR} the uncertainty of laser rangefinder assumed equal to the nominal one (i.e. 1 m); σ_{φ}, σ_{θ} and σ_{α} are the uncertainties of hypsometer angles. Despite the same instrument was used, angles measured are affected by different factors. For this reason, in this work, above-mentioned precision and covariance values were explored and estimated separately.

Table 2. Partial derivatives involved in equation 3.

Partial derivatives
$\frac{\partial H}{\partial SR} = \cos\varphi\,(\tan\theta + \tan\alpha)$
$\frac{\partial H}{\partial \varphi} = -(SR\,\sin\varphi)(\tan\theta + \tan\alpha)$
$\frac{\partial H}{\partial \alpha} = (SR\,\cos\varphi)\,(\tan^2\alpha + 1)$
$\frac{\partial H}{\partial \theta} = (SR\,\cos\varphi)\,(\tan^2\theta + 1)$

In fact, hypsometer angles uncertainty is affected by two main components and can be linearly modelled similarly to other topographic instruments [44,45]. The first is a constant term (intercept - β_0) related to the instrument accuracy itself and assumed equal for φ, θ and α. While the second one is related to operator collimation accuracy (gain - β_i) mainly dependent from SR and hand stability. Since β_0 can be estimate in laboratory, it is ordinarily provided by the producer. In this work, using TruPulse 200B, β_0 it was assumed equal to σ_{ang}, while β_i was properly calibrated using ordinary least squares involving angular measure derived from field surveys. According to previous mentioned experimental design, at each position three replica were acquired and related standard deviation computed and assumed as precision of angular measure probably related to hand operator stability. Then, precision values were fitted against the SR. Finally, β_i concerning θ and α were modelled by a power model ($\beta_i = aSR^b$) and σ_θ and σ_α computed (eq. 4 and eq. 5). Furthermore, the Mean Absolute Percentage Error (MAPE) was computed involving the residuals of regressions (power models part in eq. 4 and eq. 5). Since MAPE values are computed by removing the SR dependence from angle precision models, the remaining error component could be probably due to operator variability (i.e. hand motion and collimation accuracy). Concerning φ, it is ordinary measured without the operator collimation process but simply by pointing laser to reflecting pole. Therefore, σ_φ can be assumed equal to β_0.

$$\sigma_\theta = \beta_0 + aSR^b \quad (4)$$

$$\sigma_\alpha = \beta_0 + cSR^d \quad (5)$$

Where a, b, c and d are the model coefficients. Moreover, the covariance between θ and SR, $cov(\theta, SR)$, and covariance between α and SR, $cov(\alpha, SR)$, were computed using filed surveys involving a total of 288 angle measures. A sensitivity analysis was then performed to explore how different variables mainly affect σ_H. Some scenarios were run varying H values from 5 m to 40 m, changing φ values from 5° to 45° and SR from 10 m to 50 m using eq. 3. Then, σ_H behaviour was explored by plotting φ and SR trends parametrizing resulting functions by H values. A final scenario was computed using eq. 3, setting φ = 15° and all possible combination of H and SR in σ_H computation. The analysis requires that the above-mentioned formulas are computed using the expected angular values corresponding to a certain tree height. This can be obtained once tree height, SR, operator's height, terrain slope are known. It is worth to noting that precision values involved in eq. 3, once propagated by VPL, contribute differently to final H variance. Therefore, we measured the relative weight (importance) of each factor variance on H variance according to formula reported in table 2 and changing SR from 5 m to 50 m.

Table 3. Relative weights affecting variance of H.

Factor	*Formula*
Sum of weights	$\Sigma = \left(\frac{\partial H}{\partial SR}\right)^2 + \left(\frac{\partial H}{\partial \varphi}\right)^2 + \left(\frac{\partial H}{\partial \alpha}\right)^2 + \left(\frac{\partial H}{\partial \theta}\right)^2 + 2\left(\frac{\partial H}{\partial SR}\right)\left(\frac{\partial H}{\partial \alpha}\right) COV(SR, \alpha) + 2\left(\frac{\partial H}{\partial SR}\right)\left(\frac{\partial H}{\partial \theta}\right) COV(SR, \theta)$
Slant Range	$w_{SR} = \frac{\left(\frac{\partial H}{\partial SR}\right)^2}{\Sigma}$
Terrain slope	$w_{\varphi} = \frac{\left(\frac{\partial H}{\partial \varphi}\right)^2}{\Sigma}$
Angle pointing tree bottom	$w_{\alpha} = \frac{\left(\frac{\partial H}{\partial \alpha}\right)^2}{\Sigma}$
Angle pointing tree apex	$w_{\theta} = \frac{\left(\frac{\partial H}{\partial \theta}\right)^2}{\Sigma}$
Mixed term considering SR and α correlation	$w_{corr(SR,\alpha)} = \frac{2\left(\frac{\partial H}{\partial SR}\right)\left(\frac{\partial H}{\partial \alpha}\right) COV(SR, \alpha)}{\Sigma}$
Mixed term considering SR and θ correlation	$w_{corr(SR,\theta)} = \frac{2\left(\frac{\partial H}{\partial SR}\right)\left(\frac{\partial H}{\partial \theta}\right) COV(SR, \theta)}{\Sigma}$

2.2.2. Mapping Tree Height Uncertainty at the Global Scale

Scenarios were run to explore σ_H theoretical behaviour and which factor mainly affect it. Despite theoretical scenarios, to give a practical example aimed at proposing an operational scenario, the above-mentioned concerns were applied at the global scale using Google Earth Engine (GEE) and developing an appropriate routine. GEE is an web-based platform that allows an immediate access to geographical data and performing wide areas analysis [46]. GEE consists of a multi-petabyte analysis-ready data catalogue and its parallel computation service allows to process large geospatial datasets at the global scale. For this reason, GEE was used in this work to map σ_H at the global level implementing eq. 3. To perform such task, the following pre-processing steps were involved. GTOPO30 layer was used to compute local terrain slope, $\varphi(x, y)$, while the GFCH was assumed a reliable dataset that provides a continuous estimate of forest height, $H(x, y)$, around the world. Involving $H(x, y)$ and

$\varphi(x, y)$, eq. 3 was applied directly in GEE to estimate height uncertainty at the pixel-level. Four maps of H uncertainty, $\sigma_H(x, y)$, were computed setting SR equal to 10 m, 20 m, 30 m and 40 m respectively, in order to compute σ_H value one can expect if placed at given distance to the tree. Finally, REM biomes polygons were used as spatial basis to compute the 5th, 25th, 50th, 75th and 95th percentiles of $\sigma_H(x, y)$, providing information about the density function over world forest biomes. These maps, coupled to density function, allow operator to plan forest surveys and properly manage the tree height uncertainty during his/her surveys alerting about the significance difference existing if comparing the height measures over time or in space.

3. Results

3.1. Uncertainty Modelling

Uncertainty of angular measures from hypsometer is related to both instrument accuracy and operator skills. The former is the one provided by the producer; the latter has to be somehow estimated. Angular accuracy of hypsometer proved to follow a power model (eq. 4 and eq. 5) that was opportunely calibrated by least square-based regression (Fig. 4) involving θ and α values from field surveys. Model coefficients were reported in table 4. They showed to be significantly different from 0.

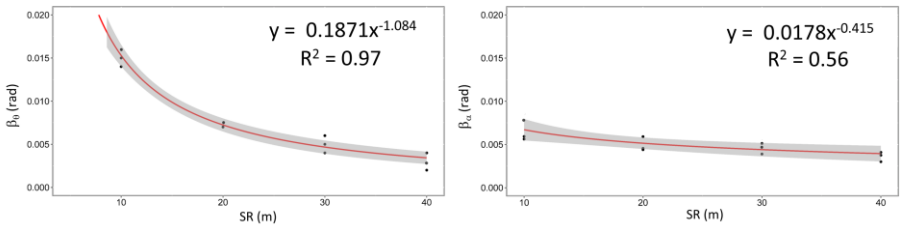

Figure 4. (left) β_θ vs SR model calibrated from field data (radians values); (right) β_α vs SR model calibrated from field data. Grey bounds are the 95% confidence intervals, red lines are the calibrated models.

Table 4. Hypsometer accuracy models coefficients (eq. 4 and eq. 5).

Coefficient	*Value*	*Standard Error*	*t*	*p-value*
a	0.1871	0.0031	3.25	0.0051
b	-1.0841	0.0874	3.92	0.0064
c	0.0178	0.0035	3.22	0.0094
d	-0.4156	0.1232	3.65	0.0053

Figure 4a shows that, generally, β_θ decreases as SR increases. In particular an increase of SR from 10 m to 20 m determines a β_θ reduction by half of its value, going from a value of 0.015 radians to one of 0.007 radians respectively. Subsequently, for SR equal to 30 m up to 40 m, β_θ decreases by 0.002-0.003 rad respectively. A similar behaviour can be observed in figure 4b. However, in this case the β_α variation appears to be milder and general a flat behaviour characterizes β_α. Nevertheless, when SR is equal to 10m, β_α is two times lower than β_θ (0.007 rad and 0.015 rad respectively); while for SR greater than 30 m β_α results to be similar β_θ (0.005 rad).

Based on results, it appears that for low SR values, uncertainty of angular measurements results to be higher in θ than in α, whereas with high SR values the two uncertainties turn out to be similar. In fact, fixing tree height, if SR increase both θ and α angles should decrease. Therefore, for higher angles (i.e. the ones generated by treetop collimation), higher their uncertainty. Similarly, also angles generated by bottom collimation follow this trend, however since they are smaller their uncertainty result lower. Concerning this issue, Bragg [47] highlighted that moving away from the target, angles measurements can be more accurate decreasing the errors related to the tree height determination. MAPE concerning β_θ is 15% while 14% for β_α. Since these MAPE values represent angle accuracy component not dependent from SR, both values suggest that about the 15% of the error is not due to operative condition (SR) but by operator-related ones. The latter could probably be due to higher/lower operator hand motion accuracy during the surveys, suggesting how a fixed support could improve hypsometer survey accuracy [6]. Using filed data $cov(\theta, SR)$ and $cov(\alpha, SR)$

were found equal to -0.95 and 0.27 respectively. These values suggest that θ is more correlated to SR than α as also proved by the determination coefficients of calibrated models ($R^2 = 0.97$ and $R^2 = 0.56$ for β_θ and β_α respectively). To assess the effects of angle accuracy and other operative conditions on tree height uncertainty, VPL was adopted, and some theoretical scenarios were proposed involved the hypsometer angle precision models previously calibrated. In particular, two scenarios were explored, the first one by applying VPL changing φ and parameterizing eq. 3 by H (Figure 5a). The second one was obtained by applying VPL changing SR and parameterizing eq. 3 by H (Figure 5b).

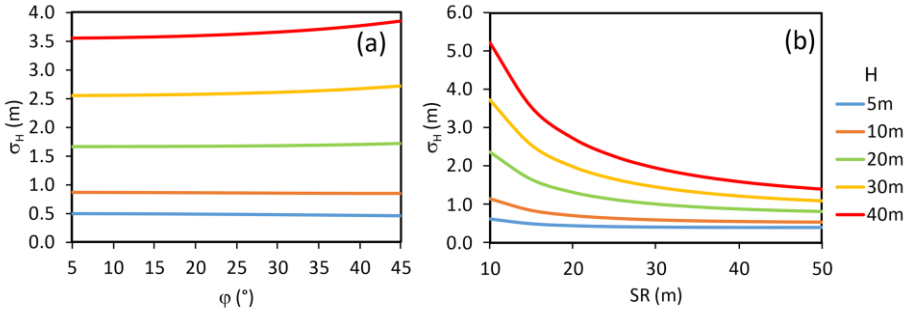

Figure 5. (a) σ_H scenarios derived by applying VPL changing φ and parameterizing eq. 3 by H; (b) σ_H scenarios derived by applying VPL changing SR and parameterizing eq. 3 by H.

Generally, Figure 5a shows that σ_H does not significantly change even if φ increases. Moreover, the σ_H value results to be very high (σ_H > 3.5 m) with H values equal to 40 m, while are lower (σ_H = 0.5 m) for H values equal to 5 m. Furthermore, it can be highlighted that with φ values greater than 35-40°, σ_H values increase slightly. For example, considering H = 40 m and φ = 25°, the σ_H value results to be equal to 3.5 m, while at 45° it turns out to be equal to 3.8 m, showing an increase of σ_H equal of about 9%. Consequently, it would appear that σ_H would only be affected by high levels of slope (φ > 30°). This result was supported by Stereńczak et al., [48] who found that slope, especially when height measurement is made below the tree base, can increase height errors. Conversely, considering Figure 5b, the σ_H value appears to be strongly affected by SR.

Specifically, σ_H tends to decrease as SR increases. For example, assuming H equal to 40 m, the σ_H value results to be 5 m, 3 m, 2.5 m, 2.2 m and 1.8 m for the respective SR values of 10 m, 20 m, 30 m, 40 m and 50 m. Whereas, if H is 5 m, σ_H remains constant around 0.80 m despite SR variations. Considering taller trees (between 20 m and 40 m), σ_H results to be very high especially for SR low values (between 10 m and 20 m); moving away from the tree (SR between 30 m and 40 m) σ_H decreases until it stops with values of SR > 40 m. However, this behaviour does not appear with smaller trees (H < 10 m). Similar results were reported by Skovsgaard [49] who shown that higher SR positively affect the estimation of tree height. Based on these results, it appears that the parameters H and SR significantly affect σ_H value. Therefore, by combining these two parameters, it was possible to report several σ_H scenarios that might normally occur during field surveys (Figure 6).

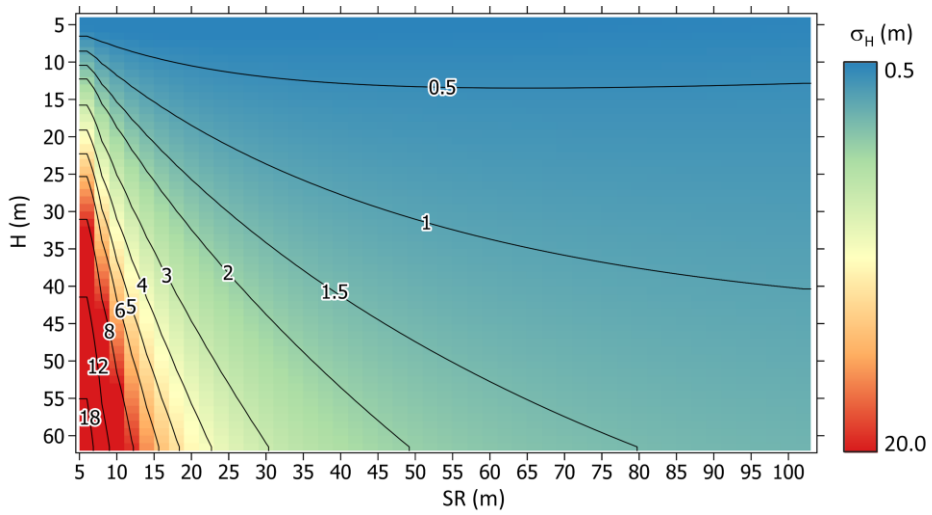

Figure 6. σ_H scenarios (φ = 15°) obtained by all possible combination between H and SR. Isolines represent line having same σ_H .

In particular figure 6 shows that σ_H values increase when H increases and SR decreases. Nevertheless, fixing H, σ_H could greatly vary depending on SR. For example, having SR and H equal to 60 m and 30 m respectively, a σ_H can be found equal to 1 m. Otherwise, having SR and H equal to 6 m and 30 m

respectively, a σ_H can be found equal to 9 m (i.e. about one order of magnitude than SR = 60 m). From an operational point of view during height survey, the proper combinations of H and SR that can be proposed based on scenarios in figure 6. Three main operative conditions can be defined: (i) distance from the target half to the tree height (SR = 0.5 H); (ii) distance from the target equal to the tree height (SR = H); (iii) distance from the target twice to the tree height (SR = 2 H). In the first case, having the H - SR ratio equal to 2:1, the σ_H value, and consequently the errors in tree height estimation, would increase considerably. For example, with H equal to 20 m and SR equal to 10 m, the σ_H values would be equal to 2.5 m resulting in an error range between 12.5% compared to the tree height. Concerning the second case, having the H - SR ratio equal to 1:1, for example a tree of 20 m and placed at 20 m, σ_H will be about 1.5 m, i.e. 7.5% error compared to H. Considering the ratio 1:2, the σ_H would decrease considerably. For example, with H = 20 m and SR = 40 m, σ_H values result to be equal to 0.8 m i.e. 3.5% error compared to H. However, it is worth to remind that the last condition is not always allowed during field surveys. In fact, several works [48,50,51] proved that moving away from the target, treetop visibility can be masked by others tree crown. Therefore, based on our results, a simple rule of thumb can be proposed: a H-SR ratio equal to 1:2 (environmental conditions permitting) would be the most reasonable operative choice to minimize relative tree height uncertainty under the 5%. In order to better assess the effect of the different parameter uncertainty involved in σ_H computation, a sensitivity analysis of σ_H was performed. In Figure 7 are reported the weights of tree height variance computed applying table 3 formulas.

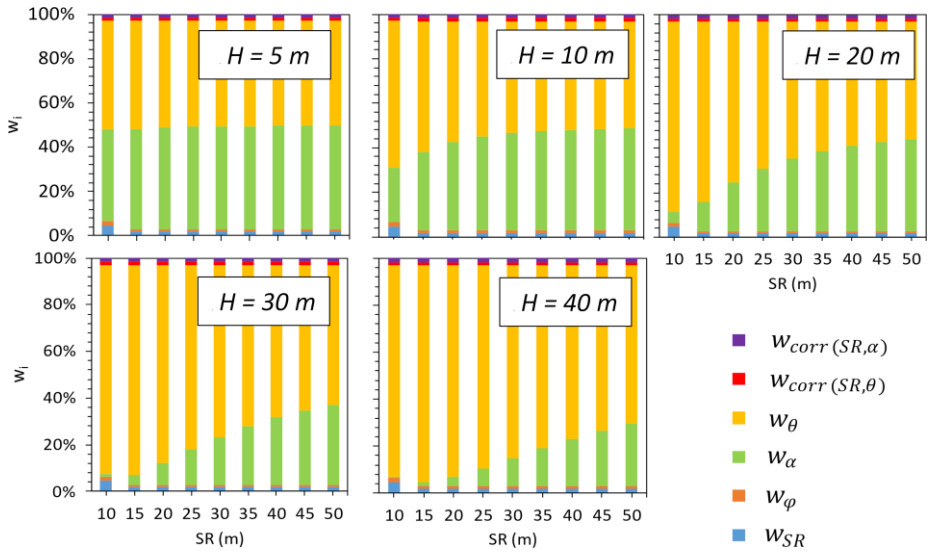

Figure 7. Relative weights (importance) of factors involved in the sensitivity analysis of $\sigma_H{}^2$. Sensitivity analysis was iteratively performed by computing w_i changing H and SR.

It can be noted that, generally, the parameters that most affect $\sigma_H{}^2$ result to be w_α and w_θ. Indeed, their sum reaches about 95% of tree height variance in all scenarios. Conversely, $w_{corr\,(SR,\alpha)}$, $w_{corr(SR,\theta)}$, w_φ and w_{SR} poorly affect $\sigma_H{}^2$ (under 2% on average). Concerning this issue, w_θ and w_α appear to be strongly affected by SR and H. In fact, for smaller tree (e.g., H = 5 m), the values of w_θ and wα are constant as SR increase; while for H > 10 m, the weight of wα increases as SR increases, while w_θ decreases. Considering weights from same SR, it can be observed wα and w_θ significantly vary according to H values, while other weights remain low. In particular, at low SR values, w_θ tends to increase according to H increase. Conversely, at high SR values, w_θ increase little as H increases. For example, with SR equal to 10 m, w_θ result to be about 47% and 90% with H equal to 5 m and 40 m respectively. Whereas with SR equal to 40 m, w_θ results to be again 47% with H equal to 5 m but about to 60% with H equal to 40 m. Therefore, the treetop angle (θ) uncertainty participates for the most of tree height uncertainty for H > 5 m. For the same H, increasing the SR value the angle θ and the corresponding w_θ in the σ_H computation decreases and as a consequence the wα increases. Another interesting conclusion concerns the importance of terrain

slope and SR accuracy. In fact, in all scenarios the w_{φ} and w_{SR} are lower than 1% suggesting that a coarse estimate of such parameters does not significantly affect tree height uncertainty. Therefore, more accurate rangefinder does not directly reflect in better tree height estimates suggesting that similar tree height accuracy can be obtained by using laser, ultrasound or optical telemeter. Similar results were found by [49,52] where different forest rangefinder where compared.

3.2. Mapping Forest Height Uncertainty at the Global Scale

To give a practical example of the theoretical scenarios, an appropriate GEE routine was developed in order to map tree height uncertainty at global scale. Since the distance between tree and the operator was found to greatly affect the height uncertainty, four different scenarios with SR equal to 10, 20, 30 and 40 m were proposed (Fig. 8). Mapping was achieved according to the same approach used for generating the graph of figure 6. In this case the local tree height estimate was obtained from GFCH and the local slope value from GTOPO30; an operator's height of 1.60 m was used for all computations. It worth to stress that GFCH was simply used to derive an estimate of local tree height in order to generate an estimate of the associated uncertainty if obtained by ground surveys operated as modelled in this work. In other words, we did not model the uncertainty of GFCH, but we used GFCH to inform users that are going to operate ground surveys in those areas about the expected theoretical accuracy of their measurements.

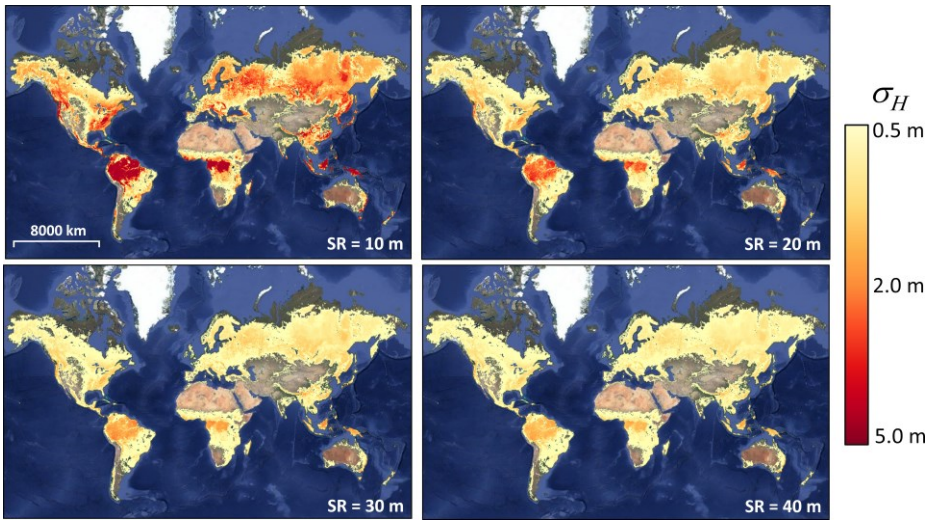

Figure 8. $\sigma_H(x, y)$ maps at global scale computed in GEE. Four operative scenarios were proposed by assuming SR at 10 m, 20 m, 30 m, 40 m respectively.

Generally, σ_H tends to decrease when SR increases confirmed the previous-mentioned role of tree-operator distance. For example, considering the Amazon zone, σ_H results to be greater than 5 m at SR = 10 m; while at SR = 40m, σ_H result about 1.5 m, thus about 75% more accurate. It is worth to remind that a coarse DEM was involved in these simulations. Therefore, slope values are affected by this low resolution probably providing underestimated slopes especially in those areas characterized by high topographic variability (e.g. mountain). To summarize $\sigma_H(x, y)$ differences at global level, $\sigma_H(x, y)$ percentiles per forest biomes were computed and reported in boxplots (Fig. 9).

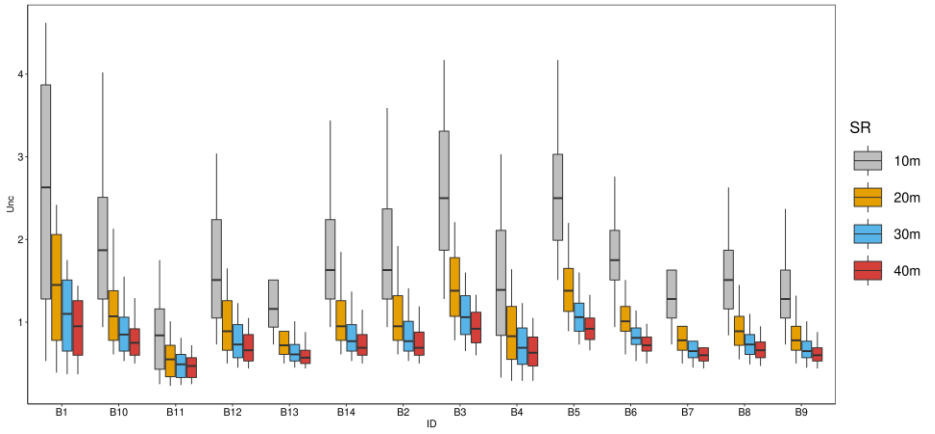

Figure 9. $\sigma_H(x, y)$ values distribution for forest biomes according to four operative scenarios.

In general, as already observed globally in figure 8, σ_H decreases as SR increases in all investigated biomes. The highest σ_H are also observed at SR = 10m, while the lowest values at SR = 40 m. In particular, the average value of σ_H result to be equal to 1.83 m, 1.05 m, 0.83 m and 0.73 m for SR equal to 10, 20, 30 and 40 m respectively. Specifically, σ_H for different biomes included in this work the following observations can be carried out: i) Tundra (B11), desert-xeric shrublands (B13) and tropical-subtropical-savannas and shrublands (B7) are the biomes with the lowest σ_H (all scenarios average was found equal to 0.60, 0.85, 0.92 m respectively); ii) Tropical and subtropical moist broadleaf forest (B1), Tropical and subtropical coniferous (B3) and temperate conifer forests (B5) are the biomes with the highest σ_H (all scenarios average was found equal to 1.50, 1.52, 1.54 m respectively). In this context, the results obtained are consistent with the theoretical assessment proposed in this work and recent literature. In particular, is well know that different vegetation, and consequently different biomes, can certainly affect tree height estimation. However, the main factors that can affect σ_H can be traced back to: forest structure, tree height, terrain topography, tree species, tree lean [26,43]. For example, regarding biome B11, represented by Tundra and therefore characterized by small vegetation, low values of σ_H were found. Conversely, considering biome B1, represented by

tropical and subtropical broadleaf forests and therefore characterized by very tall trees, high values of σ_H were found. These results are consistent to the ones reported by Hyyppa [53], Hush [50] and Korning [51]. The first one investigated forest height estimation and pointed out that the accuracy of tree height measurement decreases as vegetation height increases (especially with trees > 25 m). The second and third one highlight that deciduous trees show lower tree height accuracy.

A further consideration that can be deduced in Figure 9 is the dispersion of σ_H in the different SR classes. σ_H distribution result to be more heterogenous in the class of SR = 10 m (σ_H ranges between 2 m to 4 m), while it results to be homogenous when SR increases (around one meter). Consequently, it can be defined that within the same biome the measurement of vegetation height is affected by SR. This result is supported by Skovsgaard [6], who confirms that distance from the measured trees can affected the tree high estimation. Indeed, for some biomes the variation of SR has a considerable impact on σ_H values. For example, concerning Taiga (B6) at SR = 10 m, the σ_H values are very different from those at SR = 20 m. This behaviour generally occurs between SR equal to 10 and 20 m and takes place in other biomes as B13, B14, B3, B5, B8 and B9. Conversely, in other biomes this phenomenon is less present. For example, in B1, B11 and B4, boxplots at SR = 10 m and 20 m are similar only for 50-60% of the time, therefore in this cases SR variation seems to less affect the final $\sigma_H$value. Regarding the transition of SR between 30 m and 40 m, the differences in terms of σ_H seem to disappear or even become irrelevant in many cases. This finding can be interpreted as an absence of σ_H decrease as SR increases in some contexts for specific biomes. Consequently, from an operational point of view these findings could be extremely useful for increasing the speed of surveys (avoiding too be far away from the target) and simultaneously maintaining precise tree height estimates. For example, in Tundra and Shrublands biomes low σ_H values were found for all SR scenarios. Another interesting outcome concerning these biomes is the follows: comparing these accuracies to the expected vegetation

height in such biomes, they highlight how hypsometer is not the proper instrument for height surveys in shrublands and Tundra since the uncertainty is higher than expected vegetation height. In such biomes other instruments like graduated pole or tape measure can guarantee a rapid and more accurate measure of small vegetation height than the ones retrieved by hypsometer.

Finally, it is worth to remind that provided world-wide estimates of height uncertainty are "optimistic" since they are based on theoretical conditions. In real operative conditions other unpredictable factors like apex visibility/identification and stem curvature (e.g. in coppices) could negatively affects the height accuracy.

4. Conclusions

In this work, a statistically based operative method for estimating tree height measurement uncertainty (σ_H) was proposed using the variance propagation law. The aim was to model the behaviour of σ_H in different operative context. Therefore, several simulations were performed involving factors like: tree height, survey distances and terrain slope. Regarding the terrain slope, results shown that this parameter poorly affect σ_H. Concerning the first two parameters, results proved that σ_H could greatly be affected by H and SR resulting in a tree height error between 0.5 m up to 20 m (worst case). Moreover, in this work a simple rule of thumb was proposed (H-SR ratio equal to 1:2) to minimize height uncertainty under 5% of H. Concerning the sensitivity analysis of all parameters involved in the σ_H, results shows that the w_α and w_θ were the more relevant (their sum is about 95%). While $w_{corr\ (SR,\alpha)}$, $w_{corr(SR,\theta)}$, w_φ *and* w_{SR} contribution result to be very low in σ_H determination (under 1%). Finally, to give a practical example of such deductions tree height uncertainty was mapped at the global scale using Google Earth Engine and summarized per forest biomes. Results proved that tropical biomes have higher uncertainty (from 1 m to 4 m) while shrublands and tundra the lowest (under 1 m). Proposed approach proved to be an operative tool useful both in forest research and forest management context. It allows to better consider the uncertainty of forest estimates alerting the user about the

significance of difference that one could test between forest stands or between the same stand at different time.

Acknowledgments: We would like to thank Dr. Roberta Berretti, Dr. Evelyn Momo and Geom. Marco Anibaldi for their precious help in filed surveys.

References:

1. Segura, M.; Kanninen, M. Allometric Models for Tree Volume and Total Aboveground Biomass in a Tropical Humid Forest in Costa Rica 1. Biotropica: The Journal of Biology and Conservation 2005, 37, 2–8.

2. Laurin, G.V.; Ding, J.; Disney, M.; Bartholomeus, H.; Herold, M.; Papale, D.; Valentini, R. Tree Height in Tropical Forest as Measured by Different Ground, Proximal, and Remote Sensing Instruments, and Impacts on above Ground Biomass Estimates. International Journal of Applied Earth Observation and Geoinformation 2019, 82, 101899.

3. Hao, Z.; Zhang, J.; Song, B.; Ye, J.; Li, B. Vertical Structure and Spatial Associations of Dominant Tree Species in an Old-Growth Temperate Forest. Forest Ecology and Management 2007, 252, 1–11.

4. Song, B.; Chen, J.; Desander, P.V.; Reed, D.D.; Bradshaw, G.A.; Franklin, J.F. Modeling Canopy Structure and Heterogeneity across Scales: From Crowns to Canopy. Forest Ecology and Management 1997, 96, 217–229.

5. Spies, T.A. Forest Structure: A Key to the Ecosystem. Northwest science 1998, 72, 34–36.

6. Skovsgaard, J.P.; Johannsen, V.K.; Vanclay, J.K. Accuracy and Precision of Two Laser Dendrometers. Forestry: An International Journal of Forest Research 1998, 71, 131–139.

7. Ochal, W.; Socha, J.; Pierzchalski, M. The Effect of the Calculation Method, Plot Size, and Stand Density on the Accuracy of Top Height Estimation in Norway Spruce Stands. iForest-Biogeosciences and Forestry 2017, 10, 498.

8. Momo, E.J.; De Petris, S.; Sarvia, F.; Borgogno-Mondino, E. Addressing Management Practices of Private Forests by Remote Sensing and Open Data: A Tentative Procedure. Remote Sensing Applications: Society and Environment 2021, 100563.

9. Lund, H.G. When Is a Forest Not a Forest? Journal of Forestry 2002, 100, 21–28.

10. Sillett, S.C.; Van Pelt, R.; Koch, G.W.; Ambrose, A.R.; Carroll, A.L.; Antoine, M.E.; Mifsud, B.M. Increasing Wood Production through Old Age in Tall Trees. Forest Ecology and Management 2010, 259, 976–994.

11. Hanewinkel, M.; Hummel, S.; Albrecht, A. Assessing Natural Hazards in Forestry for Risk Management: A Review. European Journal of Forest Research 2011, 130, 329–351.

12. Martins, A.C.; Willig, M.R.; Presley, S.J.; Marinho-Filho, J. Effects of Forest Height and Vertical Complexity on Abundance and Biodiversity of Bats in Amazonia. Forest Ecology and Management 2017, 391, 427–435.

13. Bohn, F.J.; Huth, A. The Importance of Forest Structure to Biodiversity–Productivity Relationships. Royal Society open science 2017, 4, 160521.

14. Purves, D.W.; Lichstein, J.W.; Strigul, N.; Pacala, S.W. Predicting and Understanding Forest Dynamics Using a Simple Tractable Model. Proceedings of the National Academy of Sciences 2008, 105, 17018–17022.

15. Pan, Y.; Birdsey, R.A.; Fang, J.; Houghton, R.; Kauppi, P.E.; Kurz, W.A.; Phillips, O.L.; Shvidenko, A.; Lewis, S.L.; Canadell, J.G. A Large and Persistent Carbon Sink in the World's Forests. science 2011, 333, 988–993.

16. Tavoni, M.; Sohngen, B.; Bosetti, V. Forestry and the Carbon Market Response to Stabilize Climate. Energy Policy 2007, 35, 5346–5353.

17. Ter-Mikaelian, M.T.; Korzukhin, M.D. Biomass Equations for Sixty-Five North American Tree Species. Forest Ecology and Management 1997, 97, 1–24.

18. Zianis, D.; Muukkonen, P.; Mäkipää, R.; Mencuccini, M. Biomass and Stem Volume Equations for Tree Species in Europe; FI, 2005;

19. Neumann, M.; Moreno, A.; Mues, V.; Härkönen, S.; Mura, M.; Bouriaud, O.; Lang, M.; Achten, W.M.; Thivolle-Cazat, A.; Bronisz, K. Comparison of Carbon Estimation Methods for European Forests. Forest Ecology and Management 2016, 361, 397–420.

20. De Petris, S.; Sarvia, F.; Borgogno-Mondino, E. RPAS-Based Photogrammetry to Support Tree Stability Assessment: Longing for Precision Arboriculture. Urban Forestry & Urban Greening 2020, 55, 126862.

21. De Petris, S.; Berretti, R.; Sarvia, F.; Borgogno Mondino, E. When a Definition Makes the Difference: Operative Issues about Tree Height Measures from RPAS-Derived CHMs. iForest-Biogeosciences and Forestry 2020, 13, 404.

22. Yin, D.; Wang, L. How to Assess the Accuracy of the Individual Tree-Based Forest Inventory Derived from Remotely Sensed Data: A Review. International Journal of Remote Sensing 2016, 37, 4521–4553, doi:10.1080/01431161.2016.1214302.

23. West, P.W.; West, P.W. Tree and Forest Measurement; Springer, 2009;

24. Laar, A. van; Akça, A. Forest Mensuration; Managing forest ecosystems; 2. ed., completely rev. and supplemented.; Springer: Dordrecht, 2007; ISBN 978-1-4020-5990-2.

25. Larsen, D.R.; Hann, D.W.; Stearns-Smith, S.C. Accuracy and Precision of the Tangent Method of Measuring Tree Height. Western Journal of Applied Forestry 1987, 2, 26–28.

26. Stereńczak, K.; Mielcarek, M.; Wertz, B.; Bronisz, K.; Zajączkowski, G.; Jagodziński, A.M.; Ocha\l, W.; Skorupski, M. Factors Influencing the Accuracy of Ground-Based Tree-Height Measurements for Major European Tree Species. Journal of environmental management 2019, 231, 1284–1292.

27. Köhl, M.; Magnussen, S.S.; Marchetti, M. Sampling Methods, Remote Sensing and GIS Multiresource Forest Inventory; Springer Science & Business Media, 2006;

28. Vogt, J.M.; Fischer, B.C. A Protocol for Citizen Science Monitoring of Recently-Planted Urban Trees. Urban Forests, Ecosystem Services and Management; Blum, J., Ed 2017, 153–186.

29. Mascaro, J.; Detto, M.; Asner, G.P.; Muller-Landau, H.C. Evaluating Uncertainty in Mapping Forest Carbon with Airborne LiDAR. Remote Sensing of Environment 2011, 115, 3770–3774.

30. Clark, N.A.; Wynne, R.H.; Schmoldt, D.L. A Review of Past Research on Dendrometers. Forest Science 2000, 46, 570–576.

31. Pariyar, S.; Mandal, R.A. Comparative Tree Height Measurement Using Different Instrument. International Journal of Ecology and Environmental Sciences 2019, 1, 12–17.

32. Williams, M.S.; Bechtold, W.A.; LaBau, V.J. Five Instruments for Measuring Tree Height: An Evaluation. Southern Journal of Applied Forestry 1994, 18, 76–82.

33. Wing, M.G.; Solmie, D.; Kellogg, L. Comparing Digital Range Finders for Forestry Applications. Journal of forestry 2004, 102, 16–20.

34. Saliu, I.S.; Satyanarayana, B.; Fisol, M.A.B.; Wolswijk, G.; Decannière, C.; Lucas, R.; Otero, V.; Dahdouh-Guebas, F. An Accuracy Analysis of Mangrove Tree Height Mensuration Using Forestry Techniques, Hypsometers and UAVs. Estuarine, Coastal and Shelf Science 2021, 248, 106971.

35. Vasilescu, M.M. Standard Error of Tree Height Using Vertex III. Bulletin of the Transilvania University of Brasov. Forestry, Wood Industry, Agricultural Food Engineering. Series II 2013, 6, 75.

36. Schreuder, H.T.; Gregoire, T.G.; Wood, G.B. Sampling Methods for Multiresource Forest Inventory; John Wiley & Sons, 1993;

37. Ku, H.H. Notes on the Use of Propagation of Error Formulas. Journal of Research of the National Bureau of Standards 1966, 70.

38. Laser Technology Inc TruPulse 200 User's Manual 2018.

39. Simard, M.; Pinto, N.; Fisher, J.B.; Baccini, A. Mapping Forest Canopy Height Globally with Spaceborne Lidar. Journal of Geophysical Research: Biogeosciences 2011, 116.

40. Hayashi, M.; Saigusa, N.; Oguma, H.; Yamagata, Y. Forest Canopy Height Estimation Using ICESat/GLAS Data and Error Factor Analysis in Hokkaido, Japan. ISPRS Journal of Photogrammetry and Remote Sensing 2013, 81, 12–18.

41. Hastings, D.A.; Dunbar, P. Development & Assessment of the Global Land One-Km Base Elevation Digital Elevation Model (GLOBE). Group 1998, 4, 218–221.

42. Dinerstein, E.; Olson, D.; Joshi, A.; Vynne, C.; Burgess, N.D.; Wikramanayake, E.; Hahn, N.; Palminteri, S.; Hedao, P.; Noss, R. An Ecoregion-Based Approach to Protecting Half the Terrestrial Realm. BioScience 2017, 67, 534–545.

43. Ojoatre, S.; Zhang, C.; Hussin, Y.A.; Kloosterman, H.E.; Ismail, M.H. Assessing the Uncertainty of Tree Height and Aboveground Biomass from Terrestrial Laser Scanner and Hypsometer Using Airborne LiDAR Data in Tropical Rainforests. IEEE Journal of selected topics in applied earth observations and remote sensing 2019, 12, 4149–4159.

44. Lira, I. Evaluating the Measurement Uncertainty: Fundamentals and Practical Guidance; CRC Press, 2002;

45. Muelaner, J.E.; Wang, Z.; Jamshidi, J.; Maropoulos, P.G.; Mileham, A.R.; Hughes, E.B.; Forbes, A.B. Study of the Uncertainty of Angle Measurement for a Rotary-Laser Automatic Theodolite (R-LAT). Proceedings of the Institution of Mechanical Engineers, Part B: Journal of Engineering Manufacture 2009, 223, 217–229.

46. Gorelick, N.; Hancher, M.; Dixon, M.; Ilyushchenko, S.; Thau, D.; Moore, R. Google Earth Engine: Planetary-Scale Geospatial Analysis for Everyone. Remote sensing of Environment 2017, 202, 18–27.

47. Bragg, D.C. The Sine Method as a More Accurate Height Predictor for Hardwoods. e-Gen. Tech. Rep. SRS–101. US Department of Agriculture, Forest Service, Southern Research Station: 23-33.[CD-ROM]. 2007.

48. Stereńczak, K.; Mielcarek, M.; Wertz, B.; Bronisz, K.; Zajączkowski, G.; Jagodziński, A.M.; Ocha\l, W.; Skorupski, M. Factors Influencing the Accuracy of Ground-Based Tree-Height Measurements for Major European Tree Species. Journal of environmental management 2019, 231, 1284–1292.

49. Skovsgaard, J.P.; Johannsen, V.K.; Vanclay, J.K. Accuracy and Precision of Two Laser Dendrometers. Forestry: An International Journal of Forest Research 1998, 71, 131–139.

50. Husch, B.; Beers, T.W.; Kershaw Jr, J.A. Forest Mensuration; John Wiley & Sons, 2002;

51. Korning, J.; Thomsen, K. A New Method for Measuring Tree Height in Tropical Rain Forest. Journal of Vegetation Science 1994, 5, 139–140.

52. Božić, M.; Čavlović, J.; Lukić, N.; Teslak, K.; Kos, D. Efficiency of Ultrasonic Vertex III Hypsometer Compared to the Most Commonly Used Hypsometers in Croatian Forestry. Croatian Journal of Forest Engineering: Journal for Theory and Application of Forestry Engineering 2005, 26, 91–99.

53. Hyyppä, J.; Pyysalo, U.; Hyyppä, H.; Samberg, A. Elevation Accuracy of Laser Scanning-Derived Digital Terrain and Target Models in Forest Environment. In Proceedings of the Proceedings of EARSeL-SIG-Workshop LIDAR; 2000; pp. 16–17.

5.2 PHASE-BASED TECHNIQUES

5.2.1 Uncertainties and Perspectives on Forest Height Estimates by Sentinel-1 Interferometry

De Petris Samuele[a*], Sarvia Filippo[a], and Borgogno- Mondino Enrico[a]

[a]Department of Agricultural, Forest and Food Sciences (DISAFA), University of Turin, 10095 Grugliasco, Italy.

*Correspondence: samuele.depetris@unito.it

Published: 2022 in *Earth.*

Abstract: Forest height is a key parameter in forestry. SAR interferometry (InSAR) techniques have been extensively adopted to retrieve digital elevation models (DEM) giving a representation of the continuous variation of Earth' topography, including forests. Unfortunately, InSAR has been proven to fail over vegetation due to low coherence values; therefore, all phase unwrapping algorithms tend to avoid these areas, making InSAR-derived DEM over vegetation unreliable. In this work, a sensitivity analysis was performed with the aim of properly initializing the relevant operational parameters (baseline and multilooking factor) to maximize the theoretical accuracy of the height difference between the forest and reference point. Some scenarios were proposed to test the resulting "optimal values" as estimated at the previous step. A simple model was, additionally, proposed and calibrated aimed at predicting the optimal baseline value (and therefore image pair selection) for height uncertainty minimization. All our analyses were conducted using free available data from the Copernicus Sentinel-1 mission to support the operational transfer into forest sector. Finally, potential uncertainty affecting resulting height measures was quantified showing that a value lower than 5 m can be expected once all user-dependent parameters (i.e. baseline, multilooking factor, temporal baseline) are properly tuned.

Keywords: Sentinel-1; SAR; Interferometry; Phase Unwrapping Avoiding; Forest Height; Uncertainty Assessment; Topographic Levelling Approach.

1. Introduction

Forest height is a key parameter in forestry since it is adopted to retrieve AGB [1,2] and characterized canopy vertical structure [3–5]. It is often used to detect forest [6], to assess forest ecosystem services (e.g. timber production [7], forest protection capabilities against natural hazards [8], biodiversity [9,10]). Forest height is ordinarily measured through ground campaigns by means of hypsometers, whose precision ranges between 1 and 3 m [11,12]. Unfortunately, ground surveys are time and cost consuming, making them poorly dense over forested areas. Conversely, remote sensing can fill this gap providing continuous forest height measures over wide areas showing accuracy comparable to ground surveys [13]. Space-borne Earth Observation missions well-fit forest requirements making possible to map and monitor wide areas, allowing a near-early change detection and a frequent updating of forest properties [14]. Synthetic aperture radar (SAR) is known to be to be useful for estimating forest geometric features recording data in all-weather condition included equatorial/tropical ones where clouds are almost constantly over. Among SAR application and methods, SAR interferometry (InSAR) technique has been extensively adopted to generate digital elevation models (DEM), that are intended to provide a continuous representation of Earth topography, included forest areas. Theoretically speaking, radar interferometry can generate highly precise height estimates related to the difference of path length between scattered signals received by two properly positioned antennas. The ordinary InSAR processing workflow relies on a phase unwrapping step aimed at unambiguously recovering the local topography, which is generally achieved by unitarily processing the entire scene. Ordinary these algorithms tend to avoid these areas during unwrapping [15,16], so the approach has proven to consistently fail where signal coherence values are low. This makes InSAR-derived DEM over vegetation highly unreliable [17]. An alternative existing approach, not widely explored in literature [18–20], is considered in this work for obtaining more reliable and accurate estimates of forest height from InSAR data by avoiding phase unwrapping. This method changes the working

paradigm from a mapping problem involving the entire scene, to a local paradigm based on the comparison between a forest pixel interferogram and a reference one closely located outside the forest. Specifically, potentialities and limitations of such an approach were explored and discussed.

In this work, with reference to the above-mentioned approach, a sensitivity analysis was also performed with the aim of properly initializing the relevant operational parameters (i.e. baseline and multilooking factor) to maximize the theoretical accuracy of height measures. To support the technological transfer all the analyses were made with reference to SAR open data (guaranteeing a cost-effective data access) with specific focus on the Copernicus Sentinel-1 (S1) mission.

2. Materials and Methods

Given the above-mentioned goals of this work, the analysis was performed according to the workflow of figure 1. A first step was aimed at developing a reasonable model to estimate forest height and defining the conditions that it can be adopted (see section 2.2. Interferometric Phase Modelling). A second step was aimed at modelling theoretical uncertainty of estimates (see section 2.3. Modelling dh Uncertainty). A third step was aimed at tuning involved parameters to optimize operational conditions for minimizing uncertainty of forest height estimates (see section 2.4. Minimizing σ_{dh} through simulated scenarios). All simulations were performed according to Sentinel-1 data.

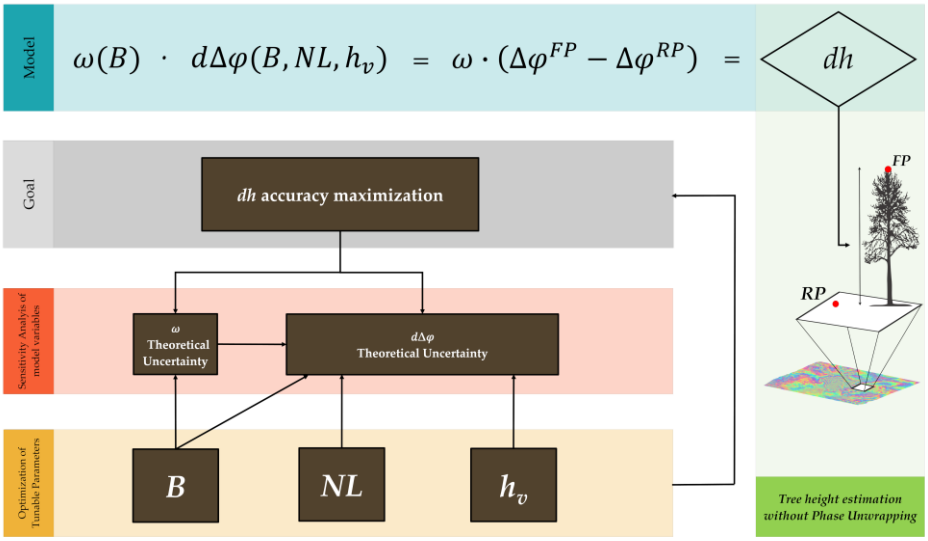

Figure 1. Workflow adopted in this work. B is the baseline; NL is the interferogram multilooking factor; hv is the expected average forest height; dh is the estimated forest height according to proposed model; $\Delta\varphi^{FP}$ and $\Delta\varphi^{RP}$ are the interferometric phases of a forest point and a reference (ground) point respectively; ω is the gain factor that allows to convert an interferometric phase difference ($d\Delta\varphi$) into the height difference.

2.1. Sentinel 1 Data

Satellite missions, such as the European Union (EU) Copernicus Sentinels, generate a significant volume of data that may be proficiently used to aid support environmental studies and land management. Nevertheless, technological transfer, presently, appears to be limited even if web-based services based on these data are becoming to be operational [21–23]. In the general context of satellite open data, SAR imagery shows a further weakness in entering the operational services mainly due to the complexity of data processing [24,25] and data availability. S1 is one of the current largest space-borne missions providing free and open accessible SAR data. Furthermore, the European Space Agency (ESA) made available for users the free software SNAP (Sentinel Application Platform) enabling an easier and focused exploitation of products from the Copernicus Programme [17,26]. S1 mission is a two satellites constellation (Sentinel-1A and Sentinel-1B) acquiring in the microwave C-band (5.6 cm wavelength). Main acquisition mode over land is the interferometric wide swath

(IW) recording backscattered signal in dual pole mode (VV and VH). Data are natively recorded as complex values (I/Q components) and in-SAR geometry (Range and Azimuth). In particular, its medium-high spatial resolution and high revisit time (6 days) make S1 mission useful for a wide range of applications including forest mapping. In literature many methods based on SAR interferometry were proposed to estimate forest height and can be summarized into three main categories: (a) Pol-InSAR methodology [27–29]; (b) Coherence-based methodology [30–32] and (c) Interferometric phase-based methodology [19,20]. Unfortunately, S1 data are not suitable for (a) due to its lack of quad-pol channels that would be required [21,33]. Approach (b) is mainly applied using tandem acquisition mode that guarantees a higher coherence over vegetation. Since S1 does not support tandem acquisition, coherence values over forest are generally low limiting this approach. Consequently, approach (c) appears to be the most promising because it is somehow consistent with technical feature of S1 data. S1 main technical features [34–37] are reported in Table 1 and used for the following simulations.

Table 1. S1 mission nominal features.

Feature	***Values***	***Units***
Frequency (λ)	5.54	cm
Nominal Satellite Altitude (H)	693	km
Look Angle (θ)	30- 45	°
Attitude accuracy (σ_θ)	0.01	°
Maximum Noise Equivalent Sigma Zero (NESZ)	-22	dB
Spatial resolution range (δ_{rg})	5	m
Spatial resolution azimuth (δ_{az})	20	m
Satellite position accuracy POD	5	cm
Bandwidth (Bw)	42-56	MHz
Antenna real length (L)	12	m

2.2. Interferometric Phase Modelling

SAR interferometry relies on image pairs processing acquired from different positions separated by a proper distance known as a baseline (B). This condition makes possible to recover "stable" objects height through a simple geometric transformation [38–40]. Unfortunately, this technique is known to suffer from many limitations in vegetated areas, mainly due to noise induced by canopy volume and interferometric signal decorrelation. Assuming a flattened interferogram with no significant ground shifts affecting the area, the contribution to the interferometric phase ($\Delta\varphi$) given by local topography can be defined according to eq.1.

$$\frac{d\Delta\varphi}{dh} = \frac{4\pi\, B}{\lambda\, R\, \tan\theta} = k_z = \frac{1}{\omega} \quad (1)$$

where $\Delta\varphi$ is the interferometric phase; h is the target point elevation; λ is the wavelength of the radar signal; R is the sensor-target slant range; θ is the antenna off-nadiral angle (look angle) and B is the baseline; ω is the gain factor needed to convert back a phase difference into the correspondent height difference. Inverting eq.1, the height difference (dh) between the two compared points can be obtained by eq. 2. This approach appears to be similar to an ordinary topographic levelling problem [41]. Subsequently, forest point absolute elevation can be obtained by adding dh to, at least, one reference point (representing the ground) having known elevation.

$$dh = h^{FP} - h^{RP} = \omega\,(\Delta\varphi^{FP} - \Delta\varphi^{RP}) \quad (2)$$

where h^{FP} and $\Delta\varphi^{FP}$ are elevation and interferometric phase of the forest point, respectively; h^{RP} and $\Delta\varphi^{RP}$ are elevation and interferometric phase of the reference point, respectively. It is worth to note that eq. 2 can be retained phase unwrapping independent if the expected forest height is maintained lower than the so called height of ambiguity (HOA) [19,30]. This condition is satisfied if no significant elevation difference exists between forest and reference ground levels. This condition can be a-priori verified using an external DEM (e.g. global SRTM

or ASTER DEMs). The condition must be tested for each interferogram pixel to mask out inadequate ones. Being HOA can be obtained multiplying 2π to ω, it is possible to model the relationship between HOA and *B*.

2.3. Modelling *dh* Uncertainty

Once the above-mentioned condition has been satisfied, one can proceed to estimate the expected uncertainty of h^{FP} taking care of the contribution of the involved parameters. h^{FP} uncertainty (σ_{dh}) can be estimated by eq. 3 and 4, assuming h^{RP} uncertainty as a-priori known. Equation 3 is the one commonly adopted in literature to estimate σ_{dh} [42].

$$\sigma_{dh} = \omega \cdot \sigma_{d\Delta\varphi} \tag{3}$$

where σ_{dh} is dh uncertainty and $\sigma_{d\Delta\varphi}$ is the interferometric phase difference uncertainty. It is worth highlighting that this formula does not take care about ω uncertainty that has to be further considered to properly model error propagation that can be proficiently estimated by the Variance Propagation Law (VPL - [43]). VPL is a statistical tool (eq. 4) useful to estimate the a-priori variance of a statistical variable (y) depending on some other independent ones (x_i).

$$\sigma_y^2 = \left(\frac{\partial y}{\partial x_1}\right)^2 \cdot \sigma_{x_1}^2 + \left(\frac{\partial y}{\partial x_2}\right)^2 \cdot \sigma_{x_2}^2 + \cdots + \left(\frac{\partial y}{\partial x_n}\right)^2 \cdot \sigma_{x_n}^2 \tag{4}$$

where $y=f(x_1, x_2, \ldots, x_n)$ is the dependent variable, x_i the independent ones and $\sigma_{x_n}^2$ their variance (supposed to be known). Application of VPL to eq. 3 results in eq. 5.

$$\sigma_{dh} = \sqrt{\left(\frac{\partial dh}{\partial \omega}\sigma_\omega\right)^2 + \left(\frac{\partial dh}{\partial d\Delta\varphi}\sigma_{d\Delta\varphi}\right)^2} \tag{5}$$

where σ_ω and $\sigma_{d\Delta\varphi}$ are the expected uncertainties for ω and $d\Delta\varphi$, respectively.

2.3.1. Theoretical Uncertainty of ω

ω uncertainty (σ_ω) depends on the parameters involved in its computation. Again, the variance propagation law can be used to get the estimate of the theoretical value of σ_ω (eq. 6).

$$\sigma_\omega = \sqrt{\left(\frac{\partial\omega}{\partial B}\right)^2 \cdot \sigma_B^2 + \left(\frac{\partial\omega}{\partial R}\right)^2 \cdot \sigma_R^2 + \left(\frac{\partial\omega}{\partial\theta}\right)^2 \cdot \sigma_\theta^2 + \left(\frac{\partial\omega}{\partial R}\frac{\partial\omega}{\partial\theta}\right)\rho_{(R,\theta)}\sigma_R\sigma_\theta} \quad (6)$$

where R is the slant range (here computed as $R = \frac{H}{\cos\theta}$); σ_B is the baseline uncertainty; σ_R and σ_θ are the slant and look angle uncertainty, respectively; $\rho_{(R,\theta)}$ is the Pearson's correlation coefficient between R and θ. These are known to be geometrically related (thus correlated) and, consequently $\rho_{(R,\theta)}$ must be set to +1. Concerning σ_B, the S1 declared positional accuracy of the ESA provided precise orbit state vectors (Precise Orbit Determination - POD) is 5 cm [35,36]. This determines a σ_B value of 12 cm. σ_θ was assumed equal to 0.01° that is the nominal antenna attitude accuracy. σ_R can be estimated by eq. 7, assuming factors contribution as additive.

$$\sigma_R = \sqrt{{\sigma_{tropo}}^2 + {\sigma_{iono}}^2 + {\sigma_{proc}}^2 + {\sigma_{TOF}}^2} \quad (7)$$

where σ_{tropo} and σ_{iono} are the uncertainty of atmospheric delay induced by troposphere and ionosphere; σ_{proc} is the estimated contribution of SAR data processing effects in the S1 IW products; σ_{TOF} is the uncertainty of slant range signal time, i.e. the minimum detectable slant range distance between two scatterers. In order to evaluate the relative contribution of factors to the final estimate of σ_ω, "weights" of Table 2 (w_i) were computed with reference to σ_ω^2 according to eq. 6.

Table 2. "Weights" defining the relative importance of factors to determine $\boldsymbol{\sigma_\omega^2}$.

Parameter	w_i *formula*
Baseline (B)	$w_B = \frac{\left(\frac{\partial \omega}{\partial B}\right)^2 \cdot \sigma_B^2}{{\sigma_\omega}^2}$
Slant range (R)	$w_R = \frac{\left(\frac{\partial \omega}{\partial R}\right)^2 \cdot \sigma_R^2}{{\sigma_\omega}^2}$
Look angle (θ)	$w_\theta = \frac{\left(\frac{\partial \omega}{\partial \theta}\right)^2 \cdot \sigma_\theta^2}{{\sigma_\omega}^2}$
Mixed term (R, θ)	$w_{corr(R,\theta)} = \frac{\left(\frac{\partial \omega}{\partial R}\frac{\partial \omega}{\partial \theta}\right) \cdot \rho_{(R,\theta)}\sigma_R\sigma_\theta}{{\sigma_\omega}^2}$

2.3.2. Theoretical Uncertainty of $d\Delta\varphi$

The theoretical uncertainty of $d\Delta\varphi$ ($\sigma_{d\Delta\varphi}$) can be computed by eq.8.

$$\sigma_{d\Delta\varphi} = \sqrt{\sigma_{\Delta\varphi FP}^2 + \sigma_{\Delta\varphi RP}^2} \tag{8}$$

where interferometric phase uncertainties, $\sigma_{\Delta\varphi FP}$, and $\sigma_{\Delta\varphi RP}$ were proved [18,44,45] to be strictly correlated to the local coherence magnitude, $|\gamma|$, according to eq. 9.

$$\sigma_{\Delta\varphi} = \frac{1}{\sqrt{2NL}} \frac{\sqrt{1-|\gamma|^2}}{|\gamma|} \tag{9}$$

where NL is the multilooking factor (i.e. number of pixels used to compute the complex multilooked interferogram). These considerations drive to admit that $\sigma_{dh} = f(\omega, \sigma_{\Delta\varphi})$ and, consequently, they depend on the operational parameters B and NL. Eq. 3 and eq. 1 show that dh accuracy is higher for long baselines. This is what is ordinarily reported in literature. Nevertheless, this condition appears to fail over vegetation. In fact, longer baselines make coherence decreasing, thus negatively affecting $\sigma_{\Delta\varphi}$ and, consequently, $\sigma_{d\Delta\varphi}$. This effect is more evident while analysing the decorrelation model of eq. 10 as proposed by

[44,46]. This model defines the coherence magnitude as the product of several contributions related to decorrelation agents.

$$\gamma_{obs} = \gamma_{thermal} \cdot \gamma_{Doppler} \cdot \gamma_{temp} \cdot \gamma_{geom} \cdot \gamma_{vol} \quad (10)$$

where γ_{obs} is the observed coherence magnitude, $\gamma_{thermal}$ is the signal decorrelation due to additive thermal noise [47]; $\gamma_{Doppler}$ accounts for non-perfect overlap of the azimuth spectra for the master and slave SAR acquisitions and misregistration error [48]; γ_{temp} is associated to changes in the dielectric and structural proprieties of the target [49]; γ_{geom} depends on geometric relationships between the two compared SAR acquisitions; γ_{vol} is the decorrelation component due to canopy scattering from multiple heights within each scattering cells. Because $\gamma_{thermal}, \gamma_{Doppler}, \gamma_{temp}$ are independent from any operational parameter that can be controlled by user, these were not taken into consideration in the optimization process authors are addressed to [50]. Differently, γ_{geom} is dependent from baseline according to eq. 11.

$$\gamma_{geom} = 1 - \frac{2\, B \cos^2 \theta\, \delta_{rg}}{\lambda R} \quad (11)$$

where δ_{rg} is the range resolution of the radar. Similarly, γ_{vol} has to be taken into consideration since caused by the volumetric decorrelation related to the vegetation canopy volume (distributed scatters). Assuming a uniform volume showing an exponential extinction of absorption and scattering, γ_{vol} can be modelled by eq. 12 ([18,49,50]). It states that SAR signal decorrelation depends on vegetation volume depth h_v (i.e. tree height) and from the system parameter k_z (see eq.1).

$$\gamma_{vol} = \frac{2 \sin\left(k_z \frac{h_v}{2}\right)}{k_z h_v} \quad (12)$$

Eq. 12 assumes a uniform radar backscatter cross section from canopy volume and no significant scattering from the background. By inverting eq.12, it would be possible to estimate forest height if decorrelation was caused entirely by

volumetric effects. Unfortunately, this is unrealistic due to: canopy signal attenuation, scatters movements and proportion of area filled by trees. These issues determine significant observational errors [50] making this approach with S1 data a poor choice. Within this framework and according to the above-mentioned simplifications, a new synthetic variable $\gamma_{baseline} = \gamma_{geom} \cdot \gamma_{vol}$ can be considered as directly related to the baseline value.

2.4. Minimizing σ_{dh} Through Simulated Scenarios

As demonstrated in the previous sections, σ_{dh} depends on both ω and $\sigma_{\Delta\varphi}$. While trying to minimize it, the only parameters a user can manage are image pair selection (spatial and temporal baseline) and the multilooking factor (NL). These can be optimized to guarantee the lowest σ_{dh}. For how to concern the temporal baseline selection, since forests are continuously changing, longer the temporal baseline, lower the associated coherence (temporal decorrelation) [51], [17]. Therefore, short temporal baseline and winter acquisitions are more suitable for forest height retrieval as discussed by [19,31,51], but, currently, no formalized model exists to support this evidence. As far as baseline optimization (i.e. B value minimizing σ_{dh}) is concerned, this must be managed going back to eq. 3, eq.11 and eq.12. These make possible to generate different scenarios depending on varying baseline and hv values (i.e. expected average forest height). With reference to the scenarios the optimal B value can be retrieved once an expected forest hv is set. To make the estimate more immediate a power model (eq. 13) was calibrated directly relating hv with the optimal B value.

$$B_{opt} = a \cdot (h_v)^b \tag{13}$$

where a and b are model parameters. Concerning NL value optimization, one has to consider eq. 5 that relates NL with $\sigma_{\Delta\varphi}$: higher NL, lower the interferometric phase uncertainty. NL can be therefore optimized by fixing an expected value for σ_{dh} once ω and local coherence are known (eq. 14).

$$NL = 0.5\left(\frac{1}{\gamma^2} - 1\right)\left(\frac{\sigma_{dh}}{\omega}\right)^2 \quad (14)$$

According to eq. 14, once set an expected σ_{dh} the correspondent NL value can be obtained. To make this information more operational, NL can be easily translated into the correspondent squared pixel size (SGRP) by eq. 15. This work under the condition that the ratio between azimuth and range pixel size is the one of S1, i.e. 1:4 (see Table 1).

$$SGRP\ (m) = \frac{\delta_{az} \cdot \sqrt{NL}}{2} \quad (15)$$

Considering that the accuracy of forest height by ground survey is lower than 3 m, in this work some simulations retrieving SGRP at σ_{dh} = 3 m were performed by changing γ value between 0.1 and 1 in eq. 14-15. This makes it possible to find an optimal value of NL suitable to guarantee the expected accuracy of forest estimates. Once optimal B and NL (or SGRP) values corresponding to an expected hv were found, that part of σ_{dh} , depending on settable operational parameters, can be finally minimized. Unfortunately, a significant part of σ_{dh} additionally depends on systematic errors like orbital-related ones, flattening residuals and atmospheric delays. These cannot be directly accounted for, because they are difficult to model. Nevertheless, one can try to remove/minimize them by considering height differences between neighbour targets in place of absolute height measures. Measure differencing is expected to reasonably remove these errors assuming that they occur similarly for close points [42].

Conversely, remaining error components depending on targets attributes, i.e. temporal decorrelation and random noise, cannot be further removed or minimized. Their joint effect on final uncertainty of dh, described in eq. 5, can be evaluated through simulations based on a sensitivity analysis approach. These were achieved by differencing a reference ground point, external to the forest, and showing a very high coherence value (≥ 0.8) with one representing the forest itself. The analysis proceeded by progressively varying the coherence value of

the forest point (γ_{FP}) from 0.05 to 1 and assuming different dh values as expected tree height ranging between 1 m and HOA.

3. Results and Discussions

To verify if dh values associated with tree heights could be reasonably estimated independently from phase unwrapping, HOA was related to B according to the above-mentioned equations, namely HOA=$2\pi \cdot \omega$ and eq. 1. B values were progressively changed to generate graphs of figure 2.

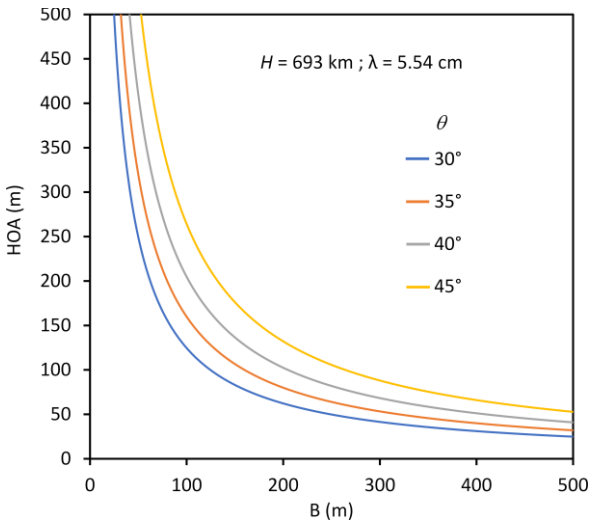

Figure 2. Maximum detectable dh (HOA), avoiding phase unwrapping, versus B and θ (simulation performed with reference to S1 nominal features).

With reference to figure 2, one can deduce that a baseline value lower than about 120 m can be used to ensure that forest height estimates can be given. In fact, rarely forests around the world show tree height higher than 100 m. If focusing on temperate forests where maximum tree height is 65 m, baseline values lower than about 270 m can be used ensuring to remain within HOA.

3.1. Theoretical Uncertainty of ω

ω is the parameter that converts the interferometric phase difference (radians) into the correspondent height difference (meters, dh). ω uncertainty (σ_ω)

depends both on the B, R, θ factors value and on their accuracy (eq. 6). Concerning σ_B, it was obtained considering the S1 declared positional accuracy of the ESA provided POD, i.e. 5 cm [35,36]. A reference value for σ_B was found to be equal to 12 cm. σ_θ was assumed equal to 0.01°, corresponding to the nominal antenna attitude accuracy for S1. σ_R was determined according to eq. 7. σ_{tropo} and σ_{iono} were set to 4 m and 1 m, respectively according to [52]. This is obviously an approximation since atmospheric conditions can locally change. The same paper [52] reports 0.4 m as reference value for σ_{proc}. σ_{TOF} was set equal to 3.3 m assuming that S1 *Bw* (see Table 1) is 46 MHz. According to the above-mentioned values σ_R was finally computed (eq. 7) resulting in 5.3 m. To investigate σ_ω dependency from involved parameters, one has to take care that R and θ change along the scene, while B and H could be assumed constant. Measuring errors affecting these system parameters (eq. 1) necessarily affect σ_ω. VPL can be used to explore how B and θ affects the theoretical value of σ_ω (eq. 6). Figure 3a shows that for B values greater than 50 m, σ_ω is lower than 10 m and increases while θ values increase (i.e. tending to the swath far range). These findings raise some doubts about eq. 3 that does not take into account error contribution of system parameters. Additionally, σ_ω appears to be highly significant. A more proper estimate of σ_{dh} could come from eq. 4 where, differently from eq. 3, σ_ω is considered.

In order to explore the importance of system parameters on σ_ω, correspondent weights (w_i) were computed according to equations reported in Table 2. Results are reported in figure 3b where it can be noted that 64%, 11% and 24% of the total variance (σ_ω^2) are due to the look angle, R and the mixed term accounting for R and θ correlation, respectively. B uncertainty participates for less than 1%. From an operational point of view, a rough sensitivity analysis can help to interpret results. For example, a look angle difference of 1° determines a Δω of about +3.7%; a satellite altitude difference of 10 km determines a Δω of about +1.4%; a slant range difference of 10 km determines a Δω of about +1.2 %. θ

appears to be the most conditioning factor for ω computation. Given these values, ω can be reasonably computed directly using the coarse estimates of θ, R, H, B as reported in the SAR metadata information or satellite approximated state vectors. While using S1 nominal features in eq. 6, it can be easily derived that σ_ω varies between 1 m to 10 m, thus demonstrating to significantly contribute to the interferometric-derived dh.

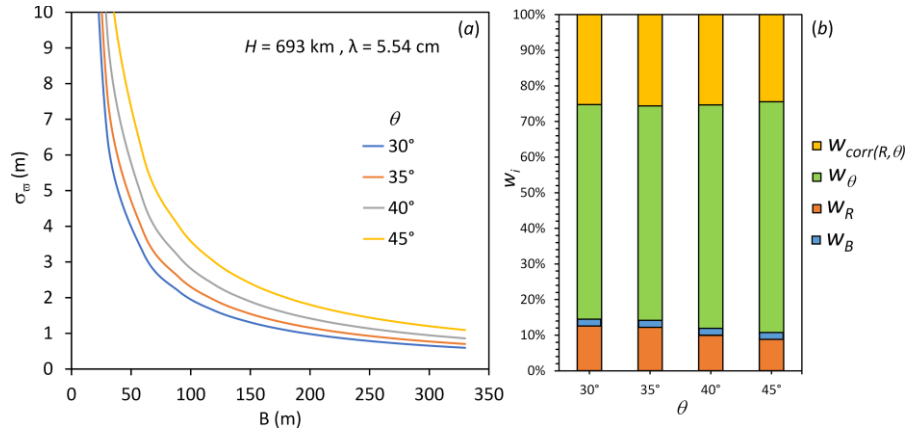

Figure 3. (a) σ_ω versus B and θ. (b) relative weights affecting ω variance involved in VPL. Note that wB is exaggerated by a factor 200.

3.2. Theoretical Uncertainty of $d\Delta\varphi$

According to eq. 11 and eq. 12, some simulations were done to explore the relationship between the baseline and γ_{geom} and γ_{vol} using S1 nominal values of table 1 (figure 4a and 4b). Figure 4a shows that expected forest height (i.e. the thickness of forest volume) does not significantly affects γ_{vol} if B is maintained lower than 50 m. Differently, for B values > 50 m, hv participates to reduce γ_{vol}. Figure 3b shows a perfect negative linear correlation between B and γ_{geom} having a steeper decreasing rate for lower look angles. Because $\gamma_{baseline} = \gamma_{geom} \cdot \gamma_{vol}$, according to eq. 9 one can admit that higher the baseline, lower $\gamma_{baseline}$ and higher $\sigma_{\Delta\varphi}$.

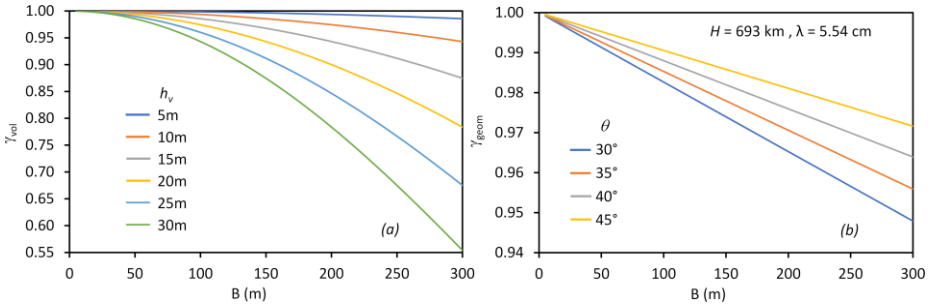

Figure 4. (a) γ_{vol} versus B and hv (θ= 35°). (b) γ_{geom} versus B and θ.

3.3. Minimizing σ_{dh} Through Simulated Scenarios

According to eq. 12, $\sigma_{d\Delta\varphi}$ depends on B and hv. To explore its dependency, B and hv were changed progressively from 5 m to 1000 m and from 5 m to 50 m, respectively, testing their effects on σ_{dh} (figure 5a).

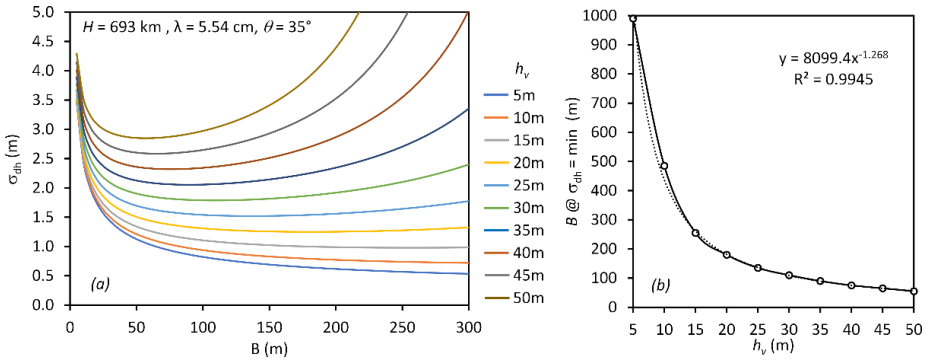

Figure 5. (a) Several scenarios of *dh* uncertainty according to h_v and B. (b) Power model relating hv and B at dh uncertainty is minimized.

Simulations in figure 5a show that hv value > 15 m (i.e. the majority of the forests), σ_{dh} presents a minimum with respect to B. It is worth noting that σ_{dh} values are certainly underestimated. In fact, $\gamma_{thermal}$, $\gamma_{Doppler}$, γ_{temp} are factors that cannot be properly modelled being independent from the features of interferometer. Considering B values minimize σ_{dh} for the different hv values, a model directly relating the "optimal" B value with the expected hv was defined (eq. 13 and figure 5b). A simple power model can be calibrated (eq.13) as

reported in figure 5b (see figure for model a, b and R2 coefficients). It is worth noting that the optimal B value occurs within the critical baseline (for S1, about 5 km) supporting the hypothesis that over vegetation the accuracy of interferometric-derived heights does not increase by using large baselines. The operational utility of this model can be easily exemplified using a case study. Suppose to investigate tree heights in a forest having an expected value of 25 m. The model of figure 5b makes possible to get an optimal baseline value of 150 m. Similarly, it can be said that the optimal B value in forests with tree heights ranging between 15 m and 30 m (the majority of forest in temperate zones) should range between 250 m and 100 m, respectively.

Since pixel size (NL/SGRP) has been proved to significantly impact $\sigma_{\Delta\varphi}$, and consequently $\sigma_{d\Delta\varphi}$ (eq. 9) some simulations were performed to describe SGRP dependency from γ (Fig. 6). Eq. 14 and eq. 15 were applied repeatedly assuming a reference σ_{dh} = 3 m, and setting the following values for the involved parameters: H = 693 km, θ = 35°, δ_{az} = 20 m. This made it possible to describe SGRP variation against γ and B. Figure 6 shows that SGRP is inversely proportional to γ.

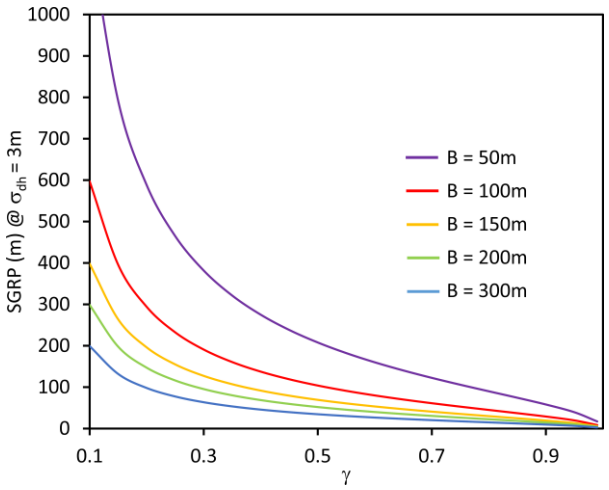

Figure 6. SGRP (squared pixel size) vs coherence. A σ_{dh} equal to 3 m was used during simulations obtained by varying γ and B.

Since vegetation usually presents medium-low coherence values expected in the range $0.2 < \gamma < 0.6$ [17], correspondent expected SGRP falls in the range 50-300m if B > 50 m. This SGRP (geometric resolution) is certainly not appropriate for a fine scale height retrieval; nevertheless, it appears to be proper for small scale analysis (wide areas) generating a granularity that is consistent with the ones from traditional forest surveys. These are, in fact characterized by a low-density of ground sampling (plots) [53].

Once the optimal B values was found and, consequently, the correspondent SGRP found, σ_{dh} can be estimated as a function of γ_{FP} and expected dh. To investigate these dependencies, a simulation was run assuming baseline values in the range 50-200 m using eq. 5 (Fig. 7). During simulations the following operational parameters were used NL = 100, $\theta = 35°$, H = 693 km. Figure 7 shows that dh values consistent with forest height in the range 10-65 m generate σ_{dh} values varying between 1 m down to 70 m depending on γ_{FP} (coherence of the forest area) and B values. The most favourable conditions occur for high γ_{FP} and larger baselines. A focus point is that σ_{dh} remains at low values while γ is higher than about 0.2, to suddenly and significantly increase once this threshold is overcome. This suggests that a γ value of 0.2 can be somehow used to define significant/reliable measures. In general, when dh tends to HOA σ_{dh} is higher, suggesting that small dh values are more accurate than large ones. Operationally speaking, since authors approach is based on height difference computation, expected dh values (10-65 m) are always lower and lower than HOA and result in a $\sigma_{dh} < 5$m. Some examples are reported in Table 3.

Table 3. Best cases from simulations in a typical Italian forest context (tree height in the range 10-30 m).

Baseline (m)	***Expected dh (m)***	***σ_{dh} (m)***
50	10-30	2
100	10-30	2
150	10-30	1
200	10-30	0.5

Similar results were found in [32,54] by using ERS-1 data where phase unwrapping was adopted. Otherwise, in the proposed approach similar accuracy was found avoiding phase unwrapping, resulting into a more robust and controllable forest height uncertainty estimation. Moreover, values of Table 3 prove that forest height estimates from S1 InSAR data can generate results having an accuracy comparable to the one from traditional surveys, making this technique an effective tool for forest structural monitoring.

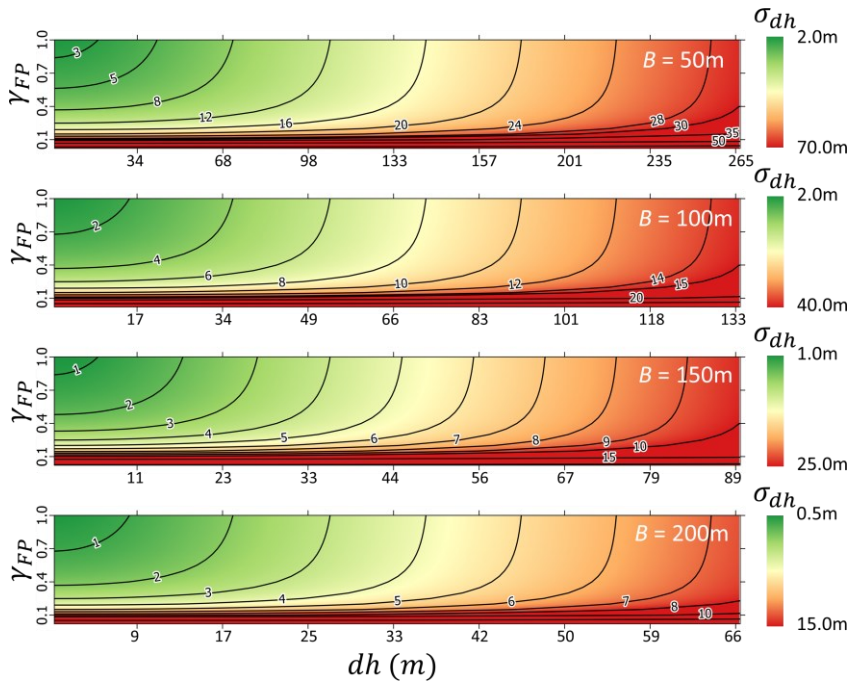

Figure 7. Several scenarios of dh uncertainty according to expected γ_{FP} and dh at different B values. Isolines refer to the same σ_{dh}values.

Once more, these evidences highlight that an InSAR technique operated according to the above mentioned optimization criteria can drive to forest height estimates consistent with the ones from ground survey. Nevertheless, some limitations still persist concerning low coherence targets where InSAR fails to retrieve reliable forest height estimates (J. Askne et al., 1997). It is worth to stress, that all these findings are based on simulations, therefore, future developments will be expected to sustain these deductions using real data and quantifying the actual (not the expected) errors in forest height retrieval.

4. Conclusions

This work proved that S1 interferometric data can be effectively adopted to retrieve forest height. In particular, adopting the topographic levelling approach based on local differencing between interferogram from a forest pixel and a neighbour bare soil one permits to operate with no phase unwrapping driving to an unambiguous height estimate. Authors proved that tuning of an optimal baseline and multilooking factor can improve the accuracy of forest height retrieval. In particular, forest heights in the range 10-30 m requires optimal baseline between 250 and 100 m. Furthermore, contrarily to the general rule that suggests large B values to improve InSAR-derived DEM accuracy, this work demonstrates that, in forest areas, the same rule fails. In fact, by increasing B, forest coherence decreases reducing interferometric phase accuracy. A simple model was, additionally, proposed and calibrated aimed at predicting the optimal B value (and therefore image pair selection) for σ_{dh} minimization. Regarding spatial density of forest height estimates, it was found that SGRP values between 50-100 m can guarantee a σ_{dh} < 3 m. This resolution is certainly not appropriate for fine scale analysis, suggesting the adoption of this method when small scale (wide areas) mapping of forest heights is required. Finally, in this paper authors proved that S1 InSAR data processed focusing on height differencing computation (see eq. 2) is more effective in retrieving forest heights with

medium-high accuracy. This has necessarily to be achieved opportunely tuning user-dependent parameters (B, NL, B_{temp}) according to the above-mentioned maximization criteria.

References:

1. Segura, M.; Kanninen, M. Allometric Models for Tree Volume and Total Aboveground Biomass in a Tropical Humid Forest in Costa Rica 1. Biotropica: The Journal of Biology and Conservation 2005, 37, 2–8.

2. Laurin, G.V.; Ding, J.; Disney, M.; Bartholomeus, H.; Herold, M.; Papale, D.; Valentini, R. Tree Height in Tropical Forest as Measured by Different Ground, Proximal, and Remote Sensing Instruments, and Impacts on above Ground Biomass Estimates. International Journal of Applied Earth Observation and Geoinformation 2019, 82, 101899.

3. Hao, Z.; Zhang, J.; Song, B.; Ye, J.; Li, B. Vertical Structure and Spatial Associations of Dominant Tree Species in an Old-Growth Temperate Forest. Forest Ecology and Management 2007, 252, 1–11.

4. Song, B.; Chen, J.; Desander, P.V.; Reed, D.D.; Bradshaw, G.A.; Franklin, J.F. Modeling Canopy Structure and Heterogeneity across Scales: From Crowns to Canopy. Forest Ecology and Management 1997, 96, 217–229.

5. Spies, T.A. Forest Structure: A Key to the Ecosystem. Northwest science 1998, 72, 34–36.

6. Lund, H.G. When Is a Forest Not a Forest? Journal of Forestry 2002, 100, 21–28.

7. Sillett, S.C.; Van Pelt, R.; Koch, G.W.; Ambrose, A.R.; Carroll, A.L.; Antoine, M.E.; Mifsud, B.M. Increasing Wood Production through Old Age in Tall Trees. Forest Ecology and Management 2010, 259, 976–994.

8. Hanewinkel, M.; Hummel, S.; Albrecht, A. Assessing Natural Hazards in Forestry for Risk Management: A Review. European Journal of Forest Research 2011, 130, 329–351.

9. Martins, A.C.; Willig, M.R.; Presley, S.J.; Marinho-Filho, J. Effects of Forest Height and Vertical Complexity on Abundance and Biodiversity of Bats in Amazonia. Forest Ecology and Management 2017, 391, 427–435.

10. Bohn, F.J.; Huth, A. The Importance of Forest Structure to Biodiversity–Productivity Relationships. Royal Society open science 2017, 4, 160521.

11. Bragg, D.C. Accurately Measuring the Height of (Real) Forest Trees. Journal of Forestry 2014, 112, 51–54, doi:10.5849/jof.13-065.

12. Larsen, D.R.; Hann, D.W.; Stearns-Smith, S.C. Accuracy and Precision of the Tangent Method of Measuring Tree Height. Western Journal of Applied Forestry 1987, 2, 26–28.

13. De Petris, S.; Berretti, R.; Sarvia, F.; Borgogno Mondino, E. When a Definition Makes the Difference: Operative Issues about Tree Height Measures from RPAS-Derived CHMs. iForest-Biogeosciences and Forestry 2020, 13, 404.

14. Hüttich, C.; Eberle, J.; Shvidenko, A.; Schepaschenko, D. Supporting a Forest Observation System for Siberia: Earth Observation for Monitoring, Assessing and Providing Forest Resource Information. 2014.

15. Goldstein, R.M.; Zebker, H.A.; Werner, C.L. Satellite Radar Interferometry: Two-Dimensional Phase Unwrapping. Radio science 1988, 23, 713–720.

16. Chen, C.W.; Zebker, H.A. Phase Unwrapping for Large SAR Interferograms: Statistical Segmentation and Generalized Network Models. IEEE Transactions on Geoscience and Remote Sensing 2002, 40, 1709–1719.

17. Braun, A. Retrieval of Digital Elevation Models from Sentinel-1 Radar Data–Open Applications, Techniques, and Limitations. Open Geosciences 2021, 13, 532–569.

18. Hagberg, J.O.; Ulander, L.M.; Askne, J. Repeat-Pass SAR Interferometry over Forested Terrain. IEEE Transactions on Geoscience and Remote Sensing 1995, 33, 331–340.

19. Santoro, M.; Askne, J.; Dammert, P.B. Tree Height Influence on ERS Interferometric Phase in Boreal Forest. IEEE Transactions on Geoscience and Remote Sensing 2005, 43, 207–217.

20. Romero-Puig, N.; Lopez-Sanchez, J.M. A Review of Crop Height Retrieval Using InSAR Strategies: Techniques and Challenges. IEEE Journal of Selected Topics in Applied Earth Observations and Remote Sensing 2021.

21. De Petris, S.; Sarvia, F.; Gullino, M.; Tarantino, E.; Borgogno-Mondino, E. Sentinel-1 Polarimetry to Map Apple Orchard Damage after a Storm. Remote Sensing 2021, 13, 1030.

22. Sarvia, F.; Xausa, E.; De Petris, S.D.; Cantamessa, G.; Borgogno-Mondino, E. A Possible Role of Copernicus Sentinel-2 Data to Support Common Agricultural Policy Controls in Agriculture. Agronomy 2021, 10, doi:https://doi.org/10.3390/ agronomy11010110.

23. De Petris, S.; Sarvia, F.; Borgogno-Mondino, E. Multi-Temporal Mapping of Flood Damage to Crops Using Sentinel-1 Imagery: A Case Study of the Sesia River (October 2020). Remote Sensing Letters 2021, 12, 459–469, doi:10.1080/2150704X.2021.1890262.

24. Vollrath, A.; Mullissa, A.; Reiche, J. Angular-Based Radiometric Slope Correction for Sentinel-1 on Google Earth Engine. Remote Sensing 2020, 12, 1867.

25. Reiche, J.; Lucas, R.; Mitchell, A.L.; Verbesselt, J.; Hoekman, D.H.; Haarpaintner, J.; Kellndorfer, J.M.; Rosenqvist, A.; Lehmann, E.A.; Woodcock, C.E. Combining Satellite Data for Better Tropical Forest Monitoring. Nature Climate Change 2016, 6, 120–122.

26. Veci, L. SENTINEL-1 Toolbox SAR Basics Tutorial. ARRAY Systems Computing, Inc. and European Space Agency: Paris, France 2015.

27. Garestier, F.; Dubois-Fernandez, P.C.; Papathanassiou, K.P. Pine Forest Height Inversion Using Single-Pass X-Band PolInSAR Data. IEEE Transactions on Geoscience and Remote Sensing 2007, 46, 59–68.

28. Managhebi, T.; Maghsoudi, Y.; Zoej, M.J.V. A Volume Optimization Method to Improve the Three-Stage Inversion Algorithm for Forest Height Estimation Using PolInSAR Data. IEEE Geoscience and Remote Sensing Letters 2018, 15, 1214–1218.

29. Cloude, S.R.; Chen, H.; Goodenough, D.G. Forest Height Estimation and Validation Using Tandem-X Polinsar. In Proceedings of the 2013 IEEE International Geoscience and Remote Sensing Symposium-IGARSS; IEEE, 2013; pp. 1889–1892.

30. Soja, M.J.; Persson, H.; Ulander, L.M. Estimation of Forest Height and Canopy Density from a Single InSAR Correlation Coefficient. IEEE Geoscience and remote sensing letters 2014, 12, 646–650.

31. Askne, J.; Santoro, M. Multitemporal Repeat Pass SAR Interferometry of Boreal Forests. IEEE Transactions on Geoscience and Remote Sensing 2005, 43, 1219–1228.

32. Askne, J.I.; Dammert, P.B.; Ulander, L.M.; Smith, G. C-Band Repeat-Pass Interferometric SAR Observations of the Forest. IEEE Transactions on Geoscience and Remote Sensing 1997, 35, 25–35.

33. Ainsworth, T.L.; Kelly, J.; Lee, J.-S. Polarimetric Analysis of Dual Polarimetric SAR Imagery. In Proceedings of the 7th European Conference on Synthetic Aperture Radar; VDE, 2008; pp. 1–4.

34. Geudtner, D.; Torres, R.; Snoeij, P.; Davidson, M.; Rommen, B. Sentinel-1 System Capabilities and Applications. In Proceedings of the 2014 IEEE Geoscience and Remote Sensing Symposium; IEEE, 2014; pp. 1457–1460.

35. Torres, R.; Snoeij, P.; Geudtner, D.; Bibby, D.; Davidson, M.; Attema, E.; Potin, P.; Rommen, B.; Floury, N.; Brown, M. GMES Sentinel-1 Mission. Remote Sensing of Environment 2012, 120, 9–24.

36. Small, D.; Schubert, A. Guide to Sentinel-1 Geocoding 2019.

37. Attema, E.; Davidson, M.; Snoeij, P.; Rommen, B.; Floury, N. Sentinel-1 Mission Overview. In Proceedings of the 2009 IEEE International Geoscience and Remote Sensing Symposium; IEEE, 2009; Vol. 1, p. I–36.

38. Li, F.K.; Goldstein, R.M. Studies of Multibaseline Spaceborne Interferometric Synthetic Aperture Radars. IEEE Transactions on Geoscience and Remote Sensing 1990, 28, 88–97.

39. Rodriguez, E.; Martin, J.M. Theory and Design of Interferometric Synthetic Aperture Radars. In Proceedings of the IEE Proceedings F (Radar and Signal Processing); IET, 1992; Vol. 139, pp. 147–159.

40. Richards, J.A. Remote Sensing with Imaging Radar; Springer, 2009; Vol. 1;.

41. Clancy, J. Site Surveying and Levelling; Routledge, 2013;

42. Hanssen, R.F. Radar Interferometry: Data Interpretation and Error Analysis; Springer Science & Business Media, 2001; Vol. 2;.

43. Hughes, I.; Hase, T. Measurements and Their Uncertainties: A Practical Guide to Modern Error Analysis; OUP Oxford, 2010;

44. Pepe, A.; Calò, F. A Review of Interferometric Synthetic Aperture RADAR (InSAR) Multi-Track Approaches for the Retrieval of Earth's Surface Displacements. Applied Sciences 2017, 7, 1264.

45. Ferretti, A.; Monti-Guarnieri, A.V.; Prati, C.M.; Rocca, F.; Massonnet, D. INSAR Principles B; ESA publications, 2007;

46. Zebker, H.A.; Villasenor, J. Decorrelation in Interferometric Radar Echoes. IEEE Transactions on geoscience and remote sensing 1992, 30, 950–959.

47. Yagüe-Martínez, N.; Prats-Iraola, P.; Gonzalez, F.R.; Brcic, R.; Shau, R.; Geudtner, D.; Eineder, M.; Bamler, R. Interferometric Processing of Sentinel-1 TOPS Data. IEEE Transactions on Geoscience and Remote Sensing 2016, 54, 2220–2234.

48. Qin, Y.; Perissin, D.; Bai, J. Investigations on the Coregistration of Sentinel-1 TOPS with the Conventional Cross-Correlation Technique. Remote Sensing 2018, 10, 1405.

49. Jung, J.; Kim, D.; Lavalle, M.; Yun, S.-H. Coherent Change Detection Using InSAR Temporal Decorrelation Model: A Case Study for Volcanic Ash Detection. IEEE Transactions on Geoscience and Remote Sensing 2016, 54, 5765–5775.

50. Ahmed, R.; Siqueira, P.; Hensley, S.; Chapman, B.; Bergen, K. A Survey of Temporal Decorrelation from Spaceborne L-Band Repeat-Pass InSAR. Remote Sensing of Environment 2011, 115, 2887–2896.

51. Santoro, M.; Shvidenko, A.; McCallum, I.; Askne, J.; Schmullius, C. Properties of ERS-1/2 Coherence in the Siberian Boreal Forest and Implications for Stem Volume Retrieval. Remote sensing of environment 2007, 106, 154–172.

52. Gisinger, C.; Schubert, A.; Breit, H.; Garthwaite, M.; Balss, U.; Willberg, M.; Small, D.; Eineder, M.; Miranda, N. In-Depth Verification of Sentinel-1 and TerraSAR-X Geolocation Accuracy Using the Australian Corner Reflector Array. IEEE Transactions on Geoscience and Remote Sensing 2020, 59, 1154–1181.

53. Wagner, F.; Rutishauser, E.; Blanc, L.; Herault, B. Effects of Plot Size and Census Interval on Descriptors of Forest Structure and Dynamics. Biotropica 2010, 42, 664–671.

54. Dammert, P.B. Accuracy of INSAR Measurements in Forested Areas. In Proceedings of the ERS SAR Interferometry; 1997; Vol. 406, p. 37.

55. Askne, J.; Dammert, P.B.; Smith, G. Interferometric SAR Observations of Forested Areas. In Proceedings of the Third ERS Symposium on Space at the service of our Environment; 1997; Vol. 414, p. 337.

5.2.2 Forest Height Estimation Using Sentinel-1 Interferometry. A Phase Unwrapping-Free Method Based on Least Squares Adjustment

De Petris Samuele[a*], Cuozzo Giovanni [b], Notarnicola Claudia[b], and Borgogno- Mondino Enrico[a]

[a]Department of Agricultural, Forest and Food Sciences (DISAFA), University of Turin, 10095 Grugliasco, Italy.

[b]Institute for Applied Remote Sensing, EURAC Research, Bolzano (BZ), Italy

*Correspondence: samuele.depetris@unito.it

Published: 2022 in *Communications in Computer and Information Science,* Book Series.

Abstract: Forest height is a fundamental parameter in forestry. SAR interferometry (InSAR) has been widely used to retrieve digital elevation models (DEM), which are designed to provide a continuous representation of Earth topography, including forests. The ordinary InSAR framework requires a further phase un-wrapping step in order to recover unambiguously the actual topography over the entire scene. The latter was proved to fail over vegetation due to low coherence values and therefore all algorithms tend to avoid these areas during the unwrapping, making InSAR-derived DEM over vegetation very unreliable. In this work, an alternate technique was coupled to least squares adjustment (LSA) with the aim of retrieving accurate forest heights avoiding phase unwrapping. It was com-puted entirely using free available Sentinel-1 data and SNAP ESA software. A mean absolute error equal to 2.6 m was found and it is consistent to the one esti-mated by LSA theoretical uncertainty. Preliminary outcomes suggest that proposed approach could be a valid alternative to retrieve forest height based on free data/software constituting an example of technological transfer of SAR technology into forest operative sector.

Keywords: Forest height, SAR, Interferometry, Least Squares Adjustment.

1. Introduction

Forest height is a fundamental parameter in forestry. It is related to AGB, timber volume [1] and canopy vertical structure [2]. Forest height is often measured using hypsometers with a precision of 1 m to 3 m during ground operations [3, 4] . Unfortunately, ground surveys take a long time and are expensive, so they are sparse across forested areas. Remote sensing, on the other hand, may cover this gap by giving continuous forest height estimates over large regions that are even more precise than ground measurements [5] . Space-based earth observation missions are well-suitable for forest needs, allowing a mapping and monitoring of large regions, as well as the early detection of changes and regular updating of forest attributes [6–9]. Synthetic aperture radar (SAR) is known to be sensitive to forest geometry characteristics, allowing data to be recorded in any weather state, even over equatorial/tropical ones where clouds are usually always present. SAR interferometry (InSAR) methodology has been widely used to retrieve digital elevation models (DEM), which are designed to provide a continuous representation of Earth topography, including forests.

In this context, satellite missions, such as the European Union's (EU) Copernicus Sentinels, are known to provide large amounts of data that may be used to support environmental research and land management. However, even if web-based services based on this data are becoming operational, technical transfer appears to be restrict-ed at the moment [10–12]. SAR imaging, in the broader context of satellite open data, exhibits a significant limitation in terms of accessing operational services, due to the complex nature of data processing and data availability [13, 14]. The typical InSAR processing methodology includes a phase unwrapping step intended at unambiguously reconstructing the local topography, which is usually accomplished by processing the entire scene unitarily. This method has proven to be particularly ineffective over vegetation due to low coherence values; as a result, ordinary algorithms avoid these areas (or failed) during unwrapping [15, 16], making InSAR-derived DEMs exceedingly unreliable over vegetation [17]. Furtherly, ordinary un-wrapping

processing that InSAR software accomplishes, in the most of cases, hides the consciousness and an easy interpretability of results, making derived measures unreliable. In this paper, an alternative technique not been extensively explored in the literature [18–20], is discussed for generating more trustworthy and precise estimations of forest height using InSAR without phase unwrapping. This method changes the working paradigms moving from a mapping problem to a retrieval one based on the comparison between a forest pixel interferogram and a reference one closely located outside the forest.

In this work, the previous-mentioned approach was combined to least squares adjustment with the aim of retrieving accurate forest heights avoiding phase unwrap-ping. In order to facilitate the operational transfer of our deductions, proposed approach relays entirely on free available and accessible SAR open data and software (guaranteed cost-effective) with a special focus on the Copernicus Sentinel-1 (S1) mission.

2. Materials and Methods

2.1. Study Area

The area of interest (AOI) is called “Staffarda forest” and is located in the lowland part of Cuneo province (NW- Italy). AOI sizes about 4 km2 (Fig. 1) and is characterized by the presence of Pedunculate oak-hornbeam forest [21]. In Italy, this type of forests has an high naturalistic values since it is one of the last remaining mixed floodplain forests in northern Italy and one of the most endangered ecosystems in Europe [22].

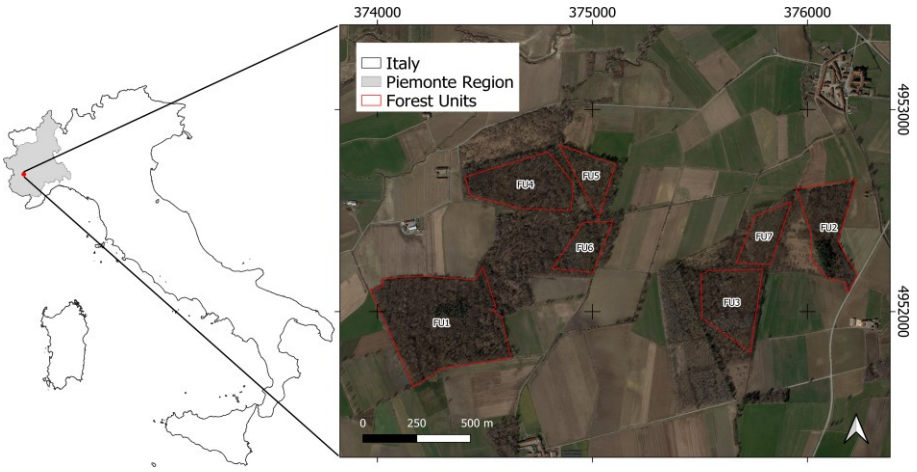

Figure 1. AOI location and forest units (FUs). Google Satellite base map was adopted (WGS84 UTM32N reference frame).

2.2. Reference Data

The digital surface model (DSM) derived by an aerial photogrammetric survey (rDSM) was adopted to test the accuracy of proposed approach (Fig. 2). The aerial survey was performed in December 2019 by Digisky s.r.l. company. After the image block bundle adjustment [23], the photogrammetric point cloud was filtered and regularized into a gridded DSM with a ground sample distance (GSD) of 0.3 m having a plano-altimetric accuracy of 0.2 m. Moreover, a global navigation satellite system (GNSS) ground survey was performed to define forest units (FUs). FUs are forest are-as having homogeneous vertical/horizontal structure and same expected silvicultural treatments adopted in forest planning [24]. A total of 7 FUs was acquired having a mean extension of about 15 ha.

Figure 2. rDSM (GSD = 0.3 m) over AOI. Google Satellite base map was adopted (WGS84 UTM32N reference frame).

2.3. Digital Elevation Model Data

In this work, the Piemonte region Digital Terrain Model (DTM) was used to geocode SAR-derived products and obtain elevation information for AOI. DTM was downloaded for free from Piemonte Geoportal (https://www.geoportale.piemonte.it/cms/). DTM has an elevation accuracy of about 0.6 m [25, 26] and was updated in 2009. It is provided already orthoprojected into WGS84 UTM 32N reference system with a GSD of 0.5 m.

2.4. Sentinel-1 Imagery

Currently, S1 is one of the largest space-borne mission giving free and open access to SAR data. The S1 mission is a two-satellite constellation that records C-band data (5.6 cm wavelength). Over land, the interferometric wide swath (IW) acquiring backscattered signal in dual pole (VV and VH) is the main acquisition mode. Images are natively recorded in SAR geometry (Range and Azimuth) and complex values (I/Q components). S1 mission is particularly suitable for a wide range of applications, including forest mapping, due to its medium-high spatial resolution and short revisit time (6 days). Furthermore, the European Space Agency (ESA) makes the free soft-ware SNAP (Sentinel Application Platform)

available to users, allowing an easier and efficient use of Copernicus Program products [17, 27]. To preliminary test the pro-posed approach a single interferometric pair was selected and downloaded from Alaska Satellite Facility online tool [28]. Ordinarily, InSAR-derived DEM accuracy is higher for long baselines [29], nevertheless, this condition appears to fail over vegetation. In fact, longer baselines make coherence decreasing, thus negatively affecting forest height accuracy. Moreover, also temporal baseline could significantly affect interferogram reliability. Since forests are continuously changing, longer the temporal baseline, lower the associated coherence (temporal decorrelation) [17, 30]. Therefore, short temporal baseline and winter acquisitions are more suitable for forest height retrieval in temperate zone [31]. To take care about these issues, two S1 single look complex (SCL) IW images in ascending mode acquired on 20th and 26th December 2019 were collected. The selected interferometric pair has a perpendicular baseline of about 90 m guaranteeing the shorter temporal baseline available from S1 mission (i.e. 6 days) during the 2019 winter season over AOI. To avoid decorrelation errors due to rainfall events, no precipitation events were found from the meteorological data (https://www.arpa.piemonte.it/) in observed period.

2.5. Methodology and Data Processing

Interferogram computation. The interferometric pair was pre-processed using the free software SNAP vs 8.0 provided by ESA and according to common used pro-cessing chain [32]. The basic steps include TOPS Split, which reduces the SLC data to selected number of bursts within a sub-swath. Then, enhanced spectral diversity [33] were applied to refine the azimuth offset estimation and exploit a better fine coregistration provided by back geocoding. Subsequently, coherence estimates were mapped using 10x2 window (range and azimuth pixels respectively) and the interferogram was computed including flat-earth phase removal. The latter was computed by fitting a 5-degree polynomial involving 501 points distributed over interferogram. Using data from orbits state vectors and images metadata the flat-earth phase was then subtracted from the complex

interferogram. After deburst, Goldstein filter was applied [34] using a window size of 3x3. Multilooking was also applied to the interferogram and coherence complex values [35] generating images having squared pixels sizing of about 30x30m. Finally, the multilooked interferogram and coherence data were projected into WGS84/UTM 32N reference frame using DTM and Range Doppler terrain correction [36].

2.5.1. Interferometric Phase Modelling.

The SAR interferometry technique is based on the image pairs processing acquired from multiple locations separated by distance known as a baseline (B). This criterion allows to recover topography via a simple geometric relationship [37]. The contribution to the interferometric phase provided by local topography is determined according to eq.1.

$$\frac{\partial \Delta\varphi}{\partial h} = \frac{4\pi\, Bn}{\lambda\, R\, \sin\theta} \quad (1)$$

where $\Delta\varphi$ is the interferometric phase; h is the target point elevation; λ is the radar wavelength; R is the sensor-target slant range; θ is the antenna off-nadiral angle (look angle) and Bn is the normal baseline length. Based on this relationship, the ordinary InSAR framework requires a further phase unwrapping step in order to recover unambiguously the actual topography over the entire scene. The latter was proved to fail over vegetation due to low coherence values and therefore all algorithms tend to avoid these areas during the unwrapping [15, 16] making InSAR-derived DEM over vegetation very unreliable [17]. An alternative approach, not widely explored in literature, to avoid phase unwrapping was proposed by [18–20]. This method changes the working paradigms moving from a mapping problem to a retrieval one involving, at least, one interferogram pixel from flat terrain close to forest and other over forest canopy. In principle, from eq.1, the elevation difference of a given point, dh(x,y), corresponding to the interferometric phase difference at that point is given by eq. 2. This approach is

similar to a topographic levelling problem [38] where the surveyed variable is the heigh difference (*dh*) between two points (eq. 2).

$$dh(x,y) = \omega\,[\Delta\varphi(x,y) - \Delta\varphi^{RP}] \quad (2)$$

Where $\Delta\varphi(x,y)$ and $\Delta\varphi^{RP}$ are the target point (in this work a forest point) and reference point interferometric phases respectively; ω is the sensitivity of the topography to an interferometric phase variation and it is computed as the inverse of eq.1 as proposed by [37]. Subsequently, forest point absolute elevation, $h(x,y)$), can be obtained by adding dh to, at least, one reference point having known elevation (h^{RP}- eq. 3).

$$h(x,y) = dh(x,y) + h^{RP} \quad (3)$$

It is worth to highlight that eq. 2 not requires phase unwrapping (phase ambiguity term) only if the expected height difference is lower than height of ambiguity (HOA) of the interferometer [19, 39]. Since in this work HOA (deduced by SNAP metadata) is equal to 161.2 m, phase ambiguity term can be neglected because temperate forest heights do not commonly exceed 60 m [2] and no significant terrain variation exists in AOI.

Forest height retrieval using least squares adjustment. In this work, the paradigm in eq. 3 was applied to flattened interferogram-derived measures and solved by a least squares adjustment (LSA) approach. LSA is a statistical tool commonly adopted to contemporarily solve levelling network and estimate the corrections to be given to the height difference measurements in order to make them all congruent to each other and satisfy the geometrical relations existing between them. In levelling network problem dh differences should be theoretically equal to 0. Unfortunately, in real levelling loop it does not happen due to measurement errors. Especially in interferometry, phase measures over vegetation are affected by many limitations mainly due to noise induced by canopy volume and signal decorrelation. This unneglectable noise deeply affects dh resulting from eq. 2

application. All systematic errors like orbital-related ones, flattening residuals and atmospheric delays can be mathematically removed by considering height differences between neighboring interferogram pixels. In fact, measure differencing is expected to reasonably remove these errors assuming that they occur similarly for close points [40] (in this work interferogram pixels are at most 2 km apart). Nevertheless, LSA can mitigates the accidental observational errors component [41, 42] by share it according to defined weights across the system of equations of eq. 4.

$$\widehat{\boldsymbol{\beta}} = \left(\boldsymbol{A^T\, W\, A}\right)^{-1} \cdot \left(\boldsymbol{A^T\, W\, L}\right) \tag{4}$$

Where $\widehat{\boldsymbol{\beta}}$ is a column vector containing the elevations of the target points, $h(x, y)$ (in m a.s.l.); **A** is the design matrix; **W** is the weights matrix; **L** is the observations vector. Starting from flattened interferogram, the average interferometric phase value ($\mu_{\Delta\varphi}$) was computed for each FU and its uncertainty estimated by applying the variance propagation law to the average operator assuming pixels having different uncertainty (eq. 5).

$$\sigma_{\mu_{\Delta\varphi}} = \sqrt{\frac{\sum_{i=1}^{n} \sigma^2_{\Delta\varphi(x,y)}}{n^2}} \tag{5}$$

Where *n* is the number of interferogram pixels for each FU; $\sigma_{\Delta\varphi(x,y)}$ is the uncertainty of interferometric phase pixel. $\sigma_{\Delta\varphi(x,y)}$ was deeply proved [18, 29, 43] to be related to local coherence magnitude and can be properly computed using eq. 6.

$$\sigma_{\Delta\varphi(x,y)} = \frac{1}{\sqrt{2NL}} \frac{\sqrt{1-|\gamma(x,y)|^2}}{|\gamma(x,y)|} \tag{6}$$

Where *NL* is the multilooking factor i.e. the number of pixels used to compute the complex multilooked interferogram (in this work set = 20); |γ(x,y)| is the local coherence magnitude. To fix the datum above so that $\widehat{\boldsymbol{\beta}}$ an be computed,

observations having known elevation are required in the LSA system. These were derived by photointerpreting some ground flat areas (GFAs) on coherence map. GFA was delineated as polygon layer searching for highly coherence patches ($\gamma > 0.8$) representing ground level having no significant vegetation cover. Built-up areas were excluded from GFA delineation by simultaneously checking their presence on the available Google Earth true colour orthophoto updated in 2019. The mean DTM and interferometric phase values were computed and assigned to GFA centroids (hereafter called reference points - RPs). A total of 7 GFA (and RP) were selected in AOI. Concerning LSA, **L** was defined as vector containing n·(n-1)/2 height differences computed by eq. 2 and involving $\mu_{\Delta\varphi}$, RP phases and ω. The latter was computed as HOA/2π, where HOA was obtained by image pair metadata available in SNAP. Additionally, RP elevations were added to **L** to fix the datum. To take in to account the uncertainty of each observation in the LSA system, **W** elements were defined as the inverse of $\sigma_{\mu_{\Delta\varphi}}$ containing $\mu_{\Delta\varphi}$ (eq. 7), while a value of 100 was assigned for constraining observations involving RP. The latter value was preventively set to 100 to give a high weight to RP elevations observations constraints.

$$\boldsymbol{W} = \begin{bmatrix} 100 & 0 & \cdots & 0 & 0 & \cdots & \cdots & \cdots & 0 \\ 0 & 100 & 0 & 0 & 0 & \cdots & \cdots & \cdots & 0 \\ \vdots & \ddots & \ddots & \vdots & 0 & \cdots & \cdots & \cdots & 0 \\ 0 & \cdots & 0 & 100 & 0 & \cdots & \cdots & \cdots & 0 \\ 0 & \cdots & \cdots & \cdots & \delta_{i,j} & 0 & \cdots & \cdots & 0 \\ 0 & \cdots & \cdots & \cdots & 0 & \vdots & \ddots & \vdots & \vdots \\ 0 & \cdots & \cdots & \cdots & 0 & \cdots & \cdots & \cdots & \delta_{i,j} \end{bmatrix} \quad (7)$$

Where $\delta_{i,j} = \frac{1}{\sigma_{\mu_{\Delta\varphi}}}$. Once $\widehat{\boldsymbol{\beta}}$ was estimated, the uncertainty of each $h(x,y)$, $\sigma_{\widehat{\beta i}}$, can be estimated according to eq. 8.

$$\sigma_{\widehat{\beta i}} = \sqrt{\mathbf{C_{\beta\beta}}ii} \quad (8)$$

Where $\mathbf{C_{\beta\beta}}ii$ are the diagonal elements of $\mathbf{C_{\beta\beta}}$.The latter is the variance-covariance matrix of the parameters computed according to eq. 9

$$\mathbf{C_{\beta\beta}} = \frac{\boldsymbol{\varepsilon^t W \varepsilon}}{m-n} \cdot \left(\boldsymbol{A^T\, W\, A}\right)^{-1} \quad (9)$$

Where ε is the LSA residuals vector; m is the number of equations in LSA (in this work 91, i.e. 14x13/2) and n is the number of unknowns (in this work equal to 14 $h(x,y)$).

2.5.2. Validation

To test the accuracy of elevation estimates over forest, a validation set based on rDSM was generated. In particular, the mean ($\overline{rDSM}$) and standard deviation (σ_{rDSM}) values were computed for each FUs. Finally, the mean absolute error (MAE) [44] was computed comparing only forest $h(x,y)$ estimates of $\widehat{\boldsymbol{\beta}}$ and $\overline{rDSM}$. To test the presence of a significant bias in the proposed approach, normality of errors was assessed by Shapiro-Wilk test [45] and the t-test was used to assess zero-mean condition of errors [46].

3. Results and Discussions

3.1. Interferogram Computation

After the pre-processing in SNAP, the multilooked flattened interferogram and coherence maps were generated (Figure 3) and subsequently managed by ordinary GIS tool.

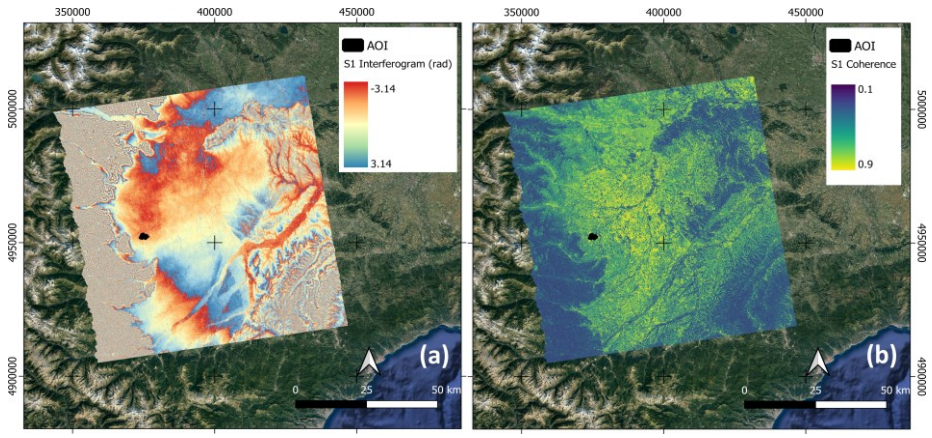

Figure 3. (a) Multilooked flattened Interferogram; (b) multilooked coherence map (WGS84 UTM32N reference frame).

3.2. Forest Height Retrieval Using Least Squares Adjustment

Staring from coherence map, GFAs and RPs were generated (Figure 4). Using a self-developed routine in R software vs 3.0.0, the LSA approach was implemented and performed involving $\mu_{\Delta\varphi}$, RP interferometric phases and ω. The latter was used as gain factor that allows to convert the interferometric phase difference into height difference (eq. 2). It was computed as HOA/2π and found equal to 25.65. To fix the datum RP elevation values were also included in the LSA.

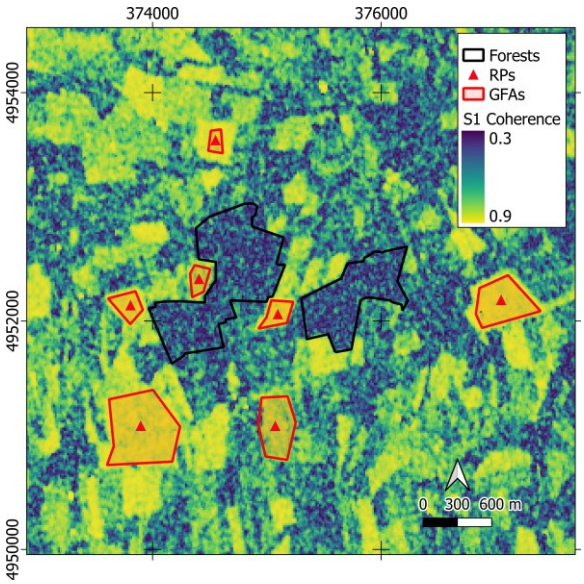

Figure 4. Coherence map, GFAs and RPs location in AOI (WGS84 UTM32N reference frame).

3.3. Validation

FU heights, $h(x,y)$, were finally estimated by LSA and compared to $\overline{rDSM}$. Results were reported in figure 5. A MAE of 2.63 m was found. It is worth to remind that such accuracy is consistent with the one obtainable from ordinary ground survey based on hypsometers (Bragg, 2014; De Petris et al., 2020) highlighting how such an approach is an effective tool that allows to give an height estimate with a density greater and greater than ordinary one based on ground surveys. It can be noted that in general, errors seldom exceed 3 m.

Shapiro-Wilk test proved that errors are normally distributed (W = 0.90, p-value = 0.33). No significant bias was detected by t-test (t = 0.87, p-value = 0.41). These results suggest that the proposed approach is not affected by systematic errors; conversely a white noise like error component is present. Moreover, $\sigma_{\hat{\beta}}$ average value was 2.19 m proving that LSA theoretical uncertainty was consistent to the MAE found by comparing results to an external validation set. Finally, considering the FU σ_{rDSM}, no significant differences exist between rDSM and InSAR-LSA estimates.

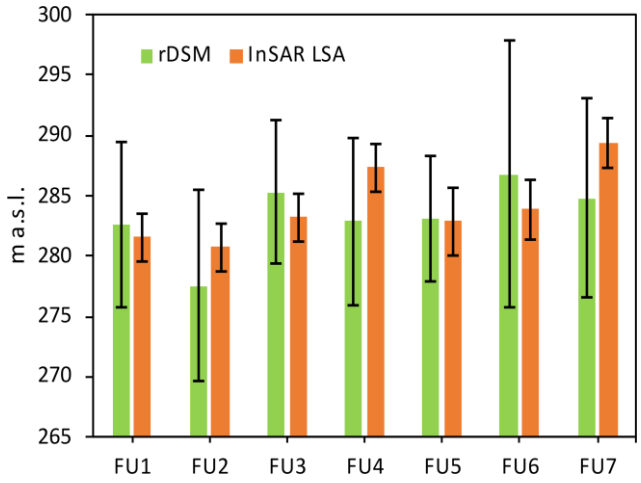

Figure 5. Comparison between reference FU forest heights and estimated ones. Error bars are for rDSM are σ_{rDSM} , while error bars of InSAR LSA derived heights are $\sigma_{\hat{\beta}}$.

4. Conclusions

In this work, LSA was applied to S1 InSAR data to retrieve forest height over AOI. Results proved that LSA using a weights matrix involving theoretical uncertainties of interferometric phases generates estimates having a MAE of 2.6 m. No significant bias was found and the uncertainty of estimates was consistent with MAE, suggesting that no need of validation set should be necessary to test the accuracy. Unfortunately, these preliminary results were explored over a single study area and using a single winter interferometric pair. Future developments will be expected to test the robust-ness of such approach over different forests

and involving many image pairs. Nevertheless, preliminary outcomes suggest that proposed approach could be a valid alter-native to retrieve forest height based on free SAR data and open software. These features make this method a first prototype of technological transfer of SAR technology into forest operative sector for supporting in cheaper way forest management.

References:

1. Segura, M., Kanninen, M.: Allometric models for tree volume and total aboveground biomass in a tropical humid forest in Costa Rica 1. Biotropica: The Journal of Biology and Conservation. 37, 2–8 (2005).

2. Hao, Z., Zhang, J., Song, B., Ye, J., Li, B.: Vertical structure and spatial associations of dominant tree species in an old-growth temperate forest. Forest Ecology and Management. 252, 1–11 (2007).

3. Larsen, D.R., Hann, D.W., Stearns-Smith, S.C.: Accuracy and precision of the tangent method of measuring tree height. Western Journal of Applied Forestry. 2, 26–28 (1987).

4. Bragg, D.C.: Accurately Measuring the Height of (Real) Forest Trees. Journal of Forestry. 112, 51–54 (2014). https://doi.org/10.5849/jof.13-065.

5. De Petris, S., Berretti, R., Sarvia, F., Borgogno Mondino, E.: When a definition makes the difference: operative issues about tree height measures from RPAS-derived CHMs. iForest-Biogeosciences and Forestry. 13, 404 (2020).

6. Hüttich, C., Eberle, J., Shvidenko, A., Schepaschenko, D.: Supporting a forest observation system for Siberia: Earth observation for monitoring, assessing and providing forest re-source information. (2014).

7. De Petris, S., Sarvia, F., Borgogno-Mondino, E.: RPAS-based photogrammetry to support tree stability assessment: Longing for precision arboriculture. Urban Forestry & Urban Greening. 55, 126862 (2020).

8. Vacchiano, G., Berretti, R., Motta, R., Mondino, E.B.: Assessing the availability of forest biomass for bioenergy by publicly available satellite imagery. (2018).

9. Accastello, C., Brun, F., Borgogno-Mondino, E.: A Spatial-Based Decision Support System for wood harvesting management in mountain areas. Land use policy. 67, 277–287 (2017).

10. De Petris, S., Sarvia, F., Orusa, Borgogno-Mondino, E.: Mapping SAR geometric distortions and their stability along time: a new tool in Google Earth Engine based on Sentinel-1 image time series. International Journal of Remote Sensing. 42, 9135–9154 (2021). https://doi.org/10.1080/01431161.2021.1992035.

11. De Petris, S., Sarvia, F., Borgogno-Mondino, E.: Multi-temporal mapping of flood damage to crops using sentinel-1 imagery: a case study of the Sesia River (October 2020). Remote Sensing Letters. 12, 459–469 (2021). https://doi.org/10.1080/2150704X.2021.1890262.

12. Sarvia, F., De Petris, S., Borgogno-Mondino E.: Multi-scale remote sensing to support insurance policies in agriculture: from mid-term to instantaneous deductions. GIScience & Remote Sensing. 57, 770–784 (2020). https://doi.org/10.1080/15481603.2020.1798600.

13. Reiche, J., Lucas, R., Mitchell, A.L., Verbesselt, J., Hoekman, D.H., Haarpaintner, J., Kellndorfer, J.M., Rosenqvist, A., Lehmann, E.A., Woodcock, C.E.: Combining satellite data for better tropical forest monitoring. Nature Climate Change. 6, 120–122 (2016).

14. Vollrath, A., Mullissa, A., Reiche, J.: Angular-Based Radiometric Slope Correction for Sentinel-1 on Google Earth Engine. Remote Sensing. 12, 1867 (2020).

15. Goldstein, R.M., Zebker, H.A., Werner, C.L.: Satellite radar interferometry: Two-dimensional phase unwrapping. Radio science. 23, 713–720 (1988).

16. Chen, C.W., Zebker, H.A.: Phase unwrapping for large SAR interferograms: Statistical segmentation and generalized network models. IEEE Transactions on Geoscience and Re-mote Sensing. 40, 1709–1719 (2002).

17. Braun, A.: Retrieval of digital elevation models from Sentinel-1 radar data–open applications, techniques, and limitations. Open Geosciences. 13, 532–569 (2021).

18. Hagberg, J.O., Ulander, L.M., Askne, J.: Repeat-pass SAR interferometry over forested terrain. IEEE Transactions on Geoscience and Remote Sensing. 33, 331–340 (1995).

19. Santoro, M., Askne, J., Dammert, P.B.: Tree height influence on ERS interferometric phase in boreal forest. IEEE Transactions on Geoscience and Remote Sensing. 43, 207–217 (2005).

20. Romero-Puig, N., Lopez-Sanchez, J.M.: A Review of Crop Height Retrieval Using InSAR Strategies: Techniques and Challenges. IEEE Journal of Selected Topics in Applied Earth Observations and Remote Sensing. (2021).

21. EEA: European forest types, (2006).

22. Chianucci, F., Minari, E., Fardusi, M.J., Merlini, P., Cutini, A., Corona, P., Mason, F.: Relationships between overstory and understory structure and diversity in semi-natural mixed floodplain forests at Bosco Fontana (Italy). iForest-Biogeosciences and Forestry. 9, 919 (2016).

23. Capolupo, A., Saponaro, M., Borgogno Mondino, E., Tarantino, E.: Combining interior orientation variables to predict the accuracy of Rpas–Sfm 3D models. Remote Sensing. 12, 2674 (2020).

24. IPLA: INDICAZIONI TECNICO-METODOLOGICHE PER LA REDAZIONE DEI PIANI FORESTALI AZIENDALI – PFA, http://www.regione.piemonte.it/foreste/images/files/pian_gest/dwd/nuova_legge/Indirizzi_PFA_2016_AllegatoA.pdf, (2009).

25. Borgogno Mondino, E., Fissore, V., Lessio, A., Motta, R.: Are the new gridded DSM/DTMs of the Piemonte Region (Italy) proper for forestry? A fast and simple ap-proach for a posteriori metric assessment. iForest - Biogeosciences and Forestry. 9, 901–909 (2016). https://doi.org/10.3832/ifor1992-009.

26. Borgogno Mondino, E., Fissore, V., Falkowski, M.J., Palik, B.: How far can we trust forestry estimates from low-density LiDAR acquisitions? The Cutfoot Sioux experimental forest (MN, USA) case study. International Journal of Remote Sensing. 41, 4551–4569 (2020).

27. Veci, L.: SENTINEL-1 Toolbox SAR Basics Tutorial. ARRAY Systems Computing, Inc. and European Space Agency: Paris, France. (2015).

28. ASF: ASF baseline tool, https://baseline.asf.alaska.edu.

29. Ferretti, A., Monti-Guarnieri, A.V., Prati, C.M., Rocca, F., Massonnet, D.: INSAR Principles B. ESA publications (2007).

30. Santoro, M., Shvidenko, A., McCallum, I., Askne, J., Schmullius, C.: Properties of ERS-1/2 coherence in the Siberian boreal forest and implications for stem volume retrieval. Re-mote sensing of environment. 106, 154–172 (2007).

31. Askne, J., Santoro, M.: Multitemporal repeat pass SAR interferometry of boreal forests. IEEE Transactions on Geoscience and Remote Sensing. 43, 1219–1228 (2005).

32. Grandin, R.: Interferometric processing of SLC Sentinel-1 TOPS data. In: FRINGE'15: Advances in the Science and Applications of SAR Interferometry and Sentinel-1 InSAR Workshop, Frascati, Italy, 23-27 March 2015 (2015).

33. Yagüe-Martínez, N., Prats-Iraola, P., Gonzalez, F.R., Brcic, R., Shau, R., Geudtner, D., Eineder, M., Bamler, R.: Interferometric processing of Sentinel-1 TOPS data. IEEE Trans-actions on Geoscience and Remote Sensing. 54, 2220–2234 (2016).

34. Goldstein, R.M., Werner, C.L.: Radar interferogram filtering for geophysical applications. Geophysical research letters. 25, 4035–4038 (1998).

35. Huang, Y., Van Genderen, J.L.: Comparison of several multi-look processing procedures in INSAR processing for ERS-1&2 tandem mode. In: ERS SAR Interferometry. p. 215 (1997).

36. Schreier, G.: SAR geocoding: data and systems. Wichmann (1993).

37. Richards, J.A.: Remote sensing with imaging radar. Springer (2009).

38. Clancy, J.: Site surveying and levelling. Routledge (2013).

39. Soja, M.J., Persson, H., Ulander, L.M.: Estimation of forest height and canopy density from a single InSAR correlation coefficient. IEEE Geoscience and remote sensing letters. 12, 646–650 (2014).

40. Hanssen, R.F.: Radar interferometry: data interpretation and error analysis. Springer Science & Business Media (2001).

41. Ebong, M.B.: Weights for least-squares adjustments of levelling networks. Survey Review. 29, 175–180 (1987).

42. Schwarz, C.R.: The trouble with constrained adjustments. Surveying and Land Information Systems. 54, 202–209 (1994).

43. Pepe, A., Calò, F.: A review of interferometric synthetic aperture RADAR (InSAR) multi-track approaches for the retrieval of Earth's surface displacements. Applied Sciences. 7, 1264 (2017).

44. Willmott, C.J., Matsuura, K.: Advantages of the mean absolute error (MAE) over the root mean square error (RMSE) in assessing average model performance. Climate research. 30, 79–82 (2005).

45. Shapiro, S.S., Wilk, M.B.: An analysis of variance test for normality (complete samples). Biometrika. 52, 591–611 (1965).

46. Ross, A., Willson, V.L.: One-sample T-test. In: Basic and Advanced Statistical Tests. pp. 9–12. Brill Sense (2017).

6 CONCLUSIONS

This thesis was aimed at exploring the potentialities and the limitations of S1 imagery for monitoring VS, longing for the technological transfer of proposed methodologies to local institutions/technicians involved in agro-forest resource management.

To achieve these tasks, two main approaches were provided, and four techniques were explored involving S1 and free software.

Preliminarily, geometric distortions of S1 images were detected and mapped in order to masking out unreliable observations and providing a more conscious use of SAR data. In fact, a mapping of these areas is desirable for a correct interpretation of derived information. In the first work (Section 3), a multitemporal mapping of SAR geometric distortions were performed using GEE and the available S1 imagery over Piemonte Region (NW Italy). An angle-based method was adopted and geometric conditions were tested at-pixel-level mapping distortion types (layover, shadow and foreshortening). The results show that proposed methodology can be proficiently used to mask unreliable observations, making possible to a priori be informed about the areas of a given territory that can be reasonably and reliably monitored by SAR data.

An operational application of the generated maps of distortions was given, concerning the possibility of monitoring different land cover classes in Piemonte. Thanks to this type of approach, it was possible to prove that, in Piemonte region, ascending orbit S1 acquisitions perform better, minimizing image deformation. Agricultural and urban areas present low distortions along the considered time series, while some forest types or bare soils show generally a low monitorability by S1. This is not a general conclusion since strictly depending on local topography. From an operational point of view, such an approach would permit to a-priori investigate if S1 data are suitable enough to monitor an area of interest.

After this propaedeutic work, the thesis was divided into two main parts.

The first part was aimed at qualifying the VS and its variation in time and space domains by using 3 different techniques: (i) amplitude-based; (ii) radar indices-based; (iii) polarimetry-based.

(i) The amplitude information was explored using S1 data and a method was proposed aimed at detecting flooded areas and giving an estimate of water depth (WD) based on free available (Section 4.1.1). The analysed flood event occurred on 3rd October 2020 in NW Italy along the Sesia river was assessed with special concern about damages affecting rice crop fields. In particular, Sentinel-1 pre- and post-event amplitude images were compared by differencing (ΔVV). ΔVV was processed at-pixel-level to detect submerged areas through the thresholding Otsu's method. The latter was adopted to make objective the selection of the proper threshold value to map areas with and without water from S1 data. The method is adaptive, making possible to automatically detect the threshold value accordingly to the specific area one is considering. A simplified morphological analysis was then performed by DTM tessellation to map WD. The simplified approach based on GIS and free available data was proposed to support flood related damage estimation. Simplicity and cheapness of the approach, coupled with the obtained WD uncertainty, are certainly interesting if compared with more complex methods based on hydrological models. These ordinarily require many inputs that are rarely available outside rivers and difficultly available for agricultural areas, especially during an unexpected and extreme event such as flood. Finally, in this work the amplitude information was proved to be effective in the detection of horizontal VS changes caused by flood.

(ii) Radar indices potentiality in the operative agro-forest sector was explored in section 4.2.1. In this work, authors highlighted that many approaches based on multitemporal analysis of optical-retrieved vegetation index time series were successfully applied to describe forest disturbances like forest fires. Conversely, only few works make use of multitemporal Synthetic Aperture Radar (SAR) data. Nevertheless, the literature about multitemporal analysis of post-fire dynamics trough the SAR imagery adoption is still limited and no works focusing on the post-fire dynamics monitoring (i.e. severity and recovery processes) were available. Moreover, forest fire effects mapping is the one related to the a-priori identification of the date when all the induced (direct and indirect) effects of the event are assumed to be detectable and concluded. Most of the approaches in literature proceed by comparing a "before" and an "after" image to map fire severity, excluding possible delayed effects affecting the whole vegetated ecosystem in the area. In the work reported in section 4.2.1, these issues were carefully considered and an alternative approach, based on dense time series of SAR-based indices exploring a large period preceding and following the date of the fire, was investigated. Proposed approach made possible to avoid any a-priori setting of the post-fire date to use for deriving differences relatable to severity and obtaining true estimate of the actual date when the local ecosystem reached its maximum of damage and, consequently, the rate of system decay. Such information was used to derive severity maps that are expected to more properly represent the actual after-event situation. Moreover, the same approach, made it possible to investigate the reaction of the system (recovery) at local (pixel) level providing a spatial representation of forest behaviour in terms of both resistance and resilience. Such mapping procedure is rare to be found in literature (even considering optical-based approaches). Anyway, even if

proposed, the adoption of SAR data in place of optical ones is expected to provide, during recovery, a more focused representation of those forest components related to significant volume changes (i.e. trees and shrubs) making other vegetated players, like grass, negligible.

(iii) Polarimetry technique was explored to detect and map both horizontal and vertical VS variations. Therefore, in the work proposed in section 4.3.1 a preliminary assessment about the polarimetric behavior of orchards after a storm was performed. The analysis was aimed at proposing a first methodological approach to detect orchard damage by a storm based on the PolSAR decomposition technique using S1 data. The joint adoption of free accessible S1 data, institutional free auxiliary data (a cadastral map and farmers' CAP application database), and open software (SNAP) constituted a peculiar trait of the proposed approach. It moves in the direction of technological transfer, aiming at making SAR data/techniques an operational tool for agronomic applications, with special concern about weather-related damages to crops, which could be of interest to insurance companies or public administrations. The results proved that storm damages significantly increase the H and α parameters. By contrast, the A parameter tends to be lower in the damaged orchards. This phenomenon is possibly related to the changes affecting VS in the damaged fields, where the crowns and branches of fallen/broken plants fill the inter-row space, changing the regular pattern ordinarily characterizing apple orchards. Based on this evidence, the authors proposed a methodology to map possibly damaged orchards that relies on the knowledge about the behavior of witness (and neighboring) undamaged orchards. The method permitted the mapping of the probability that an orchard is damaged or not, constituting a new free tool able to improve orchard

monitoring after a calamitous event by regional agencies and insurance companies. The proposed procedure is entirely based on S1 and free software making more easy the technological transfer of SAR data to the local technicians and institutions.

The second part of the thesis was aimed at quantifying VS by mainly measuring vegetation height. In particular, the InSAR techniques was explored by involving the phase component of complex SAR signal in order to measure forest height.

In this framework, InSAR techniques have been extensively adopted to retrieve digital elevation models (DEM) giving a representation of the continuous variation of Earth' topography, including forests and crops. The ordinary InSAR framework requires a further phase unwrapping step in order to recover unambiguously the actual topography over the entire scene. The latter was proved to fail over vegetation due to low coherence values and therefore all algorithms tend to avoid these areas during the unwrapping, making InSAR-derived DEM over vegetation very unreliable. In section 5.2, an alternate technique, not widely explored in literature, is considered for obtaining more reliable and accurate estimates of forest height from InSAR data by avoiding phase unwrapping. This method changes the working paradigm from a mapping problem involving the entire scene, to a local paradigm based on the comparison between a forest pixel interferogram and a reference one closely located outside the forest. Specifically, potentialities and limitations of such an approach were explored and discussed using simulated scenarios and subsequently applied to real forest area.

Theoretical scenarios were performed in the work reported in section 5.2.1, where a sensitivity analysis approach was adopted with the aim of properly initializing the relevant operational parameters (baseline and multilooking factor) to maximize the theoretical accuracy of the height difference between the forest and reference point. Some scenarios were proposed to test the resulting "optimal values" as estimated at the previous step. A simple model was, additionally, proposed and calibrated aimed at predicting the optimal baseline value (and

therefore image pair selection) for height uncertainty minimization. All our analyses were conducted using free available data from the Copernicus Sentinel-1 mission to support the operational transfer into forest sector. Finally, potential uncertainty affecting resulting height measures was quantified showing that a value lower than 5 m can be expected once all user-dependent parameters (i.e. baseline, multilooking factor, temporal baseline) are properly tuned.

To test and quantify the accuracy of proposed approach, the method proposed in section 5.2.1 was coupled to least squares adjustment (LSA) with the aim of retrieving accurate forest heights avoiding phase unwrapping. It was computed entirely using free available Sentinel-1 data and SNAP ESA software. Results presented in section 5.2.2 proved that LSA using a weights matrix involving theoretical uncertainties of interferometric phases generates estimates having a MAE of 2.6 m. No significant bias was found, and the uncertainty of estimates was consistent with MAE, suggesting that no need of validation set should be necessary to test the accuracy. Unfortunately, these preliminary results were explored over a single study area and using a single winter interferometric pair. Future developments will be expected to test the robustness of such approach over different forests and involving many image pairs. Nevertheless, preliminary outcomes suggest that proposed approach could be a valid alternative to retrieve forest height based on free SAR data and open software. These features make this method a first prototype of technological transfer of InSAR technology into forest operative sector for supporting in cheaper way forest management.

In section 5.1.1, the InSAR estimates accuracy was compared to the one obtained by ordinary ground-based forest height surveys operated through hypsometers. In fact, ordinarily, forest height is surveyed by ground sampling adopting hypsometers. The latter suffers from many errors mainly related to the correct tree apex identification (not always well visible in dense stands) and to the measurement process itself. Therefore, in section 5.1.1 an operative method for estimating height measurement uncertainty (σ_H) was proposed using the variance propagation law. Results proved that σ_H could vary between 0.5 m up to 20 m

(worst case). Sensitivity analysis shows that terrain slopes and distance poorly affect σ_H, while angles are the main drivers of height uncertainty. Finally, to give a practical example of such deductions tree height uncertainty was mapped at the global scale using Google Earth Engine and summarized per forest biomes. Results proved that in temperate zone, forest height uncertainty ranges from 0.5 m to 4 m. These results proved how the accuracy founded in section 5.2.2 using InSAR and LSA levelling net approach is consistent to the one obtained by using hypsometer. Nevertheless, the former technique allows to obtain forest height estimates over large areas and possibly with higher sampling density than the ordinary one, proving how the InSAR and LSA approach can effectively measure vertical VS longing for a technological transfer in forestry operative context like forest inventory.

Unfortunately, despite proposed works in this thesis were developed trying to fill the technological transfer gap, a real adoption of proposed procedures by local vegetation managers (i.e., farmers, local institutions, technicians) was not currently performed. Indeed, during Ph.D. period the pandemic spread of COVID-19 limited the interaction with local vegetation-related players. Despite this limitation, all presented works were developed in order to follow all the technological transfer requirements like:

(a) *Imagery coverage.*

The adoption of S1 imagery (in particular the Interferometric wide swath data) allows to acquire information about large areas with medium-high temporal resolution (6 days) improving the monitorability capability of such SAR data all over the world.

(b) *Complex processing.*

Many SAR processing techniques (like the InSAR unwrapping) computed by ordinary software, in the most of cases, hides the consciousness and an easy interpretability of results, making derived measures unreliable. The jointly adoption of SNAP and open-source

software (i.e., R and GEE) allows a more rapid access to pre-processed images allowing users to directly focus on their specific applications. Moreover, the open-source codes generated are prototypes that can be assumed as first standardized algorithms permitting a replication of proposed methodology in other study areas thanks to their designed adaptivity, making possible to automatically perform analysis accordingly to the specific area features one is considering.

(c) *Data and Software availability.*

All proposed procedures are based on free accessible data, easily downloadable from institutional repository. Moreover, the adoption of free processing software allows to explore new scenarios where SAR and Geographic data, properly managed, improved the analysis and spatialization of VS features making easier their use in a standardized and replicable way by a users' community different from that of researchers.

Future developments will be expected to implement proposed procedures into operative routines. For example, the work proposed in section 4.1.1 could be adopted by regional institution to rapidly provide local refund to farmer after flood. The work proposed in section 4.2.1, could be adopted by forest institutions to plan new silvicultural treatments to prevent new forest fires. The work proposed in section 4.3.1 could be adopted by agricultural insurances to focus their ground controls. Finally, the works in section 5.2.2 could be used to obtain a spatial estimates of forest height useful for inventory purposes.

The entire Ph.D. experience was developed by author with the opinion that agro-forest sector is very pragmatic and therefore to improve it, researchers should design their works longing for a real application of found outcomes.

Acknowledgements:

Vorrei ringraziare Martina per avermi supportato/sopportato in questi anni di gioie e fatiche. Un grazie alla mia famiglia per aver investito tempo e pazienza nella mia crescita tanto personale quanto intellettuale. Un sincero ringraziamento va ai miei amici per aver alleviato la stanchezza e lo stress di questi anni. In fine vorrei ringraziare il mio tutor e i miei colleghi con i quali ho condiviso le idee, le fatiche del lavoro ma soprattutto le soddisfazioni di una crescita comune.